Doctoral Dissertation
Jožef Stefan International Postgraduate School
Ljubljana, Slovenia, June, 2009

Supervisor: *Prof. Dr. Marija Kosec*

Evaluation board:

Prof. Dr. Tomaž Kosmač, Chairman, Institute Jožef Stefan, Ljubljana
Assist. Prof. Dr. Marko Hrovat, Member, Institute Jožef Stefan, Lubljana
Prof. Dr. Breda Mirtič, Member, Naravoslovnotehniška fakulteta, Ljubljana

Martina Oberžan

HIGH-ALUMINA PORCELAIN WITH IMPROVED MECHANICAL AND THERMAL PROPERTIES

Doctoral Dissertation

VISOKO GLINIČNI PORCELAN Z IZBOLJŠANIMI MEHANSKIMI IN TERMIČNIMI LASTNOSTMI

Doktorska disertacija

Supervisor: Prof. Dr. Marija Kosec

Co-Supervisor: Dr. Janez Holc

June 2009

MEDNARODNA PODIPLOMSKA ŠOLA JOŽEFA STEFANA
JOŽEF STEFAN INTERNATIONAL POSTGRADUATE SCHOOL
Ljubljana, Slovenia

Index

Abstract

The study presents the influence of increasing the amount of β-spodumene ($LiAlSi_2O_6$) as Li_2O-content flux on phase composition, microstructural evolution and physical properties of high alumina porcelain material containing ~61% of Al_2O_3.

New porcelain compositions based on clays and high amount of calcined alumina were developed with the introduction of Li_2O in combination with K_2O as flux. Sintering behaviour, phase composition, microstructure and physical properties of new compositions were investigated in comparison with reference composition containing K_2O and Na_2O as flux. Li_2O was added in the amount of 1.0, 1.2 and 1.6 wt.% via calcined commercial spodumene concentrate. Conventional ceramic processing routes comprising wet milling and extrusion technique were used to prepare the test samples, which were fired in the laboratory furnace at seven selected temperatures in temperature range 950−1350 °C and in the industrial gas kiln at 1315 °C.

Li_2O-bearing compositions reach higher degree of densification at lower temperature in comparison to reference composition. The influence on densification is greater with the amount of Li_2O increasing. During heat treatment the phase composition of bodies is influenced by the amount of Li_2O added. It is evident, that the diminishing of quartz at the presence of Li_2O in temperature range 1150 to 1250 °C is due to quartz reaction with β-spodumene forming lithium aluminium silicates. The first reaction product is $LiAlSi_3O_8$. The reaction at higher temperature leads to the formation of $Li_xAl_xSi_{1-x}O_2$, when the amount of Li_2O is 1.6 wt.%. In the process of quartz reaction with lithium compounds lithium aluminium silicates with higher amount of SiO_2 are formed. The presence of lithium minerals, which are characteristic by low thermal expansion, contributes to the lower CTE of bodies containing Li_2O.

Homogeneous microstructure, high bulk density and absence of quartz contribute to improved flexural strength of compositions with 1.0 and 1.2 wt. % of Li_2O fired at 1300 °C. When fired at higher temperature all compositions containing Li_2O attain noticeably lower flexural strength mainly due to bloating phenomena, which increases with the increasing amount of Li_2O as obvious from bulk density decrement.

The increasing amount of Li_2O greatly affects the deformation during firing in industrial gas kiln, which considerably increases with the increasing amount of Li_2O. Under the existent firing schedule in industrial kiln the most favourable mechanical and thermal characteristics in view of industrial perspective are attained by composition with 1.0 wt. % Li_2O.

Our investigations of Li_2O as the main flux constituent in high alumina porcelain bodies show that Li_2O is a strong fluxing agent contributing to the attainment of high mechanical strength and good thermal shock resistance, which strongly depends on its amount and firing conditions. Generally, it lowers the firing temperature. New body formulations suitable for the industrial application were developed.

Povzetek

Delo opisuje proučevanje vpliva naraščajoče količine Li_2O kot talila na sintranje, fazno sestavo, razvoj mikrostrukture in fizikalne lastnosti gliničnega porcelana z vsebnostjo Al_2O_3 ~61 ut.%.

Z uvedbo Li_2O kot talila v kombinaciji s K_2O smo razvili nove porcelanske materiale na osnovi glin, kaolinov in visoke vsebnosti kalcinirane glinice. Ponašanje novih materialov pri sintranju in njihove fizikalne lastnosti smo proučevali primerjalno z referenčnim materialom, ki je vseboval kot talilo K_2O and Na_2O. Li_2O v količini 1.0, 1.2 and 1.6 ut.% smo dodali tako, da smo uporabili kalciniran spodumnov koncentrat, $LiAlSi_2O_6$, ki je razpoložljiv na trgu. Testne vzorce, katere smo žgali v laboratorijski peči na sedmih izbranih temperaturah v temperaturnem območju 950–1350 °C in v industrijski plinski peči na temperaturi 1315 °C, smo pripravili z običajnimi keramičnimi tehnološkimi postopki, ki vključujejo mokro mletje in ekstrudiranje.

Materiali, ki vsebujejo Li_2O, dosežejo višjo stopnjo zgoščevanja pri nižji temperaturi v primerjavi z referenčnim materialom. Vpliv Li_2O na zgoščevanje je tem večji, čim večja je njegova količina. Količina dodanega Li_2O vpliva na fazno sestavo materiala v postopku toplotne obdelave. Rezultati raziskav so pokazali, da je v temperaturnem območju 1150 do 1250 °C zmanjševanje količine kremena ob prisotnosti Li_2O posledica reakcije kremena z β-spodumnom, pri čemer nastaja $LiAlSi_3O_8$. Naraščajoča količina Li_2O pospešuje reakcijo kremena z litijevimi spojinami. Pri višji temperaturi in prisotnosti Li_2O v količini 1.6 ut.% se reakcija nadaljuje, tako da nastane $Li_xAl_xSi_{1-x}O_2$. Pri reakciji kremena z litijevimi spojinami se tvorijo litijevi alumosilikati z višjo vsebnostjo SiO_2. Prisotnost litijevih mineralov, ki so značilni po nizkem termičnem raztezku, prispeva k zmanjšanju termičnega raztezka pri materialih, ki vsebujejo Li_2O.

Materiali, ki vsebujejo 1.0 in 1.2 ut. % of Li_2O imajo po žganju na temperaturi 1300 °C homogeno mikrostrukturo, visoko volumsko gostoto in izboljšano mehansko trdnost v primerjavi z lastnostmi gliničnega porcelana s standardno sestavo. Po žganju na višji temperaturi dosežejo vsi materiali z Li_2O precej nižjo upogibno trdnost v glavnem zaradi pojava napihovanja, ki je tem bolj izrazito, čim več Li_2O vsebuje material, kar se odraža tudi v zmanjšani volumski gostoti.

Naraščajoča količina Li_2O močno vpliva na deformacijo materiala pri žganju v industrijski peči, kjer se deformacija izrazito povečuje z povečevanjem vsebnosti Li_2O. Pri obstoječem režimu žganja v industrijski plinski peči je iz vidika industrijske uporabe najbolj primeren material z 1.0 ut. % Li_2O, pri katerem so dosežene najboljše mehanske in termične lastnosti.

Rezultati naših raziskav o uporabi Li_2O v visoko gliničnem porcelanu kažejo, da Li_2O kot prevladujoče talilo bistveno prispeva k doseganju visokih mehanskih trdnosti in dobri odpornosti na termične šoke, kar vse je v veliki meri odvisno od njegove količine in pogojev žganja. Prisotnost Li_2O vpliva na znižanje temperature žganja visoko gliničnega porcelana. Razvili smo sestave novih gliničnih porcelanov primernih za industrijsko uporabo.

Abbreviations

A	=	α-alumina
AL	=	Albite
BA	=	β- alumina
BEI	=	Backscattered Electron Image
BET	=	Nitrogen adsorption technique used to measure the specific surface area of a solid (Brunauer, Emmet and Teller, 1938)
BG	=	Bright grey or feldspar based glassy phase
CTE	=	Cofficient of Thermal Expansion
d_{50}	=	Median particle size determined by laser granulometry
D_B	=	Bulk density
D_w	=	Density of water at room temperature
DG	=	Dark grey or β-spodumene based glassy phase
DTA	=	Differential Thermal Analysis
EDS	=	Energy Dispersive Spectroscopy
F	=	Feldspar
Ø	=	Diameter of test sample
G	=	Glassy phase
IL	=	Illite
JCPDS	=	Joint Committee on Powder Diffraction Standards
K	=	Kaolinite
L.O.I.	=	Loss of ignition
LS	=	Lithium feldspar
LX	=	Lithium aluminium silicate
M	=	Mullite
MB	=	Microperthite
MC	=	Microcline
MM	=	Montmorillonite
MS	=	Muscovite
P	=	Pore
P_0	=	Open porosity
Q	=	α-quartz (SiO_2)
S	=	β-spodumene
SEI	=	Secondary Electron Image
SEM	=	Scanning Electron Microscopy
SN	=	Sanidine
TG	=	Thermogravimetry
XRD	=	X-ray Diffraction
XRF	=	X-ray Fluorescence
ΔT	=	Thermal shock resistance
W_d	=	Weight of dry sample
W_h	=	Weight of sample suspended in water
W_s	=	Weight of soaked sample in air

1 Introduction

Porcelain represents the basis of the ceramics knowledge and one of the most complex ceramic materials. Complexities arise first in the manufacturing process including raw materials, processing, forming and firing. The next complexities are due to the kinetic limitations, the phase transformations and the microstructure development during firing. New raw material alternatives and new research technique are opening economic legitimate reasons to continue the research of porcelains, thus enabling the modifications of materials and processing methods [1]. Advanced technologies with better energy management are currently the main efforts in the processing. They are directed towards the reduction of production costs without risking the product quality [2].

Depending on the application, such as household or technical field, porcelains are of different types. Technical porcelains find diverse application in electrotechnics, most often as insulating parts in electric transmission, distribution and protection. The development of electrical engineering dictates the necessity for porcelains with higher reliability. The reliability of porcelain strongly depends on microstructure and phase composition. Typical requirement for electrical porcelain are high mechanical strength and good thermal shock resistance.

1.1 Porcelain material

Porcelains are vitreous ceramic white wares with typical triaxial formulation, which consists of clay, acting as a binder in green state, fluxes, which are as low melting phase responsible for liquid formation in the system enabling densification, and filler for shrinkage and distortion reduction. Commonly composition of porcelain comprise about 50 wt.% clay, 25 wt.% flux and 25 wt.% filler. As typical for ceramics, porcelain formulations are heated to high temperatures during processing in order to speed up chemical reactions and to develop desired microstructure.

Microstructure of completely fired porcelains consists of coarse aggregate particles held together by almost fully dense glassy system with formed primary and secondary mullite crystals [3]. Number, type and physical distribution of phases is determined by the phase equilibrium and the thermal history of the material. Typical for the microstructure of porcelain as traditional clay-based silicate ceramics is its structure as a mixture of crystals, glass, grain boundaries, and porosity.

1.1.1 Porcelain, history and definition

The discovery of porcelain belongs to the Chinese, where in time of Han Dynasty in years 100–200 high firing glazed ceramic ware, recognized as the first true porcelain, was developed [4]. It was in time of Tang Dinasty about four hundred years later, when porcelain in nowadays aspect, as white and translucent glazed body, was developed to be manufactured in larger quantities and exported mainly to Islamic countries, where it was highly valuable. The Chinese produced porcelain from white kaoline (china clay) with high content of alkali and mica. First European porcelain was developed in 1709 by Johann Friedrich Böttger in Meiβen using kaolin, sand and chalk as raw materials. The manufacturing of feldspathic porcelain is claimed to be introduced after 1930, when the application of feldspar instead of chalk prevailed [4].

Among ceramic materials porcelain has the oldest tradition as an insulating material in electric engineering. In 1849, Werner von Siemens used the first porcelain insulators to insulate the telegraph line from Frankfurt am Main to Berlin [5]. Porcelain experienced a jump of his development in the 20-th century, his economic significance increased above all on the account of its growth into different areas of application, mostly in household and electrical engineering.

A wide range of traditional ceramic compositions is a mixture of clay, fedspar and flint. Typical composition ranges for different types of porcelains are presented in Figure 1.1-1 showing the ternary silica-leucite-mullite phase diagram [6]. By drawing the feldspar-metakaolin join on the diagram these compositions could be explained as quartz-clay-feldspar mixtures. The main differences among compositions are in the relative amounts and types of clay and feldspar used. With the increasing amount of

feldspar the amount of liquid formed at the eutectic temperature is increased and vitrification proceeds at lower temperatures. Increasing the clay amount on account of the feldspar amount increases the temperature of vitrification.

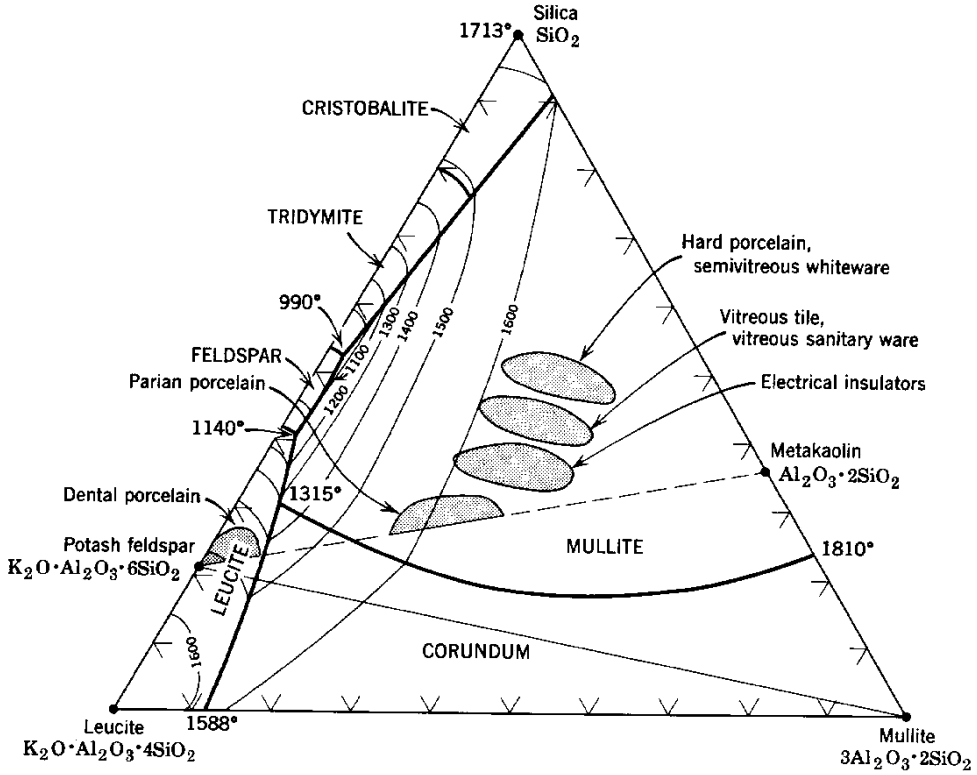

Figure 1.1-1. Phase equlibrium diagram silica-leucite-mullite. Ranges for triaxial commercial porcelain regions are identified [6].

Substantial amounts of viscous liquid are formed during firing the porcelain body. The temperature of liquid formation is lowered by the flux. It provides low melting phases that are essential for liquid formation at lower temperature. Its reaction with other constituents results in liquid which enables densification and formation of final microstructure [7].Vitrification indicates a high degree of melting on firing, which results in low open porosity and high content of glass (ordinary >40 vol. %).

Level of vitrification, pyroplastic deformation and microstructure are affected by the mineralogical composition of raw materials and by the level of equilibrium achieved [8,9]. Composition and processing parameters have a significant influence on final properties of the fired body, such as density, porosity, mechanical strength, whiteness, electrical and thermal characteristics [10].

Constant-temperature or isothermal diagrams are used to propose the forms that exist at equilibrium by subsolidus temperature. It is seen from isothermal diagram in Figure 1.1-2, which is an isothermal cut through the phase diagram from Figure 1.1-1, that the phases present at typical firing temperature of 1300 °C are mullite, quartz (almost always) and potassium aluminium silicate glass [11]. From isothermal diagram the composition of liquid and the amount of liquid for different compositions can be determined at chosen temperature.

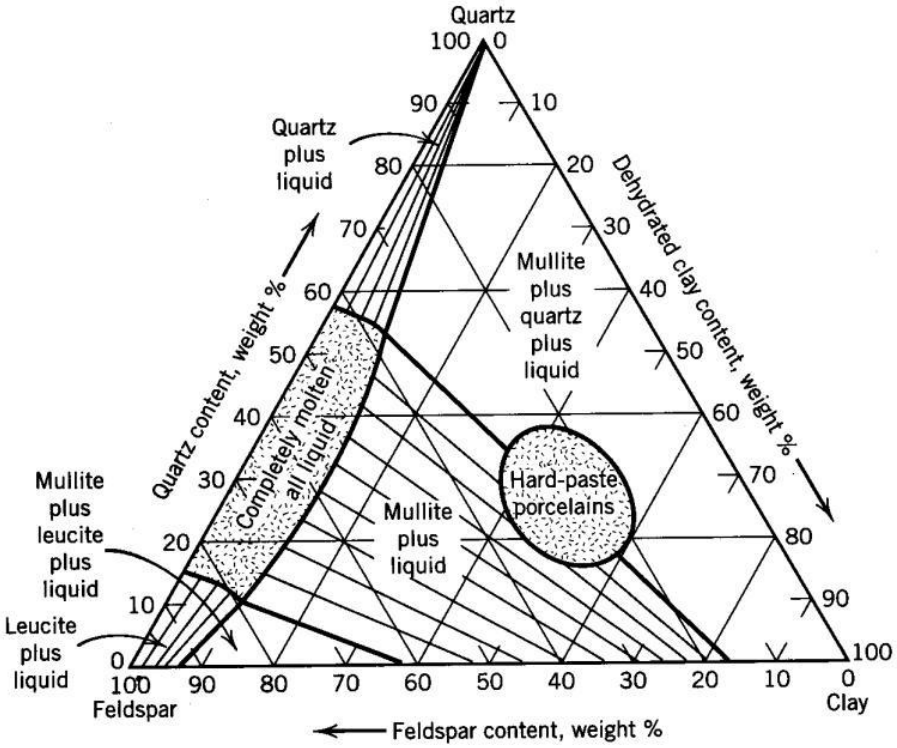

Figure 1.1-2. Isothermal phase diagram of system silica-leucite-mullite (1300 °C). At a typical firing temperature of 1300 °C phases present are mullite, quartz and potassium aluminosilicate glass [11].

The classical definition of porcelain is a translucent, impermeable ceramic with less than 0.5 vol.% of residual porosity. Its white color results from the high purity of its components. Compared with other ceramics porcelain has relatively high strength. Completely fired porcelain contains quartz or/and corundum and mullite crystals dispersed in a viscous silicate glass [11].

Porcelains are commonly classified into two types according to the firing temperature. The firing temperature depends on the ratio of kaolin, feldspar and quartz in porcelain composition [4]. First type porcelains are "hard porcelains" which are fired in temperature range ~1400 °C and second type are "soft porcelains" fired ~1200 °C. Besides, according to their use porcelains are classified as tableware, sanitary ware, chemical-technical and electrical porcelain. Ordinarily, porcelains are made of quartz, kaolin and feldspar. In alumina porcelains, which are primarily used for technical aims, corundum is partially or completely incorporated instead of quartz. Special types of porcelain are "frit porcelains" based on kaolin, quartz and alkali rich frit or "bone china" based on kaolin, pegmatite and bone ash [4].

1.1.2 Technical porcelain for electrical engineering

Technical porcelains are mainly applied in electrotechnics. They are understood to be materials in the “alkaline alumina silicate porcelain” group C 100 according to IEC 60672 [12]. Electrotechnical porcelains are grouped as a series of ceramic materials with special electrical, mechanical and thermal properties that distinguish them from other industrial materials by high dielectric strength and good resistance to the fracture. As dielectric material or insulator they play an inert rule in the electrical circuit. The prime property for an insulator is high dielectric strength and high resistivity. Eventual electrical breakdown is ordinary a consequence of both, first inherent electrical characteristics of the material, and second involved cracks, impurities, flaws, and other imperfections [13].

Insulators are inserted as a barrier between conductors and prevent or regulate current flow in electrical circuits. To be classified as an insulator material must fulfill the requirements of high resistivity, high dielectric strength, low loss factor, good mechanical properties and good dissipation of heat. Besides, insulators protect the conductors against humidity and corrosiveness from the environment. Ceramic insulators are widely used in electrical engineering where high reliability is required such as the application in power transmission lines as well as in microelectronic devices [14].

Porcelains are good insulators, because they are very resistant to the passage of electrical current.

Porcelain material is most proper for electric insulation in transmission and distribution of electricity due to its high resistivity, combined with other properties such as hardness and mechanical strength, high-temperature strength, high corrosion resistance, heat and weather resistance, complete absence of odor and taste and elegance [15]. The dielectric properties of the porcelain body are dependent on the characteristics of each phase present in the microstructure. With the variation in application temperature as well as continuous use at an elevated temperature the phase composition and microstructure of the porcelain body undergo change, thus affecting the dielectrical properties of porcelain body [16].

The strength of porcelain increases when corundum is used instead of quartz as filler [17]. Quartz inversion, from β- to α-quartz at 573 °C is responsible for deterioration in mechanical properties of the body [18]. To reach high mechanical strength in alumina porcelain its composition should consist of raw materials, which prevent the presence of quartz crystals after firing due to their mineralogical composition and particle size. α-corundum crystals embedded in microstructure essentially contribute to strength developmnent. They are characterized by high Young's modulus which is in direct correlation with strength [19].

1.2 Constituents of porcelain

Raw materials for porcelain compositions are generally grouped as primary raw materials as listed in Table 1.2-1 and less commonly used as secondary raw materials as listed in Table 1.2-2 [1].

Table 1.2-1. Primary raw materials for porcelain manufacturing [1].

Raw material	Nominal composition	Common impurities
Ball (plastic) clay	$Al_2O_3 \cdot 2SiO_2 \cdot 2H_2O$	Quartz, TiO_2, Fe_2O_3
Kaolin (china) clay	$Al_2O_3 \cdot 2SiO_2 \cdot 2H_2O$	montmorillonite, quartz
Soda feldspar	$Na_2O \cdot Al_2O_3 \cdot 6SiO_2$	K_2O, CaO, MgO, quartz
Potash feldspar	$K_2O \cdot Al_2O_3 \cdot 6SiO_2$	Na_2O, CaO, MgO, quartz
Nephelyne syenite	$K_2O \cdot 3Na_2O \cdot 4Al_2O_3 \cdot 9SiO_2$	CaO, MgO, quartz
Corundum	Al_2O_3	Na_2O
Quartz	SiO_2	TiO_2, Fe_2O_3

Table 1.2-2. Secondary raw materials for porcelain manufacturing [1].

Raw material	Nominal composition	Common impurities
Bentonite/montmorillonite*	$(M^{2+})(M^{3+})_4(SiAl)_8O_{20}(OH)_4 \cdot nH_2O$	not applicable
Glass frits	Company specific	not applicable
Petalite	$Li_2O \cdot Al_2O_3 \cdot 6SiO_2$	Na_2O, K_2O
Bone Ash**	$Ca_3(PO_4)$	Unknown
Talc	$3MgO \cdot 2SiO_2 \cdot 2H_2O$	Crysotile, CaO
Whiting	$CaCO_3$	$MgCO_3$
Zircon	$ZrO_2 \cdot SiO_2$	not applicable

*Highly variable divalent (M^{2+}) and trivalent (M^{3+}) cation levels in montmorillonites.

** Bone ash is commonly used as a flux for bone china.

1.2.1 Clays

Clays play an important role in the forming process of raw porcelain body providing the plasticity at the presence of water and assuring the green strength after drying.

Clays are natural raw materials composed mainly of clay minerals. Clay minerals are fine-grained (<0.002mm) sheet silicate minerals (phylosilicate minerals), which were formed as a result of weathering

of other silicates. They have variable amounts of water trapped in the mineral structure by polar attraction [1]. There is a vast range of clays in different locations all over the world suitable for porcelain production and different clays are often blended to reach the most desirable properties.

The main clay minerals are kaolinite, illite with mica structure and smectite as illustrated schematically in Figure 1.2-2 [1]. Kaolinite is the most common clay mineral formed by lamellar particles (typically up to 1μm long and 0.1 μm thick) arranged in cluster. Kaolinite particles firmly bind water molecules, this bond and their shape cause the plasticity in contact with water. Kaolinite has 1:1 layered structure consisting of alternate sheets of silicate tetrahedra and alumina octahedra. Naturally occurring kaolinite often coexists with minor constituents such as mica and quartz. Illite and smectite have 2:1 layered structure, where octahedral is positioned between two tetrahedra with additional interlayer cations that charge-balance substitutions in the octahedral and tetrahedral layers. Illites are characterized by Al^{3+} substitution for Si^{4+} and with the charge balance provided by interlayer K^{+}. Smectites take up water in the interlayer spaces, where it associates with the interlayer cations and causes an expansion. Dioctahedral smectite is montmorillonite which incorporates water and other impurities. Illite and smectite group clays are often located interstratified, and so many clays contain minerals from both groups [20,21].

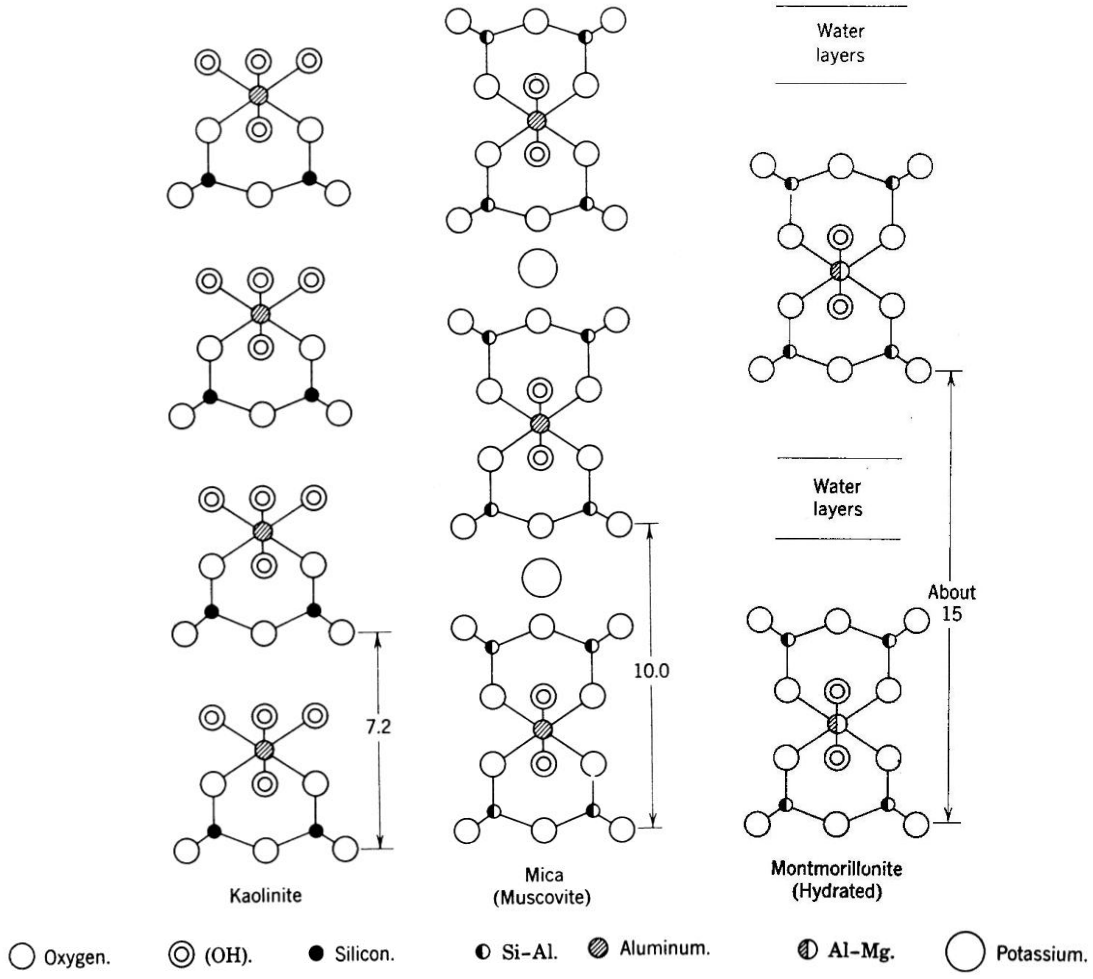

Figure 1.2-1. Schematic illustration of the layer structure of kaolinite, mica, and montmorillonite, showing the relative spacing between layers (in Ångstroms) [6].

In compounding porcelain formulations, the clay substance should be introduced as refined kaolin together with illite clay. At least part of kaolin must be fine grained type of kaolin, such as kaolin Zettlitz, assuring higher plasticity. The addition of illite clay was found to be advantageous since illite simultaneously improved the workability and increased the fusibility of the body and therefore permits higher content of filler like quartz or calcined alumina [20]. The average strength of porcelain body is increased with the illite addition because the more plastic body has superior workability and is less likely to develop ″structures″. Illite clays are commonly low in iron oxide content and as such not effecting in great

deal the desirable white colour of porcelain. Besides, low content of iron oxide simplifies the firing process, and there is less danger of overfiring. The beneficial effect of illite clay to mechanical strength is ascribed mostly to its plasticity and not to its flux properties [20].

1.2.2 Fillers

Fillers are classified as inert and non-plastic constituents in triaxial porcelain body. They provide resistance to cracking during drying and form a skeletal network during firing process [1]. They are generally the coarsest fraction of a porcelain body and have significantly larger particle size than the clays. They also have influence on reducing the viscosity and plasticity of raw body. As a skeleton former, fillers lower pyroplastic deformation during firing process. They have higher refractoriness than the fluxes, thereby preventing the densifying body from shrinking, warping and sagging excessively. Fillers strongly affect the mechanical performance of fired body as a result of strengthening and toughening the body at the microstructural level. In general, quartz and alumina are classified as filler in porcelain body.

Quartz is most commonly used filler in porcelain bodies because of its abundance and economy. It is the main crystalline polymorph form of silica group minerals [22]. Silica, SiO_2, occurs in various crystalline phases and its minerals are the most abundant minerals on the earth's crust. Quartz is stable up to 867 °C where transforms to β-tridymite, following the transformation at 1470 °C to β-cristobalite, which melts at 1713 °C [23]. In quartz structure silicon atom is tetrahedrally coordinated to four oxygen atoms. Every oxygen atom is bonded to two silicon atoms so that the tethahedral units are corner linked to form continuos chains forming a helix around the *c*-axis. An illustration of structural symmetry is shown in Figure 1.2-3, where a structural unit of α-quartz along the *c* –axis is presented [24].

Quartz has two crystalline forms, trigonal α-quartz or low quartz and hexagonal β-quartz or high quartz with its reversible transition at 573°C. Because of the reversible transition only α-quartz is present at room temperature. This phase change from α to β-quartz is accompanied by a change in symmetry, volume and shape, where β-phase has higher symmetry and higher volume [25]. Density of α-quartz is 2.65 g/cm^3. The high quartz structure (β-quartz) has been found much harder and more brittle than low quartz (α-quartz) despite their very close structural similarity [22].

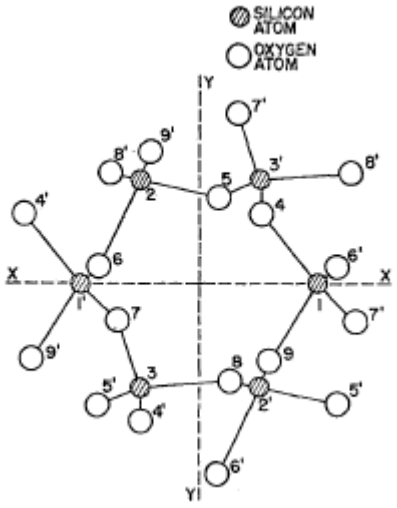

Figure 1.2-2. Structural unit of α-quartz along *c*- axis [24].

A classic fired porcelain body consists of 20 to 40 wt. % of quartz. Quartz remains unreactive at low temperatures and at high temperatures forms a high viscous liquid. Because of its patial melting together with feldspar in eutectic composition quartz is recognized as semi-inert filler. Larger quartz grains, which remain undissolved during firing process, are identified as α-quartz. It has been confirmed by previous investigations that quartz grains in different sizes have significant effects on mechanical strength of porcelain bodies [26].

The transformation of the undissolved quartz grains from β → α causes relatively large volume contraction ($\Delta V/V$ = - 0.68% for free quartz grain) and creates the basic source of cracking during cooling process [27]. Microcracks in quartz grains and the circumferential microcracks can be observed by electron

or light microscopy. They are a result of releasing the mechanical stress, which besides from the difference in thermal expansion between the quartz grains (α (20–750 °C) = 23 x $10^{-6}K^{-1}$) and glassy matrix (α (20–750°C) = 3 x $10^{-6}K^{-1}$) mainly occurs from β → α transformation. Cracks are commonly identified in and around quartz grains with size >20 μm.

The substitution of quartz is often related to actual studies of porcelain bodies with the aim to use waste products or to shorten firing cycles. One of important criteria in selecting the substitute is the requirement for low iron oxide content. Additionally, the modification of composition is necessary, if the substitute affects the rheological characteristics of raw body and thus influences the forming process. As waste products porcelain fired scraps [28] or flyash (a calcined byproduct of thermal power plant) can be used partly instead of the quartz in porcelain body [29]. For fast firing technologies the incorporation of pyrophyllite ($AlSi_2O_5OH$) as a replacement for quartz in porcelain body contributes to early vitrification, substantial reduction in the thermal expansion, reduction in shrinkage during firing and improved flexural strength in comparison to standard body [30,31].

Corundum (α-Al_2O_3) is the second commonly applied filler in porcelain body. Among the main criteria in selecting the most proper corundum for particular porcelain body are the chemical purity and the primary crystal size. In alumina porcelain bodies α-Al_2O_3 with >99.8% of Al_2O_3 and low sodium oxide (<0.2%) content is used. Grains of α-Al_2O_3 are normally composed of single flat crystals with the thickness of about one fifth of its diameter. The crystalline form of α-Al_2O_3 is of the corundum type with rhombohedral structure which is very close to hexagonal structure. The unit cell contains two Al_2O_3 molecules, where the oxygen atoms are arranged in nearly hexagonal close packing with the aluminium atoms occupying two-thirds of the octahedral interstices. As shown in Figure 1.2-3, the corundum structure could as well be viewed as a hexagonal cell consisting of six Al_2O_3 molecules with alternate layers of aluminium and oxygen atoms located perpendicular to the *c*-axis [32].

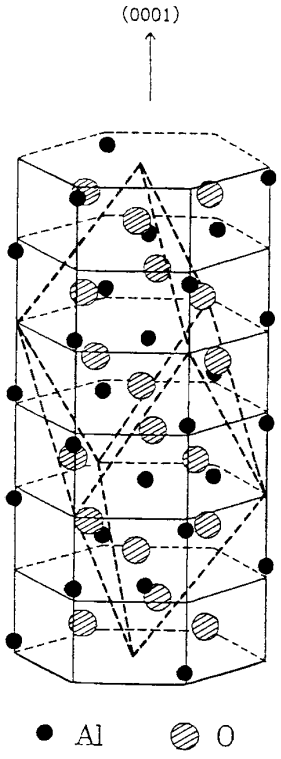

Figure 1.2-3. The structure of corundum viewed as hexagonal close packing with alternate layers of oxygen and aluminium atoms [32].

Corundum is electrical insulator with high heat resistance and excellent resistance to corrosion and wear. It has the melting point of 2054 °C, the density of 3.97 g/cm^3 and hardness of 9 according to Mohs scale. Regarding the hardness corundum is the second hardest material after diamond. Polycrystalline sintered α-Al_2O_3 with ≥99.5 wt. % of Al_2O_3, relative density of ≥0.98 and nominal grain size 5 μm is characteristic by the CTE of 8.1 x $10^{-6}K^{-1}$ in temperature range from 0 to 1000 °C, thermal conductivity of 33 $W{\cdot}m^{-1}{\cdot}K^{-1}$ at 20 °C, elastic modulus of 416 GPa at 20 °C and flexural strength of 380 MPa at 20 °C [33].

A lot of research work has been done since Austin et al. [34] in 1946 published the results of strengthening the whiteware bodies by introducing calcined alumina in standard bodies and established its priorities in comparison to quartz. It was confirmed later by other researchers that finely ground α-alumina improved the mechanical properties of porcelain body which was ascertained by the increased bending strength, elastic modulus, microhardness and fracture toughness [5,35,36,]. α-alumina particles present in a viscous glassy matrix of porcelain act as fracture resistant dispersoids [33]. The composition with smaller dispersed particles, with an average particle diameter of around 10 μm, has higher strength due to the fact, that small particles decrease the mean free fracture path per unit value more effectively than larger particles [19]. In alumina porcelain body corundum particles exist as inert inclusions in the feldspatic glassy phase up to 1350 °C as determined from that height and width of corundum X-ray diffraction peaks, which remain unchanged in temperature range from 1200 to 1350 °C [36].

Alumina porcelain bodies are classified as low-alumina with α-alumina addition up to 30 wt.% and high-alumina with 30 to 40 wt.% of α-alumina added. The flexural strength is commonly over 90 MPa for low- and over 140 MPa for high-alumina porcelain bodies [12]. Since the cost of α-alumina is relatively high, the main goal of many prior investigations was to achieve the high mechanical strength of porcelain body with complete or partial replacement of α-alumina without significantly affecting the firing temperature. Sintered bauxite with low content of iron oxide is possible substitute for α-alumina as claimed in the research reports by Libermann [5,19]. The flexural strength over 200 MPa was attained with the introduction of fine quartz powder (mean particle size 1.0 μm), which transformed into cristobalite, at alumina porcelain bodies containing only 15 wt.% of corundum and firing temperature between 1300 and 1350 °C [36,38]. Boehmite gel addition as partial replacement for alumina was found to contribute both mechanical strength and thermal shock resistance of alumina porcelain body fired at 1300 °C [39].

1.2.3 Fluxes

Flux provides low melting phase and lowers the temperature of liquid formation during firing process. The liquid phase reacts with other constituents of the body, affecting their solubility and new crystal formation [40]. Viscous liquid consisting of flux and decomposition particles of clay in porcelain body enables vitrifying process, which starts ~1000 °C. Besides filling interconnected pores the liquid promotes the mobility of species through diffusion during maturing process. The viscosity of the liquid phase is greatly influenced by the type of fluxing agent and the firing schedule. It substantially affects the microstructure of fired body, particularly amount, morphology and size of porosity [41,36]. Viscous liquid solidifies to a glass, while fired body is cooling. This glassy phase acts as a matrix for dispersed persistent and newly formed crystal phases [20].

Feldspars are most often used in porcelain bodies as fluxes. Feldspars are low-melting aluminum silicate minerals classified as K-feldspars (microcline, sanidine, orthoclase) and as plagioclase feldspars (albite, oligoclase, andesine, labradorite, bytownite, anorthite). Most commonly used are potassium, sodium and calcium feldspars.

Potassium feldspar ($K_2O{\cdot}Al_2O_3{\cdot}6SiO_2$) is major and mostly used flux in porcelain formulations. It is present in monoclinic crystalline form as orthoclase or sanidine and triclinic form as microcline, among them orthoclase is the most common. Potassium feldspar also contains minerals albite (sodium feldspar) and anorthite (calcium feldspar). The melting point of pure potassium feldspar is 1150 °C. Depending on the composition of potassium feldspar, its particle-size distribution and its firing schedule, the eutectic melt forms between 900 and 1000 °C. The starting point of densification process is congruent with the start of melt formation at eutectic temperature [8]. According to the ternary phase diagram for the system K_2O-Al_2O_3-SiO_2 [42], as shown in Figure 1.2-4, the eutectic composition of potash feldspar and silica melts at 985 °C. Potassium feldspar forms high viscous molten phases which slowly change their viscosity during firing process, thus less effecting the pyroplastic deformation of porcelain body at higher temperatures.

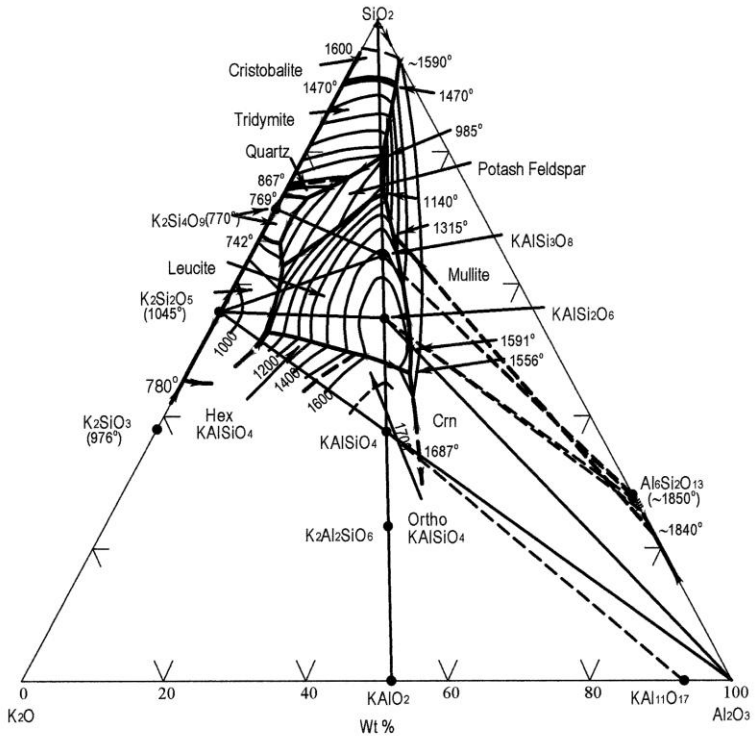

Figure 1.2-4. Ternary phase diagram for the system K_2O-Al_2O_3-SiO_2. Crystalline phases: Cristobalite, SiO_2; Trydimite, SiO_2; Quartz, SiO_2; Corundum, Al_2O_3; Mullite, $3Al_2O_3{\cdot}SiO_2$; Potash feldspar, $K_2O{\cdot}Al_2O_3{\cdot}6SiO_2$; Leucite, $K_2O{\cdot}Al_2O_3{\cdot}4SiO_2$ [42].

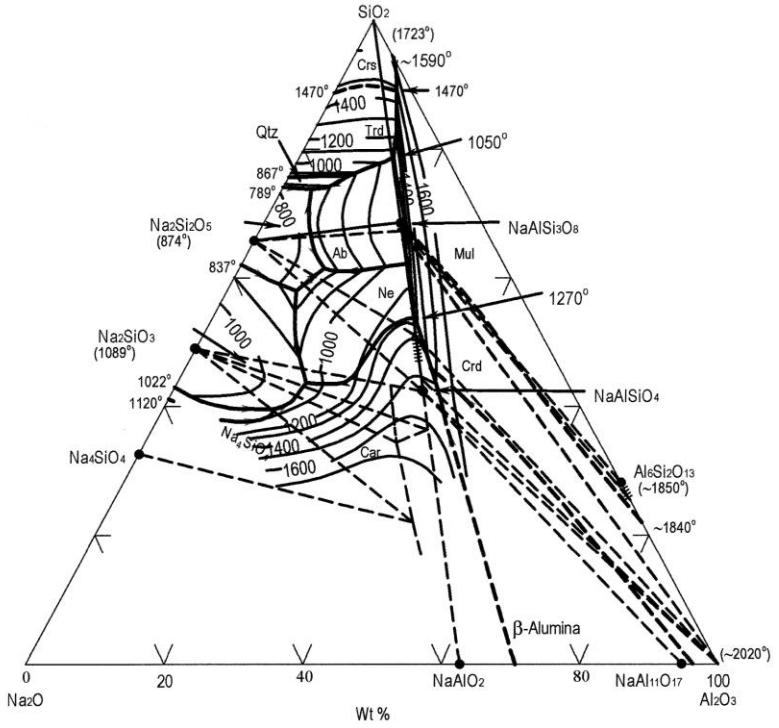

Figure 1.2-5. Ternary phase diagram for the system N_2O-Al_2O_3-SiO_2. Crystalline phases: Crs - Cristobalite, SiO_2; Trd – Trydimite, SiO_2; Qtz - Quartz, SiO_2; Corundum, Al_2O_3; β-alumina, $NaAl_{11}O_{17}$, Mul - Mullite, $3Al_2O_3{\cdot}SiO_2$; Ab - Albite, $Na_2O{\cdot}Al_2O_3{\cdot}6SiO_2$; Ne - Nepheline, $Na_2O{\cdot}Al_2O_3{\cdot}2SiO_2$; Crd – Carnegieite, $Na_2O{\cdot}Al_2O_3{\cdot}2SiO_2$ [43].

Albite ($Na_2O{\cdot}Al_2O_3{\cdot}6SiO_2$) is commonly applied as sodium feldspar in porcelain bodies. Its crystal structure is triclinic. The melting point of pure sodium feldspar is 1118 °C [4]. Sodium feldspar molten phases are less viscous at the same temperature than those of potassium feldspar, thus more effecting pyroplastic deformation, and this should be considered when applying it as principal or auxiliary flux [4]. Sodium feldspar and silica form the eutectic melt at 1050 °C as shown by ternary phase diagram for the system N_2O-Al_2O_3-SiO_2 [43] in the Figure 1.2-5, which indicates that sodium feldspar has higher liquid formation temperatures by the presence of silica in comparison to potassium feldspar. The eutectic composition of sodium feldspar contains 3.2 mol% less SiO_2 than the corresponding potassium eutectic composition [8].

As an auxiliary flux in porcelain bodies nepheline syenite and lithium bearing mineral may be used to reduce the firing temperature [1,44].

Nepheline syenite ($K_2O{\cdot}3Na_2O{\cdot}4Al_2O_3{\cdot}9SiO_2$) consists of minerals nepheline, albite and microcline, while the prevailing minerals are nepheline and albite. It is distinguished from feldspar in higher alkali and alumina oxide content. Typically, it has higher alkali:silica ratio (4:9) in comparison with feldspars (1:6), while alkali:alumina ratio is the same. Compared to feldspar nepheline syenite is lower in silica and contains no free quartz. Its melting point is around 1020 °C C [45]. In whiteware bodies nepheline syenite increases the alkali content of glassy phase and decreases the firing temperature. The viscosity of glassy phase decreases with the amount of nepheline syenite added. Due to its strong fluxing action it considerably decreases the soaking time required to attain the optimal microstructural characteristics [41]. It was found through investigations that a porcelain body containing both potassium feldspar and nepheline syenite gained a more optimal glassy phase composition and favorable internal stress, which increased the strength [46,47]. In high alumina porcelain with lower total amount of flux the combination of nepheline syenite and feldspar was determined as most adequate [19].

Among thirteen known lithium minerals major commercial sources of lithium are spodumene ($Li_2O.Al_2O_3.4SiO_2$ or $LiAlSi_2O_6$), petalite ($Li_2O.Al_2O_3.8SiO_2$ or $LiAlSi_4O_{10}$), lepidolite ($(K_2(Li,Al)_{5\text{-}6}[Si_{6\text{-}7}Al_{2\text{-}1}O_{20}](OH,F)_4$), called also lithium mica, and amblygonite ($LiAl(PO_4)(F,OH)$). Lithium minerals are mostly found in pegmatites. The approximate chemical composition and lithia content of main minerals that are of commercial interest is presented in Table 1.2-3 [48].

Table 1.2-3. Lithia content in commercial lithium minerals.

Mineral	General formula	Li_2O (wt.%)
Spodumene	$Li_2O{\cdot}Al_2O_3{\cdot}4SiO_2$	4 -7
Petalite	$Li_2O{\cdot}Al_2O_3{\cdot}8SiO_2$	3.5 – 4
Lepidolite	$K_2(Li,Al)_{5\text{-}6}[Si_{6\text{-}7}Al_{2\text{-}1}O_{20}](OH,F)_4$	3-4
Amblygonite	$LiAl(PO_4)(F,OH)$	8 - 9

Spodumene as a flux with Li_2O content from 4 to 7 wt.% is most widely used in ceramic whitewares [48]. It is a monoclinic pyroksene and coverts irreversibly to tetragonal β-phase when heated to 1080 °C. The phase transformation is accomplished by volume expansion of ~30% and a decrease in specific gravity from 3.2 to 2.4 g/cm^3. The resulting β-spodumene is tetragonal and characterized by its low thermal expansion coefficient (~ 0.9 x10^{-6}K^{-1} in temperature range 20–1000 °C). β-spodumene has melting point at 1423 °C.

The colour of spodumene varies depending on iron content from nearly white in low-iron to dark green in high-iron crystals. Spodumene is higher in Li_2O content than petalite and thereby a little more readily fusible. Commercially available spodumene concentrates have higher contents of lithia up to 7.6 wt.%, which is very close to theoretical value of 8.03 wt.%.

Detailed information of Li-flux application in ceramics is described in Chapter 1.6.

1.3 Microstructure development of porcelain body

Different changes occur during firing of porcelain body resulting in more compact structure comprised of glass, crystals, and porosity. Vitrification process, i. e. densification with the aid of viscous liquid phase, is the main process during firing in almost all of silicate systems. Sintering mechanisms, such as melting, pore

coalescence and coarsening, are evolving contemporarily thus enabling densification. Other processes occurring during firing are attributed to phase transformations, which include as typical decomposition of clay minerals, polymorphic transformation, formation of amorphous phases, partial melting of feldspars and quartz due to their eutectic conditions, and formation of mullite continued by its growth.

A great part of porcelain studies was devoted to microstructure development during heat treatment and its correlation with final properties [49,50,51]. The complexity of microstructural evolution during heat treatment of porcelain body is the consequence of incomplete mixing and agglomeration of raw materials [3]. A series of chemical reactions appear during heat treatment of porcelain bodies. The sequence of single process mostly depends on the type of raw materials in the body. For conventional clay-quartz-feldspar system the process of firing could be simply divided into the main reactions, which consist of the transformations of the major component kaolinite through kaolinite-mullite reaction series to mullite, quartz inversion and dissolution, and fedspar transformation through sanidine continued by eutectic liquid formation.

Thermal behavior of single raw material or the mixture are recently investigated at a molecular/microscopic scale by combined *in situ* optical dilatometry and X-ray powder diffraction [25]. Kaolinite-mullite reaction series, as studied on natural kaolinite, begins with dehydroxylation to form metakaolinite ($Al_2O_3{\cdot}2SiO_2$) at ~550 °C[1,52]. This process can be represented by following equation

$$\underset{\text{kaolinite}}{Al_2O_3{\cdot}2SiO_2{\cdot}2H_2O} \xrightarrow{\sim 550\ ^\circ C} \underset{\text{metakaolinite}}{Al_2O_3{\cdot}2SiO_2} + 2H_2O\uparrow \qquad \text{Eq. 1.3-1}$$

Dehydroxylation process is an endothermic process, in which octahedrally coordinated aluminum in kaolinite reorganizes to mostly tertahedrally coordinated aluminum in metakaolinite. The transformation process from kaolinite to metakaolinite was studied in detail with electron diffraction data acquired by an enery-filtering transmission electron microscope by Lee *et al.* [51]. They reported that X-ray diffraction pattern of metakaolinite had no distinct diffraction peak, which indicates its amorphous nature. Corresponding electron diffraction patterns demonstrate that it still had some crystalline features. During heating in dehydroxylation process only $Al(O,OH)_6$ octahedral sheet might be disturbed, while SiO_4 terahedral sheet was not effected. Metakaolinite retained a short-range order at this temperature.

The next transformation occurs at ~950-1000 °C, when metakaolinite transforms to spinel-type structure and free silica as presented by the following chemical equation [1,52]

$$3(Al_2O_3{\cdot}2SiO_2) \xrightarrow{\sim 950\text{–}1000\ ^\circ C} 0.282Al_8(Al_{13.33}\oplus_{2.66})O_{32} + 6SiO_2 \qquad \text{Eq. 1.3-2}$$

or

$$3(Al_2O_3{\cdot}2SiO_2) \xrightarrow{\sim 950\text{–}1000\ ^\circ C} 0.562Si_8(Al_{10.67}\oplus_{5.33})O_{32} + 3SiO_2 \qquad \text{Eq. 1.3-3}$$

where $\oplus$ represents a vacancy. The predicted reaction products are γ-alumina-type phase ($0.282Al_8(Al_{13.33}\oplus_{2.66})O_{32}$) and an aluminosilicate spinel ($0.562Si_8(Al_{10.67}\oplus_{5.33})O_{32}$). Silica product is in amorphous form. According to the quotation of Carty and Senapaty [1] the exact structure of spinel phase is contraversial, since conflicting evidence present in the literature demonstrate the existence of either phase. They suggested the conversion to mullite by the reaction:

$$0.282Al_8(Al_{13.33}\oplus_{2.66})O_{32} \xrightarrow{\sim 1075\ ^\circ C} 3Al_2O_3{\cdot}2SiO_2 + 4SiO_2 \qquad \text{Eq. 1.3-4}$$

or

$$0.562Si_8(Al_{10.67}\oplus_{5.33})O_{32} \xrightarrow{\sim 1075\ ^\circ C} 3Al_2O_3{\cdot}2SiO_2 + 4SiO_2 \qquad \text{Eq. 1.3-5}$$

Lee *et al.* [51] showed that metakolinite maintains its short-order at least up to 920 °C, when the spinel-

type phase is formed. At 940 °C the gradual decomposition of metakaolinite promotes the formation of amorphous silica and nucleation of random oriented mullite crystals. In the early stage ~940 °C microcrystalline mullite was less then 10 nm, persisting up to ~1100 °C, and then abruptly increased at 1200 °C. The spinel-type phase, which is formed in advance of the mullite phase, coexists with the metakaolinite and the mullite phase up to around 1200 °C, which triggers the abrupt growth of mullite at 1200 °C. The initially formed spinel-type and mullite phases appeared to be Al-rich, while at higher temperatures it incorporates silica. The reactions in kaolinite lead to the formation of mullite before the melting process.

Mullite is generally termed as primary and secondary mullite. Primary mullite crystals are present in the clay relicts as compact aggregates (<0.5 μm long) of small crystals (~200 nm x 40 nm x 40 nm) with composition close to 2:1 mullite ($2Al_2O_3{\cdot}SiO_2$) [7]. The chemical composition of primary mullite is the consequence of more Al_2O_3-rich clay relicts. Chemical composition may vary dependent on the chemical composition of glassy environment [10]. Secondary mullite is characteristized by its prismatic needles, which are longer (>1μm) and situated in feldspar relicts. These acicular mullite is 3:2 type ($3Al_2O_3{\cdot}2SiO_2$). Primary mullite relicts serve as a seed for secondary mullite nucleation. The growth of mullite crystals from the clay-feldspar interface to less viscous feldspar relicts designates the transformation of primary mullite into secondary mullite [7]. Secondary mullite crystals are indicated after firing above 1200 °C [1,10,40].

Small mullite crystals recognized as tertiary mullite in size ~50 nm × 10 nm × 10 nm were identified joined to corundum grains in fired alumina porcelain [10]. They were formed by precipitation from Al_2O_3-rich glass in late stage of the microstructural evolution.

Mullite formation from clay systems is often influenced by the presence of impurities in the natural materials [53]. Illite group clays dehydroxylate between 350 and 600 °C and their original crystal structure is maintained until 700 °C, while kaolinite XRD reflections are lost upon dehydrohylation below 500 °C. The relict illite structure breaks down between 700 and 850 °C when liquid phase begins to form. Then spinel crystallizes from the octahedral portion (with the content of aluminium, magnesium and iron), grows in crystal size up to 1100 °C and melts at 1300 °C. The tetrahedral part of illite structure combines with any alkali oxide present and, beginning at 950 °C, forms a liquid phase. Thereby mullite derived from different types of clays grow to different sizes after similar heat treatment (>10 μm from illite clays, >1 μm from smectite clays and ~0.5 μm from kaolinite clay). The high alkali and Fe_2O_3 content of illite clay generates relatively low viscous silicate liquid facilitating the growth of mullite crystals. It was established that Fe_2O_3 acts as a mineraliser promoting the growth of mullite crystals in clay-based systems [7]. The collapse of illite structure and subsequent crystallization of metastable γ-alumina (indicated as spinel) is also observed by marked contraction of the dilatometric curve in the 900–1100 °C.

Mullite designates various Al to Si ratios referring to the solid solution $Al_{4+2x}Si_{2-2x}O_{10-x}$, with *x* raging between about 0.2 and 0.9 (about 55 to 90 mol% Al_2O_3) [54]. At different temperature and atmosphere conditions mullite is able to incorporate a number of transition metal cations and other foreign atoms. The crystal structure of mullite is characterized by very stiff chains of edge-connected AlO_6 octahedra running parallel to the crystallographic *c*-axis and cross-linked by tetrahedral chains consisting of $(Al,Si)O_4$ tertahedra. In mullite some of oxygen atoms positioned on tetrahedral connections are removed for charge compensation. This gives rise to formation of oxygen vacancies. The anisotropy of the bonding system has a major effect on the anisotropy of its physical properties. Parallel to crystallographic *c*-axis the highest longitudinal elastic stiffness, maximum of the thermal conductivity, fastest crystal growth, and highest corrosion is observed. Thermal expansion is highest parallel to crystallographic *b*-axis.

Highly reactive amorphous silica is formed during metakolinite decomposition. Feldspar grains and amorphous silica form the eutectic melt at around 1000 °C. The eutectic temperature is dependent on the type of feldspar. According to the ternary phase diagram for the system K_2O-Al_2O_3-SiO_2, as shown in Figure 1.2-4 and ternary phase diagram for the system N_2O-Al_2O_3-SiO_2 as shown in Figure 1.2-5, the eutectic composition of potash feldspar and silica melts at about 70 °C lower than the eutectic composition of sodium feldspar and silica. In porcelain bodies natural feldspars are used, where commonly both potassium and sodium feldspar are present in different amounts. Proposed ternary diagram for the typical porcelain system $NaAlSiO_4$-$KAlSiO_4$-SiO_2 is shown Figure 1.3-1 [55] indicating the eutectic between potassium feldspar, sodium feldspar and silica at 1020 °C.

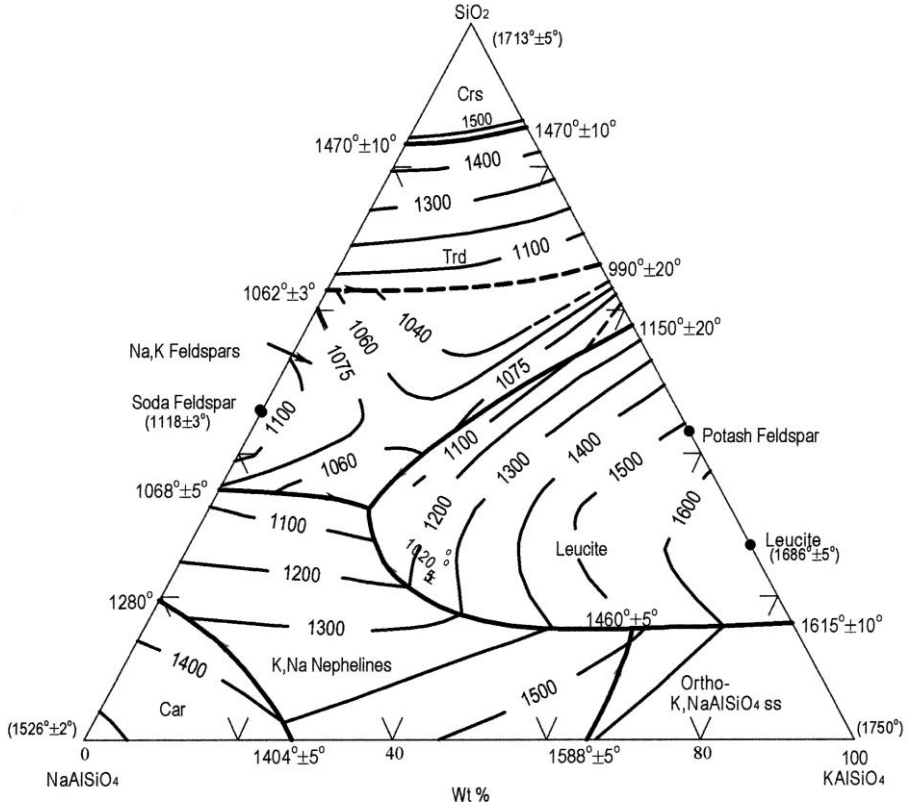

Figure 1.3-1. Ternary diagram for the system $NaAlSiO_4$-$KAlSiO_4$-SiO_2 [55].

With increasing temperature open porosity is gradually eliminated through liquid phase sintering. The fluidity of liquid phase is greatly affected by the composition of the flux. Cations in silicate melt act as glass formers (such as Si^{4+}), glass modifiers (such as K^+, Na^+) and amphoterics (such as Al^{3+}). The latter may behave either as glass modifiers or glass formers. The viscosity of fluid matrix increases with increased amount of silica or alumina and decreases with temperature rise. The amount and viscosity of liquid phase must correspond to the proper time of densification to prevent slumping and warping of the body under force of gravity. The viscosity of overall composition mainly depends on viscosity and amount of liquid phase present [6]. Silica rich glass composition in fired porcelain matrix shows local heterogeneities, but it is not possible to determine its exact composition by EDS peaks due to presence of small primary and tertiary mullite crystals, thus overlapping glass and crystal analysis [3].

Quartz, which is present in traixial porcelain body as a filler and/or impurity in clays and feldspars, undergoes the inversion of α to β-quartz at 573 °C without great effect on the constituents, since packed particle network has great flexibility. At higher temperatures quartz gradually dissolves in feldpatic melt. Above 1250 °C the dissolution of quartz increases and forms a silica-rich melt. The viscosity of melt increases with the increased amount of silica. The dissolution of quartz depends on the size of quartz grains, composition of the melt and firing temperature [8]. Undissolved quartz grains surrounded by amorphous silica-rich solution regions are uneven distributed in a complex matrix. Wide solution regions around quartz grains demonstrate their extensive dissolution. Large quartz grains (>30 μm) are subjected to cause cracks in grains and vitreous phase in their vicinity. These cracks are formed during cooling process by the release of microstresses within quartz grains and the glassy phase around them. Microstresses originate from the big difference in expansion coefficient between the crystalline quartz and glassy phase [56]. The quartz inversion from high temperature β-polymorph to low temperature α-polymorph accompanied by the guartz volume decrease produces sufficient strain to cause cracking of the quartz grain and the glassy matrix [21]. The extension of cracking is dictated by the quartz particle size and the cooling rate.

The microstructure of alumina porcelain containing around 51 wt.% of alumina is illustrated in Figure 1.3-2, where two SEM/SEI images of unetched surface of the same sample are presented. In image (a) the large quartz grain (>30 μm) with typical cracks is visible in glassy matrix with dispersed alumina grains and pores. Mullite grains embedded in glassy matrix are shown in image (b), which is recorded with higher

magnification than (a).

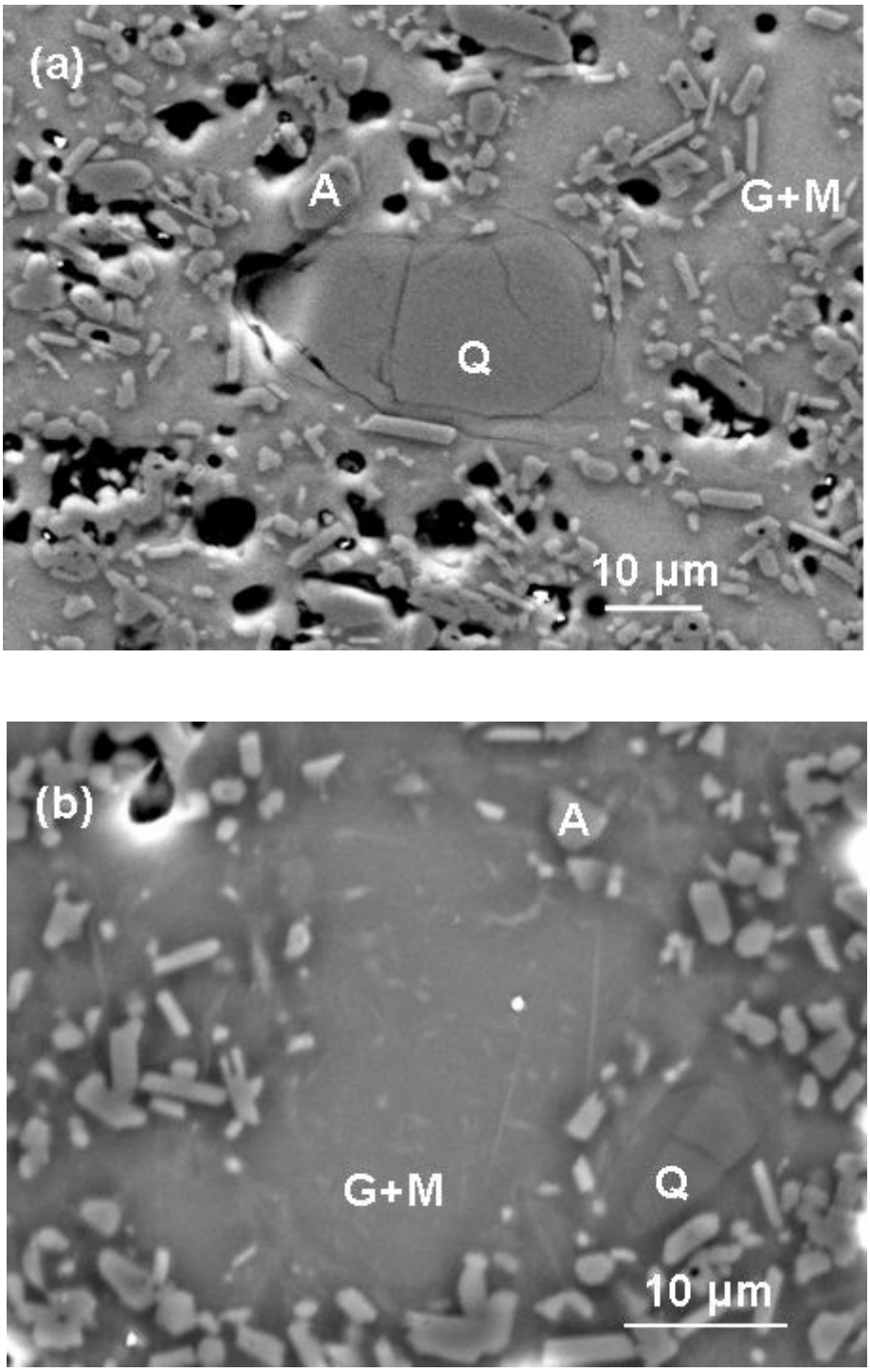

Figure 1.3-2. Microstructure of alumina porcelain. (a) Large quartz grain with cracks is visible in glassy matrix. (b) Mullite grains are embedded in glassy phase. Q – quartz, A – corundum, G +M – glassy phase with mullite grains (By courtesy of Danjela Kuščer, IJS).

Alumina porcelain bodies ordinary contain lower amount of glassy phase than typical quartz porcelain body, when defined part of quartz and/or clay is replaced by calcined alumina acting as insoluble second phase [17]. Adaptation of fluxing agent is necessary when the amount of alumina is increased in porcelain body [19]. The adaptation should reach the formation of highly reactive liquid phase being most homogenously distributed at ~1000 °C. Most of the quartz should be dissolved in this molten phase. The

low viscosity of initial molten phase should increase to achieve sufficient stability in densification during firing process. The introduction of illite clays and nepheline syenite into high alumina porcelain body was found to be suitable [19].

At a typical firing temperature of 1300 °C the phases present in common triaxial porcelain body are mullite, quartz and potassium alumino-silicate glass. In alumina porcelain body additionally corundum is present as shown in Figure 1.3-2. The phase distribution or microstructure of the fired body depends on the initial fabrication techniques, raw materials used, phase-equilibrium relations, and kinetics of firing process [1].

1.4 Mechanical strength of porcelain body

The mechanical strength of porcelain has been extensively studied and several theoretical considerations of factors affecting the strength of porcelain have been proposed. Three major theories attempt to explain the prevailing factors determining the strength.

According to mullite hypothesis and its later versions the strength of porcelain depends on the total amount of the interlocking mullite needles and glassy phase [50]. The formation of proper amount and size of mullite needles greatly depends on firing temperature. Mullite formation is effected by the composition and viscosity of liquid in which it grows [7]. Secondary mullite might increase strength more than primary mullite due to its acicular morphology and smaller needle diameter [52]. However, it was proven by further investigations, that besides the mullite amount and morphology other factors greatly affect the strength of porcelain body [57,18,58,26,17].

Matrix reinforcement hypothesis referenced in the literature as the prestressed theory claims, that mechanical strength of porcelain is mainly influenced by the prestresses induced between glassy matrix and crystalline material with higher thermal expansion than that of the glassy matrix [57]. Mechanical strength is improved by the mechanism, where the quartz is under the tensile stress and the glassy matrix around the quartz is under compressive stress which acts as prestress, since glassy matrix has lower thermal expansion than quartz. As claimed by Mattyasovszky-Zsolnay [57] the most favorable prestresses in quartz porcelain are attained, when the quartz grains are uniformly distributed in size of about 15 to 30 μm. The prestressing effect is related to the presence of quartz grains and firing temperature. Carbajal *et al.* found that the mechanical strength of porcelain body, in which the glassy phase is dominant, is mainly influenced by the stresses set up in glassy matrix, induced by the quartz grains [59].

When Warshau and Seider [18] studied the effect of quartz grain size from 125 μm to 3 μm on mechanical properties of porcelain body they found that the increase in strength is not mainly influenced by the prestresses. They ascribed the increase in strength to the transition in type of fracture from interconnected matrix fracture, which was found with the large grain sizes of quartz, to internal and peripheral fracture for quartz grains in size 25 μm and below. The maximum flexural strength in their investigations was attained with quartz grains around 25 μm. It is proposed by Ece and Nakagawa [26] that homogenous distribution of 10 – 20 μm grains of quartz within the glassy matrix has the most favorable effect on mechanical strength. Large grains are subject to cause cracks in vitreous phase, and, on the contrary, fine grains melt easily and reduce the bending strength.

As claimed by the dispersion-strengtening hypothesis the strength is increased due to the size limitation of Griffith flaws by crystalline particles dispersed in glassy matrix. It was established by strength and fracture studies that the strength is dependent on the volume fraction of dispersed particles at low volume fractions, while at higher volume fractions of dispersed particles the strength depends additionally on the size of dispersed particles [37]. This theory was proposed to be applied for glasses as well as ceramics containing appreciable fractions of glassy phase. The strength is improved by crystalline particles, such as corundum or sillimate, acting as fracture-resistant dispersoids in glassy matix, thus inhibiting the crack propagation [35].

All of these theories explain the mechanisms of strengthening the porcelain body, but none of them is universal. The mechanical strength in multiphase porcelain body greatly depends on firing process, which affects the main factors influencing the strength, such as thermal expansion coefficient of the phases, elastic properties of the phases, volume fraction of different phases, particle size of the crystalline phase, and phase transformation, which all contribute to stresses configuration in glassy matrix [1].

Mechanical strength of porcelain body is affected by the size, amount and distribution of isolated pores. Maximum mechanical strength is attained when the open porosity reaches zero. Uniformly distributed small pores with size less than 20 μm were found to have positive effect on strength of porcelain body,

while irregulary distributed large pores negatively influence the strength [26,36].

Fracture resistant calcined alumina, which is characteristic by its high Young's modulus, is generally used to improve the mechanical strength of porcelain body. Incorporation of calcined alumina up to ~20 wt.% improves the mechanical strength of porcelain body without appreciably affecting the shrinkage, firing schedule and maturing temperatures, while the addition of more than 20 wt.% of calcined alumina requires prolonged firing process, increases the overall thermal expansion and reduces translucency [18,34]. The increase in strength of alumina porcelain body is achieved with decrease in grain size of homogenously dispersed corundum crystallites. Small particles more effectively decrease the mean free fracture path per unit volume than large particles, thereby contribute to strength increase.

Mechanical strength of alumina porcelain is strongly affected by total amount of glassy phase. If the amount of feldspar in liquid phase is too low, the densification leads to porous body. On the contrary, excess amount of feldspar in liquid phase generates closed pores in the body and thus lowers the mechanical strength [36].

1.5 Thermal shock resistance of ceramics

Many factors affect thermal shock resistance of vitrified ceramic material, for this reason the intercomparison is very complex [6]. When size of specimen, method of preparation and method of test are the same, intercomparison is more precise. Under such conditions thermal conductivity, thermal expansion and mechanical strength are recognized as the main factors affecting the thermal shock resistance of vitrified ceramic [60,61].

The susceptibility of ceramic materials to thermal stresses and thermal shock failure is crucial for components to be used at elevated temperatures [6]. The thermal shock resistance is one of the main factors limiting the usefulness of certain ceramic material to be used at medium or high temperature range. Structural properties of material might be satisfactory at operating temperature, but in heating or cooling cycle failures might occur. Substantial stresses develop in ceramic material subjected to rapid change in temperature. Thermal endurance, thermal stress resistance, or thermal shock resistance are most often used terms for resistance of material to weakening or fracture under temperature changing conditions.

Sudden temperature changes create a sharp temperature gradient accompanied by temperature induced changes of volume and large stresses are produced within specimen [6]. An increase in temperature causes the surface to be under compression when material's coefficient of thermal expansion is positive. During heating such specimen rarely fail because the compressive strength of most ceramic materials is high. Sudden lowering of temperature causes the surface to be under tensile stresses and, as the tensile strength is frequently relatively low, specimen fail more often. Therefore, tensile stresses during cooling will be less severe by materials with lower thermal expansion.

Thermal shock causes cracks that yield to fracture of the material. The failure in material as a consequence of thermal stress depends on stress characteristics, such as stress level, stress duration and stress distribution in the body, and material characteristics, such as ductility, porosity, homogeneity and pre-existing flows [6].

1.5.1 Thermal-shock resistance theories

Traditional measure of thermal shock resistance is the maximum stroke in surface temperature which a brittle material is able to sustain without failure [61]. There are many different theories and models to explain and evaluate the thermal shock resistance of ceramic material. Most commonly, the access to explain the thermal shock resistance originates in thermal shock fracture theory or critical stress theory and thermal shock damage theory being further broadened with additional investigated parameters.

According to thermal shock fracture theory, which is based on thermo elasticity theory, there exists the equilibrium of surface stress σ_{ts} and strength of material σ_f as the criterion of thermal shock resistance [62,63]. When the material is quenched between a temperature T and a lower temperature T_0, temperature difference ΔT causes the surface stress σ_{ts}, which is greater than fracture strength σ_f. Consequently crack will yield and result in an instant fracture in the material. Under hypothetical conditions with infinitely fast quench and no heat conduction within the material the critical surface stress σ_{ts} is calculated by Eq. 1.4-1:

$$\sigma_{ts} = \frac{E\alpha\Delta T}{1-\mu}$$ Eq. 1.5-1

where E is Young's modulus, $\Delta T = (T - T_0)$, α is the mean thermal expansion coefficient, and μ is the Poisson ratio. This equation defines the maximum stress produced by quenching theoretically. Regarding practical conditions the efficiency of heat transfer to the surface and the thermal conductivity has to be considered. Surface stress σ_{ts} is corrected by a factor ψ and expressed as:

$$\sigma_{ts} = \frac{\Psi E\alpha\Delta T}{1-\mu}$$ Eq. 1.5-2

Factor ψ is a function of time and the Biot modulus $\beta = ah/k$, where a is the radius of half-width of the specimen, h is the heat-transfer coefficient between the body and the quenching specimen and k is thermal conductivity.

Related thermal shock resistance factors (R) express the ability of a material to resist this thermal stress. In the simplest case of stress arising from the infinitely fast quench of an infinite slab of material with constant heat transfer coefficient factor R is calculated by the equation as follows:

$$R = \frac{\sigma_f(1-\mu)}{E\alpha}$$ Eq. 1.5-3

where σ_f is fracture strength. In general a set of factors, R, R' and R'', is used to express different conditions for damage by crack initiation at heating or cooling. Factors R' and R'' are specified as:

$$R' = \frac{\sigma_f(1-\mu)k}{E\alpha}$$ Eq. 1.5-4

$$R'' = \frac{\sigma_f(1-\mu)A}{E\alpha}$$ Eq. 1.5-5

where k is thermal conductivity and A is a stress reduction term correlated with Biot modulus β. Thermal shock resistance factor R is applicable in case of quick temperature change on surface. In case of slow heat transfer Biot modulus is small, so factor R' is more appropriate. Factor R'' is used at constant heating or cooling rate.

According to the thermal shock fracture theory the increase in fracture strength and thermal conductivity, and the decrease in coefficient of thermal expansion and Young's modulus will improve thermal shock resistance of ceramic material.

Thermal shock damage theory originates from the theory of fracture mechanics which explains the crack propagation in brittle ceramics subjected to thermal shock. Contrary to thermal fracture theory it excludes the equilibrium of the fracture surface energy and the thermo elastic strain energy as the main criterion. Hasselman suggested an alternative thermal shock parameter, which measures the ratio of fracture energy for crack initiation to the fracture energy for continuous crack propagation [64]. This approach explains the conditions of severe thermal environments, where the initiation of thermal stress fracture cannot be avoided and the major demand is to minimize the extent of crack propagation [63]. Derived thermal shock parameters from thermal shock damage theory are specified as R''' and R''''.

Crack propagation under thermal stress conditions generally occurs from the forces derived from the field within the thermal shocked specimen in the absence of external body forces. When a prior existing crack is propagated by the thermal stress, its surfaces increases to the maximum surface area (S_{max}) according to:

$$S_{max} \le \frac{U}{\gamma_{WOF}}$$ Eq. 1.5-6

where U is the stored elastic energy at fracture and γ_{WOF} is the effective surface energy. As long as the elastic energy released from the stress field surrounding the crack is greater then the surface energy, the crack propagation continues. Stored elastic energy is proportionally related to tensile strength of material. Parameters R''' and R'''' are given by:

$$R''' = \frac{E}{\sigma_f{}^2(1-\mu)} \qquad \text{Eq. 1.5-7}$$

$$R'''' = \frac{E\gamma_{WOF}}{\sigma_f{}^2(1-\mu)} \qquad \text{Eq. 1.5-8}$$

Parameter R''' is used for materials with similar effective surface energy or similar work of fracture per unit projected area of fracture face. Parameter R'''' is more appropriate for materials with greater differences in brittle-ductile behavior characterized by differing values of effective surface energy. Considering conditions of crack propagation high Young modulus and surface energy, together with low strength are required to minimize thermal shock damage.

The results of the two theories cannot be taken as exact criterion in forecasting the thermal shock behavior of ceramic body since their results in general contradict. The reason to be adverse arises from different initial criterion and their rationales [6,65].

According to thermal shock fracture theory, ceramics are ideal brittle material without pores and micro-cracks. Upon thermal stress initiated crack immediately expands and material ruptures. In real ceramics micro-pores and micro-cracks are normally present and cracks cannot expand unless enough energy exists. In general, the approach based on thermal shock fracture theory is more suitable for glasses, porcelain, whitewares, electronic ceramics etc.

Thermal shock damage theory is based on the presumption that ceramics have a lot of not interacted pores and defects like in porous ceramics. The effects of thermal mismatch and thermal expansion on thermal endurance of ceramics are not considered. Parameter R''' is higher at lower tensile strength of material. In real ceramics high tensile strength and materials with limited amount of pores and defects are often required. The approach based on thermal shock damage theory is more appropriate for porous refractory materials.

Ceramics are exposed to several impacts during thermal shock process, which includes the process of crack initiation, crack extension and finally fracture. Supplementary attempts were investigated with corrected assumption to extent the two theories supported by new models.

Zhou [65] developed a new model with relatively good agreement with experimental data for Al_2O_3–ZrO2 composite with different Al_2O_3 loadings, where critical thermal-shock temperature difference ΔT_c was directly correlative to the mechanical properties of the ceramics upon conditions that there is not any phase transformations in the materials, that the cracks do not interact, that the physical dimension's factor of the material is not considered and that the material is isotropic.

1.5.2 Thermal shock testing

The purpose of thermal shock testing is to provide a basis for the prediction of probability the mechanical failure will occur in ceramic material during operation if sudden temperature change is involved [63]. Thermal shock process is in physical changes related to theories of elasticity and heat conduction. Thermal shock resistance is not an intrinsic property of material, therefore thermal shock test should not be used as material test due to the fact that for most materials R and R' are not constant but strongly dependent on temperature. The use of thermal shock test to determine the temperature dependence of other variables in equation is inconceivable. Thermal shock test with standard plates, bars or spheres is conceivable for quality control in production and simulated service tests. Thermal stress tests are ordinary classified according to the method of establishing temperature gradients and by the method implementing thermal stress resistance.

Based on thermoelastic theory the thermal shock resistance is determined by quenching from high temperature and the measure for thermo shock resistance is critical temperature change required to cause complete failure.

Residual strength method is frequently used to determine the critical thermal-shock temperature difference ΔT_c under quick cooling conditions [65,67,68]. The flexural strength of the sample is measured before and after thermal shock. In the σ_f–ΔT curve the temperature at the point where the strength σ_f has an abrupt decline is ΔT_c. The number of cycles needed to cause a defined extend of mechanical failure is also a frequent evaluation in case of second approach. Beside the bending strength degradation when using heating and water quenching assessment for thermal shock evaluation, the estimation can be done by visual inspection for cracks. Liquid dye is used when the failure criterion should be achieved by visual determination of crack formation [38].

Ultrasonic measurements are used as nondestructive quantification of thermal shock damage. Dynamic Young modulus of elasticity and strength degradation can be calculated using measured values of ultrasonic velocities obtained by ultrasonic measurements. The formation of cracks decreases the velocity of ultrasonic pulses traveling in the ceramic material [69].

1.5.3 Microstructure influence on thermal shock resistance

Both the mineralogical composition and the microstructure influence the thermal shock resistance of porcelains [67]. When body is a mixture of different materials, such as porcelain, the thermal stress is influenced by the elastic properties of constituents and by the stresses that arise due to the difference in expansion between crystal phases and glass [62].

Stress concentrators improve thermal endurance of ceramic body. When the mechanical strength is not the main concern microctructural heterogeneities of any form, which serve as stress concentrators in material, improve the resistance to catastrophic crack propagation [6]. When stress concentrators are introduced in the composition fracture may take place locally in the materials, then average stress is lower and catastrophic failure is avoided. Stress concentrators are often cracks with the size sufficient to lead to quasi-statically crack propagation. Also blunt flows resulting from intergranular shrinkage cracking provide resistance to catastrophic failure. Another example is intergranular shrinkage voids which serve to blunt initially sharp cracks and hinder crack propagation.

1.5.4 Thermal shock resistance of porcelain bodies

Differential thermal expansion of present constituents, such as mullite, quartz, corundum and glassy phase, mainly influence the thermal shock resistance of porcelain body [67]. Thermal expansion is the tendency of material to increase in size as it increases in temperature. The importance of thermal expansion in the ultimate usefulness of different types of porcelain materials is generally recognized [70]. Standard practice to increase the strength of porcelain body is the use of glaze with thermal expansion lower than the body [4,6]. Due to difference of thermal expansion between body and glaze residual stresses are generated in glaze and body after cooling. When the thermal coefficient of glaze is lower than that of the body the compressive stresses are induced in glaze, which improves the strength of the body. It was found that considerable strength improvement was reached, when the difference in thermal coefficient of body and glaze is between 1.5 and $2.0 \times 10^{-6}K^{-1}$ [38].

For crystalline nonmetalic compounds the values of thermal expansion coefficient range from near $10 \times 10^{-7}K^{-1}$ (20–1000°C) for beryl and β-spodumene to near $140 \times 10^{-7}K^{-1}$ (20–1800°C) for MgO**.** When interpreting the values of thermal expansion, it is necessary to state in what range the thermal expansion coefficient was calculated. Normal progress of thermal dilatation may give a curve that is very often concave upward.

Thermal expansion characteristics of porcelain bodies are considerably different in similar starting compositions [71]. The reason for distinctions partly arises from variations in the type of clay and feldspars used in formulations and do to differences in firing treatment and degree of vitrification.

Most of the data on thermal expansion of fluxes have been obtained on glassy-crystal aggregates. [72]. In fired porcelain body quartz has the highest thermal expansion, beside only in special formulations present cristobalite. All the crystalline phases of silica have higher thermal expansion than glassy silica. Thermal expansion of crystalline quartz in temperature range 20–750 °C is $\sim 23 \times 10^{-6}K^{-1}$ while that of the glassy phase in ordinary porcelain body amounts $\sim 3 \times 10^{-6}K^{-1}$ [56]. Quartz crystallites and cristobalite are detrimental inhomogeneities in temperature shocked porcelain body. Microcracked structure of such bodies causes fracture under thermal stress [5].

Due to its chained structure mullite is characteristized by different thermal expansion along crystallographic axes, therefore its thermal expansion coefficient α_{ij} depends on direction. Highest

expansion was observed parallel to crystallographic *b*-axis and considerably lower parallel to *a*-axis, while parallel to *c*-axis closer to that by *b*-axis. In the temperature range 25–900 °C the observed values of α_{11}, α_{12} and α_{13} were 2.3, 7.6 and 4.8 $\times$ $10^{-6}K^{-1}$, respectively [54]. Better interlocked mullite crystals are proposed to improve thermal shock resistance of body [10].

Thermal expansion coefficient of polycrystalline alumina in temperature range 0–1000 °C is 8.1 $\times$ $10^{-6}K^{-1}$ [33]. Austin et al. [34] studied the calcined alumina addition as a replacement for quartz in whiteware bodies. They reported that calcined alumina in porcelain body tends to increase the overall thermal expansion in temperature range 30–1000 °C. When up to 10 wt.% of calcined alumina was added the increase of thermal expansion was not significant, while with more than 40 wt.% of calcined alumina added the thermal expansion of bodies was markedly higher than in comparable quartz bodies. They found that the introduction of calcined alumina in whiteware bodies improved the mechanical strength, while no consistent improvement of thermal shock resistance was shown. Higher thermal expansion of alumina porcelain bodies negatively influenced their thermal shock resistance. Slightly higher thermal expansion of alumina porcelain bodies in comparison to quartz porcelain bodies were reported by Amigó et al. [17] who ascertained the thermal expansion coefficient in temperature interval 20–600 °C of 6.3 $\times$ $10^{-6}K^{-1}$ for alumina porcelain bodies with Al_2O_3 content around 46 wt.% and of 6.2 $\times$ $10^{-6}K^{-1}$ for silica porcelain bodies with Al_2O_3 content around 29 wt.%.

1.6 Lithium in ceramics

Lithium compounds, mainly as natural minerals, are used in different types of ceramics. In alkali aluminosilicate ceramics theye are applied as strong fluxing agent or low expansion filler with the aim to reduce firing cycle and improve mechanical strength and/or thermal shock resistance. In glazes and enamels the presence of lithia generally contributes to lower viscosity, better brilliance, lower maturation time and temperature, lower thermal expansion, lower surface tension and better chemical resistance.

To improve thermal endurance lithium compounds can be introduced in other types of ceramics, such as alumina ceramics [73,74], mullite ceramics [75] or magnesium aluminium silicate ceramics [76,77]. Lithium compounds are a great deal applied in lithium aluminium silicate glass-ceramics [78,79,80], characteristic by their low thermal expansion and high mechanical resistance, and also in lithium silicate glass-ceramics possessing high strength [81].

1.6.1 Properties of lithium aluminium silicates

A great deal of work on phase diagram study of ternary system Li_2O-Al_2O_3-SiO_2 was done by Roy and Osborn [82]. The presence of minerals petalite, $Li_2O{\cdot}Al_2O_3{\cdot}8SiO_2$, ″lithium orthoclase″, $Li_2O{\cdot}Al_2O_3{\cdot}6SiO_2$, spodumene, $Li_2O{\cdot}Al_2O_3{\cdot}4SiO_2$ and eucryptite, $Li_2O{\cdot}Al_2O_3{\cdot}2SiO_2$ in ternary phase diagram Li_2O-Al_2O_3-SiO_2 by Roy and Osborn are shown in Figure 1.6-1 [83]. Phase diagram depicting phase equilibrium along the join eucryptite ($Li_2O{\cdot}Al_2O_3{\cdot}2SiO_2$)–silica ($SiO_2$) in Figure 1.6-2 [84] shows the appropriate limits of β-spodumene and β-eucryptite at high temperatures.

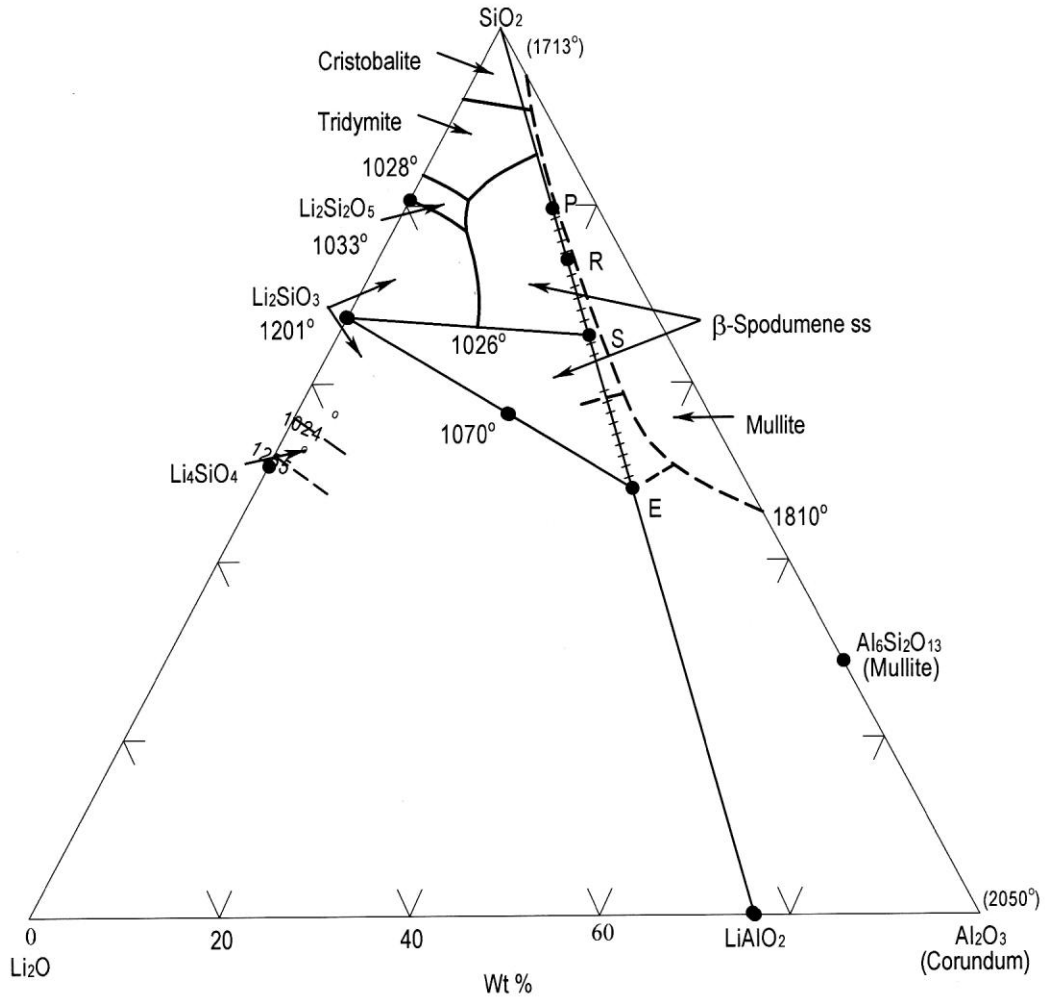

Figure 1.6-1. The system Li_2O-Al_2O_3-SiO_2 showing lithium metasilicate-β-euryptite join. P - $Li_2O{\cdot}Al_2O_3{\cdot}8SiO_2$ (petalite), R - $Li_2O{\cdot}Al_2O_3{\cdot}6SiO_2$ (″lithium orthoclase″), S - $Li_2O{\cdot}Al_2O_3{\cdot}4SiO_2$ (spodumene) and E - $Li_2O{\cdot}Al_2O_3{\cdot}2SiO_2$ (eucryptite).

It is obvious from the phase diagram in Figure 1.6-2 that compounds β-eucryptite, β-spodumene and respective solid solutions can be prepared in the system Li_2O-Al_2O_3-SiO_2.

According to Hammel's investigations the compositions of ternary system Li_2O-Al_2O_3-SiO_2 are ranging from molecular ration 1:1:2 to 1:1:15 when heated to 1300 °C [85]. His research was centered on mineral composition and mineral identification in order to explain thermal expansion behavior of existent compounds. All identified lithium aluminosilicates possessed very low thermal expansion. Mole composition, oxide composition in wt.% and thermal expansion coefficient of compounds according to Hummel's investigations are given in Table 1.5-1.

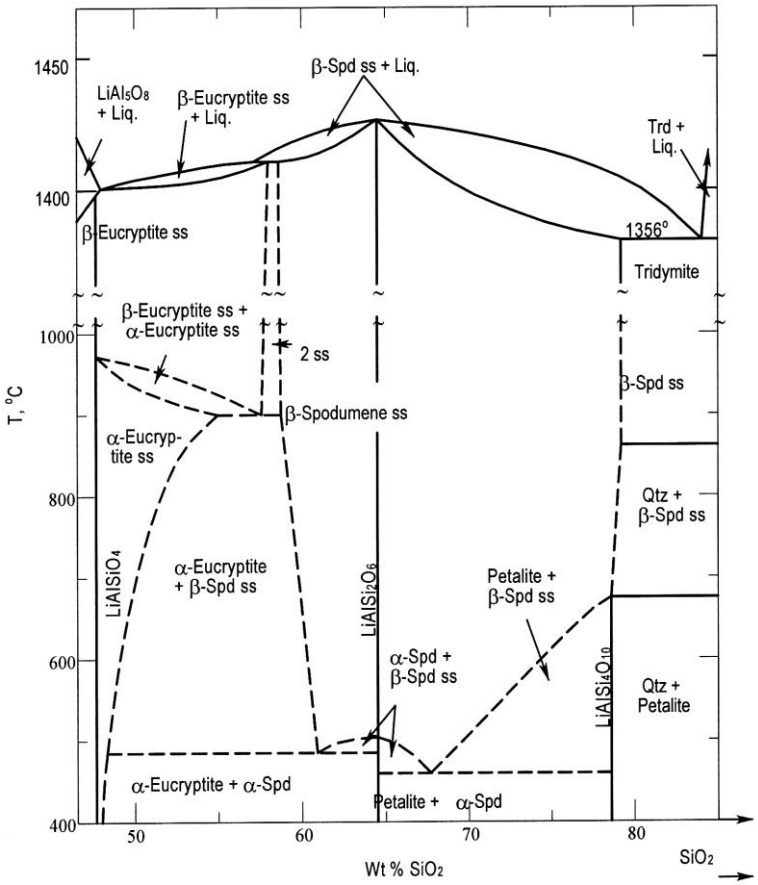

Figure 1.6-2. Diagram depicting phase-equilibrium relations along the join eucryptite ($Li_2O{\cdot}Al_2O_3{\cdot}2SiO_2$)–silica ($SiO_2$).

Table 1.6-1. Compositions and coefficient of thermal expansion in ternary system Li_2O-Al_2O_3-SiO_2 by Hummel [85].

Mole composition	Composition (wt.%)			Linear thermal expansion
	Li_2O	Al_2O_3	SiO_2	($x10^{-6}K^{-1}$ in range 25–1000 °C)
$Li_2O{\cdot}Al_2O_3{\cdot}2SiO_2$	11.8	40.5	47.7	negative (~0.6)
$Li_2O{\cdot}Al_2O_3{\cdot}3SiO_2$	9.6	32.7	57.7	negative (~0.6)
$Li_2O{\cdot}Al_2O_3{\cdot}4SiO_2$	8.0	27.4	64.6	0.9
$Li_2O{\cdot}Al_2O_3{\cdot}6SiO_2$	6.1	20.7	73.2	0.6
$Li_2O{\cdot}Al_2O_3{\cdot}8SiO_2$	4.9	16.6	78.5	0.3
$Li_2O{\cdot}Al_2O_3{\cdot}10SiO_2$	4.1	13.9	82.0	0.5
$Li_2O{\cdot}Al_2O_3{\cdot}12SiO_2$	3.5	12.0	84.5	-*
$Li_2O{\cdot}Al_2O_3{\cdot}15SiO_2$	2.9	9.9	87.2	-*

*not established

First composition in the series Li_2O-Al_2O_3-SiO_2 with the molecular ratio 1:1:2 has the structure of β-eucryptite ($Li_2O{\cdot}Al_2O_3{\cdot}2SiO_2$). β-eucryptite shows close similarity to high quartz in habit and optical character. α-eucryptite inverts to the high-temperature form of eucryptite (β-eucryptite) at 972 ± 10 °C [82]. The crystal structure of β-eucryptite in form of hexagonal spiral is the same as that of high-quartz considering the arrangement in the direction of the *c* axis. This type of structure exhibits either very low expansions or contractions.

The crystal structure of $Li_2O{\cdot}Al_2O_3{\cdot}3SiO_2$ with the molecular ratio 1:1:3 shows similarity to that of β-spodumene.

The next composition $Li_2O{\cdot}Al_2O_3{\cdot}4SiO_2$ with higher amount of SiO_2, where molar ratio is 1:1:4, has β-spodumene structure. β-spodumene has a tetragonal dipyramidal crystal structure which is uniaxial

positive. The structure consists of fairly rigid Si–O, Al–O tetrahedral arranged around a 4-fold screw axis. This is a common characteristic of materials which possess an anisotropic thermal expansion.

Among compositions with higher amount of SiO_2 than β-spodumene those with molecular ratio 1:1:6 and 1:1:8 have β-spodumene structure. The reaction products of compositions 1:1:10, 1:1:12 and 1:1:15 contain cristobalite and quartz besides β-spodumene with cristobalite increasing being the predominant phase in composition 1:1:15.

Thermal expansion characteristics of a series of lithia-alumina-silica glasses lying along the $Li_2O{\cdot}Al_2O_3$–$4SiO_2$ join in the ternary system was studied with the aim to investigate the influence of increasing quantity of lithia on thermal expansion of glass [86]. Glasses were prepared by melting at 1500 to 1600 °C. At about 500 °C the glass with $Li_2O{\cdot}Al_2O_3{\cdot}2SiO_2$ composition began to devitrify and the cristallization of less dense eucryptite proceeds. Mean coefficients of expansion in the interval 30 to 500 °C of studied glass compositions are listed in Table 1.6-2.

Table 1.6-2. Compositions and coefficient of thermal expansion of Li_2O-Al_2O_3-SiO_2 glasses.

Composition	CTE ($\times10^{-6}K^{-1}$ in range 30°- 500°C)
$Li_2O{\cdot}Al_2O_3{\cdot}2SiO_2$	7.60
$Li_2O{\cdot}Al_2O_3{\cdot}4SiO_2$	6.66
$Li_2O{\cdot}Al_2O_3{\cdot}6SiO_2$	5.52
$Li_2O{\cdot}Al_2O_3{\cdot}8SiO_2$	4.36
$Li_2O{\cdot}Al_2O_3{\cdot}10SiO_2$	3.93

Thermal expansion coefficient of lithia-alumina-silica glasses varies as the molecular ratio Li_2O:Al_2O_3:SiO_2 varies from 1:1:2 to 1:1:10. It is evident that increasing the share of silica moles in molar ratio contributes to lower expansion of glass.

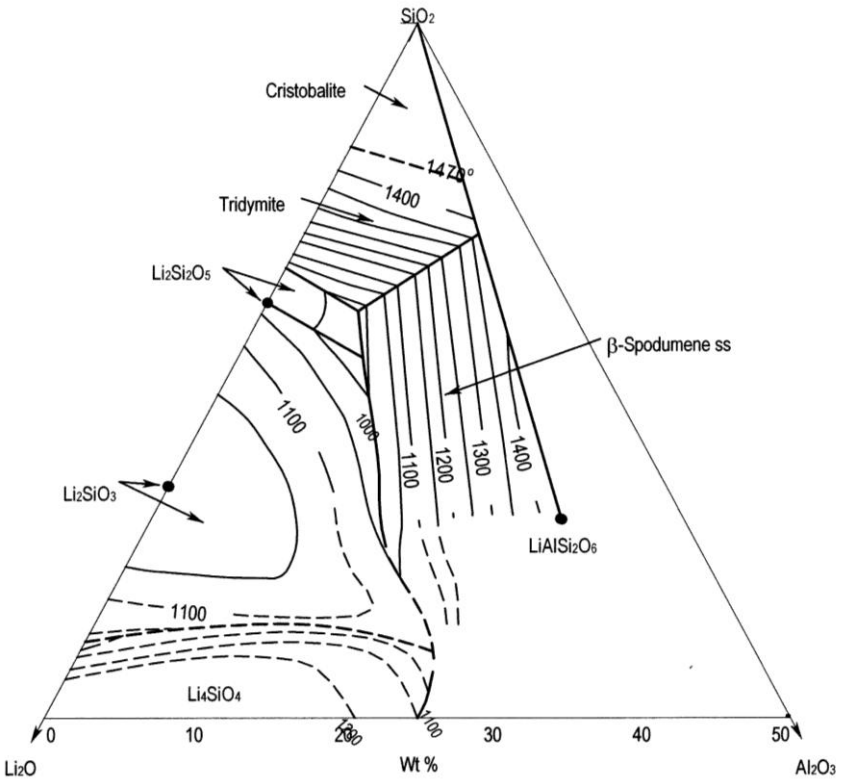

Figure 1.6-3. The system lithia-alumina-silica showing liquidus relations.

A great deal of attention had received investigations of phase relations in system Li_2O-Al_2O_3-SiO_2 by

the process of glass formation and recrystallization in lithium metasilicate region. They were applied in improvement of glass ceramic materials. It was found that the stability of the vitreous state in the lithium metasilicate region is a function of the concentration of lithia [87]. The stability of glass was lower at higher lithia content.

The stability of vitreous state in the system Li_2O-Al_2O_3-SiO_2 was determined as a function of the constituents present as shown in phase diagram by Eppler in Figure 1.6-3 [88]. The phase diagram the system Li_2O-Al_2O_3-SiO_2 presented in Figure 1.6-3, applied commonly in the field of lithium aluminum glass-ceramics, is a part of phase diagram from Figure 1.6-1 supplemented by the eutectic temperatures of lithium aluminium silicate compositions in the region with alumina content below 50 wt. %. Phase lithium metasilicate ($Li_2O{\cdot}SiO_2$) is the primary constituent in the region 10 to 40 wt.% of lithia, 0 to 25 wt.% of alumina, and 50 to 80 wt.% of silica [87]. After devitrification process in temperature range 500 to 900 °C the thermal expansion and phase composition were determined. The thermal expansion coefficient varied from 10 to 3×10^{-6} K^{-1} as various phases were present as a function of time, temperature and constituents present.

1.6.2 Lithium in porcelain bodies

In porcelain bodies lithium compounds are commonly applied as a flux componenet. As claimed by Merivale [89] high thermal stability, high fluxing capability or improved viscosity, and better thermal shock resistance are the main benefits of lithia for current ceramic manufacturing process which tends to lower firing temperatures and shorten firing cycles.

In 1928 Twells [90] published the results of his experiments with lepidoilte, which was used instead of feldspar or with its combinations in high tension electrical porcelain body. It was found that compared to feldspar lepidolite is a violent flux, which promotes the early vitrification of a body without greatly affecting its firing range. The total addition of flux could be reduced up to 10 wt.% when a combination of potash feldspar and lepidolite is used. Produced porcelain bodies were unusually white, mechanical strength was high and they had good resistance to thermal shock.

These early claims about benefits of lithia as a flux in porcelain body were the subject of further investigations that brought to actual application of lithia in whitewares and other types of ceramics. It was the price and the availability of lithium-bearing minerals which made it less attractive for low price whiteware bodies in the past. Lithium occurs in deposits that are not as uniform and plentiful as feldspar-bearing mineral, although there are available large tonnages of sufficiently high-grade lithium ores and they are being used in increasing quantities in the ceramic field [91].

The object of research work deduced by Smoke [60] was the development of ceramic bodies with negative thermal expansion. He was inspired by results and explanations published by Hummel [85] who investigated thermal expansion properties of some synthetic lithia minerals and the associated solid solutions and concluded that the thermal expansion of synthetic lithium-aluminum-silicates with Li_2O-Al_2O_3-SiO_2 ration of 1:1:3 to 1:1:8 are extremely low and have formed the bases of new technical porcelains. Smoke made several compositions based on Li_2CO_3, clay, flint and alumina. In the system Li_2O-Al_2O_3-SiO_2 he determined the two areas in which the linear thermal expansion is negative. In areas, where β-eucryptite and β-spodumene solid solutions are the principal crystalline phases the linear expansion ranges from zero to -0.38% from room temperature up to 600 °C. New synthesized compositions could be prepared by normal ceramic processes and gave remarkably high thermal endurance. As emphasized in his report, the chief difficulty was to obtain vitrified bodies because of short firing range.

The modifications are needed in body formulations, when lithium minerals are used instead of potassium or sodium feldspar as a flux. Based on results of his experimental work on sanitary chinaware bodies Cowan [44] drawn the conclusions, that spodumene is of little benefit in high temperature (>1280 °C) low-flux bodies as a partial replacement for feldspar, but more advantage in low-temperature (<1230 °C) high-flux bodies as a partial replacement for feldspar or nepheline syenite. He also found out that the flux combinations, consisting of spodumene, talcum and nepheline syenite, produce low-fire (1160 °C) bodies with flexural strength around 70 MPa. The enhancement of mechanical strength and lowering the sintering temperature by the addtition of spodumene was confirmed also by Ismatova [92], who investigated the application of spodumene as a principal or auxiliary flux in electrical porcelain. She concluded that the properties of the glassy phase of porcelain can be improved by introducing Li_2O. Replacing feldspar with spodumene did not lead to change in the moisture content, plasticity, and the shrinkage. Firing temperature decreased with increasing content of spodumene. Bodies with spodumene attained more uniform microstructure than those with feldspar, improved mechanical strength, thermal shock resistance, and dielectric properties.

In his book, Application of Lithium in Ceramics, Fishwick [48] reports that lithia can be added in whitewares in varying amounts. Lithia is completely dissolved in the glassy phase when used as a flux in small amounts. The glassy phase containing lithia is less viscous, thus lowering the firing temperature. When used in relatively large amounts, some of lithia is dissolved in glassy phase, but most of it is present in low expansion lithium aluminosicates. Fishwick suggests that the amount of free silica in a whiteware body can be reduced by the addition of spodumene, which enables the assimilation of free silica in the β-spodumene structure at firing conditions that promote this reaction. Solid solution with assimilated free silica exhibits even lower thermal expansion than that of β-spodumene.

Tulyaganov et al. [93] systematically investigated standard triaxial porcelain body with the addition of Li_2O from 0.44 to 3.16 wt.%. Li_2CO_3 was used as a source of lithia. The results showed that desirable properties for tableware porcelain can be attained if Li_2O content is below 1.5 wt.%. Proceeded from the previous conclusions the new porcelain formulations with 0.5 and 0.9 wt.% of Li_2O were developed using natural rocks containing spodumene or petalite. The most important finding was that compositions with natural Li-bearing minerals matured at temperatures 100–120 °C lower than standard composition without lithia. Besides, when fired under industrial conditions in temperature range from 1365 to 1380 °C these compositions exhibited remarkable resistance to pyroplastic deformation and attained high mechanical strength, which was comperable with that determined for firing in laboratory furnace at 1250 °C. It was also noted that Li_2O plays important role in firing process effecting densification, the evolution of crystalline phases and microstructure, all greatly dependent on its amount.

In her survey of dense and porous aluminosilicate ceramic materials containing lithium Maslenikova [94] quoted that lithium containing bodies based on products from chemical processing and natural lithium containing ore sinter differently. The sintering process of synthetic materials takes place principally by solid-state reactions, while with natural minerals, such as spodumene and eucryptite, the appearance of liquid phase is involved. Materials based on β-spodumene are characterized by stable values of apparent density and porosity during heat treatment. However, those based on α-spodumene, which is transformed to its β-form with increased grain volume, possess lower density due to isothermal expansion and increased closed porosity.

The mechanical characteristics of a standard body mix for porcelain stoneware tiles with the addition of calcined alumina and spodumene were investigated [95]. Spodumene was introduced in 10 wt.% as a replacement for sodium feldspar, and as reinforcing material high purity calcined alumina and calcined bauxite were used. The presence of spodumene improved the sintering performance of modified compositions, reduced the porosity and favored the crystallization of rather elongated needle like mullite. It was assumed, that energy and scrap reduction can be realized with the presence of spodumene due to its capability to reduce firing temperature and shrinkage.

2 Aims and Hypothesis

The aim of present work was to develop high-alumina porcelain bodies with high mechanical strength and good thermal endurance, which could be used in electrotechnics or as structural ceramics and fired at temperatures around 1300 °C. High alumina porcelain bodies with good performance should be processed within disposable technological and economical frames along with considering the requirements for health and environmental protection and low energy consumption.

Li_2O has already been investigated and introduced in different types of ceramics. Regarding the porcelain bodies, it was found that lithia as a powerful flux introduced in triaxial porcelain bodies contributes to improved mechanical strength and better thermal shock resistance [44,92]. Li_2O is commonly introduced in porcelain or other ceramic bodies via natural minerals such as most often used spodumene, which contains relatively high amount of Li_2O. The studies of the Li_2O application in high alumina porcelain have not been noticed yet.

It has been ascertained through previous investigations and explained in literature that the mechanical strength of porcelain body is in correlation with the amount of calcined alumina applied. The high mechanical strength was proposed to be achieved with the amount of calcined alumina as high as possible within the requirements of industrial application and firing temperature around 1300 °C.

It is commonly accepted ascertainment that the avoidance of free quartz in alumina porcelain material is one of the main concerns when the high mechanical strength and good thermal endurance are desired. Therefore, it is necessary that the composition, the selection of raw materials and the complete technological process set up the conditions to eliminate the presence of free quartz in the fired body.

The mechanical strength of porcelain body is influenced by the established prestress in the glassy matrix as claimed by the prestressed theory. The prestress in glassy matrix arises in the cooling process of firing as a result of thermal expansion mismatch between the glassy phase and the crystalline phases present. Generally, in alumina porcelain the crystalline phases embedded in the glassy matrix comprise corundum and mullite. We intend to increase the thermal expansion mismatch between the crystalline phases and glassy phase of high alumina porcelain body with decreasing the thermal expansion of glassy phase, thus creating the conditions for establishing more favorable prestress in the glassy phase, which should contribute to the improvement of the mechanical strength.

The thermal expansion of glassy phase of porcelain body is influenced by the alkali oxides present. Alkali oxides mostly originate from flux constituents. K_2O and Na_2O are commonly present alkali oxides in glassy phase of porcelain body. They are introduced in porcelain bodies via potassium and sodium feldspar. With the modification of glassy phase, in which Li_2O is introduced as a partial substitute for K_2O and Na_2O, the glassy phase with lower thermal expansion than that containing K_2O and Na_2O is proposed to be formed. In modified glassy phase Li_2O and K_2O are the prevailing alkali oxides. Lithium alumino slilicate glasses are characteristic by lower thermal expansion than feldspar glasses, therby the presence of Li_2O should contribute to lower thermal expansion of glassy phase [70]. In new formulations the amount of Na_2O is attempt to be diminished to minimum as possible applying the raw materials with very low content of Na_2O, since thermal expansion of sodium feldspar glasses is higher than that of potassium glasses [96].

The overall thermal expansion of porcelain body depens on the thermal expansion of constituents. With increasing the amount of corundum the overall thermal expansion increases due to higher thermal expansion of corundum in comparison to that of glassy phase and mullite. Thermal expansion and mechanical strength mainly influence the thermal shock resistance of porcelain body, when elastic modulus and Poisson's ratio are nearly constant. We intend to improve the thermal shock resistance of high alumina porcelain body by the enhancement of mechanical strength and by lowering the overall thermal expansion. The modified glassy phase with lower thermal expansion is expected to improve the mechanical strength and lower the overall thermal expansion of alumina porcelain, thus improving its thermal shock resistance.

The aim of present research work is to investigate the influence of Li_2O on sintering, phase composition, microstructure development and physical properties of high alumina porcelain bodies during heat treatment in temperature range from 950 to 1350 °C. By new developed bodies the processes taking place during heat treatment are expected to be affected by the the presence and the amount of Li_2O. The main reactions enabling formation of new phases and densification of porcelain body take place in this

temperature range. The main processes that generally occur during the firing of triaxial porcelain body are: (a) transformation of kaolinite into metakaolinite at ~550 °C; (b) α to β quartz inversion at 573 °C; (c) metakaolinite transformation to a spinel-type structure and amorphous silica at 950-1000 °C, (d) first liquid phase formation at the eutectic potassium feldspar-silica at 985 °C, (e) the formation of primary mullite in clay relicts and melting of potassium feldspar accompanied by diffusion of alkalis out of feldspar at ~1100 °C, and (f) nucleation and growth od secondary mullite and quartz dissolution at increasing temperature to the final stage of firing. The influence of Li_2O on reactions and phase transformations will be studied on new developed bodies, with the amount of Li_2O increasing from 1.0 to 1.6 wt.%.

Li_2O is introduced in the increasing amount as the main flux in combination with K_2O and small amount of Na_2O. The source of Li_2O is β-spodumene prepared by the calcination of commercially available Li-bearing mineral spodumene. The behaviour of Li_2O-containing bodies under heating will be studied from dilatometric, TG and DTA curves. After firing at different firing temperatures in temperature range 950−1350 °C the phase composition by XRD analysis, microstructural investigations by SEM observations and physical properties determination will be performed on bodies containing Li_2O in comparison to reference body.

The introduction of Li_2O in high alumina porcelain formulations is investigated in the view of, first, its influence on phase composition and microstucture development at different firing temperatures, and second, its impact on properties of fired bodies, among which the mechanical and thermal properties are of the main concern. All investigations of Li_2O-containing compositions are done in comparison with reference composition, which is characteristic by the flux system based on K_2O and Na_2O. It is expected that based on the results of investigations the optimum firing conditions of new developed bodies, where higher mechanical strength and lower thermal expansion in comparison to reference composition, will be established.

The firing behaviour and properties of Li_2O-containing bodies will be additionally investigated after firing in industrial gas kiln with the aim to evaluate their industrial perspective regarding existent or adaptable firing conditions. The investigations of samples after firing under industrial conditions will be oriented towards mechanical strength, deformation during firing and thermal shock resistance. The optimum firing conditions for the bodies containing Li_2O are expected to be at lower firing temperatures than existent in the gas kiln.

3 Materials and Methods

3.1 Chemical and mineralogical composition of raw materials

All raw materials used in the studied bodies are commercially available and normally applied in quartz and alumina porcelain bodies. Generally, they are distinctive in their purity regarding the low content of Fe_2O_3, TiO_2 and CaO. Each raw material is characterized by its chemical composition, mineralogical composition and granulation. Since they are in origin based on natural materials their chemical composition can vary between deliveries inside certain limits specified by supplier.

Raw materials applied in studied compositions are in majority divided into three groups as they are normally treated in triaxial porcelain systems:

a) calcined alumina as a filler,
b) feldspars and spodumene as fluxes, and
c) kaolins and clays as clay system.

All of the raw materials were applied in wet milling process in form as delivered by suppliers, except spodumene, which was calcined at 1150 °C in laboratory kiln before application. The moisture of raw materials was measured before their application and taken into account by the calculation of batches.

3.1.1 Calcined alumina

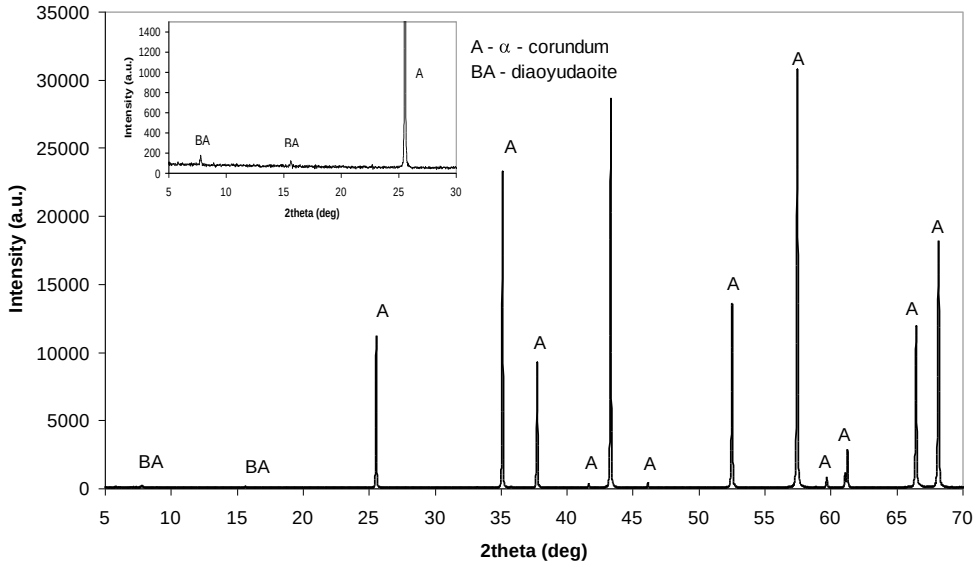

Figure 3.1-1. XRD pattern of calcined alumina HVA FG.

As calcined alumina intermediate soda calcined alumina type HVA FG produced by Almatis was used in all studied bodies. According to supplier specification this type of alumina besides Al_2O_3 typically contains 0.1 wt.% Na_2O, 0.02 wt.% Fe_2O_3, 0.01 wt.% SiO_2 and 0.02 wt.% CaO. The content of α-corundum in HVA FG is more than 98%. It has typical primary crystal size of 2.8 μm, specific surface area (BET) of 0.7 m^2/g and median particle size (d_{50}, Cilas) of 5.3 μm.

XRD pattern recorded on powder of calcined alumina used in all studied formulations is shown in Figure 3.1-1. α-corundum (Al_2O_3, JCPDS 71-1123) is identified as the main mineral from XRD pattern. As

accompanying mineral only low intensity of β-corundum type mineral ($NaAl_{11}O_{17}$, JCPDS 79-2288) named as diaoyudaoite is detected. Due to low intensity of its peaks in 2θ range 5–30°, as obvious from the inserted diagram in Figure 3.1-1, the amount of $NaAl_{11}O_{17}$ is assessed to ~1%.

3.1.2 Feldspars and spodumene

As potassium feldspar Dorkasil 90, supplied from Geremany by Gebrüder Dorfner GmbH&Co., was used in all compositions. It is grained to the grain size below 0.5 mm. XRF analysis with typical chemical composition based on supplier's data is shown in Table 3.1-1, idicating that Dorkasil 90 has high content of K_2O, 14.2 wt.%, and low content of Na_2O, which is characteristic for high potassium feldspar. It is also characteristic by its low content of Fe_2O_3. According to mineralogical composition specified by supplier in Dorkasil 90 mainly potassium feldspar in amount about 84% is present. Other minerals present are sodium feldspar (about 6%), quartz (about 8%) and kaolinite (about 2%).

XRD pattern recorded on powdered feldspar Dorkasil 90 is presented in Figure 3.1-2. Minerals microcline ($KAlSi_3O_8$, JCPDS 76-0918), $K_{0.96}Na_{0.04}AlSi_3O_8$ (JCPDS 83-1895), named as microperthite and α-quartz (JCPDS 85-0796) are identified from XRD patterns.

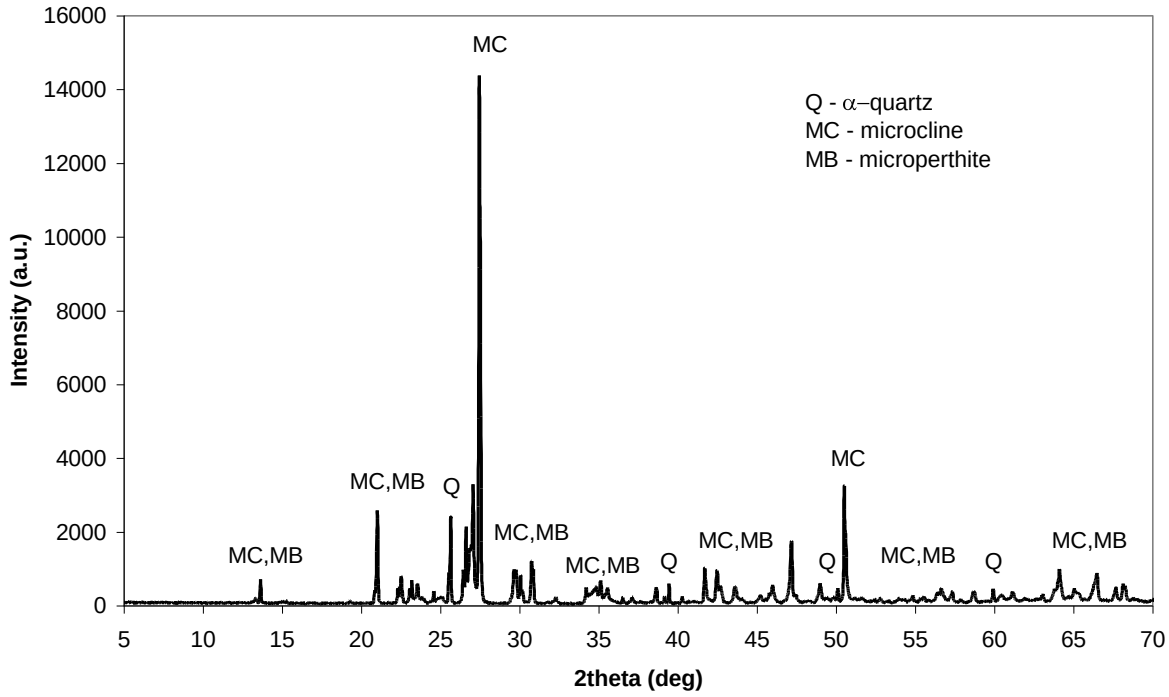

Figure 3.1-2. XRD pattern of feldspar Dorkasil 90.

Feldspar FS 960 M6 was applied in the reference composition as potassium-sodium feldspar. It is supplied by AKW-Amberger Kaolinwerke Eduard Kick GmbH&Co.KG from Germany in form of fine milled grains with the size below 90 μm. Its typical chemical composition based on supplier's data is shown in Table 3.1-1. Among alkali oxides feldspar FS 960 M6 contains 7.4 wt.% of K_2O and 5.0 wt.% of Na_2O, which is characteristic for potassium-sodium feldspars. The amount of Fe_2O_3 is low, 0.05 wt. %. The mineralogical composition as specified by supplier comprise of potassium feldspar (about 44%), sodium feldspar (about 42%), quartz (about 7%) and kaolinite (about 2%).

In Figure 3.1-3 XRD pattern recorded on powdered feldspar FS 960 M6 is shown. Minerals microcline ($KAlSi_3O_8$, JCPDS 19-0926), albite ($NaAlSi_3O_8$, JCPDS 74-0603), sanidine ($(K_{0.93}Na_{0.07})(AlSi_3O_8)$, JCPDS 87-0684) and α-quartz (JCPDS 85-0796) are identified from XRD patterns.

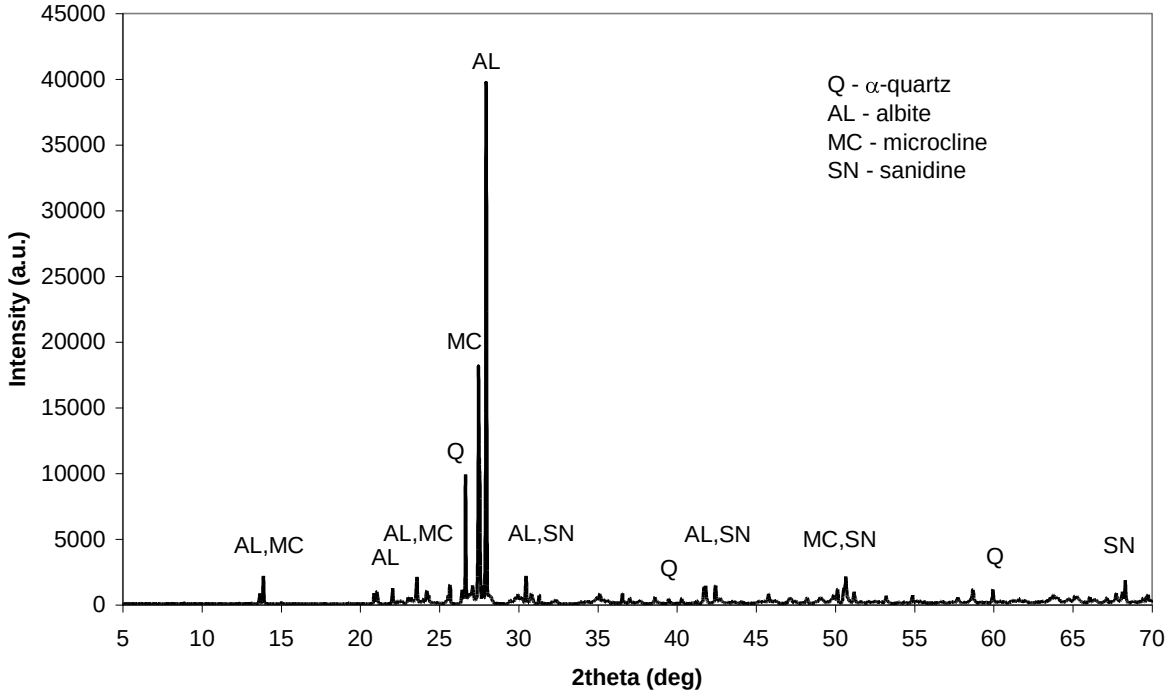

Figure 3.1-3. XRD pattern of feldspar FS 960 M6.

Li-bearing mineral spodumene was introduced in newly developed compositions as a source of Li_2O. Spodumene concentrate was selected because of its high content of lithia and high purity. The concentrate spodumene type 7.5 CO 75μm is supplied by Talison Minerals pty Ltd and produced by Australian Greenbushes Mine. Spodumene is milled to the grain size below 75 μm. Its chemical composition, as specified by supplier, is shown in Table 3.1-1. Based on supplier's data its mineralogical composition consists of about 92% of α-spodumene and less than 8% of quartz. Before applied in model compositions natural spodumene concentrate was calcined in laboratory furnace at 1150 °C with 2 hours holding time.

XRD pattern of calcined spodumene is shown in Figure 3.1-3. β-spodumene (JCPDS 71-2058) as the main mineral and α-quartz (JCPDS 85-0796) are identified from XRD-patterns.

Table 3.1-1. Typical chemical composition of fluxes used in the studied compositions (wt.%).

Oxide	Dorkasil 90*	FS 960 M6*	7.5 CO 75μm*
SiO_2	66.9	67.4	64.50
Al_2O_3	17.4	18.5	26.50
Fe_2O_3	0.042	0.05	0.07
MgO	0.01	0.01	-
CaO	0.02	1.07	0.05
Na_2O	0.70	5.00	0.15
K_2O	14.2	7.40	0.08
TiO_2	0.06	0.02	0.01
BaO	0.32	-	-
Li_2O	-	-	7.60
L.O.I.	0.3	0.3	0.2

*supplier's data

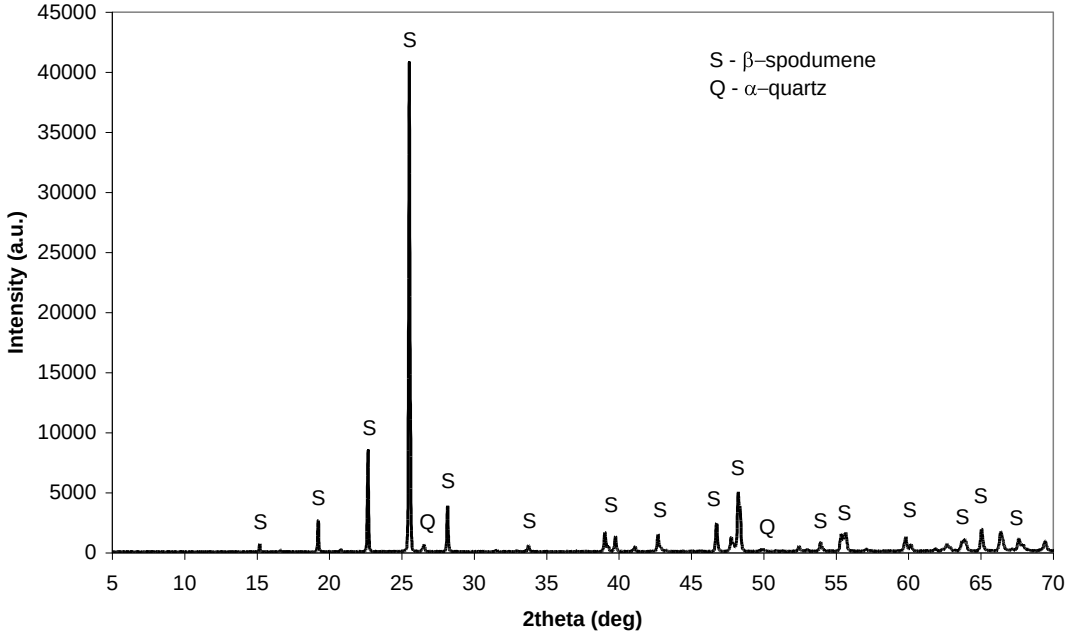

Figure 3.1-4. XRD pattern of calcined spodumene 7.5CO 75 μm.

3.1.3 Kaolins and clays

Kaolin Zettlitz 1a was used in the new developed compositions containing Li_2O. It is supplied by Sedlecký Kaolin A.S. from Czech Republic in form of lumps as noodles in size about Ø10 × 10–30 mm, with moisture content around 10 wt.%. Chemical composition as shown in Table 3.1-2 is determined by XRF analysis, indicating that kaolin Zettlitz 1a is characteristic by its low content of K_2O, 0.94 wt.%, and extremely low content of Na_2O, 0.03 wt.%. According to the mineralogical composition as quoted by supplier kaolin Zettlitz 1a consists of 89–91% kaolinite, 6–8% micaceous minerals and 1–3% quartz. Kaolin Zettlitz 1a has 63% particles <2μm. It is refered as kaolin with high plasticity due to its high amount of clay minerals and particles <2μm.

Table 3.1-2. Typical chemical composition of kaolins used in the studied compositions (wt.%).

Oxide	Zettlitz 1a*	K1*	GO*
SiO_2	47.4	49.0	54.7
Al_2O_3	37.0	35.8	32.3
Fe_2O_3	0.85	0.36	0.28
MgO	0.23	0.15	0.30
CaO	0.30	0.06	0.14
Na_2O	0.03	0.13	0.02
K_2O	0.94	1.60	0.17
TiO_2	0.18	0.35	0.13
L.O.I.	13.0	12.0	11.9

*supplier's data

In Figure 3.1-4 the XRD pattern, which was recorded on dry powder of kaolin Zettlitz 1a, is shown. Identified minerals are kaolinite (JCPDS 89-6538), as the main mineral, α-quartz (JCPDS 85-0796) and illite/muscovite (JCPDS 26-0911).

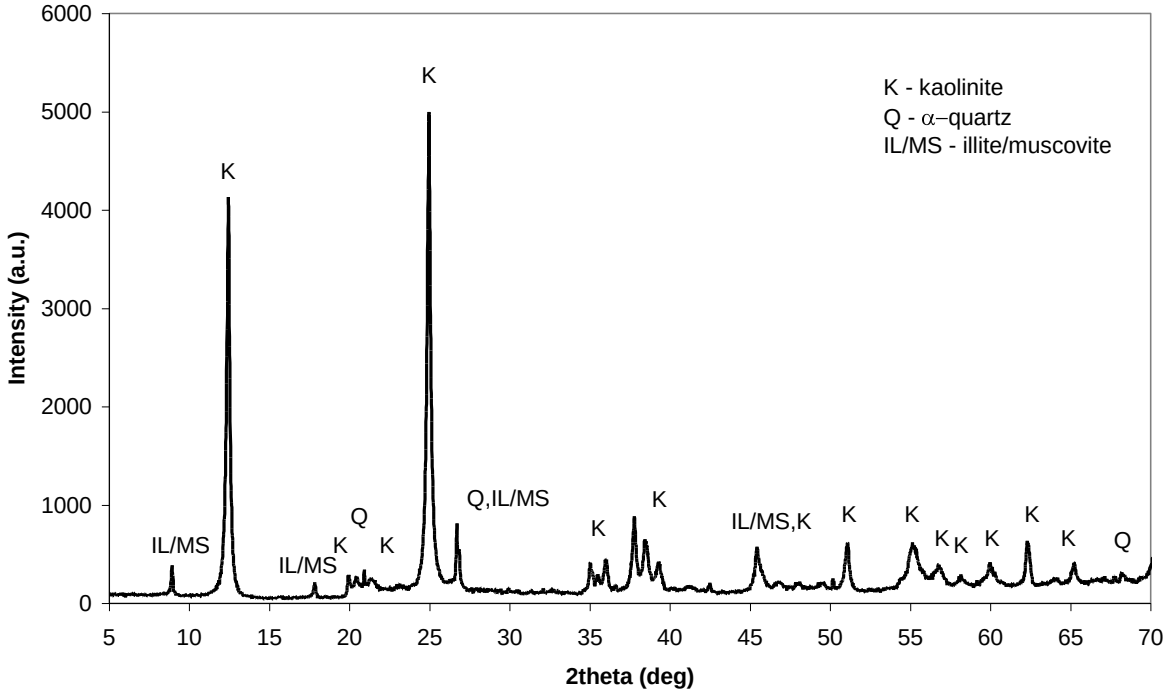

Figure 3.1-5. XRD pattern of kaolin Zettlitz 1a.

Kaolin K1 is used in the reference composition. It is supplied from Germany by Gebrüder Dorfner GmbH&Co. in form of lumps as noodles in the same size as that of kaolin Zettlitz 1a, with moisture content around 8 wt. %. Chemical composition of kaolin K1 based on XRF analysis is specified in Table 3.1.-2. Kaolin K1 contains 1.6 wt.% of K_2O and 0.13 wt.% of Na_2O, which indicates that it is more alkali rich than kaolin Zettlitz 1a. Its mineralogical composition comprise around 86% of kaolinite, around 10% of potassium feldspar, around 1% of sodium feldspar and around 2% of quartz as specified by supplier. The amount of particles <2μm is 46 %. Kaolin K1 has lower plasticity than kaolin Zettlitz 1a due to its considerably lower amount of particles <2μm.

Kaolin GO, supplied by AKW-Amberger Kaolinwerke Eduard Kick GmbH&Co.KG. from Germany, is used in the reference composition. It is delivered in similar form as kaolin Zettlitz 1a, with moisture content around 8 wt.%. Regarding its chemical composition specified in Table 3.1-3 kaolin GO is very low in alkalis containing 0.17 wt.% of K_2O and 0.02 wt.% of Na_2O. Kaolin GO is characteristic by its lower amount of Al_2O_3, Fe_2O_3 and TiO_2 in comparison to kaolins Zettlizt 1a and K1. As quoted by supplier the mineralogical complosition of kaolin GO consists of around 74% of kaolinite, around 8% of illite and montmorillonite, and around 18% of quartz. Kaolin GO has 62% particles <2μm, while its plasticity is lower in comparison to Zettliz 1a due to its lower content of clay minerals.

Clay M1M, refered as illitic clay, was applied as the main clay in all the studied bodies. It is mined by Marx Bergbau in Dornburg, Germany, and supplied by Stephan Smidt Gruppe. It is delivered in shredded form with water content about 12 wt.%. Typical chemical composition of clay M1M as quoted by supplier is shown in Table 3.1-3. Clay M1M is characteristic by its relatively low content of Fe_2O_3, which is about 1.2 wt.%. According to suppliers data for mineral composition clay M1M contains around 35% of minerals from mica group, around 30% minerals from kaolinite group and around 30% of quartz. Beside mineral composition relatively high plasticity of clay M1M is due to the 76% portion of particles <2μm.

In Figure 3.1-5 XRD pattern of clay M1M is presented. It was recorded on dry powder of clay M1M. Minerals kaolinite (JCPDS 06-0221), α-quartz (JCPDS 85-0796) and illite/muscovite (JCPDS 07-0032) are identified from patterns.

Table 3.1-3. Typical chemical composition of clays used in the studied compositions (wt.%).

Oxide	M1M*	Portaclay A 90*	Globoko**
SiO_2	62.6	63	43.3
Al_2O_3	25.8	19	28.2
Fe_2O_3	1.2	4	2.37
MgO	0.4	2.4	0.9
CaO	0.2	1.45	1.15
Na_2O	0.1	2.2	0.22
K_2O	2.9	0.55	1.54
TiO_2	1.3	0.2	0.89
L.O.I.	4.5	6	20.9

*supplier's data

** ETI data

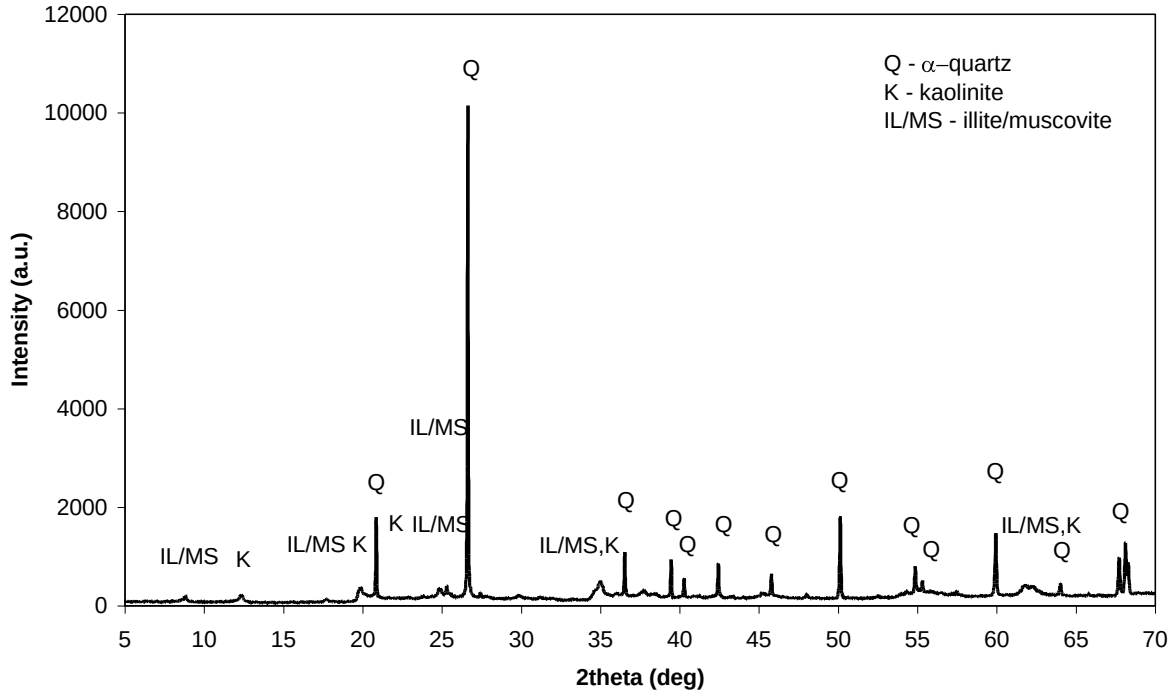

Figure 3.1-6. XRD pattern of clay M1M.

Bentonite Portaclay A 90 from USA, delivered by Ankerpoort nv, was applied in small amount, 1–2 wt.%, in new developed compositions containing Li_2O. Portaclay A 90 is delivered in powder form with moisture content around 9 wt.%. Typical chemical composition of Portaclay A 90 based on supplier's data is shown in Table 3.1-3. Regarding its chemical composition Portaclay A contains relatively low amount of alkali oxides and alkaline-earth oxides as common for bentonites. Regarding the supplier's data, Portaclay A 90 contains around 90% of montmorillonite and around 5% of quartz.

Figure 3.1-6 presents the XRD pattern of bentonite Portaclay A 90 as recorded on powder of bentonite. Minerals montmorillonite (JCPDS 29-1499), illite (JCPDS 02-0050), α-quartz (JCPDS 85-0796), albite ($NaAlSi_3O_8$, JCPDS 74-0603) and microcline (JCPDS 87-1788) are identified.

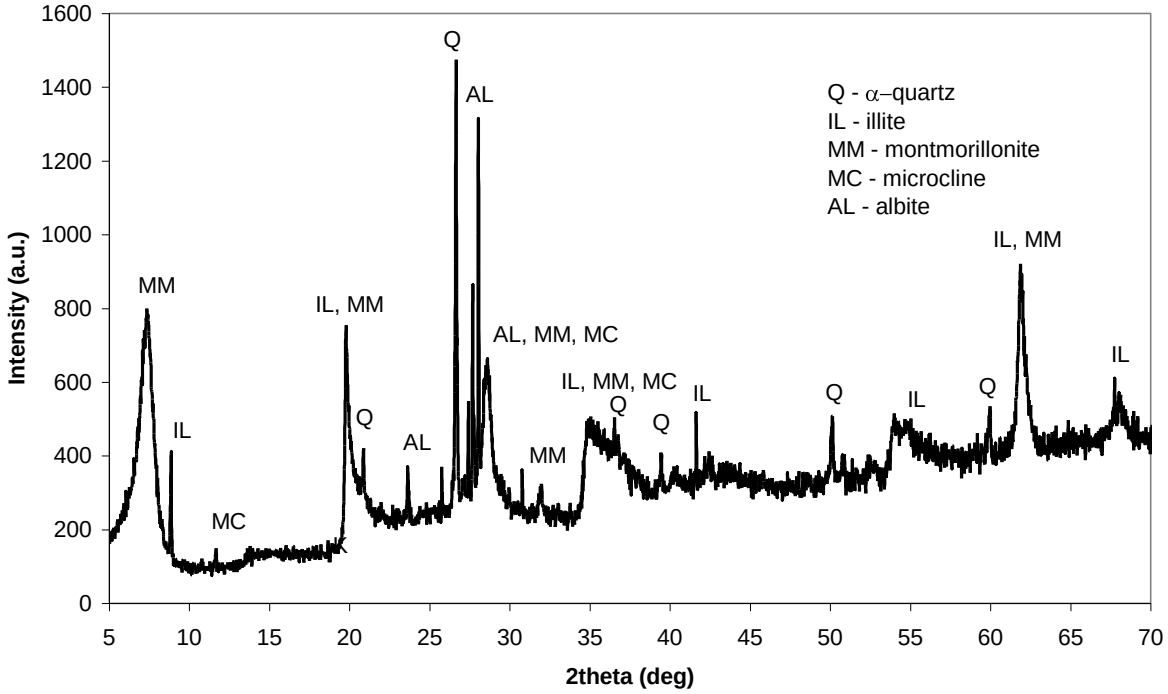

Figure 3.1-7. XRD pattern of bentonite Portaclay A 90.

Clay Globoko, which is local clay supplied by Salonit Anhovo, was applied in reference body. It is delivered in crude state with moisture content around 20 wt.%. Its typical chemical composition based on XRF analysis is specified in Table 3.1.-3. Clay Globoko is characteristic by its very high loss of ignition indicating the presence of high amount of organic impurities. It contains around 40% of kaolinite, around 10% of illite, around 25% of montmorillonite and around 15% of quartz, as quoted by supplier.

3.1.4 Microcrystalline talc

Talc EC 125, delivered by Luzenac, was applied in very small amount, 0.5 wt.%, in reference body. It is microcrystalline talc from Australia. It is delivered in powdered form with grains <125 μm and moisture content below 1.0 wt.%. Its typical chemical composition, as specified by supplier, is shown in Table 3.1-4. Mineralogical composition of EC 125 consists of around 96% of talc and around 3% of chlorite, as quoted by supplier

Table 3.1-4. Typical chemical composition of talc used in composition EN (wt.%).

Oxide	EC 125*
SiO_2	61.0
Al_2O_3	1.0
Fe_2O_3	0.9
MgO	31.2
CaO	0.3
L.O.I.	5.5

*supplier's data

3.2 Milling and mixing of raw materials

The raw bodies of the new developed compositions A, B and C were prepaired on laboratory level, while EN, as the reference body, was produced under industrial conditions. All the raw materials for raw bodies of A, B and C were from the same delivery. The used raw materials for model and reference body were

applied in form as delivered by supplier, i. e. they were not dried or ground before application, except spodumene, which was calcined before application.

For the batch formulations of A, B and C the raw materials were wet milled with alumina balls in the cylindrical laboratory mill. The weight of dry substance in batch was 2900 g. Besides raw materials each batch consisted of 40.5 wt.% of tap water, 0.18 wt.% of deflocculant based on sodium polyphosphate and 0.3 wt.% of binder based on polyvinyl alcohol. All suspensions were milled to the residue of 1.0–1.5 wt.% on control sieve 25 µm. The milling time was around 11 hours. After milling the suspensions were dried on plaster moulds at room temperature to water content of around 20 wt.% by A and B and to around 19 wt.% by C to be suitable for extrusion.

The reference raw body EN was prepared by wet milling of raw materials in an industrial mill with flint balls. The batch comprised of 5000 kg dry substance and 3400 kg tap water. The suspension of EN contained the same amount of water and additives as suspensions of A, B and C. It was milled in time around 18 hours to the residue of 1.8 wt.% on control sieve 25 µm. After milling the suspension of EN was dried on a spray dryer into granulate with the size <0.5 mm and moisture content around 4 wt.%. The spray dried granulate of EN was mixed in Z-mixer with about 19 wt.% of water for 30 minutes.

The particle size and the particle size distribution of raw bodies were measured by granulometry. The particle size distribution curves of studied compositions are shown in Figure 3.2-1.

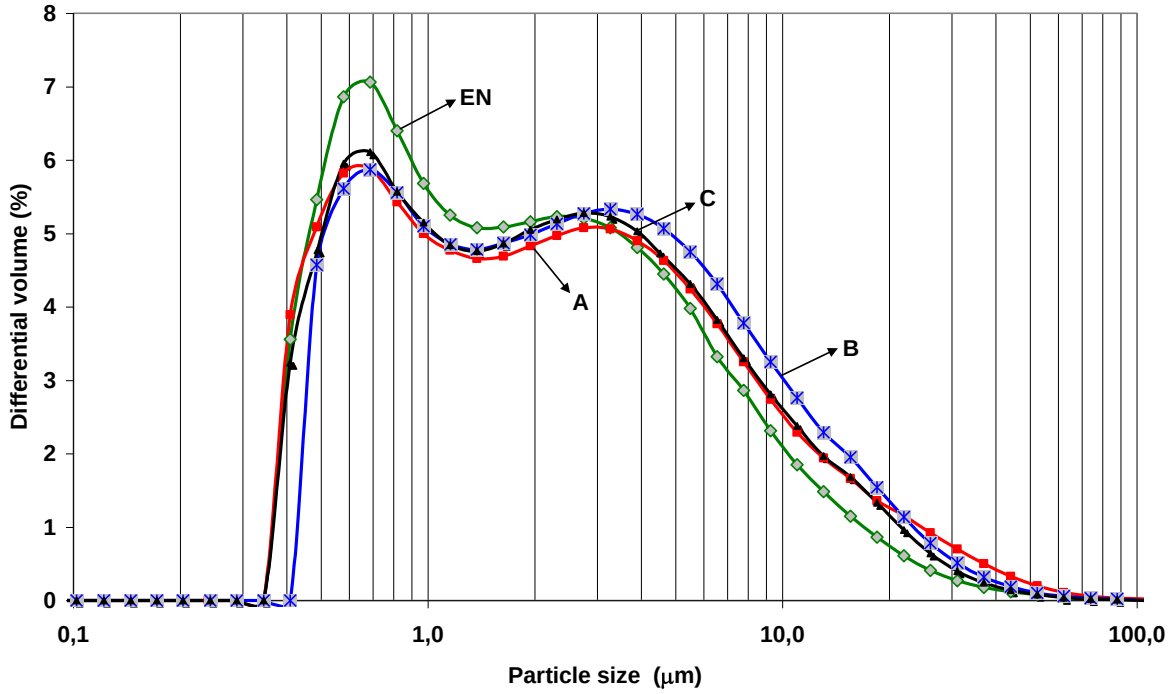

Figure 3.2-1. Particle size distribution of raw bodies EN, A, B and C.

The particle size distribution of raw bodies A, B and C is very similar after the wet milling process, which is confirmed by the resemblence of their granulometric curves. The curves show bimodal particle size distribution with the first maximum around 0.6 µm and the second one between 3 and 4 µm. The similarity in the size of particles for compositions A, B and C is perceived also from rather closed value of d_{50}, which is 1.94 µm for A, 2.21 µm for B and 1.92 µm for C.

The granulometric curve presenting the particle size distribution of raw body EN shows bimodal particle size distribution and its trend is similar to the trend in granulometric curves of raw bodies A, B and C. The d_{50} of EN is 1.61 µm, which is slightly lower as for the model compositions. The first maximum around 0.6 µm in the curve of EN is positioned above the first maximum of A, B and C, thus confirming the lower d_{50} value of EN due to higher amount of fine particles below 1 µm in EN.

3.3 Forming of samples

The test samples of studied compositions were prepaired in the form of circular bars by extrusion technique on the laboratory vacuum machine (Netzsch, V5). The diameter and the length of extruded samples were dependent on the type of measuring method. The die diameter of extrusion machine was 12.05 mm for all samples except for the dilatometric measurements, when the die of 8.15 mm was placed. The extruded bars were cut by knife on required length of 120 mm or 180 mm regarding the type of investigation.

The extruded test samples were drying one day at room temperature followed by 4 hours drying in an oven at 105 °C.

3.4 Firing of samples

Firing was carried out in laboratory electric furnace (Naber, N20/14) with resistance heating elements and in industrial batch kiln, respectively. Before firing the test samples were set in refractory saggars. Refractory saggars are made of porous material based on 97 wt.% of Al_2O_3. The inner horizontal surface of refractory saggars was sprinkled with fine quartz grains <200 μm before each firing.

3.4.1 Firing in laboratory furnace

The samples for XRD, microstructural and physical properties (visual appearance, bulk density, open porosity, thermal expansion and flexural strength) investigations were fired in laboratory furnace in temperature range 950−1350 °C. The temperature range was divided into seven firing cycles. The firing conditions were equal for each firing cycle, including the number of the samples and their arrangement in the saggars of the same type and size. The firing process with 4 °/min heating rate and 15 min soaking time was the same for each firing. The seven different maximum temperatures comprehend of 950, 1050, 1150, 1200, 1250, 1300 and 1350 °C. Upon soaking at the maximum temperature samples were cooled to room temperature at the natural rate for the laboratory furnace.

In the laboratory furnace samples were fired under oxidizing atmosphere with no forced gas flow. The heating rate of 4 °/min was chosen because it is comparable with the average heating rate at industrial conditions.

3.4.2 Firing in industrial kiln

The firing of samples under industrial conditions was carried out in the intermittent shuttle kiln heated by earth gas. Samples fired under industrial condtions were used for for XRD, microstructural and physical properties (bulk density, open porosity, thermal expansion, deformation during firing, thermal shock resistance and flexural strength) investigations. The firing cycle was the same as commonly applied in the ceramic production by company ETI, when extruded products based on alumina porcelain containing around 45 wt.% of Al_2O_3 are fired. The duration of complete firing cycle with maximum temperature of 1315 °C and soaking time of 60 min was eleven hours. In the firing process the oxidation atmosphere is prevailing up to 1100 °C, followed by reduction atmosphere until the end of firing at maximum temperature. The complete cooling process runs under oxidation atmosphere. The industial gas kiln is shown in Figure 3.4-1.

Figure 3.4-1. Industrial gas kiln.

3.5 Characterization

The flow chart illustrating the processing of the samples and their characterization is shown in Figure 3.5-2.

3.5.1 Particle size measurements

The particle size distribution and median particle size (d_{50}) were determined by laser granulometry (Matroc Microtrac S3500) in izopropanol. Samples of extruded dried bars Ø7x25 mm were dispersed in water.

3.5.2 X-ray Diffraction (XRD)

Phase composition of fired samples was studied from X-ray powder-diffraction patterns recorded on powders (>63 μm) at room temperature (PANalytical, X'Pert PRO MPD, The Nedherlands) using CuKα radiation. The data were collected in the 2θ range from 10 to 80°, in steps 0.034°, with an integration time 100 s. By means of XRD the crystal phases were identified, using a complete ICDD powder pattern file and the PC software X'Pert.

3.5.3 Optical and Scanning Electron Microscopy (SEM)

Microstructure was observed by optical microscope (Nikon, Eclipse TS 100 equipped with digital camera Coolpix 5400) and scanning electron microscope (SEM, Jeol 5800 equipped with a Tracor-Norther energy-dispersive spectrometer (EDS)). Samples for microstructural observation were cut from fired test bars with diameter ~10 mm with cross-sectional orientation and prepared with grinding and polishing using standard metallographic technique. Samples for mullite morphology observations were etched in 3 wt.% HF for 60 sec. Previous to analysis in the SEM, the samples were coated with carbon to provide electrical conductivity.

3.5.4 Sintering by dilatometer and heating microscope

The behaviour of bodies during heat treatment was studied from sintering curves recorded by dilatometer (Baehr, heating rate 5K/min) upon heating up to 1340 °C and by heating microscope (Leitz, heating rate 10K/min) upon heating up to 1390 °C. Test samples of raw bodies for dilatometer were in form of bars ~Ø7x25 mm. They were cut off from dried extruded bars. Test samples for heating microscope were in form of bars ~Ø5x13 mm, prepared by cutting off and dry grinding from dried extruded bars Ø7x25 mm.

3.5.5 Thermal analysis (TG/DTA)

The thermal behaviour of dried bodies was investigated from room temperature to 1200 °C using thermogravimetric analysis (TG) and differential thermal analysis (DTA) (Netzsch STA 429, 5K/min).

DTA and TG curves were recorded on powdered samples prepared from dried extruded bars ~Ø7x25 mm. Fired bodies were investigated from DTA curves recorded under the same conditions as DTA curves of raw bodies. Powdered samples of fired bodies were prepared from bars ~Ø10x120 mm.

3.5.6 Open porosity and bulk density measurments

Open porosity and bulk density of fired bodies were determined by the amount of water absorbed in open pores [97]. Two samples of half-cut test bars, Ø10x120 mm, were used for the open-porosity and bulk-density measurments. Samples were first dried in the oven (105 °C/2h) and then their dry weight, W_d, was measured. They were placed in the vessel with deionized water, in which they were boiled for 3 hours. As immersed in water they were allowed to cool to room temperature and remained in water at room temperature for 24 hours. Samples were taken out of the vessel and their weight, W_h, as suspended in water was measured by placing the samples on hanger immersed in water. Samples were removed from hanger, wiped with damp-free cloth and then reweighed in air to determine the weight of soaked sample, W_s. Open porosity (Eq. 3.6-1) and bulk density (Eq. 3.6-2) were calculated as follows:

$$P_0 = \frac{100(W_s - W_d)}{(W_s - W_h)} \qquad \text{Eq. 3.5-1}$$

$$D_B = \frac{W_d}{(W_s - W_h)} \qquad \text{Eq. 3.5-2}$$

where
P_0 is open porosity;
D_B is bulk density;
W_s is weight of soaked sample in air;
W_d is weight of dry sample and
W_h is weight of sample suspended in water.

3.5.7 Coefficient of thermal expansion (CTE) by dilatometer

CTE was determined on fired samples by dilatometer (Netzsch DIL 402EP, heating rate 5K/min) in temperature range 30–980 °C. Samples were in form of test bars Ø ~6×50 mm.

3.5.8 Mechanical strength determination

Mechanical strength was determined by measuring flexural strength of circular test bars Ø10x120 mm using a three-point bend tester (Netzsch 401/3, Bend tester, both yearly controlled by ZAG) with a 100 mm span width. The procedure of mechanical strength testing followed the directions stated in standard IEC-60672-2 [98]. Seven test bars were used to perform each measurement. Maximum and minimum values were eliminated from measurements, thus flexural strength was calculated as an average of five measured values.

3.5.9 Deformation during firing

Deformation during firing in gas kiln was measured as test bars bending from the horizontal surface. Test bars Ø10x180 mm were set on special refractory support with 100 mm height and 150 mm span width. The bending was measured at the maximum distance of sample from the horizontal firm basis. Five samples were measured for each determination and the average value of their bending states as deformation during firing. Figure 3.6-1 illustrates the set up of samples on refractory saggar showing the bended samples after firing in gas kiln.

Figure 3.5-1. Refractory saggar with deformed samples after firing in gas kiln.

3.5.10 Thermal shock resistance

The procedure of thermal shock testing followed the directions stated in standard IEC-60672-2 [98]. Thermal shock evaluations were determined by heating test bars Ø10x120 mm to desired temperature in an oven (Binder, model FD) for 30 min. The samples were quenched into a container of water with temperature 20 °C and stayed immersed in water for 10 min. The amount of water in container was about 40 liters assuring that the temperature increase of water with quenched samples was ~0.5 °C, which is in agreement with maximum 1 °C increase as required by standard. After immersion in water samples were wiped with paper towel and air dried. Dry samples were immersed into 5 wt.% fuchsine alcohol solution for 30 minutes, washed with tap water and dried at room temperature. Cracks were identified visually. Five samples were used for each testing. ΔT (thermal shock resistance) represents the temperature difference between oven and water temperature when cracks appear on two of five samples.

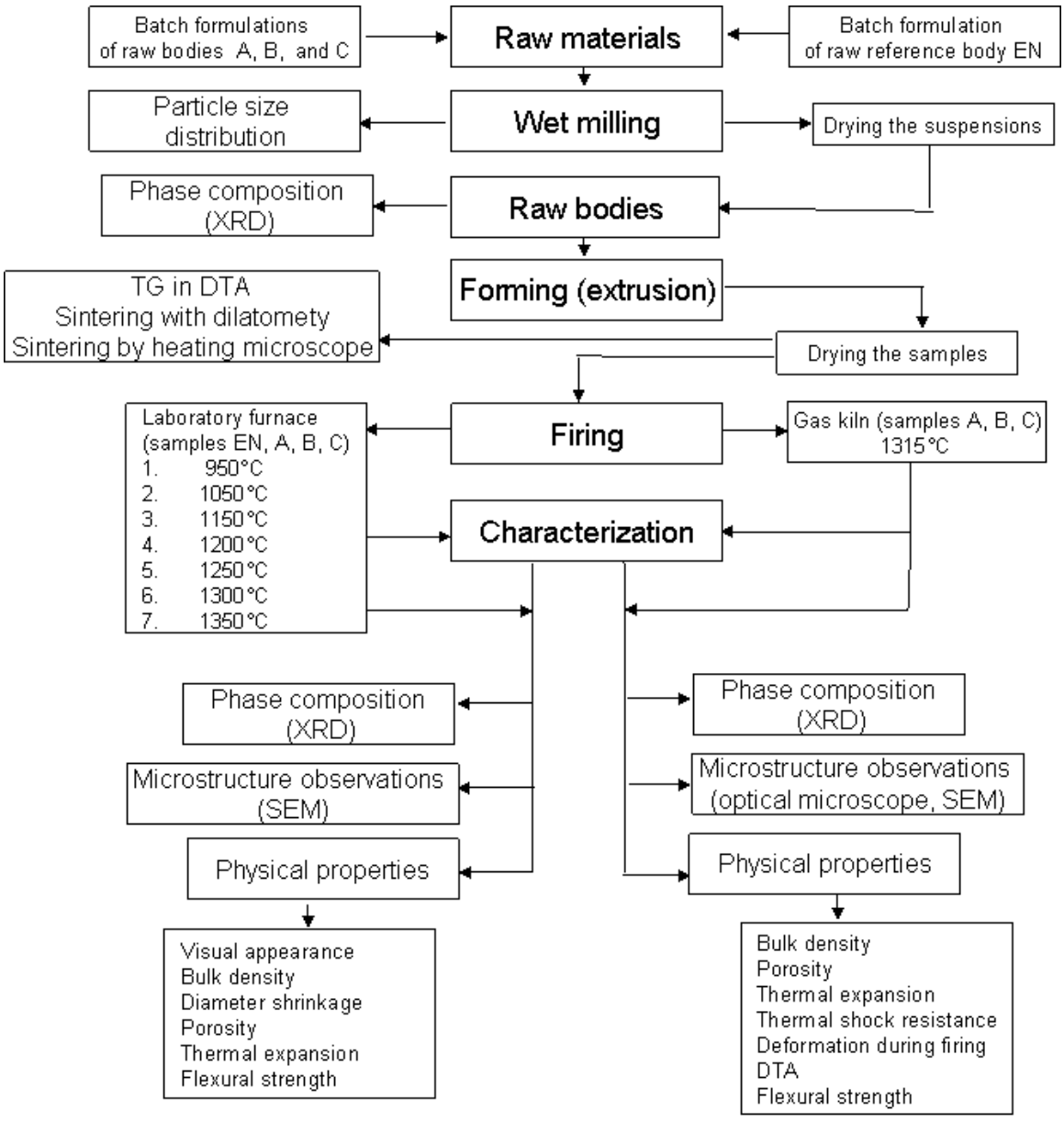

Figure 3.5-2. Flow chart illustrating the processing and the characterization of studied bodies.

4 Results and Discussions

4.1 Composition

The selection of raw materials was oriented to gain the anticipated chemical composition of fired bodies, which was the major criterion of new formulations. The next requirement in formulating the new bodies was their suitability for processing and firing under existent production conditions in factory. The technological framework thus set the limitations on the selection of raw materials, preparation methods, forming technique and firing process.

Regarding the chemical composition the fired high alumina porcelain bodies investigated in present study were aimed to contain approximately the same amount of Al_2O_3, (around 61 wt.%) and relatively low amount of Fe_2O_3 (below 0.5 wt.%) and TiO_2 (below 0.3 wt.%). In the new developed formulations, specified as A, B and C, the increasing amount of Li_2O was added as the main flux.

4.1.1 Batch composition of raw bodies

Three model compositions A, B, and C were prepared for comparable investigations with reference material EN. The mineralogical characteristics of selected raw materials assure suitable plasticity for extrusion and desirable green strength.

Table 4.1-1. Batch formulations of raw bodies EN, A, B and C (wt. %).

Raw material	EN	A	B	C
Alumina HVA FG	43.5	43.0	44.0	44.0
Clay M1M	7.7	12.0	9.0	7.0
Feldspar Dorkasil 90	10.3	9.0	9.0	10.0
β-Spodumene 7.5 CO	-	13.0	15.0	20.0
Kaolin Zettlitz	-	22.0	21.0	17.0
Bentonite Portaclay A 90	-	1.0	2.0	2.0
Kaolin GO	13.0	-	-	-
Kaolin K1	9.7	-	-	-
Feldspar FS 960 M6	11.0	-	-	-
Clay Globoko	4.3	-	-	-
Talcum EC 125	0.5	-	-	-

The batch formulations of raw bodies are specified in table 4.1-1. Raw bodies EN, A, B and C contain about the same amount of calcined alumina HVA FG and potassium feldspar Dorkasil 90. The clay system regarding the sum of all clays and kaolins is similar by A and EN, while lower at B and C. In composition EN feldspar FS 960 is introduced as the source of Na_2O. As a source of Li_2O β-spodumene is applied in increasing amount in compositions A, B and C, where it is added in quantity 13, 15, and 20 wt.%, respectively.

Mineralogical composition of raw bodies as presented in Table 4.1-2 is calculated based on suppliers' data specifying the quantity of minerals preset in the raw materials. Calculated mineralogical composition can not be considered as absolute, since the data for calculation are quoted as ″around″. However, by comparing the mineralogical composition between raw bodies significant differences could be recognized.

Table 4.1-2. Mineralogical composition (calculated) of raw bodies (wt.%).

Mineral	EN	A	B	C
α-Corundum	42.6	42.1	43.1	43.1
Quartz	7.0	5.8	5.1	4.9
Kaolinite	22.4	23.8	22.0	17.8
Illite	4.2	5.7	4.6	3.6
Montmorillonite	1.1	0.9	1.8	1.8
Microcline	14.5	7.6	7.6	8.4
Albite	5.3	0.5	0.5	0.6
β-Spodumene	-	12.0	13.8	18.4
Talcum	0.48	-	-	-
Residuals	2.4	1.5	1.4	1.3

The main difference in mineralogical composition among raw bodies is in applied fluxes. In raw body EN microcline and albite represent the flux minerals, while in model raw bodies the flux minerals are microcline and β-spodumene.

Among studied raw bodies EN is characteristic by its slightly higher amount of free quartz and C with its lower content of kaolinite.

The plasticity of raw bodies is attributed to the type and total amount of clay minerals present. Clay minerals kaolinite, illite and montmorillonite are present in all raw bodies in about comparable proportion. The ratio clay/nonclay minerals is 0.39 for EN, 0.45 for A, 0.40 for B and 0.30 for C. Raw bodies distinguish in plasticity owing to the differences in the relative amount of clay minerals to non/clay minerals. Raw body A has the highest ratio clay/nonclay minerals, indicating its higher plasticity in comparison to other raw bodies, while raw body C has the lowest plasticity.

4.1.2 Chemical composition of fired bodies

Considering the loss of ignition of each raw material the chemical composition of fired body is calculated from its batch formulation.

Table 4.1-3. Calculated chemical composition of fired bodies (wt. %).

Oxide	EN	A	B	C
SiO_2	34.34	34.34	33.76	34.27
Al_2O_3	60.51	61.15	61.68	60.87
Fe_2O_3	0.33	0.44	0.42	0.36
MgO	0.31	0.13	0.13	0.12
CaO	0.23	0.13	0.14	0.12
Na_2O	0.66	0.17	0.19	0.20
K_2O	2.98	1.96	1.86	1.90
TiO_2	0.20	0.20	0.16	0.13
Li_2O	-	1.02	1.18	1.56

Calculated chemical composition of studied bodies is presented in Table 4.1-3. Fired compositions EN, A, B and C are relatively similar regarding types and quantities of all oxides except alkali oxides. The amounts of SiO_2, Al_2O_3, Fe_2O_3, MgO, CaO and TiO_2 are relatively close. Compositions A, B, and C have nearly equal amounts of K_2O, around 1.9 wt.%, and Na_2O, around and 0.2 wt.%. They differentiate in the amount of Li_2O, which is 1.02 wt.% by A, 1.18 wt.% by B and 1.56 wt.% by C. Reference composition EN is characteristic by its high content of K_2O, 2.98 wt.%, and Na_2O, 0.6 wt.%.

4.2 Behavior of samples under heating

4.2.1 Thermal gravimetry and differential thermal analysis results

The behaviour of samples under heating was first investigated by changes in weight and heat evolution as observed in TG and DTA curves recorded up to 1200 °C.

TG and DTA curves of reference body EN and Li_2O-containing bodies A, B and C are shown in Figure 4.2-1. In the TG traces the weight loss up to 400 °C is nearly equal about 1% for all samples. In heating range 400-800 °C the weight loss values for EN, A, B and C are 3.6%, 3.9%, 3.5% and 3.0 %, respectively. When samples are heated from 800 °C to 1200 °C they all attain only about 0.2 % weight loss. In DTA curves an endothermic effect is observed with its maximum at ~525 °C by samples EN, A and B, and ~518 °C by C. An exothermic effect appears with its maximum at 985 °C for EN, at 971 °C for A, at 968 °C for B and at 967 °C by C. The declination in DTA curve is observed with the onset at 1079 °C for EN, at 1076 °C for A, at 1070 °C for B and at 1064 °C for C.

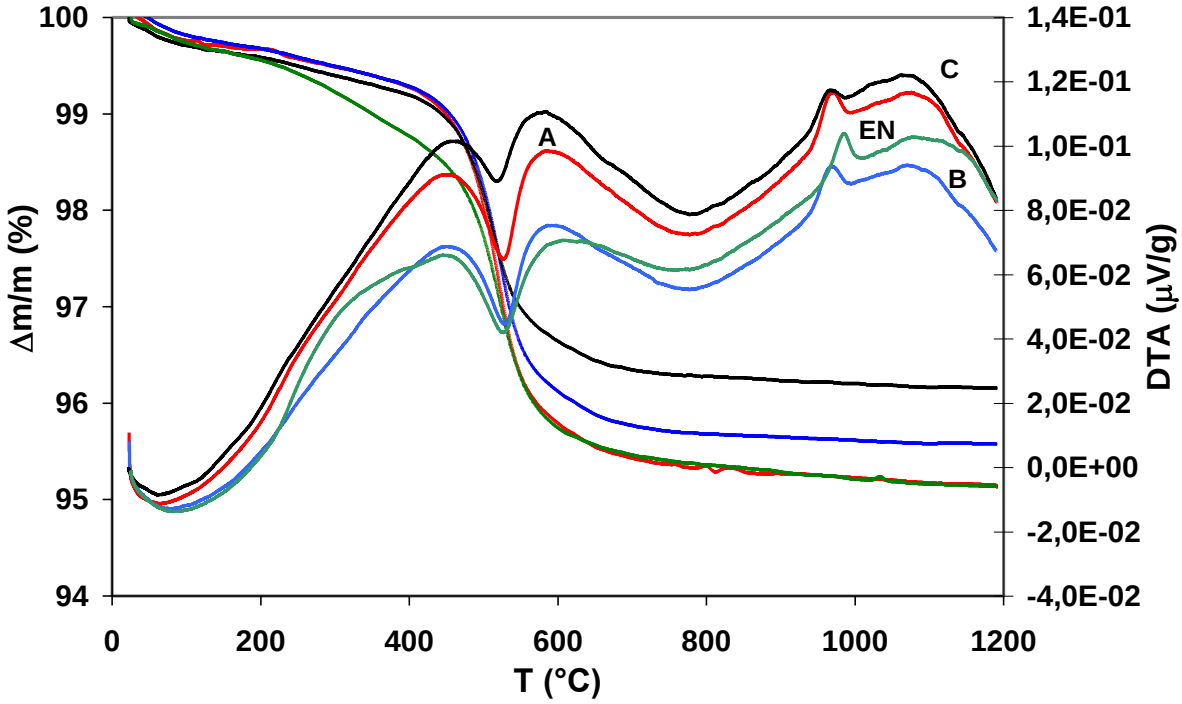

Figure 4.2-1. DTA and TG curves of samples EN, A, B and C recorded in the temperature range 25 to 1200 °C.

It is evident from DTA and TG curves that similar reactions take place in all the samples up to 1200 °C. The weight loss in TG traces determined in range 400–800 °C is related to the quantity of the clay system loosing water with the lowest value by composition C, which contains the lowest amount of clay components. Both, endothermic and exothermic effects observed in DTA curves and weight loss in TG curves in temperature range 400–800 °C are characteristic for kaolinite-to-mullite reaction series [51,99,100]. The weigth loss in temperature range 400–800 °C is correlated with the endothermic dehydroxylation reaction of kaolinite in the range 450–600 °C, completed at about 900 °C. The exothermic effect in temperature range 800–1000 °C, which occurs without weight losses, is attributed to the transformation of metakolinite, in which the Al-Si spinel and amorphous silica is formed. Al-Si spinel phase is recognized as the precursor of mullite.

The addition of Li_2O lowers the temperature of the mullite formation since the maximum of exothermic effect in temperature range 800–1000 °C is 14, 17 and 18 °C lower for composition A, B and C as compared to reference composition. It was found by Carbajal *et al* [59], who studied the porcelain stoneware compositions, that the enhanced amount of fluxes activates the metakaolinite transformation and produces a decreasing of the transformation temperature as identified from their DTA curves. Talyaganov

et al. [101] ascertained from DTA investigations of Li_2O-doped porcelain bodies that the beginning of mullite formation was affected by the presence and the amount of Li_2O, since the exotermic peak was shifted to lower temperatures with Li_2O added. In their investigations, the addition of 0.44 and 0.88 wt.% of Li_2O lowered the maximum of exothermic peak for 14 and 26 °C.

The beginning of melting process is affected by the presence of Li_2O since the start of endothermic effect correlated to the feldspar fusion and the partial quartz dissolution, registered as an onset in DTA curves, is 3, 9 and 15 °C lower for compositions A, B and C in comparison to reference composition. The endothermic effect, due to the feldspar fusion and partial quartz dissolution is influenced by the amount of liquid phase [102]. Li_2O should favour the formation of liquid phase by facilitating feldspar melting [101].

As confirmed with DTA and TG curves the main reactions that occur up to 1000 °C are attributed to the clay constituents and their amount in the samples. Comparing the DTA curves the same transformation processes occur in all studied compositions during heating up to 1200 °C. However, in compositions containing Li_2O the beginning of mullitization process is noticeably lowered dependent on the amount of Li_2O.

4.2.2 Sintering behavior with dilatometry

The next step in investigating thermal behavior of samples was to determine the sintering behaviour in temperature range up to 1340 °C. Sintering behaviour, where dimensional changes of bodies during heat treatement were recorded, was studied from sintering curves recorded by dilatometer with heating rate 5K/min. The heating rate of 5K/min in dilatometer is very similar to an average heating rate in firing process of porcelain under industrial conditions.

Sintering curves of studied compositions are displayed in Figure 4.2-2.

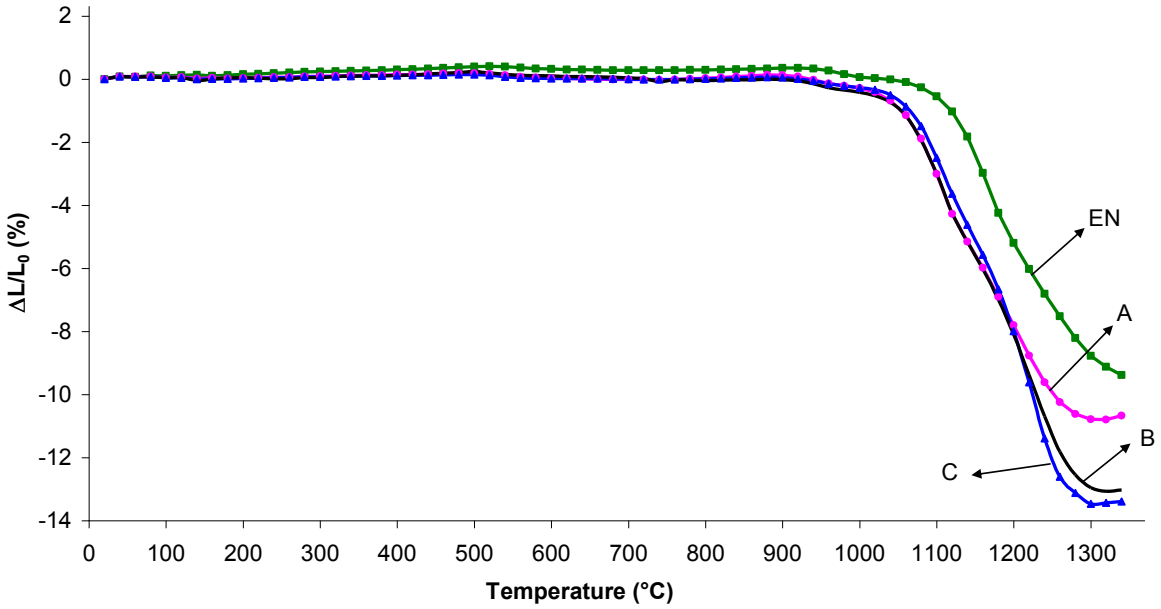

Figure 4.2-2. Sintering curves of samples A, B, C and EN recorded by dilatometer in temperature range 25−1340 °C.

It is noticeable from sintering curves, that there appear only small variations of dilatation by all compositions in the initial stage of sintering up to 1000 °C, where they were close to linear and lower than 0.4%. The curves of compositions A, B and C overlap, while the reference composition EN, which has similar trend, lies slightly above with maximum expansion of 0.4%.

The comparable dilatation behaviour in all the samples up to 1000 °C is attributed to the similar reactions that take place as confirmed by the DTA curves in Fig. 4.2.-1. All reactions taking place during heating up to 1000 °C obviously don't cause any volume changes or minimal volume changes as observed

also by others [25].

The onset temperature of intensive shrinkage, determined as temperature at tangent intersection point, is around 1060 °C for A, B and C and around 1110 °C for EN. The onset temperature is perceived at around 50 °C lower temperature by the Li_2O-containing compositions in comparison to EN. The influence of Li_2O on the beginning of the densification process was ascertained also by Talyaganov *et al.* [93], who reported that porcelain bodies containing 0.5 and 0.9 wt.% of Li_2O experienced earlier shrinkage at lower temperature (~ 970 °C) than the conventional composition (~1080 °C).

The eutectic temperature of potassium feldspar and silica defines the first melt formation at ~990°C [1,40]. The onset temperature of intensive shrinkage is correlated with more intensive melt formation above the eutectic temperature, which is also seen in DTA curves in Fig. 4.2.-1 as the beginning of an endothermic effect around 1070 °C.

The decline of all sintering curves strongly increases beyond the onset temperature. Attributable to densification process with temperature increasing the shrinkage remarkably increases by all compositions, which is expressed by sharp decline of sintering curves up to maximum densification. The reference composition EN attains shrinkage of 9.4% at 1340 °C. The lowest point in sintering curve of EN is not confirmed. The maximum shrinkage values for compositions A, B and C are 10.8%, 13.1% and 13.5%, respectively. Compositions A and B achieve their maximum shrinkage at the same temperature 1320°C, while C completes to shrink at 1300 °C. Above the temperature of maximum shrinkage the small expansion appears by all compositions containing Li_2O, indicating the bloating of bodies. It should be noted that samples of composition C showed small bubbles on the surface and were stuck on platinum sheet in dilatometer assembly after dilatometric measurement.

Compositions with Li_2O achieve their maximum densification at lower temperatures in comparison to EN. With increasing the amount of Li_2O from 1.2 wt.% to 1.6 wt.% the temperature of maximum shrinkage in decreased for ~20°C, while with 1.0 wt.% and 1.2 wt.% Li_2O added the maximum shrinkage is attained at above the same temperature.

The results show that the densification process of the bodies is enhanced by the presence of Li_2O, in a similar way to that reported for triaxial porcelain bodies [93] and bodies for porcelain stoneware tiles [95].

4.2.3 Sintering behavior by heating microscope

Sintering behavior of samples during heat treatment was additionally recorded in heating microscope where sample is free standing with no pressure on its surface. In heating microscope the sample is heated similarly as when fired under industrial condition. The effect of volume increase and deformation due to overfiring are more reliable to be determined from the heating microscope records. The heating rate in heating microscope was 10K/min, which is similar to the heating rate by faster firing schedules of ceramics.

The sintering curves based on data recorded by heating microscope are shown in Figure 4.2-3. Sintering curves are presented in temperature range 800–1390 °C to emphasize and show more evidently the differences in sintering behavior among studying compositions at the end of firing process.

There are no significant differences in shrinkage among all studied compositions up to 1100 °C with sintering curves almost overlapping. The onset temperature of intensive shrinkage is estimated around 1100 °C for A, B and C and around 1130 °C for composition EN. Beyond 1100 °C and up to around 1280 °C the sintering curve of EN lies almost parallel above the sintering curves of A and B. EN achieves its maximum shrinkage of 14.7 % around 1340 °C.

The shrinkage proceeds very similar by the compositions A and B in the temperature range from 800 °C to 1350 °C. Composition A attains shrinkage of 15.0% at 1370 °C with the curve still in decline. The maximum shrinkage of A is not confirmed. B attains its maximum shrinkage of 15.4% around 1340 °C. The maximum shrinkage of 17.3 % is achieved by C around 1300 °C.

Beyond the temperature of maximum shrinkage the expansion is observed for compositions EN, B and C, being most extensive for C, as seen from the sintering curves. The tendency to expansion above the temperature of maximum shrinkage is similar for EN and B.

Composition C is distinguished by its expressive expansion beyond the temperature of maximum shrinkage. The presence of Li_2O in the amount 1.6 wt.% strongly affects the tendency to bloating which results in expansion of the body. The expansion is caused by overfiring due to bloating phenomena of the formed melt, in which the number and/or the size of pores is increased.

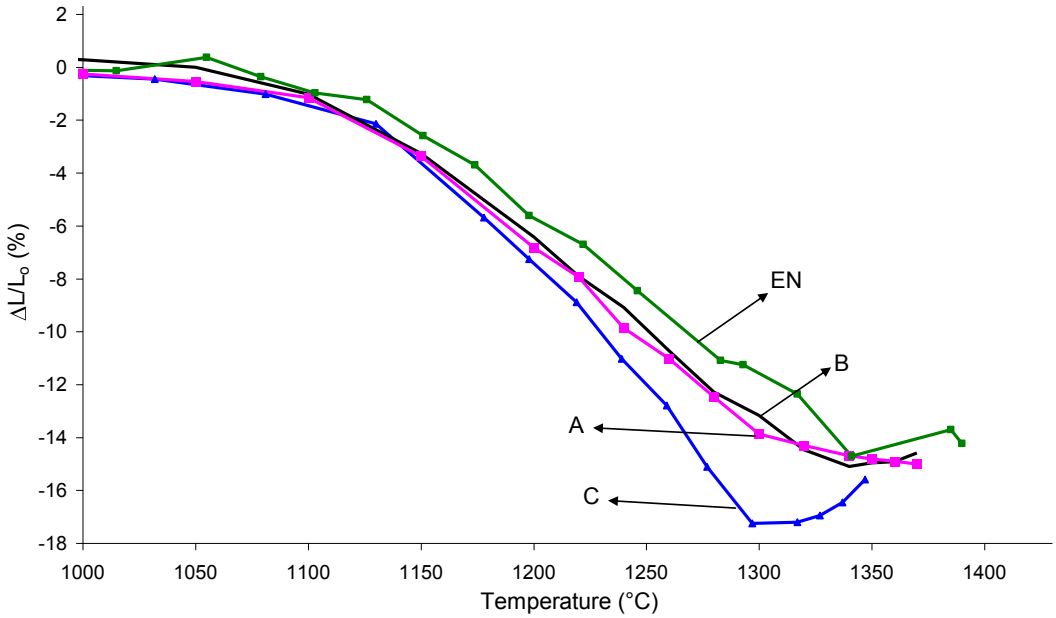

Figure 4.2-3. Sintering curves of samples EN, A, B and C recorded by heating microscope in temperature range 800−1390 °C.

There are some distinctions in sintering behaviour of the studied samples heated in dilatometer or in heating microscope, which are mainly attributed to the differences in heating rate, which was 10 K/min in heating microscope and 5 K/min in dilatometer, and partially to the method of measuring. In the heating microscope the sample is subjected to its own force of gravity as free standing during heating, while in the pushrod dilatometer the sample is positioned into specimen holder and subjected to an additional force during heating.

The sintering behaviour of all studied compositions examined from curves recorded by dilatometer or by heating microscope is resembled in the initial stage of sintering up to 1000 °C with sintering curves almost overlapping. The onset temperature of intensive shrinkage is ~40° C lower for A, B and C and around 20 °C lower for EN when determined by dilatometer. The lower onset temperature should be correlated to lower heating rate in dilatometer. The maximum shrinkage of EN is around 1340 °C in heating microscope, while in dilatometer at 1340 °C the sintering curve of EN is still in decline. In heating microscope the sintering curve of A is still in decline around 1370 °C, while the maximum shrinkage of A is attained around 1320 °C in dilatometer. The maximum shrinkage of B and C is around 1340 and 1300 °C in heating microscope, while around 1320 and 1300 °C in dilatometer. The maximum shrinkage is for all compositions higher in the heating microscope. The higher temperatures of maximun shrinkage for A and B in the heating microscope should be correlated with the higher heating rate in heating microscope than in dilatometer, while the differences in temperature of maximum shrinkage of C and EN are not made clear.

The expansion of C due to bloating is less expressive in the dilatometer than in the heating microscope, which might be attributed to the position of the sample in specimen holder.

4.3 Phase composition and microstructure of bodies fired between 950 °C and 1350 °C

We investigated the phase composition, the microstructure and the physical properties of samples fired in the temperature range from 950 to 1350 °C due to the major shrinkages observed in this range from the sintering curves in Figure 4.2-2 and in Figure 4.2-3. Seven firing temperatures were selected in this temperature range with closer temperature intervals in the region of sintering curve where the rate of densification was the greatest. The test samples of all studied compositions were fired at 950, 1050, 1150, 1200, 1250, 1300 and 1350 °C in the laboratory electric furnace.

We performed the XRD analysis of the raw bodies before implementing the firing cycles at increasing temperatures with the aim to assist the phase interpretation of the fired samples. The mineralogical composition of the raw bodies was determined from the XRD spectra recorded on powders of dried extruded samples.

4.3.1 Phase composition of raw and fired bodies

The recorded XRD spectra of each studied composition fired at different temperatures are collected in one graph (a) in columns. The XRD spectrum of raw bodies is presented below (b).

In Table 4.3-1 the identified main minerals from XRD spectra of raw bodies are stated. In all the green bodies, corundum (α-Al_2O_3) prevailed as the primary mineral phase. However, kaolinite ($(Al_2Si_2O_5(OH)_4$), microcline ($KAlSi_3O_8$) and α-quartz (SiO_2) were also present in all the green bodies. The kaolinite came from the clay part, the microcline was present as the main mineral in potassium feldspar, and the presence of α-quartz (SiO_2) is the result of quartz being the accompanying mineral of clays and fluxes. Albite ($NaAlSi_3O_8$) was only identified in the reference composition, EN, where the flux system consisted of potassium and sodium feldspar. β-spodumene ($LiAlSi_2O_6$) was only present in the model compositions A, B and C, where it was added as the main flux component.

The identified phases from XRD patterns of raw bodies confirm that studied compositions differentiate mainly in the flux minerals.

Table 4.3-1. The main minerals dentified from XRD spectra of raw bodies

Mineral	EN	A	B	C
Corundum	×	×	×	×
Kaolinite	×	×	×	×
Microcline	×	×	×	×
Quartz low	×	×	×	×
β-spodumene		×	×	×
Albite low	×			

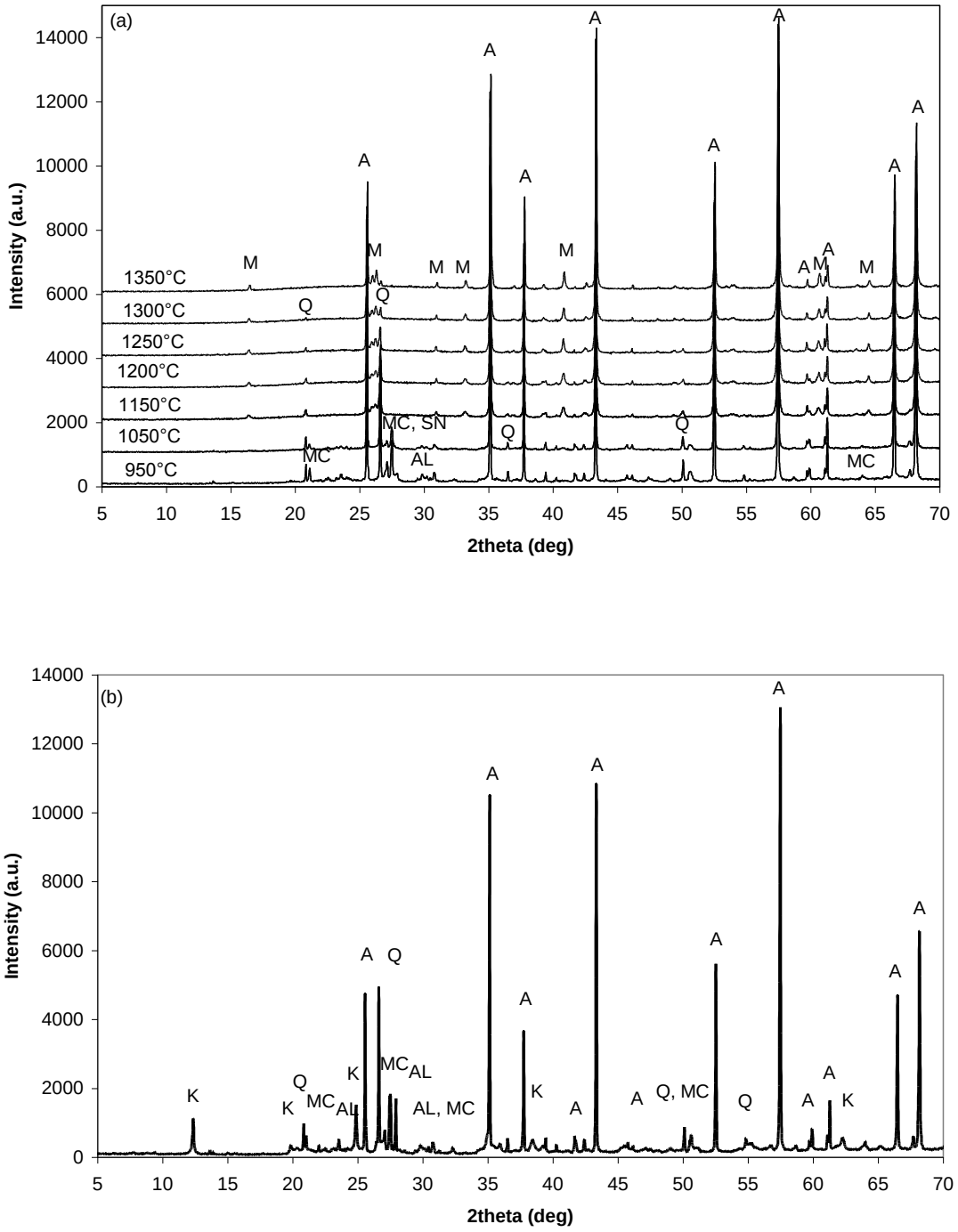

Figure 4.3-1. XRD patterns of sample EN (a) fired in temperature range 950–1350°C and (b) XRD pattern of corresponding raw body. In grouped XRD patterns of fired bodies revealed minerals are corundum (A), mullite (M), α-quartz (Q), microcline (MC), sanidine (SN) and albite (AL). In raw body the identified minerals are corundum (A), kaolinite (K), α-quartz (Q), microcline (MC) and albite (AL).

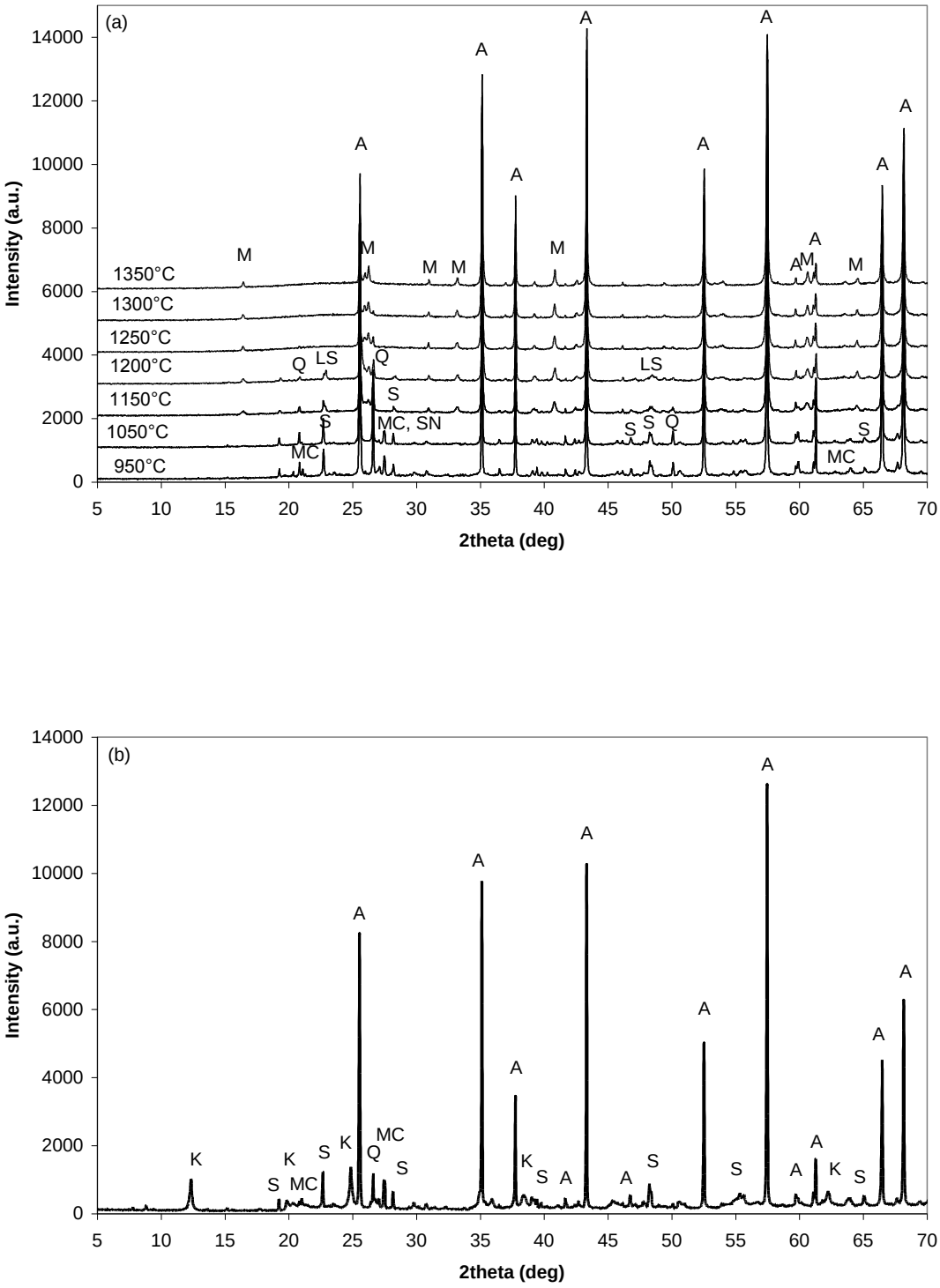

Figure 4.3-2. XRD patterns of sample A (a) fired in temperature range 950–1350°C and (b) XRD pattern of corresponding raw body. In grouped XRD patterns of fired bodies minerals corundum (A), mullite (M), α-quartz (Q), microcline (MC), sanidine (SN), β-spodumene (S) and $LiAlSi_3O_8$ (LS) are revealed. In raw body the identified minerals are corundum (A), kaolinite (K), α-quartz (Q), microcline (MC) and β-spodumene (S).

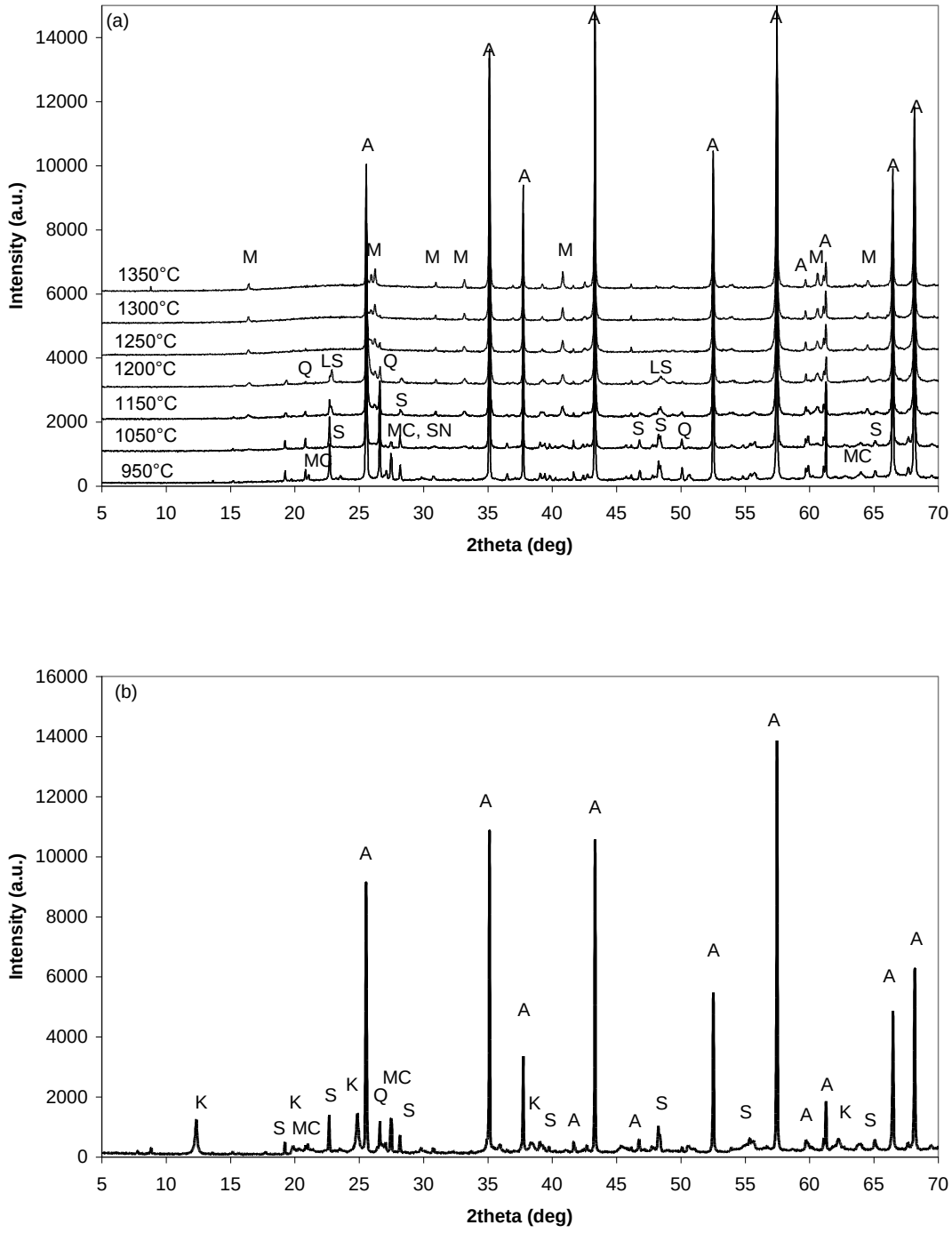

Figure 4.3-3. XRD patterns of sample B (a) fired in temperature range 950−1350°C and (b) XRD pattern of corresponding raw body. In grouped XRD patterns of fired bodies minerals corundum (A), mullite (M), α-quartz (Q), microcline (MC), sanidine (SN), β-spodumene (S) and $LiAlSi_3O_8$ (LS) are revealed. In raw body the identified minerals are corundum (A), kaolinite (K), α-quartz (Q), microcline (MC) and β-spodumene (S).

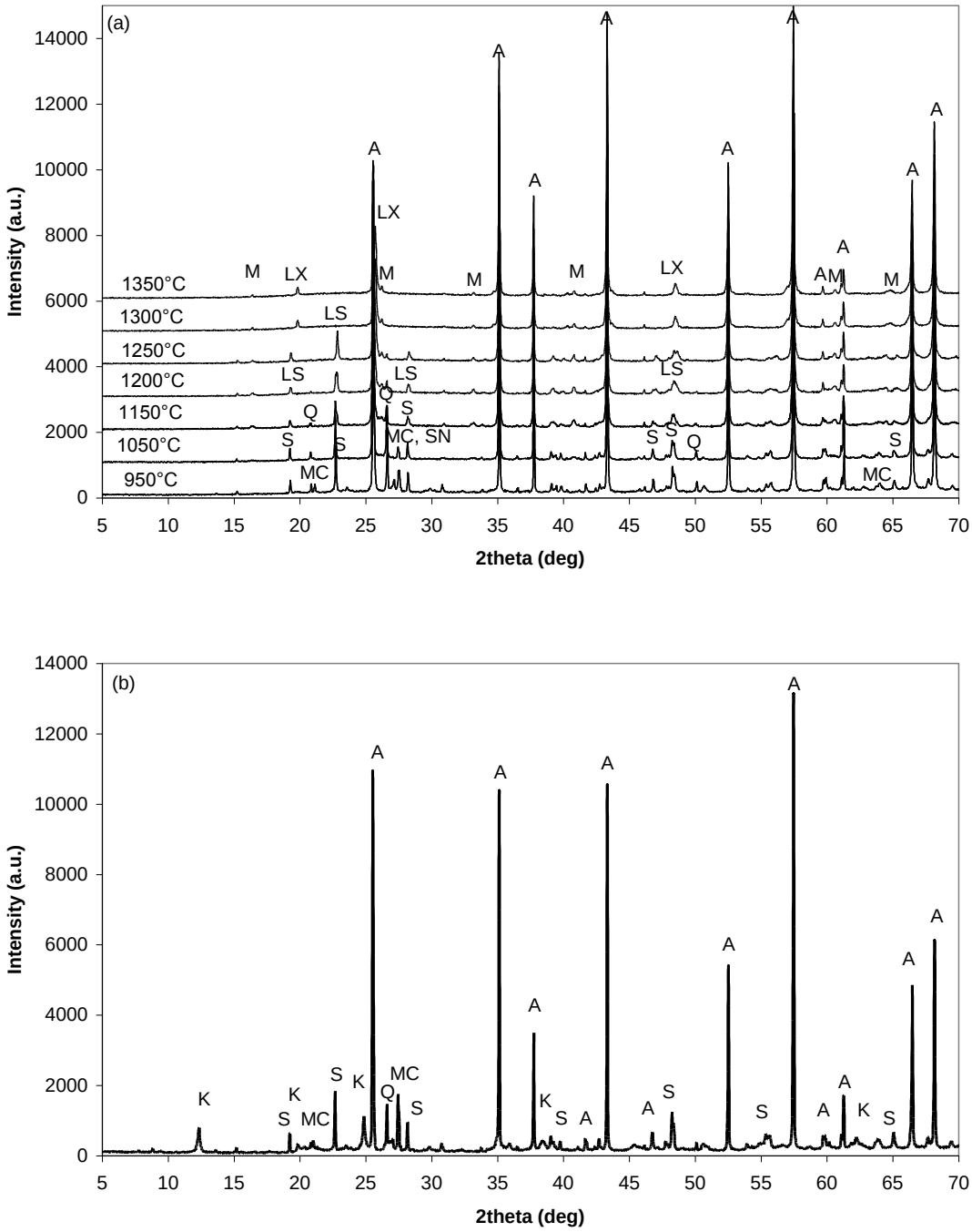

Figure 4.3-4. XRD patterns of sample C (a) fired in temperature range 950−1350 °C and (b) XRD pattern of corresponding raw body. In grouped XRD patterns of fired bodies minerals corundum (A), mullite (M), α-quartz (Q), microcline (MC), sanidine (SN), β-spodumene (S), $LiAlSi_3O_8$ (LS) and $Li_xAl_xSi_{1-x}O_2$ (LX) are revealed. In raw mix the identified minerals are corundum (A), kaolinite (K), α-quartz (Q), microcline (MC) and β-spodumene (S).

Fig. 4.3-1 (a) presents the XRD spectra of the composition EN, fired at different temperatures. Corundum, as the predominating crystalline phase, is observed in all the fired samples. The more phases in addition to corundum in the samples fired at 950 and 1050 °C are the flux minerals microcline, sanidine and albite with their peak intensities decreasing with increasing temperature due to gradual melting up to 1150 °C, at which point they disappear. The vanishing of flux minerals is in agreement with the investigations of physical and chemical processes during porcelain heating by Schüller [4], who explains that all the fedspar components are melted at the latest at 1150 °C. Their melting is correlated with the

ternary eutectic $K_2O–Al_2O_3–SiO_2$ eutectic in Figure 1.2-4, indicating feldspar and silica eutectic at 985 °C, and $NaAlSiO_4–KAlSiO_4–SiO_2$ eutectic in Figure 1.3-1, indicating eutectic between potash feldspar, sodium feldspar and silica at 1020 °C. Microcline and its high temperature form sanidine partially melted above 950 °C as seen from the peak intensities diminution at 1050 °C. Above this temperature they completely melted, since at 1150 °C the absence of all feldspars was observed, which was confirmed also with the results of former studies on heating porcelain compositions by Iqbal and Lee [40] and by Tarvornpanich *et a.l* [103] who investigated the microstructural evolution of porcelain body based on kaolin, nepheline syenite and silica. It was shown by Martín-Márques *et al.* [104] that the heating rate affects the melting processes of feldspars in porcelain stoneware composition based on kaolin, feldspar and quartz. They found that at very high heating rate, such as 45-50 °C/min, the albite and microcline phases remain as partially melted in the fired body up to 1100 °C, while they are completely melted up to 1230 °C.

The intensity of the α-quartz peaks gradually diminishes with increasing temperature, indicating its partial melting in the feldspar melt [10]. However, the α-quartz is still present at 1350 °C. Mullite formation is revealed at 1150 °C. The process of mullitization continues with increasing temperature. The phase composition and phase-transformation process of the EN material is comparable with the processes occurring in a typical triaxial porcelain body [1,10,25,40], except that corundum, as the main phase, is additionally present at all the firing temperatures.

Fig. 4.3-2 (a) presents the phase composition of sample A fired at different temperatures. It is clear that corundum prevails in all the samples. The flux minerals microcline and sanidine were identified at 950 °C and 1050°C. Microcline and its high temperature form sanidine underwent similar melting processes as by EN. β-$LiAlSi_2O_6$ (JCPDS 071-2058) is detected up to 1200 °C, and at 1150 °C and 1200 °C $LiAlSi_3O_8$ (JCPDS 035-0794) coexists with β-$LiAlSi_2O_6$. In contrast, α-quartz is identified at all temperatures. However, the amount α-quartz decreases with temperature faster than for EN, suggesting that the dissolving of α-quartz is enhanced by the presence of Li_2O. Mullite is first detected at 1150 °C and its amount increases with temperature.

In Fig. 4.3-3 (a) the occurrence of phases in sample B after firing at different temperatures is shown. The phase compositions of A and B are identical at all the firing temperatures, except that at 1350 °C the α-quartz cannot be detected in B, suggesting that the increasing amount of Li_2O tends to enhance the dissolution of the α-quartz.

Fig. 4.3-4 displays the phase composition of sample C after heating at different temperatures. The minerals identified in C are different to those in A and B in the temperature range above 1200 °C, since $LiAlSi_3O_8$ is still detected at 1250 °C, while at 1300 °C and 1350 °C the new Li-containing phase, $Li_xAl_xSi_{1-x}O_2$ (JCPDS 040-0073), is identified. The α-quartz disappears at temperatures below 1300 °C.

In Li_2O-containing compositions the dissolution of microcline and sanidine is similar to the case of EN, indicating that the presence of β-spodumene has no perceivable effect on the breakdown of sanidine and microcline below 1150 °C. The amount of β-spodumene decreases gradually above 1050 °C and at 1250 °C disappears. Simultaneously the amount of α-quartz decreases with temperature. It is proposed, that above 1050°C β-spodumene reacts with quartz.

Due to quartz reaction and its assimilation in β-spodumene structure, $LiAlSi_3O_8$ is formed as identified from XRD spectra of all Li_2O-containing bodies, fired at 1150 °C. The reactions of lithium minerals correlated with quartz reaction at temperatures above 1200 °C are affected by the amount of Li_2O. In A and B with 1.0 and 1.2 wt% Li_2O, respectively, $LiAlSi_3O_8$ is identified only at 1150 and 1200 °C, whereas at higher temperatures it appears that it melts in feldspathic liquid, since none of Li-minerals is detected at 1250 °C or above. In C with 1.6 wt.% of Li_2O $LiAlSi_3O_8$ is identified at 1150, 1200 and 1250 °C. The continued reaction for composition C leads to the formation of $Li_xAl_xSi_{1-x}O_2$ at 1300 °C. $Li_xAl_xSi_{1-x}O_2$ appears as stable phase and does not dissolve with temperature increasing.

Among Li_2O-containing bodies, fired at 1350 °C, low intensity α-quartz is identified only in composition A, which suggests that the amount of Li_2O of 1.0 wt.% is not sufficient for complete quartz dissolution and assimilation. Regarding the available α-quartz elimination during firing process the amount of Li_2O of 1.2 wt.% and 1.6 wt.% is more favorable.

Mullite formation in compositions containing Li_2O is first identified at 1150 °C, which is the same temperature when mullite is detected in EN. The intensities of mullite peaks are comparable between EN and compositions containing 1.0 and 1.2 wt.% of Li_2O. The intensity of mullite peak in composition C with 1.6 wt.% of Li_2O is noticeably lower, which indicates that crystallization of lithium aluminium silicate might hinder the mullite formation.

The results show that phase composition of fired high-alumina porcelain body depends on the amount of Li_2O added.

4.3.2 Phase composition and microstructure as a function of firing temperature

The effect of Li_2O on the microstructure evolution during firing process was studied from the phase composition, as identified by XRD, and SEM observations of corresponding samples. For each firing temperature the presence of studied phases is demonstrated with the XRD patterns in 2θ range 15–35 °. Microstructure was observed by SEM equipped with EDS. The identification of individual phase in the microstructure, as investigated by SEM, is based on the shape and chemical composition of the phase. The chemical composition of the individual phase was accomplished by EDS where lithium with the atomic number three cannot be detected [105]. For porous samples, where the surface of the sample is uneven, we performed the standard less point EDS analysis. The calculated oxide compositions are semi-quantitative, particularly the amount of Na_2O is too low.

The distinctive phases that were most often observed by SEM in the microstructure of investigated samples are described from the following figures supported by corresponding EDS spectra.

Figure 4.3-5 shows the SEM image of sample A fired at 1050 °C. The microstructure consists of different types of grains, which differ in morphology, size and contrast. The distinctive grains, which were anlysed by EDS, are marked on the SEM image as A, Q, F and S.

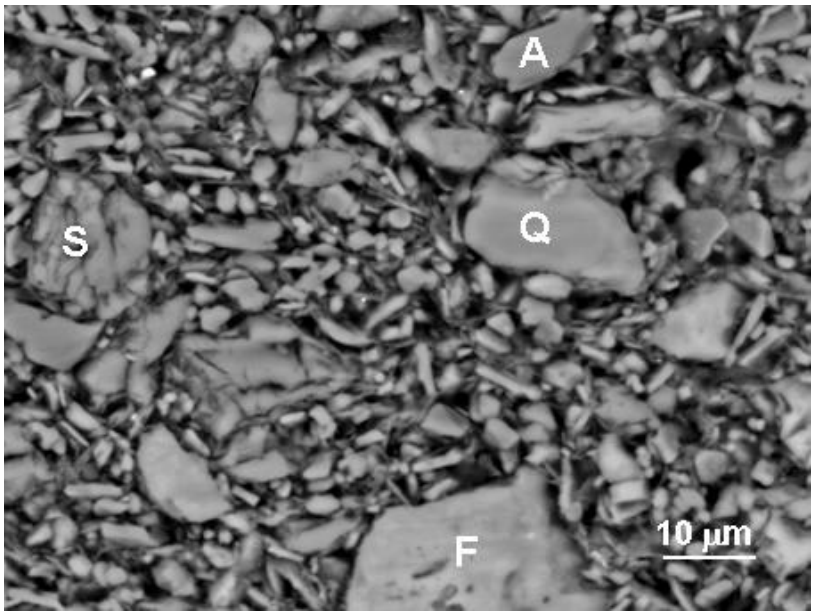

Figure 4.3-5. SEM/BEI of sample A fired at 1050 °C with marked phases (A, Q, F and S) analysed by EDS.

In Figure 4.3-6 the EDS spectrum of surface elements detected in angular grain marked as A in Figure 4.3-5 is shown, indicating the prevailing presence of Al and small amount of Si. The EDS analysis show, that the grain contains 97.6 % Al_2O_3 and 2.4 % SiO_2. The grain A is recognized as corundum grain. The presence of SiO_2 is probably from the background or due to the sample preparation.

In Figure 4.3-7 the EDS spectrum of angular grain marked as Q in Figure 4.3-5 is presented. The spectrum shows the presence of Si, indicating pure SiO_2, which confirms that grain Q is quartz grain.

Figure 4.3-8 shows the EDS spectrum of the largest grain marked as F in Figure 4.3-5. The presence of Na, Al, Si and K is identified from the spectrum. According to EDS analysis the grain F contains 0.7% Na_2O, 18.0% Al_2O_3, 66.6% SiO_2 and 14.7% K_2O, idicating that that grain F is feldspar grain.

The EDS spectrum of dark scaly grain marked as S in Figure 4.3-5 is illustrated in Figure 4.3-9. Al and Si are evident from the spectrum of phase S, containing 29.3% Al_2O_3 and 70.7% SiO_2. Despite lithium not detected by EDS, the grain S is cosidered to be β-spodumene grain, due to the ratio between Al_2O_3 and SiO_2, which is the same as for spodumene.

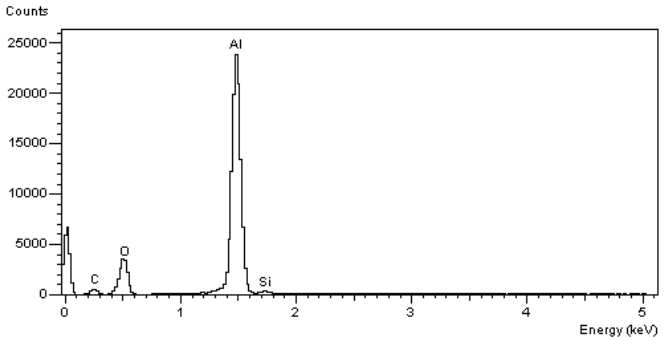

Figure 4.3-6. EDS spectrum of elements detected in the phase marked as A in Figure 4.3-5.

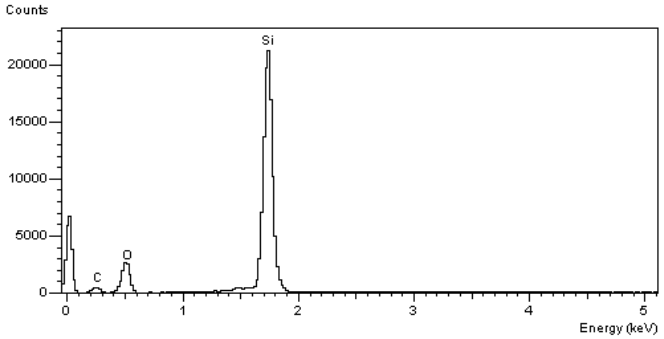

Figure 4.3-7. EDS spectrum of elements detected in the phase marked as Q in Figure 4.3-5.

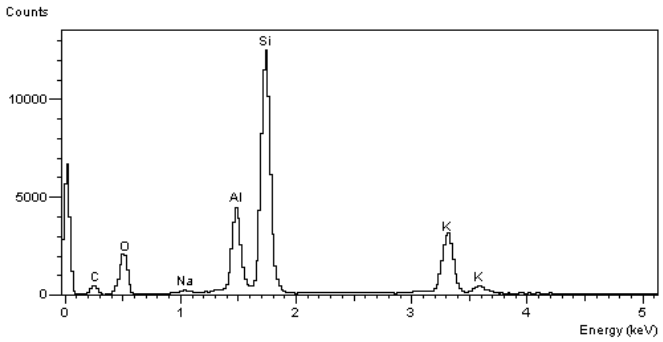

Figure 4.3-8. EDS spectrum of elements detected in the marked as F in Figure 4.3-5.

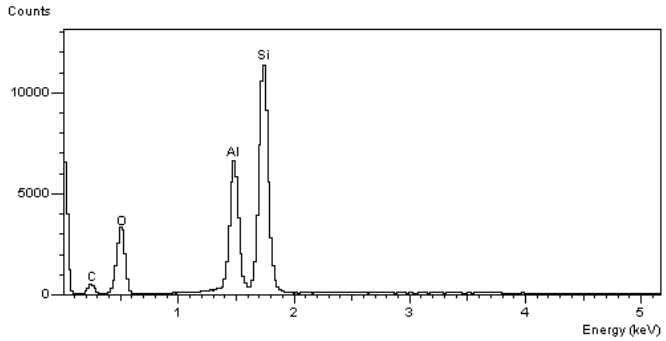

Figure 4.3-9. EDS spectrum of elements detected in the phase marked as S in Figure 4.3-5.

Figure 4.3-10 shows the SEM images of sample B fired at 1150 °C. The phases visible in the microstructure are inhomogeniously dispersed glassy phase and grains located as barriers of glassy phase. The glassy phase is distinctive by dark and bright contrast. The distinctive phases, which were analysed by EDS, are marked on the SEM image in Figure 4.3-10 as BG, DG, A and Q.

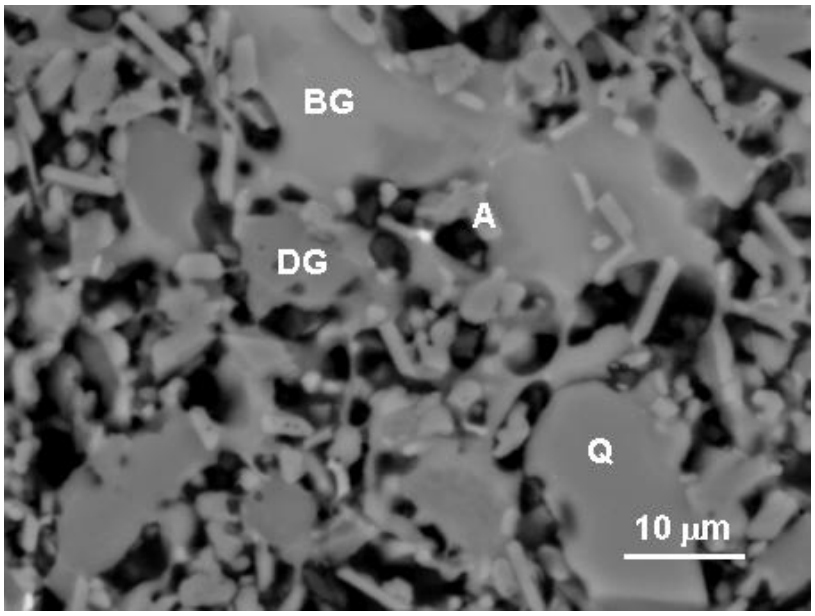

Figure 4.3-10. SEM/BEI of sample B fired at 1150 °C with marked phases (BG, DG, A and Q) analysed by EDS.

Figure 4.3-11 illustrates the EDS spectrum of glassy phase with bright contrast, marked as BG in Figure 4.3-10. Na, Al, Si and K are identified from the spectra. The EDS analysis shows, that the glassy phase contains 0.6% Na_2O, 20.8% Al_2O_3, 71.8% SiO_2 and 6.9% K_2O. The glassy phase originates from melted feldspar grain due the presence of Na and K and the ratio of Al_2O_3 and SiO_2, which is similat to that of pure feldspasr. The bright grey glassy phase, BG, is regarded as feldspar based glassy phase.

In Figure 4.3-12 the EDS spectrum of glassy phase with dark contrast, marked as DG in Figure 4.3-10, is shown. The presence of Mg, Al and Si is detected from the spectrum and the oxide composition

demostrates that glassy phase DG contains 0.7% MgO, 29.5% Al_2O_3 and 69.9% SiO_2. The glassy phase of type DG originates from melted β-spodumene grain due to the ratio of Al_2O_3 and SiO_2, which is similat to that of β-spodumene. The dark grey glassy phase is recognozied as β-spodumene based glassy phase.

Figure 4.3-13 shows the EDS spectrum of the grain, which is marked as A in Figure 4.3-10. From the spectrum mainly Al and some Si is detected. The determined oxide composition, which shows that the grain contains 97.2% Al_2O_3 and 2.8% SiO_2, confirms that phase A is corundum grain. The corundum grains are of whitish contrast in form of oblong lamellas. Some of corundum lamellas are not completely compact having one or more small holes. The major part of corundum lamellas have the length below 10 μm.

Figure 4.3-14 illustrates the EDS spectrum of relatively large grain marked as Q in Figure 4.3-10. The EDS spectrum and analysis, indicating pure silica, show that the grain market as Q is α-quartz grain. The quartz grain is of darker contrast. The identified quartz grain is angular in shape and considerably larger in comparison to corundum grains.

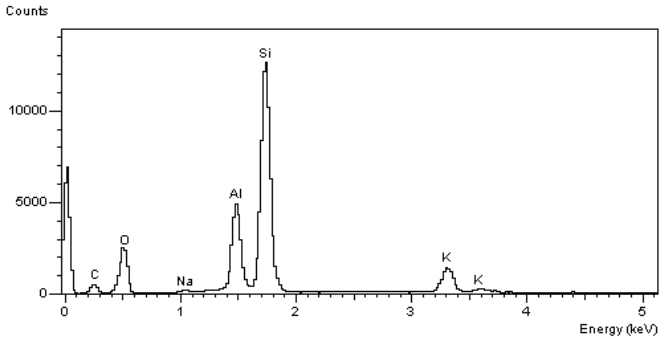

Figure 4.3-11. EDS spectrum of elements detected in the phase marked as BG in Figure 4.3-10.

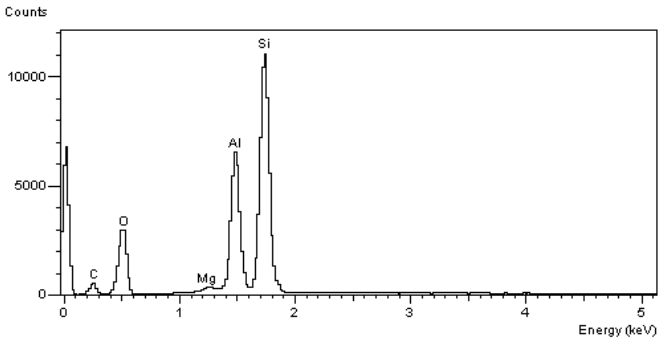

Figure 4.3-12. EDS spectrum of elements detected in the phase marked as DG in Figure 4.3-10.

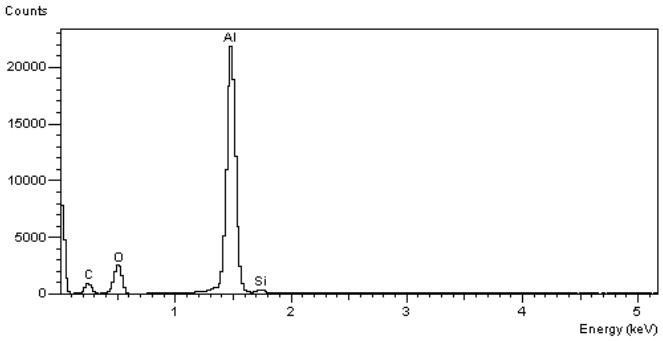

Figure 4.3-13. EDS spectrum of elements detected in the phase marked as A in Figure 4.3-10.

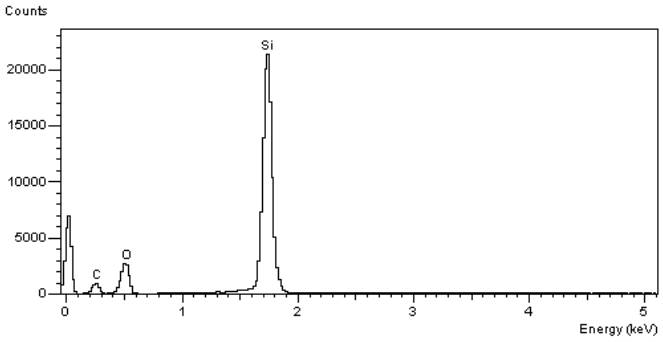

Figure 4.3-14. EDS spectrum of elements detected in the phase marked as Q in Figure 4.3-10.

In Figure 4.3-15 the SEM image of sample EN fired at 1300 °C is presented. The distinctive phases observed in the microstructure are glassy phase and grains, which are embedded in the glassy matrix. The middle zone of the glassy phase, marked as G, and the grains, marked as A and Q, were analysed by EDS.

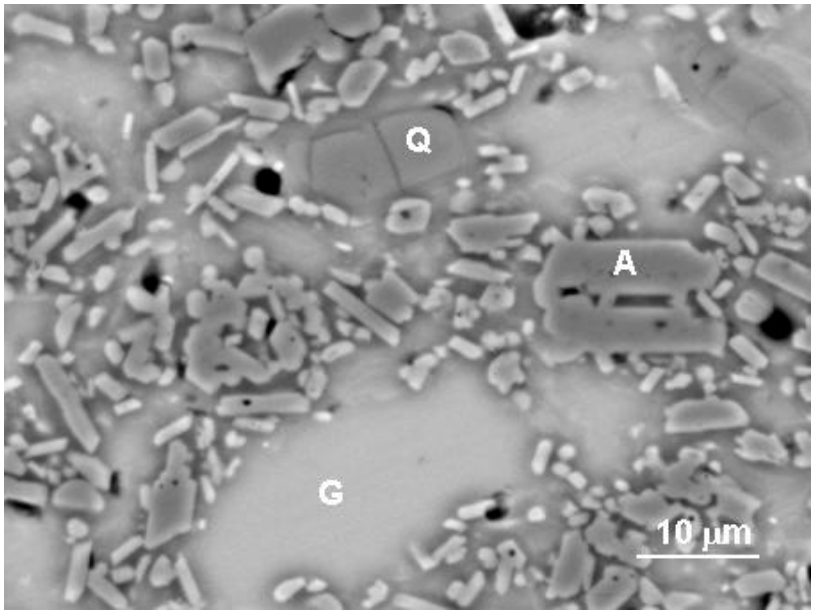

Figure 4.3-15. SEM/BEI of sample EN fired at 1300 °C with marked phases (G, A and Q) analysed by EDS.

Figure 4.3-16 shows the EDS spectrum of the middle zone of glassy phase marked as G in Figure 4.3-15. Na, Mg, Al, Si and K are detected from the spectrum. The oxides of glassy phase comprise of 1.0% Na_2O, 0.5% MgO, 18.2% Al_2O_3, 72.9% SiO_2 and 7.4% K_2O. The glassy phase G is feldspar based, due to the presence of Na and K. Besides, the ratio between Al_2O_3 and SiO_2 in the glassy phase G is similar as that in feldspar.

The EDS spectrum of the large grain marked as A in Figure 4.3-15 is presented Figure 4.3-17. The presence of Al and Si is identified from the spectrum. The oxide composition shows that the grain A contains 97.8% Al_2O_3 and 2.2% SiO_2, which indicates that the grain A is corundum grain. The analysed corundum grain, marked as A in Figure 4.3-15, is distinguishing as one of the largest corundum grains with the length around 15 μm, while the greater part of other corundum grains are smaller than 10 μm.

In Figure 4.3-18 the EDS spectrum of cracked grain marked as Q in Figure 4.3-15 is illustrated. This grain has darker contrast in comparison to corundum grains. Only Si is identified from the spectrum, thus confirming that the grain Q is the grain of α-quartz. Quartz grain Q embedded in the glassy matrix is of angular morphology having an evident crack in the middle.

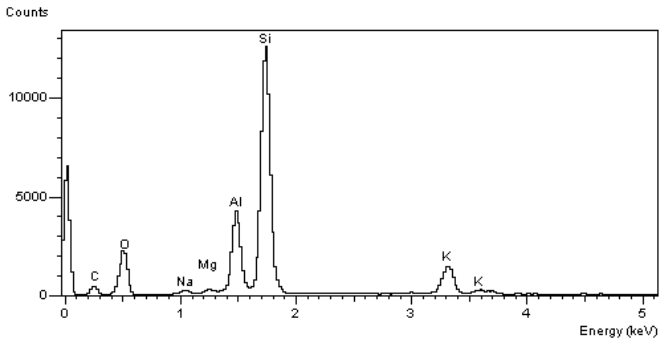

Figure 4.3-16. EDS spectrum of elements detected in the phase marked as G in Figure 4.3-15.

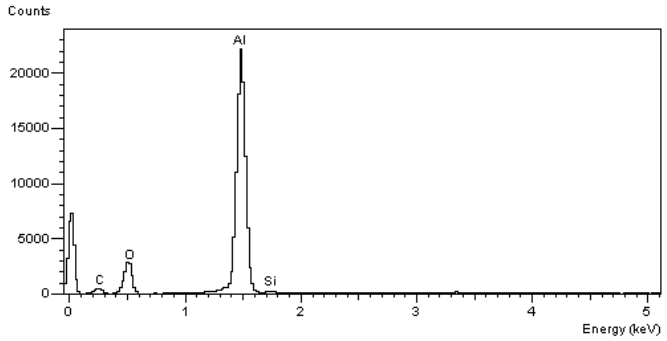

Figure 4.3-17. EDS spectrum of elements detected in the phase marked as A in Figure 4.3-15.

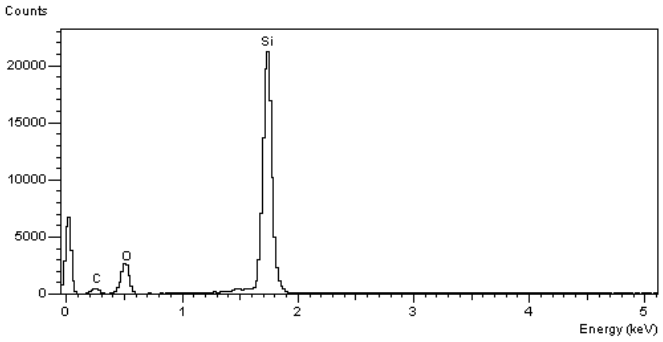

Figure 4.3-18. EDS spectrum of elements detected in the phase marked as Q in Figure 4.3-15.

The SEM image of sample C fired at 1300 °C is presented in Figure 4.3-19. The glassy phase with non-uniformly dispersed grains is observed in the microstructure. The glassy phase is inhomogenous with bright contrast and dark contrast zones. The distinctive types of glassy phase, located as seen on the image, are marked as BG and DG. The EDS analysis was performed on phases marked as BG, DG and A.

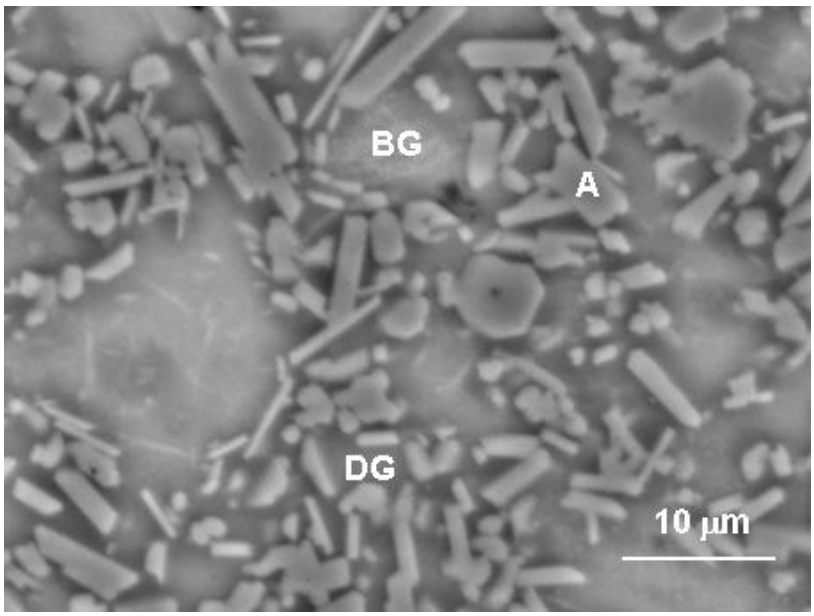

Figure 4.3-19. SEM/BEI of sample C fired at 1300 °C with marked phases (BG, DG and A) analysed by EDS.

Figure 4.3-20 shows the EDS spectrum of the bright contrast glassy phase zone, marked as BG in Figure 4.3-19. From the EDS spectrum the presence of Al, Si and K is identified. The analysis shows that the amount of Al_2O_3 is 24.9%, the amount of SiO_2 is 70.7% and the amount of K_2O is 4.4%, indicating that the bright contrast glassy phase is of feldspar origin due to the presence of K. The glassy phase BG of sample C fired at 1300 °C is found to be more Al rich in comparison to the glassy phase BG of sample B fired at 1150 °C.

The EDS spectrum of the dark contrast glassy phase zone, marked as DG in Figure 4.3-19, is presented in Figure 4.3-21. Al, Si and K are identified from the spectrum. The oxide composition includes 29.9% of Al_2O_3, 67.7% of SiO_2 and 2.4% of K_2O. The amount of K_2O in glassy phase DG is lower than in the glassy phase BG, besides the glassy phase DG is more Al rich, which indicates that it is of β-spodumene origin.

In Figure 4.3-22 the EDS spectrum of the bright contrast grain, marked as A in Figure 4.3-19, is illustrated. The spectrum shows the presence of Al and Si, where Al is the major element present, which is confirmed also by the corresponding analysis resulting in 97.5% of Al_2O_3 and 2.5 % of SiO_2. The grain A is a typical corundum grain with about the same spectrum as found in all samples analysed by EDS.

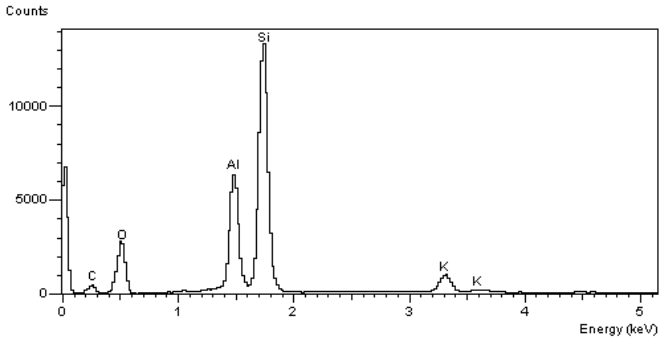

Figure 4.3-20. EDS spectrum of elements detected in the phase marked as BG in Figure 4.3-19.

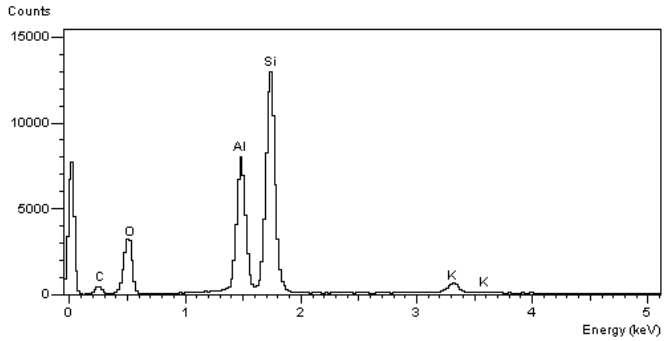

Figure 4.3-21. EDS spectrum of elements detected in the phase marked as DG in Figure 4.3-19.

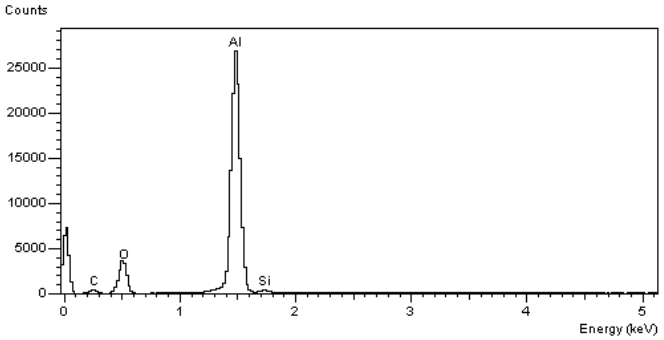

Figure 4.3-22. EDS spectrum of elements detected in the phase marked as A in Figure 4.3-19.

Figure 4.3-23, showing a part of SEM image from Figure 4.3-19, illustrates the inhomogeneity of the glassy phase, where the dark contrast glassy phase, marked in the image as DG, is in the centre of the bright contrast glassy phase, marked as BG. To identify the distribution of K, Al and Si in the glassy phase the mapping of these elements was performed by EDS.

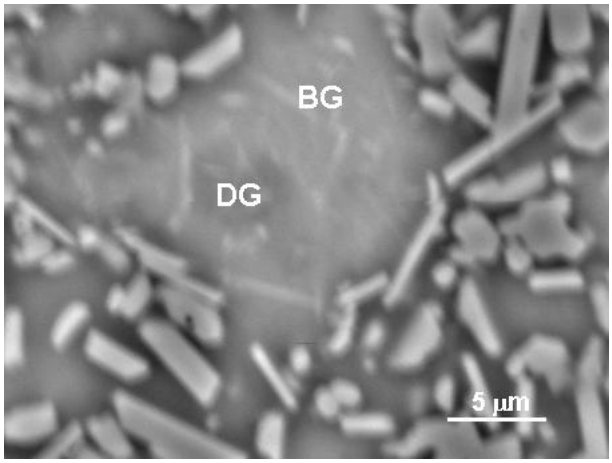

Figure 4.3-23. SEM/BEI image of sample C fired at 1300 °C with marked zones of BG – bright contrast glassy phase and DG – dark contrast glassy phase. It shows the inhomogeneity of the glassy phase.

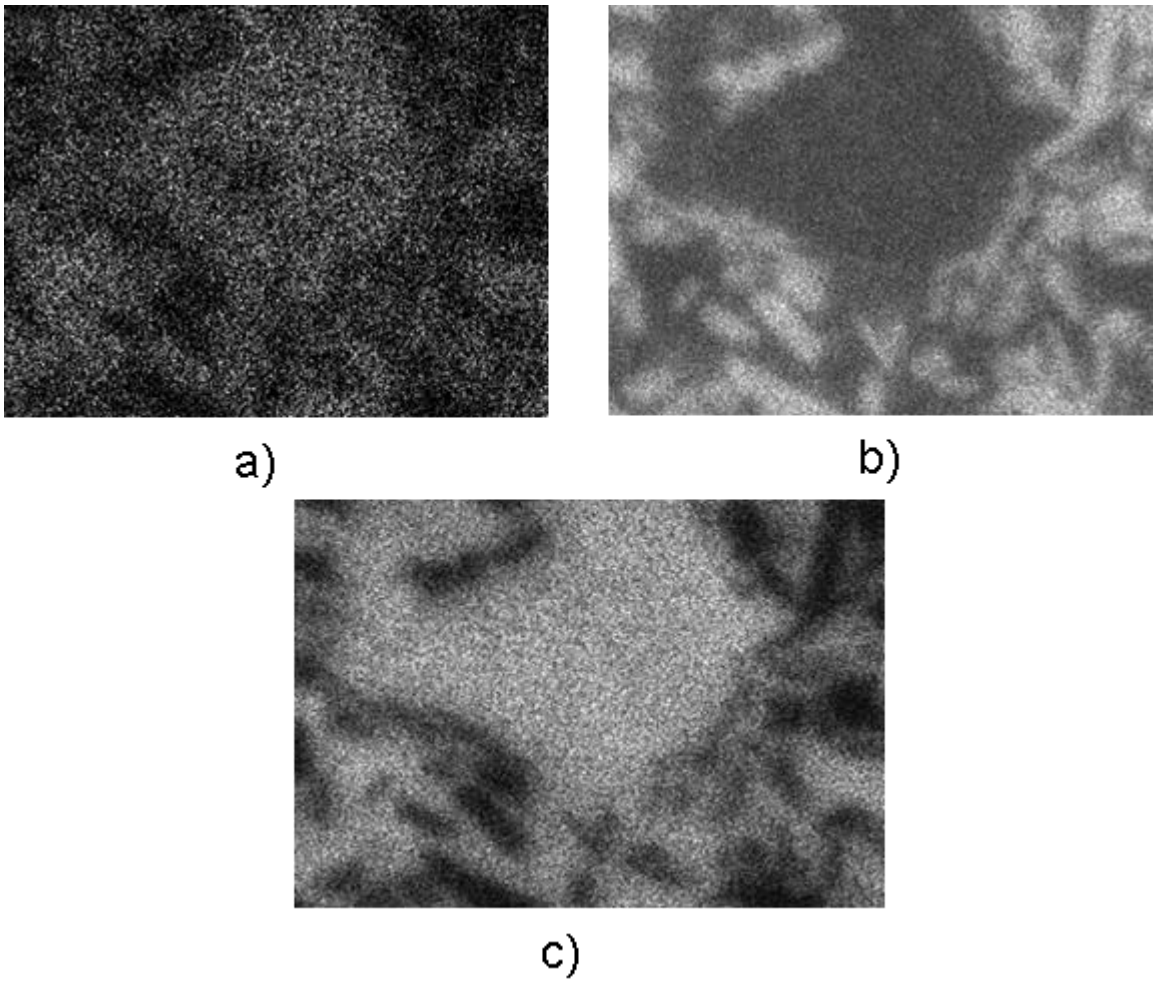

Figure 4.3-24. Mapping of surface elements of sample C as shown Figure 4.3-23. The distribution of (a) K, (b) Al and (c) Si is presented.

Figure 4.3-24 shows the distribution of (a) K, (b) Al and (c) Si as determined by mapping of surface elements on the area of sample C presented in Figure 4.3-23.

The presence of K and its distribution, as presented in Figure 4.3-24, image (a), is referred to the presence and distribution of the glassy phase. It is obviously seen that the region marked as DG in Figure 4.3-23 is less rich with K than the surrounding glassy phase marked as BG, indicationg that the glassy

phase is inhomogenous regarding the amount of K. Due to inhomogeneous content of K the local heterogeneity of glassy phase in the sample is evident.

The distribution and the presence of Al, as seen in Figure 4.3-24, image (b), is refered to the Al present in corundum grains and Al present in the other phases. The presence and the distribution of corundum grains is evident due to the high concentration of Al in corundum grains, while noticeable differences in the distribution of Al in the glassy phase zones are not ascertained.

In Figure 4.3-24, image (c), the presence and the distribution of Si is shown. The highest concentration of Si is evident in the the glassy phase. No differences in Si concentration are evident between the BG and DG glassy phase zones.

4.3.2.1 Phase composition and microstructure after firing at 950 °C

The identified mineralogical composition from XRD patterns of studied bodies fired at 950 °C is presented in Table 4.3-2 and illustrated with corresponding spectra in 2θ-range 15–35° in Figure 4.3-25. Besides corundum, which is the main phase, quartz and the flux minerals including microcline and sanidine are detected in all compositions. In composition EN additionally albite as flux mineral is revealed, while in all model compositions β-spodumene is present. The stronger intensity of β-spodumene peak is clearly seen for composition C with the highest amount of Li_2O.

The identified mineralogical compositions of studied bodies fired at 950 °C differentiate from that of raw bodies in clay minerals disappearance and partial formation of sanidine from feldspar. Sanidine ($(K,Na)AlSi_3O_8$), the high temperature form of potassium feldspar ($KAlSi_3O_8$), crystallizes between 700 and 1000 °C, but disappears above 1000 °C together with microcline [103].The temperature of sanidine formation is dependent on the ratio between sodium and potassium [1] , whereas in porcelain body based on nepheline syenite as the main flux component, the presence of sanidine was confirmed already at 600 °C [40,106].

Table 4.3-2. Identified mineralogical composition of samples EN, A, B and C fired at 950 °C.

Mineral	EN	A	B	C
Corundum	×	×	×	×
α-quartz	×	×	×	×
Microcline	×	×	×	×
Sanidine	×	×	×	×
β-spodumene		×	×	×
Albite	×			

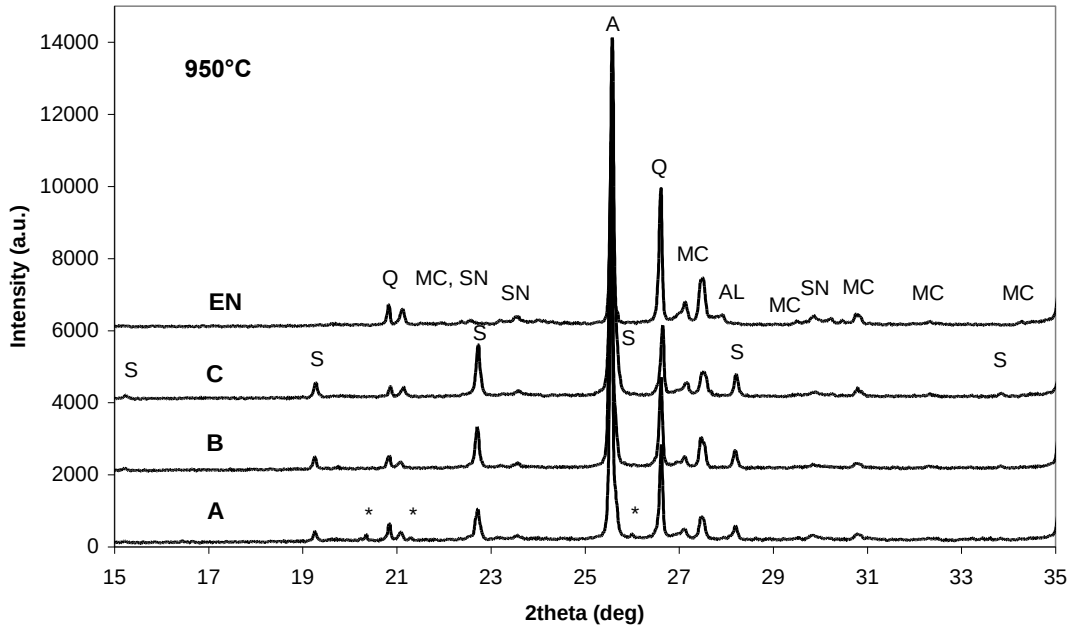

Figure 4.3-25. XRD pattern of samples EN, A, B and C fired at 950 °C in 2θ-range 15–35°. Identified minerals are A – corundum, Q – α-quartz, S - β-spodumene, MC – microcline and SN – sanidine, *- undefined peaks.

Figure 4.3-26 shows the SEM/BE images of composition EN fired at 950 °C. The microstructure of high-interconnected porosity consists of grains (a), which are mostly below 30 μm. The great part of grains is angular, while some grains are more acicular. Pores are located among agglomerates of different types of grains. In image (b) and (c) the grain of corundum (A), feldspar (F) and large quartz (Q) grain around 30μm are identified.

SEM/BE images of composition A fired at 950 °C are shown in Figure 4.3-27. The microstructure consisting of angular and acicular grains below 30 μm, as seen in image (a), is similar to the microstructure of EN. The identified grains of corundum (A) and feldspar are marked in image (b) and (c).

SEM/BE images of composition B fired at 950 °C are presented in Figure 4.2-28. The porous microstructure of B consisting of grains below 30 μm is comparable to that of EN and A. The grains of corundum (A) and feldspar (F) are identified, as designated in image (b) and (c).

In Figure 4.2-29 the SEM/BE images of composition C fired at 950 °C are presented. The microstructure of C, consisiting of grains below 30 μm and inter-connected pores, is similar to that of EN, A and B. In image (b) the recognized grains of corundum (A) and feldspar (F) are marked.

After firing at 950 °C all the studied samples are characteristic by porous microstructure with angular and acicular grains agglomerated around pores. The pores in all the samples are of comparable shape and size. The pores originate from the green body, because in the green body there are voids between the clay platelets and non-plastic particles dispersed in clay matrix [21].

Regarding the grain size, which is below 30 μm, all the samples have comparable grain size with the grains below 10 μm as prevailing. The similarity in grain size for all the samples is in agreement with the similarity in grain size of raw bodies as seen from the particle size distribution curves in Figure 3.2-1.The size of grains is dependent on the initial granulation of the raw materials and the milling time of raw bodies, which was comparable for all the samples.

The general microstructure of all the samples fired at 950 °C consists of a complex mixture of grains connected with amorphous clay derived products. Only larger grains of corundum, feldspar and quartz are recognized by EDS. As determined by XRD the grains in EN consist of corundum, quartz, microcline, sanidine and albite grains, while in model compositions the grains comprise corundum, quartz, microcline and β-spodumene grains. Grains are spread in fine matrix of clay transformation products, which are amorphous since kaolinite is not identified in XRD spectra of corresponding samples. The clay relicts can not be cleary identified from our SEM images. The clay relicts in size ≤1 μm are adjusted to non-plastic particles aligned with their large plane tangential to the surface of non-plastic particle. [21].

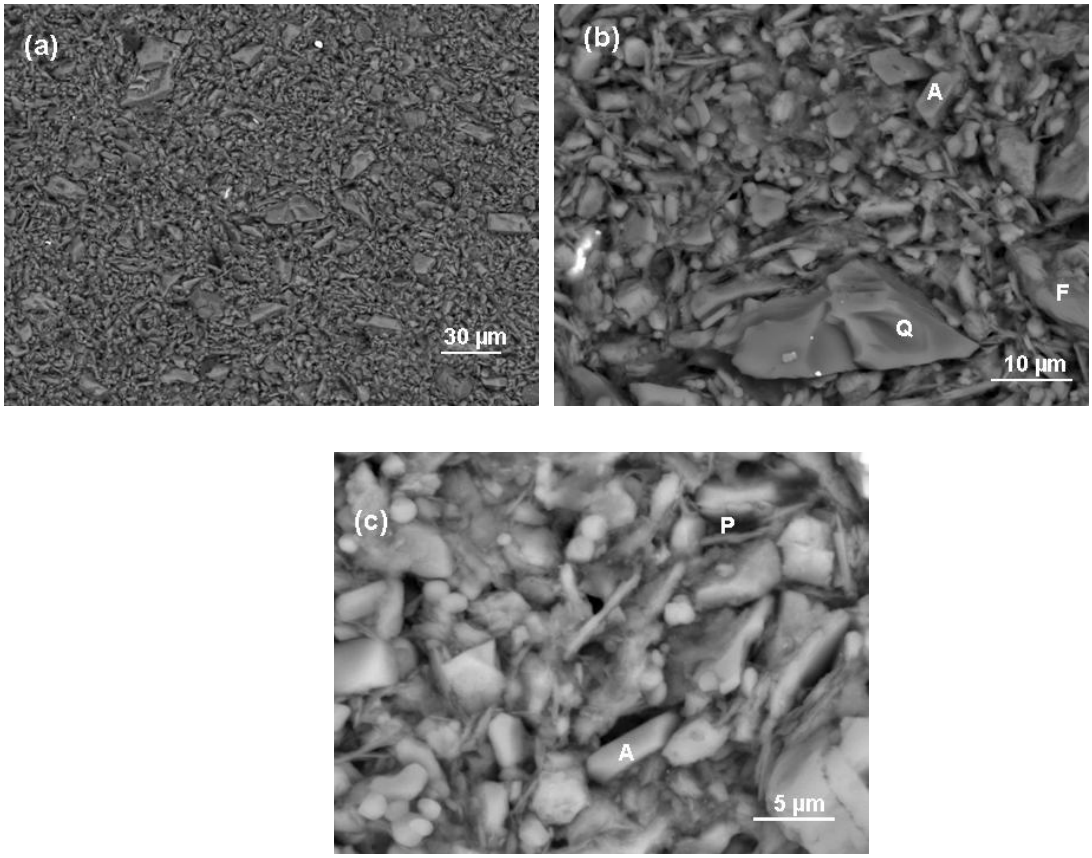

Figure 4.3-26. SEM/BEI of sample EN fired at 950 °C. A – corundum, F – feldspar, Q – quartz, P – pore.

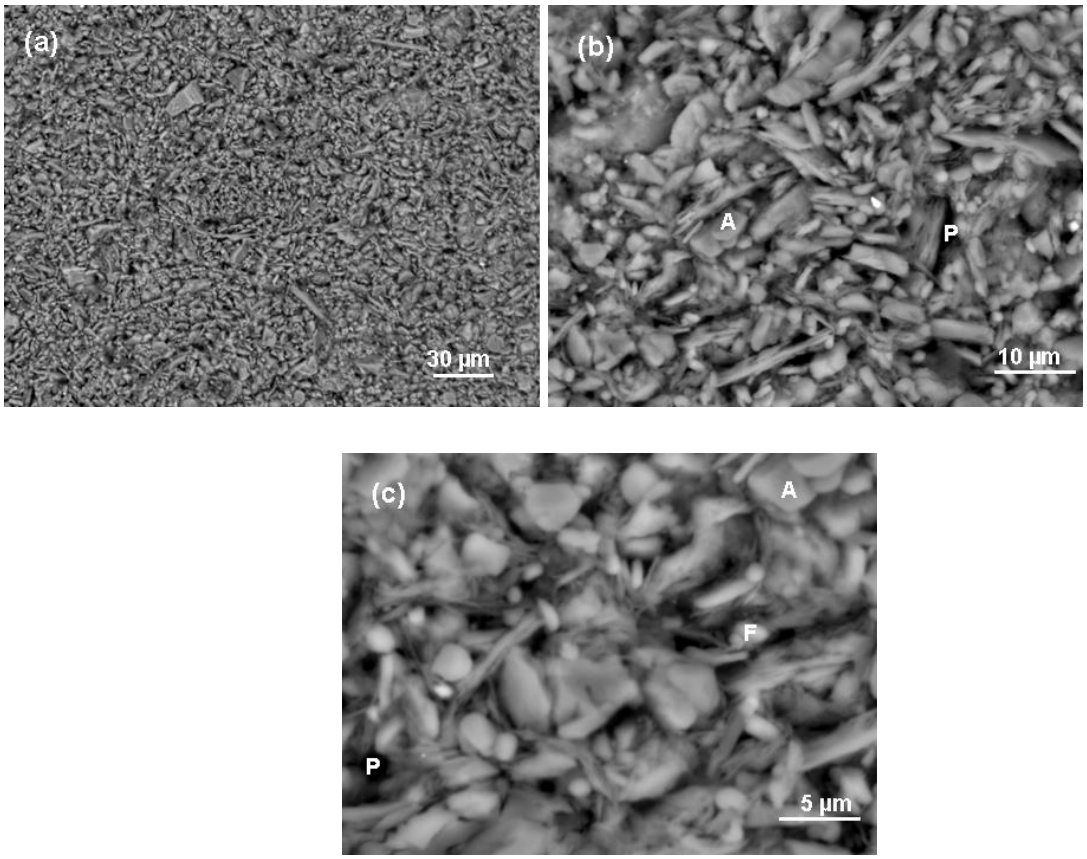

Figure 4.3-27. SEM/BEI of sample A fired at 950 °C. A – corundum, F – feldspar, P – pore.

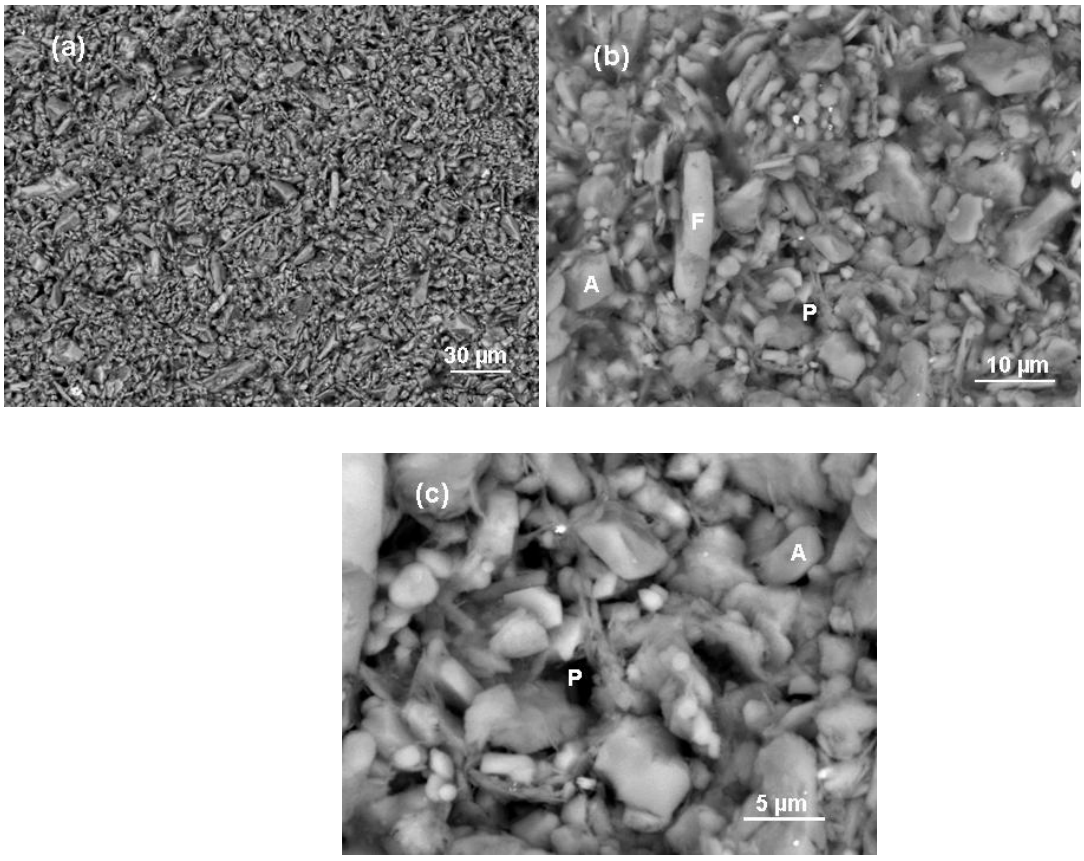

Figure 4.3-28. SEM/BEI of sample B fired at 950 °C. A – corundum, F – feldspar, P – pore.

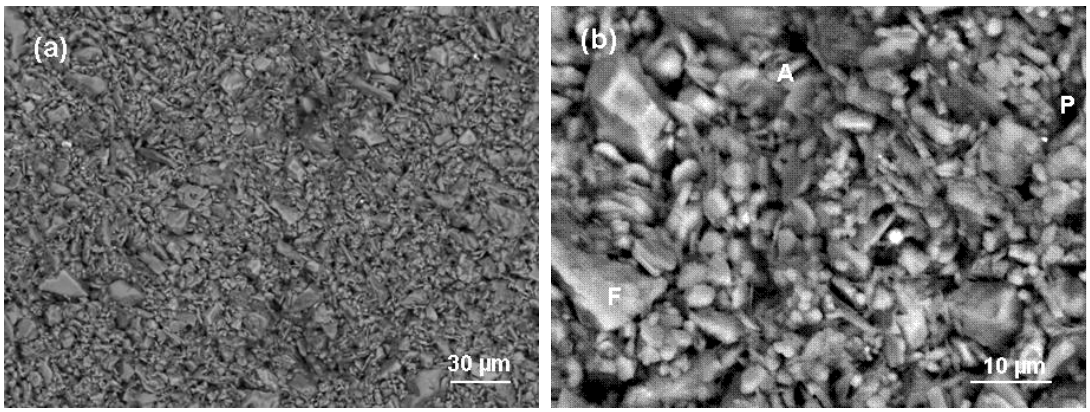

Figure 4.3-29. SEM/BEI of sample C fired at 950 °C. A – corundum, F – feldspar, P – pore.

4.3.2.2 Phase composition and microstructure after firing at 1050 °C

The phase composition of studied bodies fired at 1050 °C is presented in Table 4.3-3 and illustrated with respective XRD patterns in 2θ-range 15–35° in Figure 4.3-30. Corundum as the main phase is identified for all the samples. α-quartz and microcline are as well present in all the samples. The presence of sanidine and albite is identified only in composition EN. β-spodumene is detected in all model compositions with the intensity of its peaks comparable to that at 950 °C.

Comparing the phase composition of EN fired at 1050 °C with that fired at 950 °C we see that there is no change in the phase composition of EN. However, the peak intensity of microcline, albite and sanidine is lower at 1050 °C, suggesting that the melting process of feldspar minerals is taking place between 950 and 1050 °C in EN. The melting process is obvious in compositions with Li_2O, too. The peak intensity of

microcline in A, B and C is diminished and the presence of sanidine is not detected at 1050 °C.

Table 4.3-3. Identified mineralogical composition of samples EN, A, B and C fired at 1050 °C.

Mineral	EN	A	B	C
Corundum	×	×	×	×
α-quartz	×	×	×	×
Microcline	×	×	×	×
Sanidine	×			
Albite	×			
β-spodumene		×	×	×

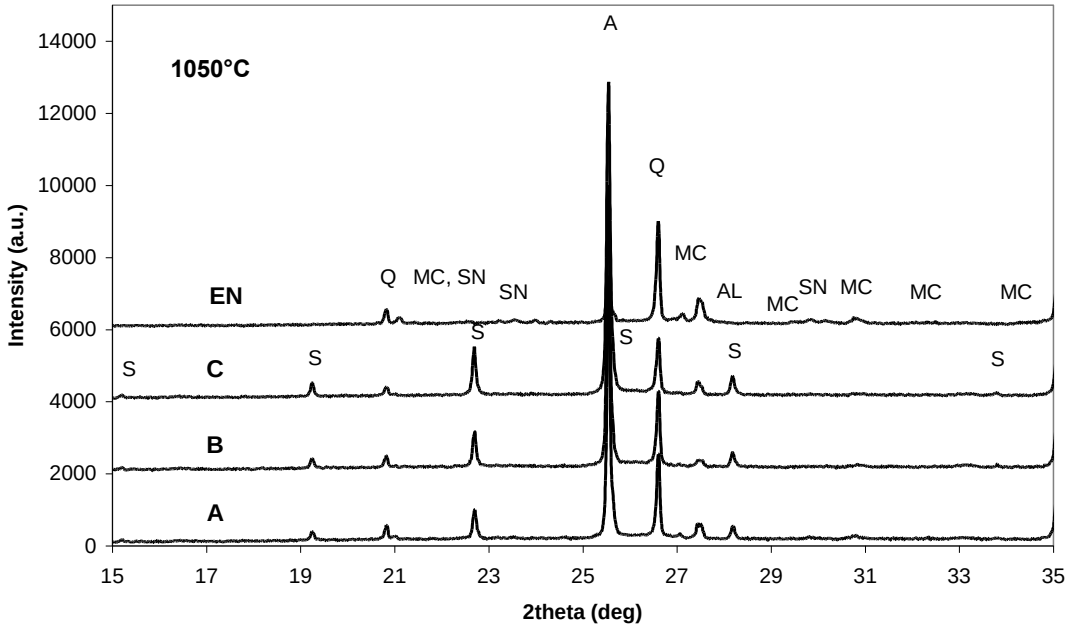

Figure 4.3-30. XRD patterns of samples EN, A, B and C fired at 1050 °C in 2θ-range 15–35°. Identified minerals are A – corundum, Q – α-quartz, S - β-spodumene, MC – microcline and SN – sanidine.

In Figure 4.2-31 SEM/BE images of sample EN fired at 1050 °C are shown. The microstructure of EN consists of a mixture of grains below 30 μm and inter-connected pores (a). Corundum (A) and fedspar (F) grain are identified as marked in image (b). The grains are angular and acicular.

SEM/BE images of composition A fired at 1050 °C are presented in Figure 4.2-32. Regarding the grain size and pores the microstructure of A, as shown in image (a), appears similar to that of EN. Angular corundum (A), feldspar (F) and β-spodumene (S) grains are marked in image (b).

SEM/BE images of composition B fired at 1050 °C are shown in Figure 4.2-33. The porous microstructure of B, consisting of grains and pores, is comparable to that of EN and A. Grains of corundum (A) and feldspar (F) are marked in image (b).

SEM/BE images of composition C fired at 1050 °C are presented in Figure 4.2-34. Porous and granular microstructure of C is similar to that of EN, A and B in view of the grain and the pore size.

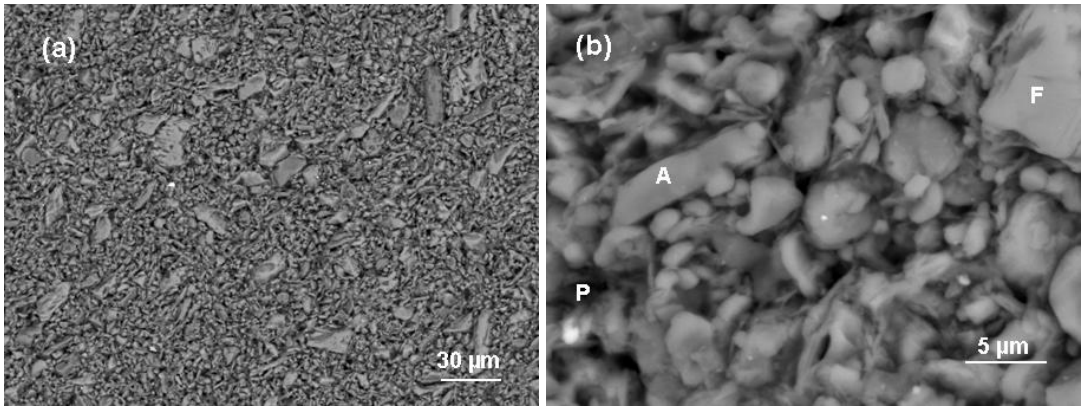

Figure 4.3-31. SEM/BEI of sample EN fired at 1050 °C. A – corundum, F – feldspar, P – pore.

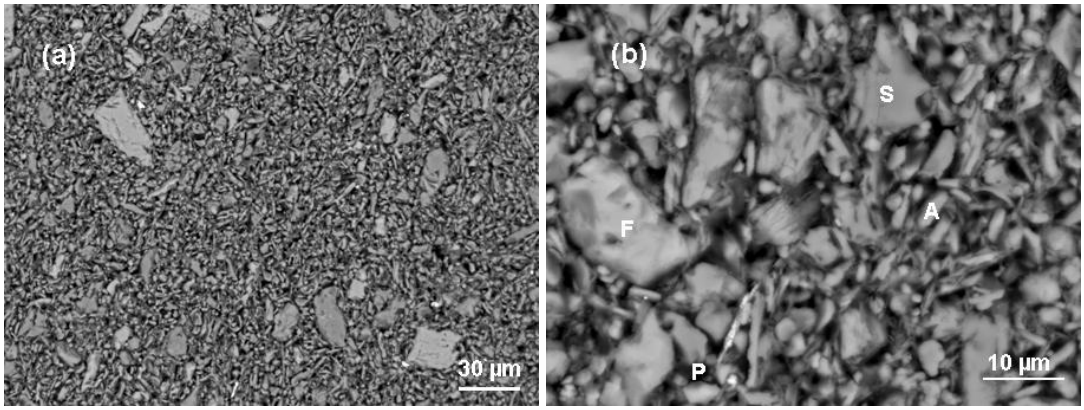

Figure 4.3-32. SEM/BEI of sample A fired at 1050 °C. A – corundum, F – feldspar, S - β-spodumene, P – pore.

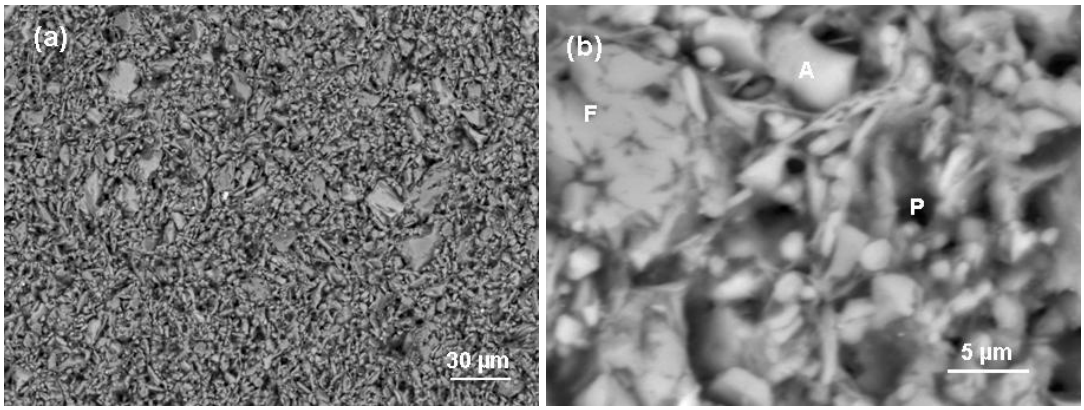

Figure 4.3-33. SEM/BEI of sample B fired at 1050 °C. A – corundum, F – feldspar, P – pore.

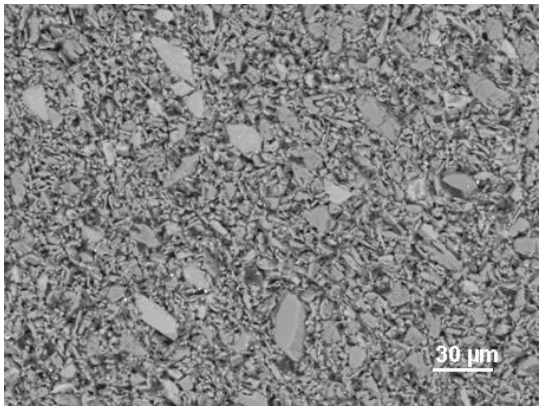

Figure 4.3-34. SEM/BEI of sample C fired at 1050 °C.

The porous and granular microstructure of all the samples fired at 1050 °C, consisting of angular and acicular grains, is similar to the microstructure of samples fired at 950 °C. However, it appears more compact than that fired at 950 °C. As ascertained by XRD, the grains in EN comprise corundum, quartz, microcline, sanidine and albite grains, while in samples A, B and C the grains of corundum, quartz, microcline and β-spodumene are present. Larger grains of corundum, feldspar and spodumene grains were identified by EDS as illustrated in Figure 4.3-5.

The thickening of the microstructure at 1050 °C for all the samples is detectable through closer particle compaction. The liquid phase formation in temperature range 950−1050 °C could be explained with the equilibrium phase diagram. Liquid formation is associated with melting of feldspar system and silica discarded from metakaolin via the $K_2O–Al_2O_3–SiO_2$ eutectic (equilibrium phase diagram in Figure 1.2-4), indicating feldspar and silica eutectic at 985 °C, and $NaAlSiO_4–KAlSiO_4–SiO_2$ eutectic (equlibrium phase diagram in Figure 1.3-1), indicating eutectic between potash feldspar, sodium feldspar and silica at 1020 °C. With regard to the shrinkage as seen from dilatometric curves in Figure 4.2-2 the liquid phase formation at 1050 °C is relatively low.

4.3.2.3 Phase composition and microstructure after firing at 1150 °C

The identified phase composition of studied bodies fired at 1150 °C is shown in Table 4.3-4 and illustrated with respective XRD patterns in Figure 4.3-35. In XRD patterns of all the samples corundum revealed as the major crystal phase. α-quartz is identified in all samples with the intensity of its peaks decreasing in comparison to the intensity at 1050 °C. The presence of mullite peak is detected in all compositions with about the same intensity, indicating that the process of mullitization is in progress.

In the phase composition of EN the flux minerals are not identified, suggesting that microcline, sanidine and albite are completely melted in temperature range from 1050 to 1150 °C.

In all compositions containing Li_2O two lithium minerals are identified, β-spodumene ($LiAlSi_2O_6$) and new lithium mineral named as lithium feldspar ($LiAlSi_3O_8$).

Table 4.3-4. Identified mineralogical composition of samples EN, A, B and C fired at 1150 °C.

Mineral	EN	A	B	C
Corundum	×	×	×	×
α-quartz	×	×	×	×
β-spodumene		×	×	×
Lithium feldspar		×	×	×
Mullite	×	×	×	×

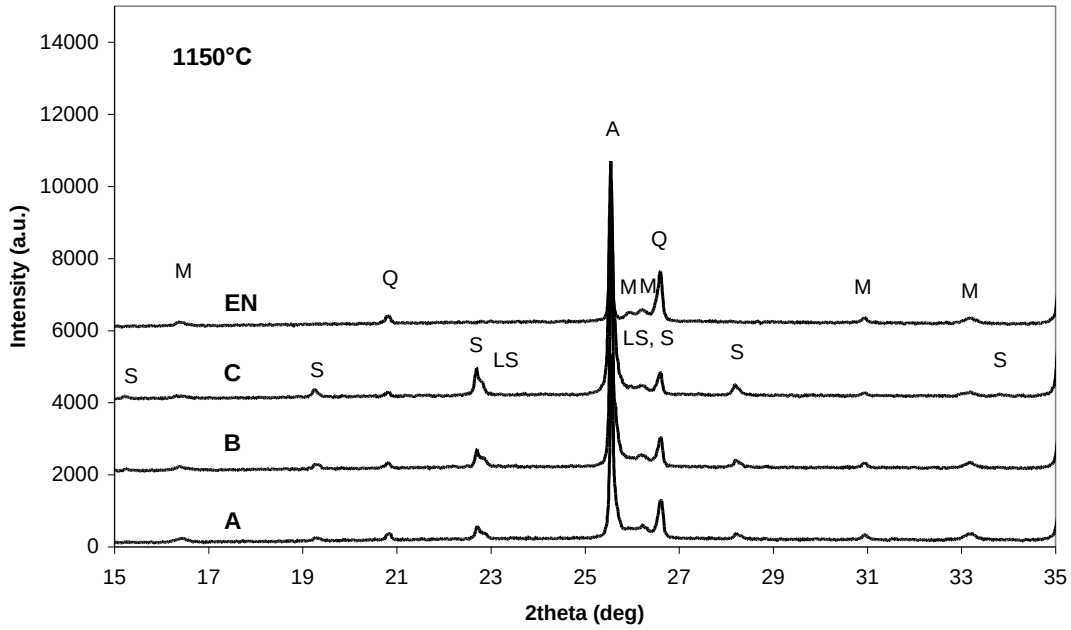

Figure 4.3-35. XRD patterns of samples EN, A, B in C fired at 1150 °C in 2θ range 15–35°. Identified minerals are A – corundum, Q – α-quartz, S - β-spodumene, LS – lithium feldspar ($LiAlSi_3O_8$) and M - mullite.

The appearance of lithium fedspar and simultaneously decreasing of quartz can be explained with the following reaction taking place between β-spodumene and silica. The following reaction is suggested:

$$\underset{\text{β-spodumene}}{Li_2O{\cdot}Al_2O_3{\cdot}4SiO_2} + \underset{\text{silica}}{2SiO_2} \rightarrow \underset{\text{lithium feldspar}}{Li_2O{\cdot}Al_2O_3{\cdot}6SiO_2} \qquad \text{Eq. 4.3-1}$$

The reaction in Eq. 4.3-1 shows the assimilation of silica in the β-spodumene structure, thus lowering the amount of deteriorative quartz in the final porcelain body. The structure of lithium feldspar retains strong structure similarities with β-spodumene, which is characteristic by its derivative quartz structure [85]. The existence of $Li_2O{\cdot}Al_2O_3{\cdot}6SiO_2$ was dedicated to solid solution between β-spodumene and silica. Regarding the ternary phase diagram of the system Li_2O-Al_2O_3-SiO_2 in Figure 1.6-1 an extensive region of solid solution exists between β-spodumene and silica [85].

The reaction between β-spodumene and silica has been prior demonstrated by Fishwick [48], who explained that at appropriate firing conditions the reaction between β-spodumene and silica leads to assimilation of free quartz, thus lowering the free quartz content in whiteware bodies.

SEM/BE images of composition EN fired at 1150 °C are presented in Figure 4.3-36. Elongated zones of glassy phase are distributed in the porous structure with connected pores (a). Corundum grains are agglomerated as barriers of glassy phase zones, as obvious from image (b). The glassy phase (G) contains Al, Si, K and Na as established by EDS.

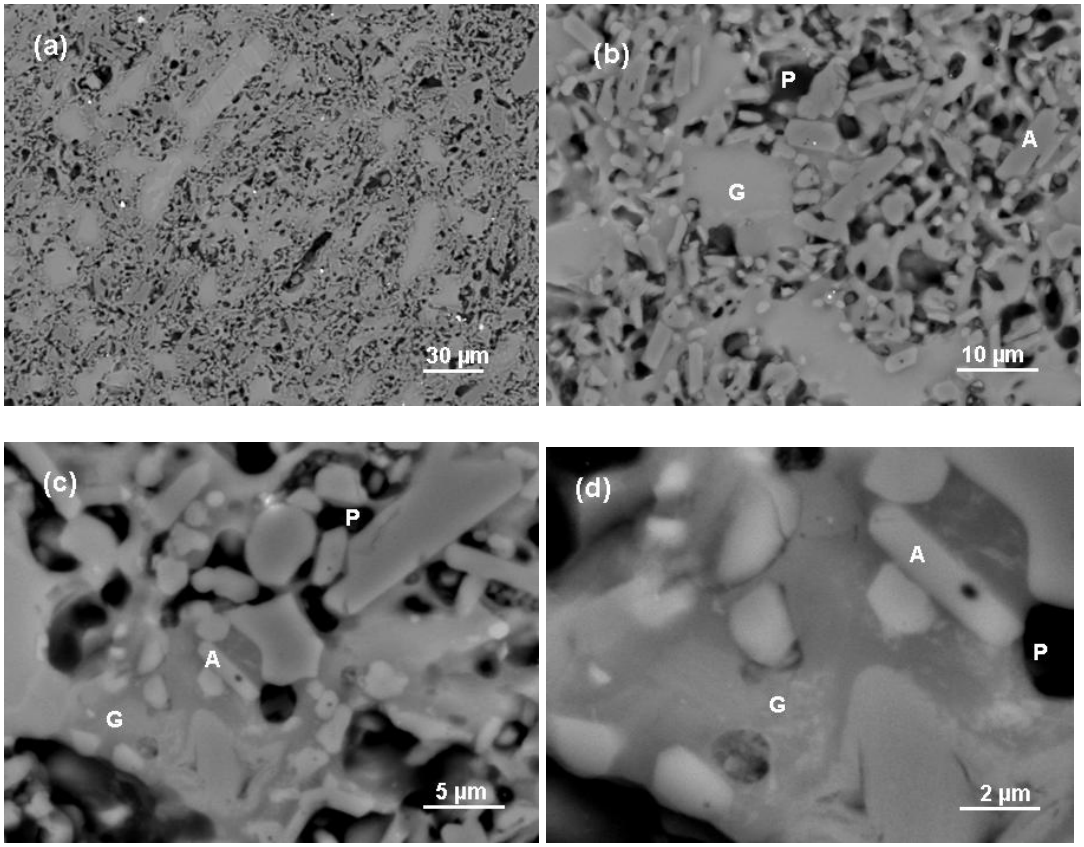

Figure 4.3-36. SEM/BEI of sample EN fired at 1150 °C. A – corundum, G – glassy phase, P – pore.

In Figure 4.3-37 the SEM/BE images of composition A fired at 1150 °C are shown. The microstructure with inter-connected porosity is a mixuture of grains and glassy phase zones (a). The glassy phase zones are smaller in comparison to those in EN. Corundum grains (A) are mostly covered with glassy phase, but also found as revealed in agglomerates, as seen in image (b). The glassy phase zones derived from molten constituents appear with bright contrast (BG), which is identified as feldspar derived glassy phase, and with dark contrast (DG), which is identified as β-spodumene derived glassy phase.

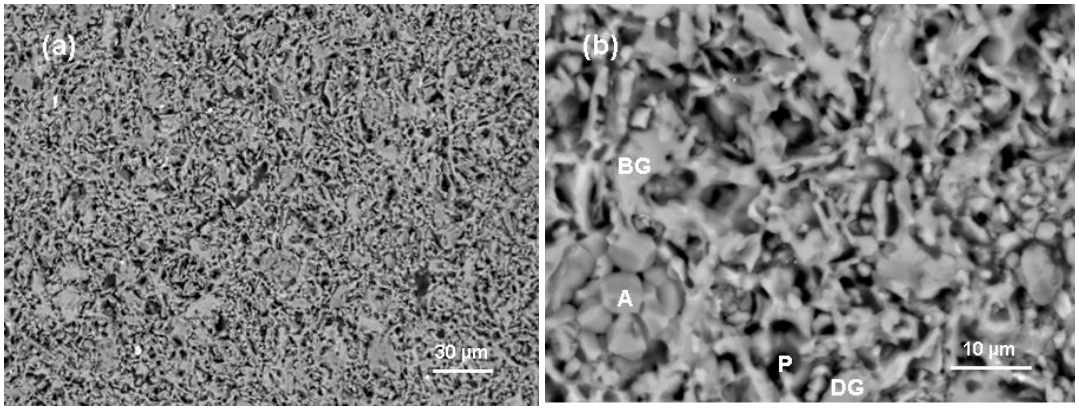

Figure 4.3-37. SEM/BEI of composition A fired at 1150°C. A – corundum, BG – bright contrast or feldspar derived glassy phase, DG – dark contrast or β-spodumene derived glassy phase, P – pore.

SEM/BE images of composition B fired at 1150 °C are presented in Figure 4.3-38. The glassy phase zones are dispersed in porous structure with connected pores (a). The corundum grains (A) are agglomerated around the glassy phase zones (b). Two types of the glassy phase are distinctive. The bright contrast (BG) or feldspar derived glassy phase appears more vitrified in comparison to the dark contrast (DG) or β-spodumene derived glassy phase, which contains elongated pores <5µm.

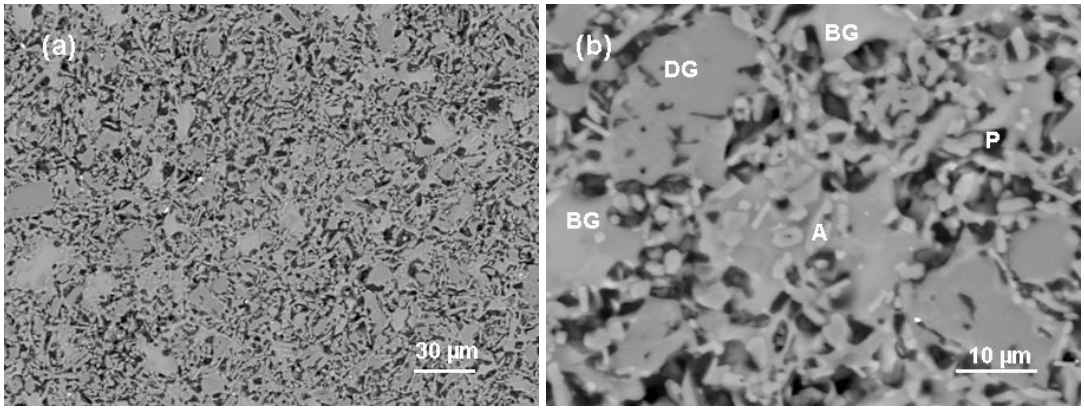

Figure 4.3-38. SEM/BEI of composition B fired at 1150 °C. A – corundum, BG – bright contrast or feldspar derived glassy phase, DG – dark contrast or β-spodumene derived glassy phase, P – pore.

In Figure 4.3-39 the SEM/BE images of composition C fired at 1150 °C are presented. The microstructure consists of glassy phase zones and pores (a). The glassy phase regions are clearly formed indicating that material underwent the vitrification process. Agglomerated corundum grains (A) appear as barriers of glassy phase regions. Inter-connected pores (P) are located among corundum grains. The bright contrast (BG) and the dark contrast (DG) glassy phases are inhomogenously spread in the microstructure. Some of the glassy regions, as (G) in image (b), appear spotty consisting of two types of glassy phases.

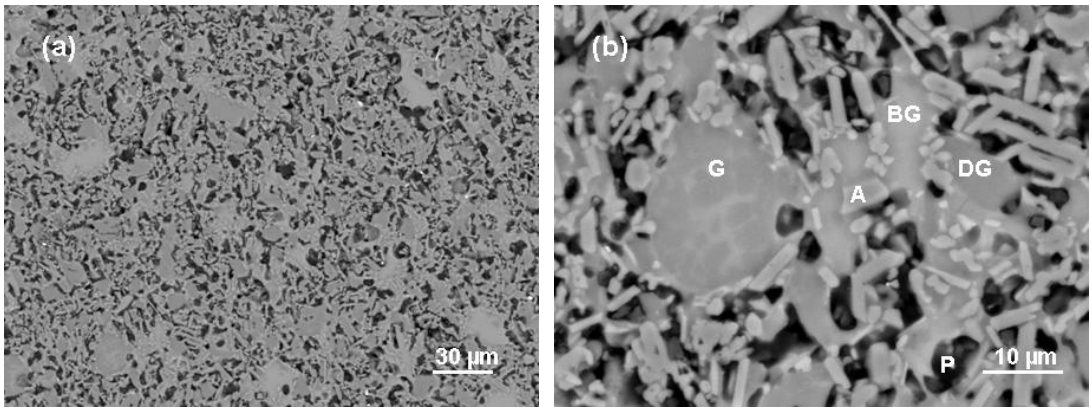

Figure 4.3-39. SEM/BEI of composition C fired at 1150 °C. A – corundum, G – glassy phase, spotty, BG – bright contrast or feldspar derived glassy phase, DG – dark contrast or β-spodumene derived glassy phase, P – pore.

All compositions fired at 1150 °C are characterized by noticeable melt formation within porous structure, where the glassy phase is clearly ditinguished. The glassy phase is localized among the agglomerates of corundum grains and connected pores. The sharp increase in shrinkage from 1050 to 1150 °C, as observed in dilatometric curves presented in Figure 4.2-2, is in accordance with the increase of clearly appeared melt formation among the porous regions with corundum grains.

The microstructure of EN, which is based on flux system containing K_2O and Na_2O, appears to be more vitrified with larger glassy phase regions in comparison to compositions containing Li_2O. The glassy phase forms clearly elongated zones surrounded by the corundum agglomeratess. However, the glassy phase is non-uniformly dispersed in the matrix. Intensive melt formation in EN is confirmed also with XRD analysis of corresponding sample, where no flux minerals are identified at 1150 °C, indicating their intensive melting in temperature range from 1050 to 1150 °C.

The microstructure of compositions containing Li_2O is more porous with lower amount of glassy zones in comparison to the microstructure of EN. The presence of glassy phase is mainly contributed to melted fedspar minerals, since they are not identified in XRD analysis of corresponding samples. The amount of glassy zones clearly increases with increasing the amount of Li_2O in compositions. Composition A is characterized by structure consisting of grains partly melted and joined together in porous matrix, where the glassy phase is in form threads or ‘cobweb’, which round the grains. More intensive liquid formation is

evident with Li_2O content increasing, since the glassy regions are formed in shape of puddles in the samples B and C. The sample C appears to be the most vitrified, since no interspaces are visible in liquid phase regions, which appear completely melted. The glassy phase zones in Li_2O containing samples appear as non-homogenous due to the mixture of liquid phases with different chemical composition.

The observed melting process in SEM images of all the samples fired at 1150 °C is confirmed also with the determined onset temperatures in the sintering curves of samples heated by dilatometer or by heating microscope in temperature range from 1050 to 1150 °C. The onset temperature, which indicates the beginning of intensive shrinkage, was found to be around 1060 °C for samples A, B and C, and around 1110 °C for sample EN, when samples were heated in dilatometer. Comparing the shrinkage from dilatometric curves at 1150 °C, we see that the shrinkage is consirably lower for EN in comparison to the shrinkage of compositions with Li_2O, where A riched the highest shrinkage. From SEM observations we found the most intensive glassy phase formation in samples EN and C, while the shrinkage in these samples is considerably different, which suggests that the observed shrinkage at 1150 °C could be influenced by the different porosity of green bodies, more than the amount of glassy phase, similarly as ascertained by Belnou *et al*., who investigated the sintering behaviour of alumina porcelain bodies, where shrinkage at 1150 °C was influenced by the green density of raw samples [107].

4.3.2.4 Phase composition and microstructure after firing at 1200 °C

The identified mineralogical composition of studied bodies fired at 1200 °C is shown in Table 4.3-5 and illustrated with respective XRD patterns in Figure 4.3-40. At 1200 °C the same phase composition for all the samples is detected from the XRD spectra in comparison to the phases present in corresponding samples fired at 1150 °C. The amount of α-quartz is diminishing in all the compositions in comparison to the amount of α-quartz at 1150 °C, but no considerable increase is noticeable for the mullite peak. In compositions with Li_2O the amount of β-spodumene slightly decreases, while the amount of lithium feldspar increases in comparison to their amounts at 1150 °C.

Regarding the identified minerals in compositions containing Li_2O they consist of the same phases as fired at 1150 °C. The quartz assimilation in β-spodumene structure continues with lithium feldspar formation, thus lowering the amount of undesired quartz in final body. The reduction of quartz in Li_2O containing bodies is more intense than in EN.

Table 4.3-5. Identified mineralogical composition of samples EN, A, B and C fired at 1200 °C.

Mineral	EN	A	B	C
Corundum	×	×	×	×
α-quartz	×	×	×	×
β-spodumene		×	×	×
Lithium feldspar		×	×	×
Mullite	×	×	×	×

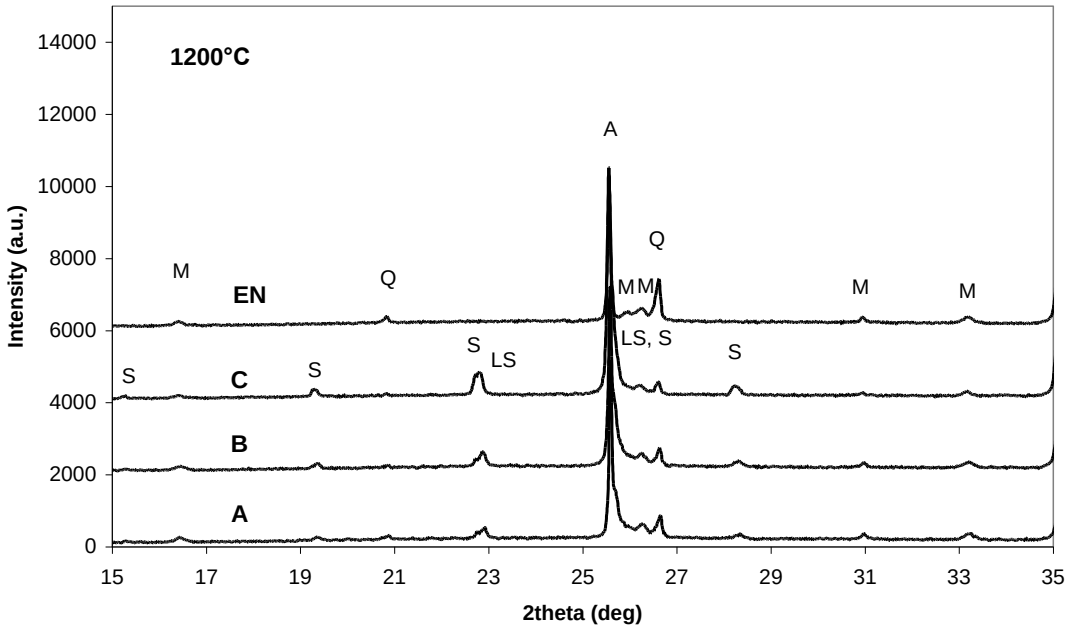

Figure 4.3-40. XRD patterns of samples EN, A, B and C fired at 1200 °C in 2θ-range 15–35°. The identified minerals are A – corundum, Q – α-quartz, S - β-spodumene, LS – lithium feldspar ($LiAlSi_3O_8$), and M – mullite.

Recorded SEM/BE images of composition EN fired at 1200 °C are presented in Figure 4.3-41. The microstructure appears a great deal vitrified (a). The glassy phase zones (G) are spread among porous regions relatively non-uniformly. The corundum grains (A) are mainly gathered in agglomerates, which frequently contain pores (P). The pores are mostly elongated and in great deal interconnected. However, rounded closed pores <5 μm are also perceived. The pore distribution appears rather irregular. The quartz grain (Q) in a void as seen in image (b) or in the glassy phase as seen in image (c) was identified by EDS.

In Figure 4.3-42 the SEM/BE images of composition A fired at 1200 °C are shown. The glassy phase is clearly formed among the porous regions (a). The agglomerates of corundum grains (A) and pores (P) appear as baariers of glassy phase zones. As obvious from image (b) the glassy phase zones are not homogenous, consisting of feldspar (BG) and spodumene (DG) derived glassy phase. Large corundum grain (A) in size ~25 μm is visible in image (b).

SEM/BE images of composition B fired at 1200 °C are seen in Figure 4.3-43. The microstructure is more homogeneous regarding the distribution of glassy phase zones with enhanced glassy phase formed in comparison to that at 1150 °C, as seen in image (a). The glassy phase, surrounded with the agglomerates of corundum grains (A) and the interconnected pores (P), appears as a mixture of dark (DG) and bright (BG) zones, where liquid phases penetrate into each other.

SEM/BE images of composition C fired at 1200 °C are shown in Figure 4.3-44. The microstructure appears a great deal vitrified, but non-uniform regarding the distribution of glassy phase and pores (a). The pores (P) are distinguished in shape and size with the size varying from ~3 to ~20 μm. The agglomerates of corundum grains (A) are embedded in glassy phase. The large quartz grain (Q) ~20 μm with the characteristic cracks is identified as indicated in image (c). The glassy phase is characteristic to be spotty consisting of fedspar (BG) and β-spodumene (DG) derived zones.

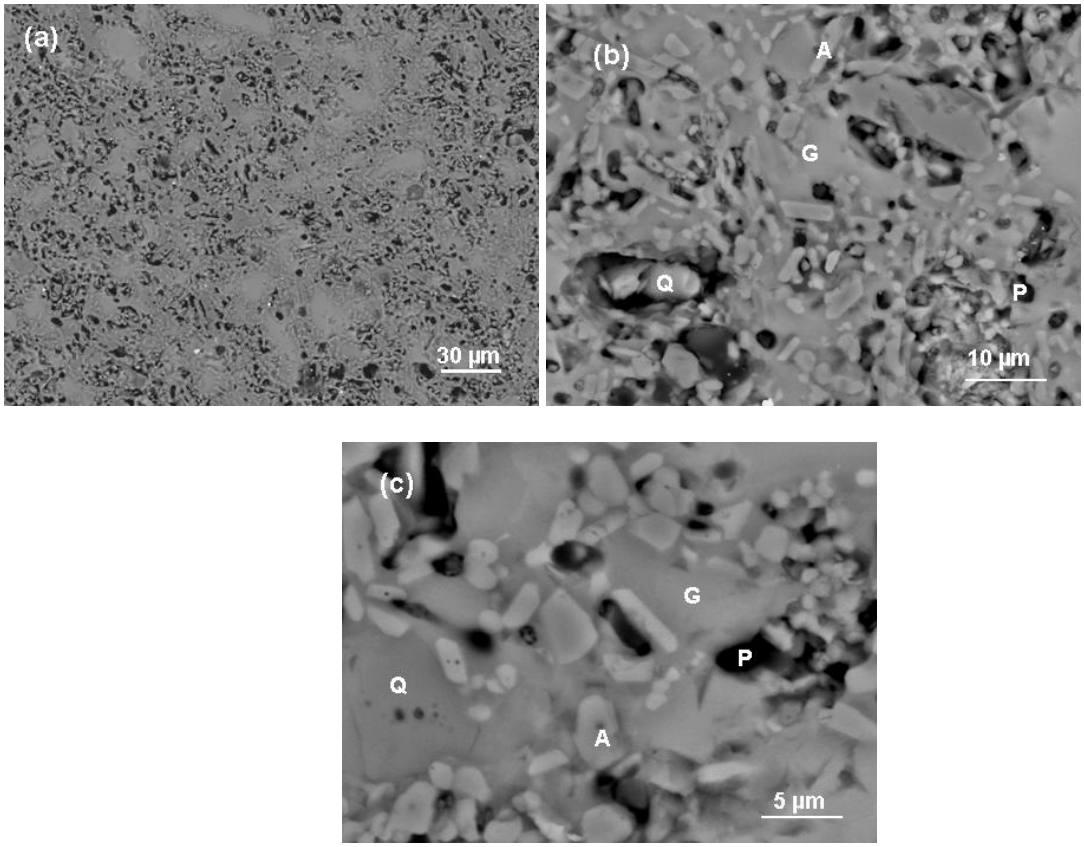

Figure 4.3-41. SEM/BEI of sample EN fired at 1200 °C. A – corundum, G – glassy phase, Q – quartz, P – pore.

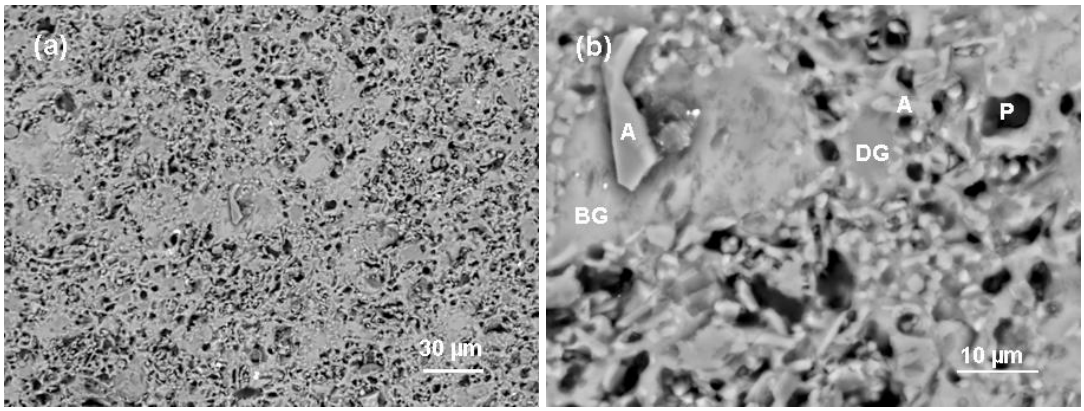

Figure 4.3-42. SEM/BEI of sample A fired at 1200 °C. A – corundum, BG – bright contrast or feldspar derived glassy phase, DG – dark contrast or β-spodumene derived glassy phase, P – pore.

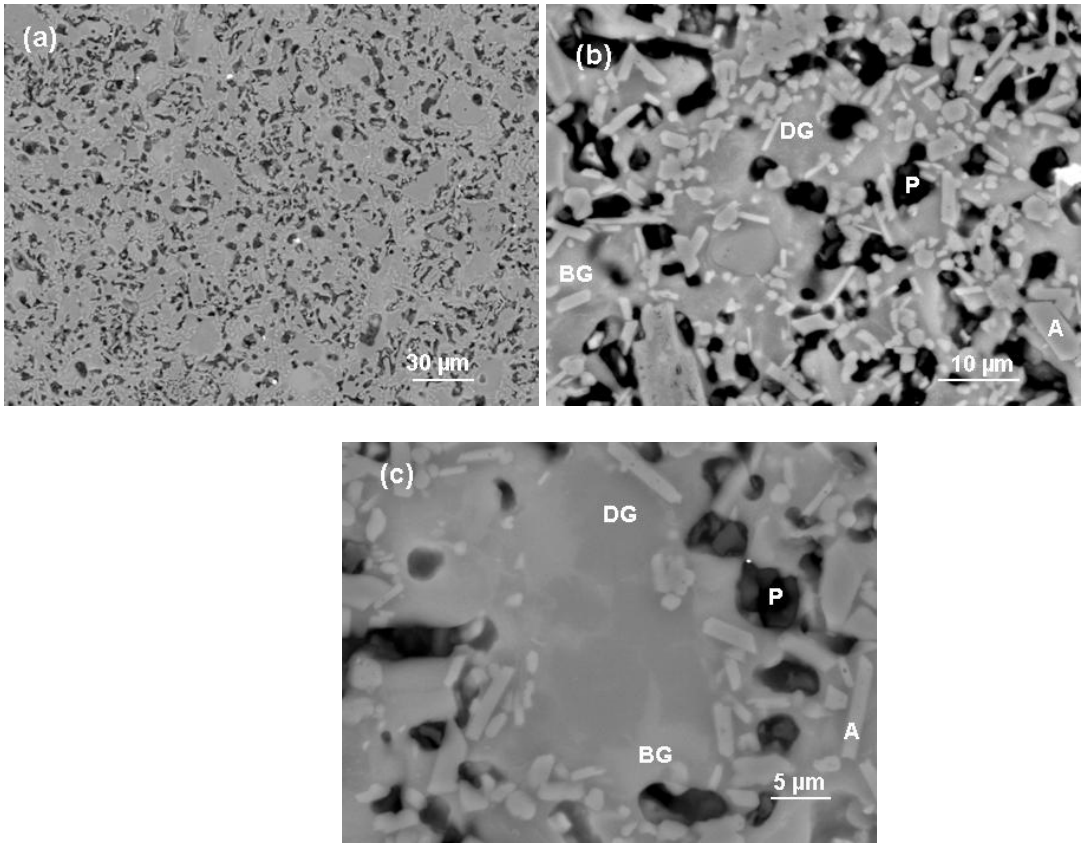

Figure 4.3-43. SEM/BEI of sample B fired at 1200 °C. A – corundum, BG – bright contrast or feldspar derived glassy phase, DG – dark contrast or β-spodumene derived glassy phase, P – pore.

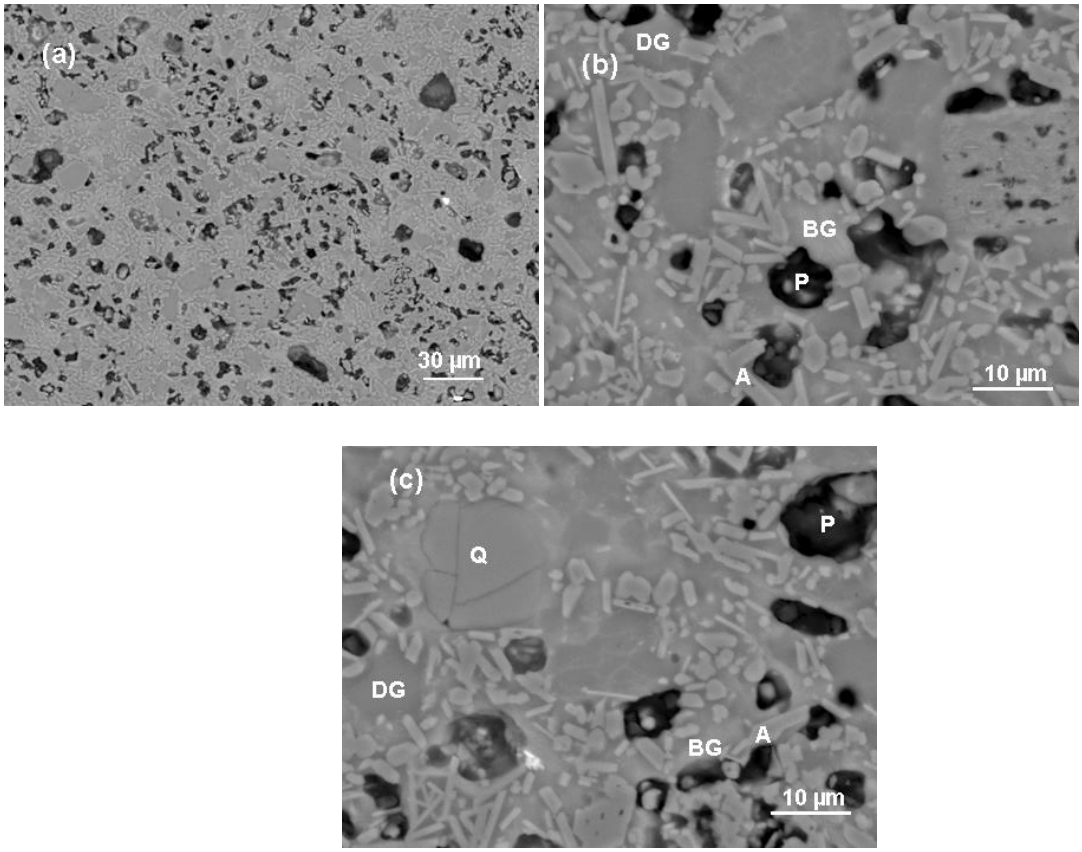

Figure 4.3-44. SEM/BEI of sample C fired at 1200 °C. A – corundum, BG – bright contrast or feldspar derived glassy phase, DG – dark contrast or β-spodumene derived glassy phase, Q – quartz, P – pore.

As fired at 1200 °C all the compositions underwent an intensive pore closing with an increased amount of glassy phase formed, which is in accordance with the intensive shrinkage process as observed around 1200 °C from the sintering curves in Figure 4.2-2.

After firing at 1200 °C the glassy phase distribution in composition EN is more equal in size and shape in comparison to that after firing at 1150 °C, which suggests that with the increasing temperature less viscous liquid phase is formed enabling enhanced penetration of liquid phase among corundum grains. The process of vitrification is in progress from 1150 to 1200 °C. This is in agreement with the phase composition of EN after firing at 1200 °C, where no significant changes are identified in phase composition, except the quartz dissolution due to its peak intensity slightly diminishing. The rounding of pores is noticeable. The microstructure of EN seems comparable compact, but less homogeneous regarding the shape and the distribution of pores in comparison to those in compositions containing Li_2O.

The microstructure of compositions containing Li_2O is characterized with an increase in the glassy regions and in higher degree of the glassy phase homogenization compared to the corresponding samples fired at 1150 °C. Among Li_2O-containing compositions the microstructure of A appears as the most porous, even more porous than that of EN. The small pores in A are spherical and disconected, while the larger pores are of irregular shape and often connected in groups. The melting process in B is more intense than in A due to its more compact microstructure with more spherical pores and greater amount of the glassy phase. The closing of pores and the elimination of small pores is most intensive for C, which has the most compact microstructure with the greatest amount of the glassy phase formed.

The melting process in compositions containing Li_2O is enhanced with increasing the amount of Li_2O. The composition C with the highest amount of Li_2O appears as the most vitrified. However, composition C has relatively high amount of large closed pores up to 30 μm indicating that with increasing the amount of Li_2O the growth of closed pores is more intense.

The glassy phase of compositions containing Li_2O is a heterogeneous mixture of feldspar and β-spodumene derived liquid phase.

4.3.2.5 Phase composition and microstructure after firing at 1250 °C

The identified mineralogical composition of studied bodies fired at 1250 °C is shown in Table 4.3-6 and illustrated with respective XRD patterns in Figure 4.3-45. After firing at 1250 °C the crystalline phases of corundum, quartz and mullite are identified in all studied compositions. In composition C additionally lithium feldspar ($LiAlSi_3O_8$) is identified.

The mineralogical composition of EN remains the same as fired at 1200 °C, consisting of corundum, mullite and quartz. The quartz peak intensity slightly diminishes in comparison with its intensity at 1200 °C.

The compositions containing Li_2O experience main changes in the content of lithium minerals. β-spodumene is not identified in any of the model compositions, which suggests its complete transformation and dissolution. The only lithium mineral detected is lithium feldspar ($LiAlSi_3O_8$), which clearly reveals in composition C.

The quartz peak intensity is slightly diminished in all the Li_2O-bearing compositions in comparison to its intensity at 1200 °C, indicating continuation of quartz dissolution. For composition C the quartz diminishing is additionally related to the formation of lithium feldspar containing higher amount of SiO_2, which was identified only in C.

Table 4.3-6. Identified mineralogical composition of samples EN, A, B and C fired at 1250 °C.

Mineral	EN	A	B	C
Corundum	×	×	×	×
α-quartz	×	×	×	×
Lithium feldspar				×
Mullite	×	×	×	×

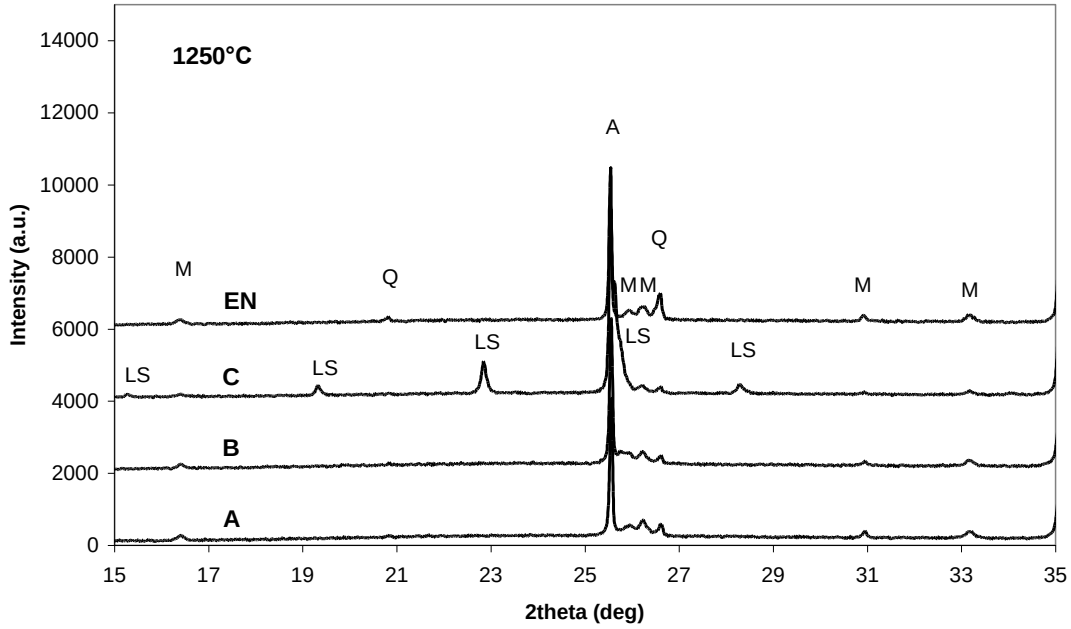

Figure 4.3-45. XRD patterns of samples EN, A, B and C fired at 1250 °C in 2θ-range 15–35°. Identified minerals are A – corundum, Q – α-quartz, LS – lithium feldspar ($LiAlSi_3O_8$) and M – mullite.

Recorded SEM/BE images of composition EN fired at 1250 °C are presented in Figure 4.3-46. The microstructure of EN consisits of glassy phase with embedded corundum grains and heterogeniously dispersed pores, whish are mostly disconnected and gathered in groups (a). The glassy phase (G) regions, which are non-uniform in size and shape, are distributed among pores (P) and agglomerates of corundum grains (A). The pores are rounded and located mainly inside corundum agglomerates. The size of pores is below ~20 μm. Typical quartz grain (Q) with the crack is indicated on image (b).

In Figure 4.3-47 SEM/BE images of composition A at 1250 °C are shown. The microstructutre of A appears more porous in comparison to that of EN as obvious from image (a). However, regarding the size and shape of glassy phase distribution it reveals more homogenous than by EN. The size of pores is below ~20 μm. Glassy phase regions (G) are relatively uniformly spread in microstructure with many pores (P), which are mostly spherical. Corundum grains (A) located around glassy phase regions are gatherted in groups.

Figure 4.3-48 shows SEM/BE images of composition B fired at 1250 °C. The microstructure of B is more vitrified than that of A (a). Relatively uniformly dispersed glassy phase zones (G) surrounded with corundum grains (a) are observed. The pores (P) are mostly spherical with the size below ~20 μm. Besides, pores are disconnected indicating closed porosity. The quartz grain (Q) in size ~20μm is visible in image (c).

SEM/BE images of composition C fired at 1250 °C are presented in Figure 4.3-49. Microstructure seems dense with homogenously dispersed corundum grains and glassy phase zones (a). Pores (P) appear almost spherical and their amount is relatively low. Irregularly distributed dark contrast (DG) and bright contrast (BG) glassy phase zones are visible.

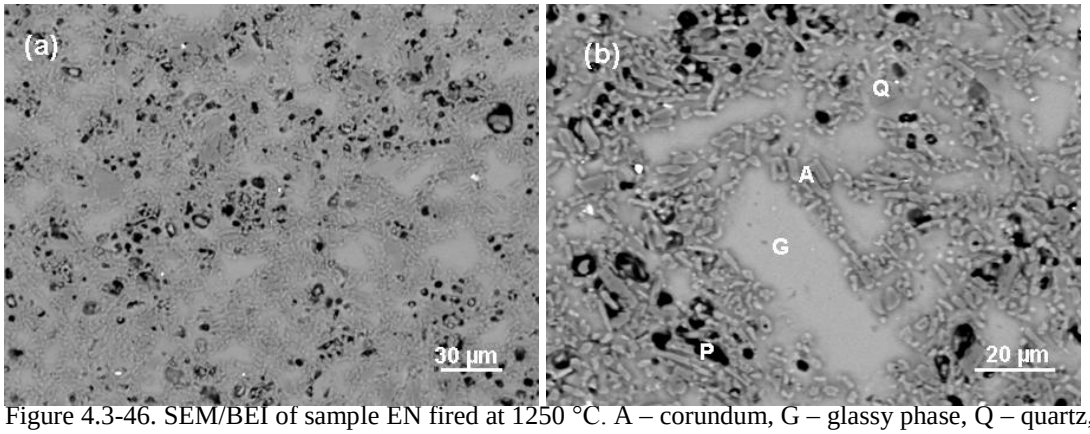

Figure 4.3-46. SEM/BEI of sample EN fired at 1250 °C. A – corundum, G – glassy phase, Q – quartz, P – pore.

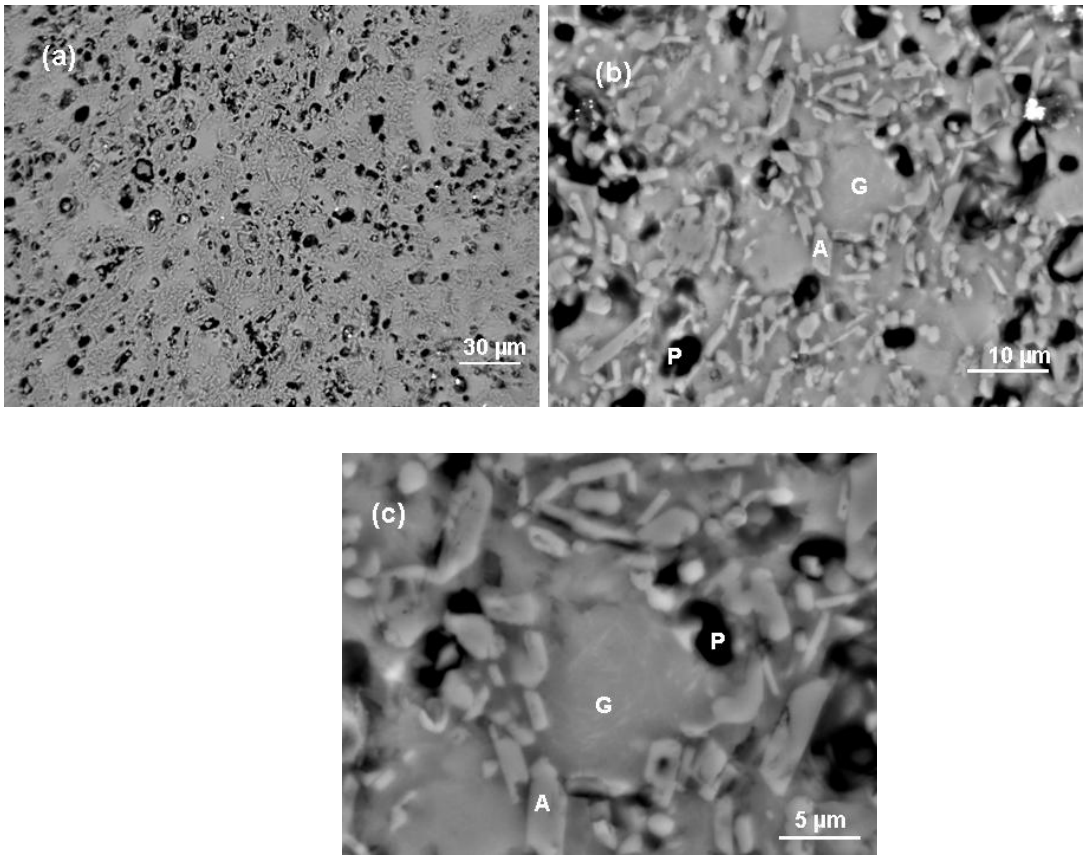

Figure 4.3-47. SEM/BEI of sample A fired at 1250 °C. A – corundum, G – glassy phase, P – pore.

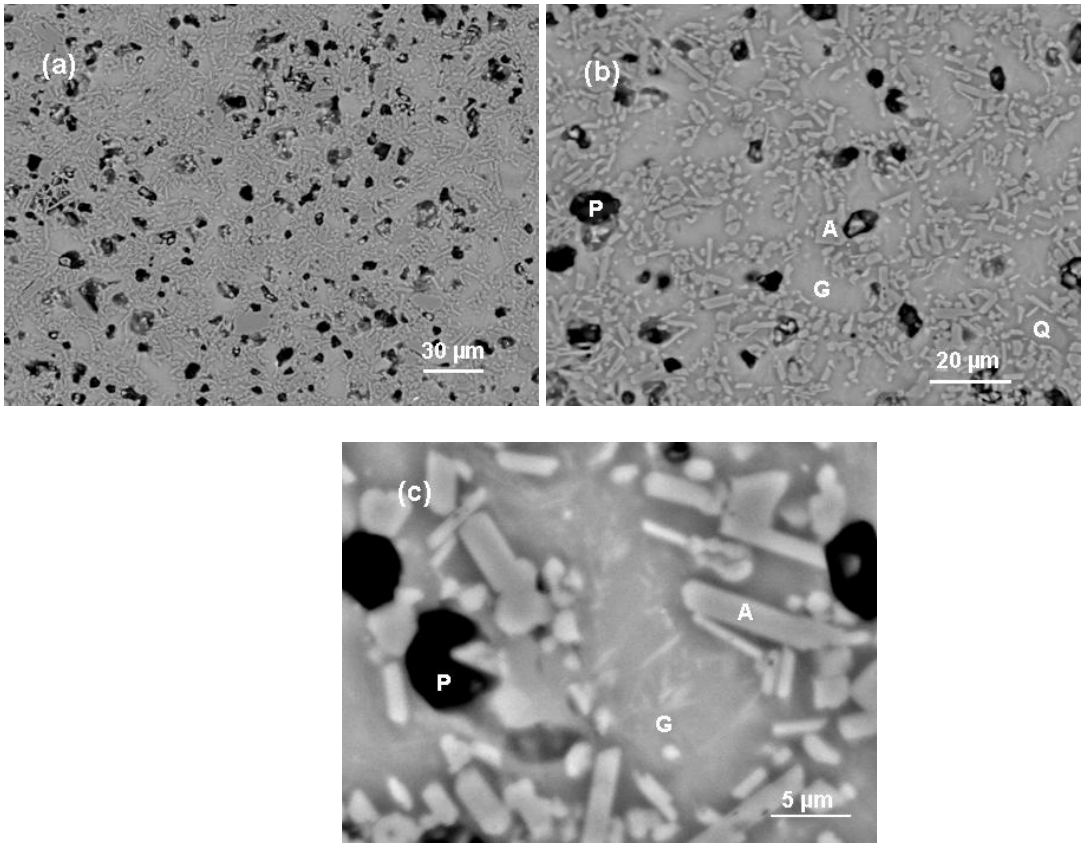

Figure 4.3-48. SEM/BEI of sample B fired at 1250 °C. A – corundum, G – glassy phase, Q – quartz, P – pore.

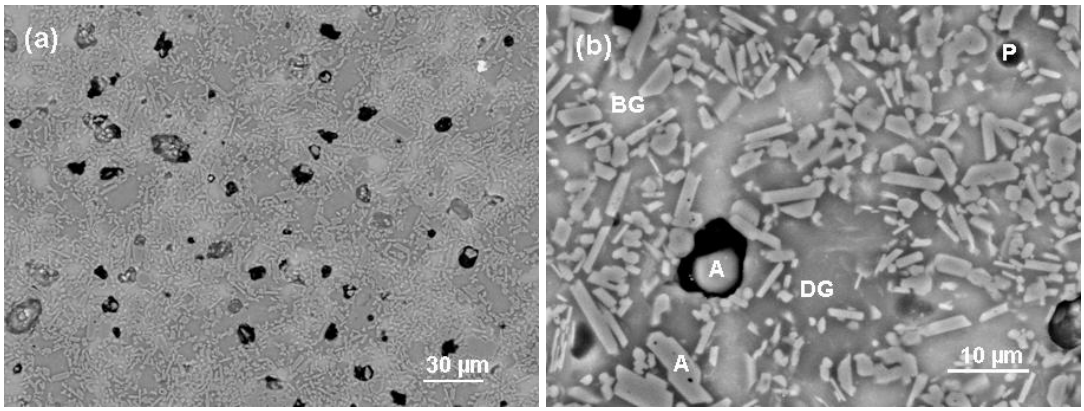

Figure 4.3-49. SEM/BEI of sample C fired at 1250 °C. A – corundum, BG – bright contrast or feldspar derived glassy phase, DG – dark contrast or β-spodumene derived glassy phase, P – pore.

SEM images of all studied compositions fired at 1250 °C are characterized by uniformly dispersed groups of corundum grains among glassy regions and pores. The process of pore uniting and pore elimination markedly underwent in the firing range from 1200 to 1250 °C.

The resulted microstructure in all compositions is characterized by mainly disconnected pores. The pores in EN reveal smaller and more irregularily dispersed in comparison to the pores in A, B and C. The pore elimination process in Li_2O-containing compositions is enhanced with the increasing amount of Li_2O as evident from strongly expressed pore separation in B and C.

In microstructure of compositions containing Li_2O the amount of pores decreases with increasing amount of Li_2O in the body. Increasing the amount of Li_2O contributes to more fluid liquid phase, which

easier flows into pores, and results in higher rate of densification. The effect of Li_2O on pore elimination is evident from the pore appearance in A, B and C. Composition A contains relatively large amount of non-uniformly distributed pores. Pores of composition B are more equal in size and shape. The amount of pores is the lowest by composition C, where the microstructure shows the highest degree of homogeneity concerning the distribution of pores, the glassy phase zones and surrounded corundum grains. The glassy phase zones with bright and dark contrast are clearly ditinguishable only in C, indicating that locally feldspar rich and lithium rich glassy phases are still present in C.

Regarding the size of the glassy phase zones surrounded by the corundum grain agglomerates they appear to be the largest in composition EN, which might be due to higher viscosity of its liquid phase. The quartz dissolution contributes to higher viscosity of liquid phase [57].

The process of quartz diminishing in all composition in temperature range from 1200 to 1250 °C is observed also from the corresponding XRD spectra. In EN, A and B the quartz diminishing is attributed merely to its dissolution in the liquid phase. However, in C the diminishing of quartz is enhanced due to its assimilation process leading to the formation of lithium feldspar.

The distinctive effect of Li_2O on promoting the vitrification process in temperature range 1200 to 1250 °C is obvious as well from dilatometric curves in Fig. 4.2-2. Compositions containing Li_2O attain the highest degree of densification, indicated as the inclination in sintering curve, in the temperature range from 1200 to 1250 °C. The densification process is enhanced with more Li_2O present. It has been ascertained that in bodies for stoneware tiles the improved densification is attributable to viscous flow closing the open porosity promoted by the presence of Li_2O in liquid phase [95].

4.3.2.6 Phase composition and microstructure after firing at 1300 °C

The identified mineralogical composition of studied bodies fired at 1300 °C is shown in Table 4.3-7 and illustrated with respective XRD patterns in Figure 4.3-50. After firing at 1300 °C corundum, α-quartz, mullite and lithium aluminium silicate are identified in studied compositions. Corundum as the main crystalline phase reveals in all the compositions. Also mullite is present in all the samples. Quartz is identified in all compositions except in composition C. Lithium aluminium silicate, as newly formed lithium mineral, is identified in C.

The mineralogical composition of EN remains unchanged in comparison to that after firing at 1250 °C with noticeable decrease in the intensity of quartz peak, indicating that that the process of quartz dissolution is in progress with increasing temperature.

Table 4.3-7. Identified mineralogical composition of samples EN, A, B and C fired at 1300 °C.

Mineral	EN	A	B	C
Corundum	×	×	×	×
α-quartz	×	×	×	
Lithium aluminium silicate				×
Mullite	×	×	×	×

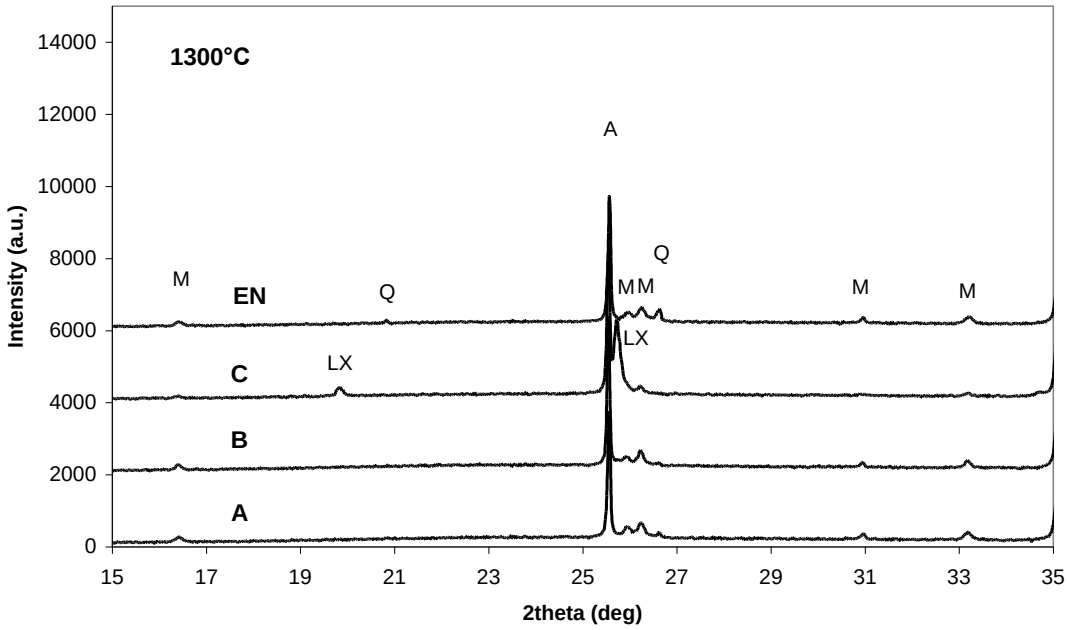

Figure 4.3-50. XRD patterns of samples EN, A, B and C fired at 1300 °C in 2θ-range 15–35°. Revealed minerals are A – corundum, Q – α-quartz, LX – lithium aluminium silicate ($Li_xAl_xSi_{1-x}O_2$) and M – mullite.

Among compositions containing Li_2O only in composition C lithium aluminium silicate is identified. The reaction of lithium feldspar leads to the formation of lithium aluminium silicate, which contains more SiO_2 than β-spodumene. General formula for lithium aluminium silicate, $Li_xAl_xSi_{1-x}O_2$, where x = 0 for the keatite form of SiO_2 and 0.33 for the β-spodumene form, describes the variations in the compositions, when the amount of silicon due to silica assimilation increases [108].

The process of silica incorporation, first in β-spodumene and second, in lithium feldspar can be described with the following reactions. The reaction taking place between β-spodumene and quartz is described by the following equation:

$$0.75(Li_{0.33}\ Al_{0.33}\ Si_{0.67}O_2) + 0.25(SiO_2) \rightarrow Li_{0.25}\ Al_{0.25}\ Si_{0.75}O_2 \qquad \text{Eq. 4.3-2}$$

The reaction product is $Li_{0.25}\ Al_{0.25}\ Si_{0.75}O_2$, which is equivalent to $LiAlSi_3O_8$ containing more SiO_2 than β-spodumene. When derived from the general formula for lithium aluminium silicate, the above equation can be written as follows:

$$y(Li_x\ Al_x\ Si_{1-x}O_2) + (1-y)(SiO_2) \rightarrow Li_{yx}\ Al_{yx}\ Si_{1-yx}O_2 \qquad \text{Eq. 4.3-3}$$

where y = 0.75 and x = 0.33 for β-spodumene. $Li_{0.25}\ Al_{0.25}\ Si_{0.75}O_2$ continues to react with quartz for the same equation (Eq. 4.3-3), except that x = 0.25. The final reaction product with more SiO_2 is formed.

In composition C with the highest amount of Li_2O no quartz is identified, which suggests that quartz is eliminated with dissolution and partial assimilation forming lithium aluminium silicate. Free quartz is still identified in compositions A and B. The amount of lithium oxide in C might be sufficient for more intense quartz assimilation, while in A and B the quartz elimination continues merely with its dissolution promoted by higher temperatures.

Recorded SEM/BE images of composition EN fired at 1300 °C are shown in Figure 4.2-51. The microstructure of EN appears vitrified with relatively low amount of pores (a). Almost spherical disconnected pores (P), comprised of small pores <10μm gathered in groups and separated large pores ~20 μm, are spread in relatively dense microstructure. Corundum grains (A) are gathered in agglomerates, which are relatively uniformly dispersed around glassy phase regions (G). The glassy phase regions, as obvious from image (b), are still elongated, while smaller in comparison to those after firing at 1250 °C due to increased penetration of glassy phase among corundum grains in agglomerates. The quartz grain (Q)

with cracks and melted edges is clearly visible in images (b) and (c).

In Figure 4.3-52 the images of composition A fired at 1300 °C are presented. The microstructure of A seems vitrified with disconnected oblong pores, which are dispersed in the glassy matrix with agglomerated corundum grains (a). The zones of glassy phase (G) reveal as homogeneously dispersed among agglomerates of corundum grains (A). However, the pores (P) are irregularly spread in the glassy matrix. In image (c) the mullite needles are visible in the glassy phase.

SEM/BE images of composition B fired at 1300 °C are shown in Figure 4.3-53. The microstructure of B is similar to that of A, but with lower amount of irregularly spread disconnected pores (a). The glassy phase regions (G) and agglomerates of corundum grains (A) are relatively uniformly dispersed in the microstructure. The pores (P) have near spherical shape and their size is below ~20 μm. Mullite needles are visible in the glassy phase in image (c).

In Figure 4.2-54 the SEM/BE images of composition C fired at 1300 °C are represented. The microstructure of C is characteristic by the uniformity in the size of closed pores. There is relatively large amount of spherical pores ~30 μm distributed in compact matrix (a). Dark contrast (DG) and bright contrast (BG) glassy phase zones are visible surrounded by corundum (A) agglomerates.

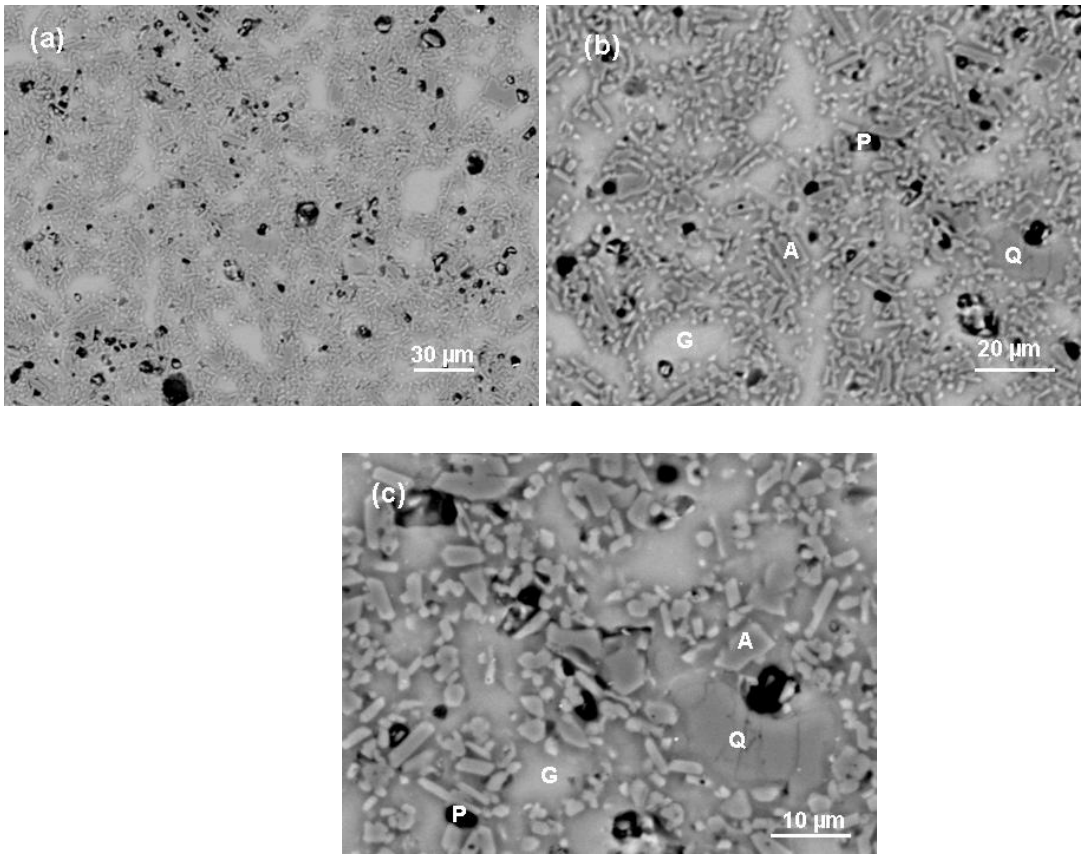

Figure 4.3-51. SEM/BEI of sample EN fired at 1300 °C. A – corundum, G – glassy phase, Q – quartz, P – pore.

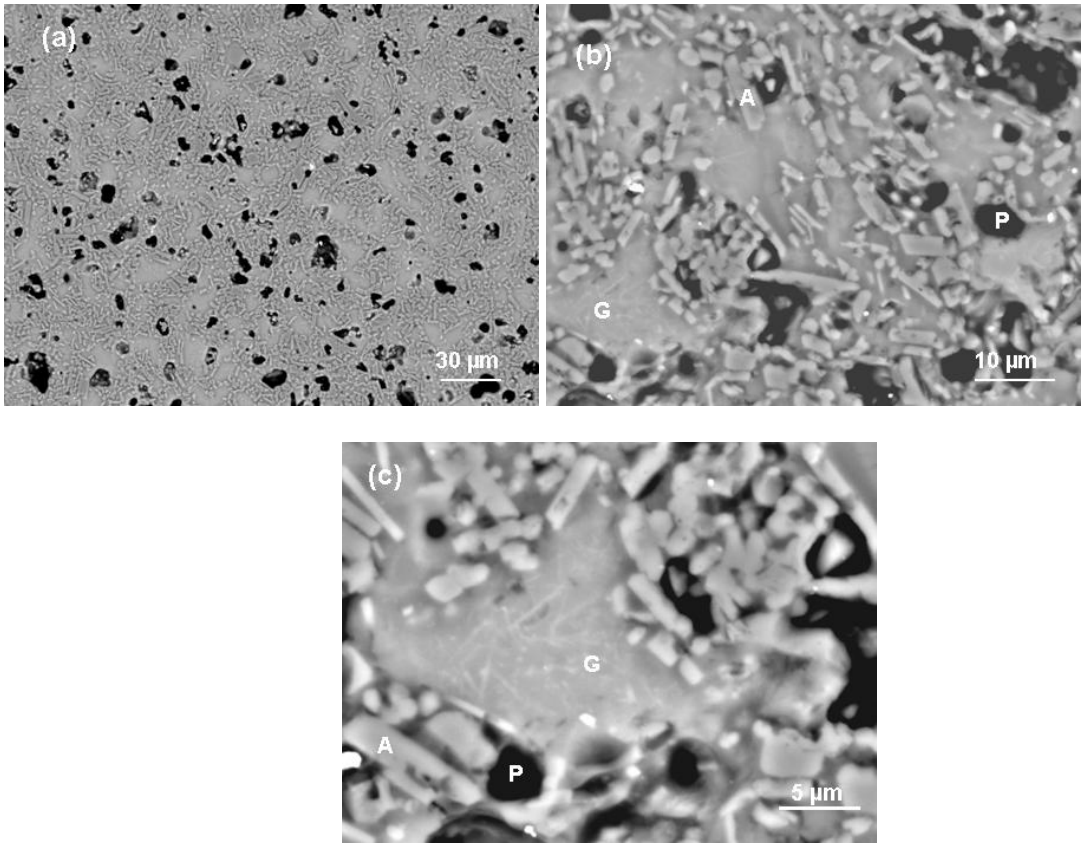

Figure 4.3-52. SEM/BEI of sample A fired at 1300 °C. A – corundum, G – glassy phase, P – pore.

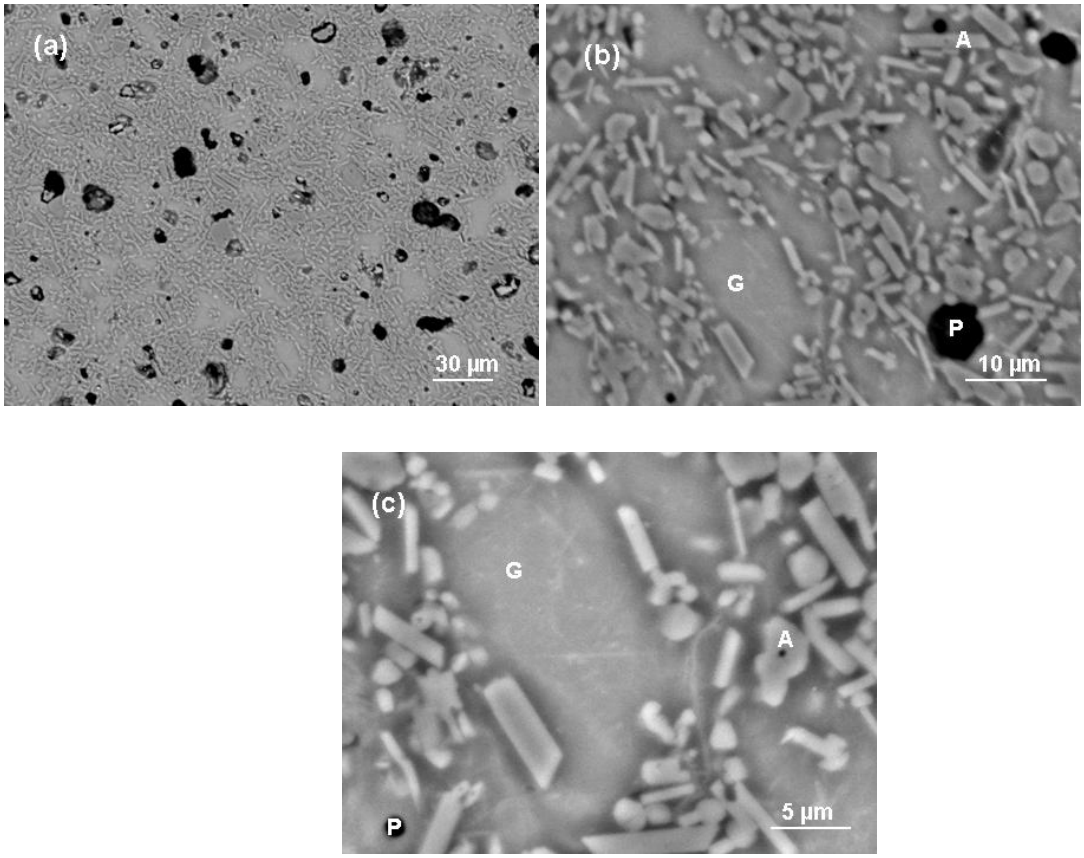

Figure 4.3-53. SEM/BEI of sample B fired at 1300 °C. A – corundum, G – glassy phase, P – pore.

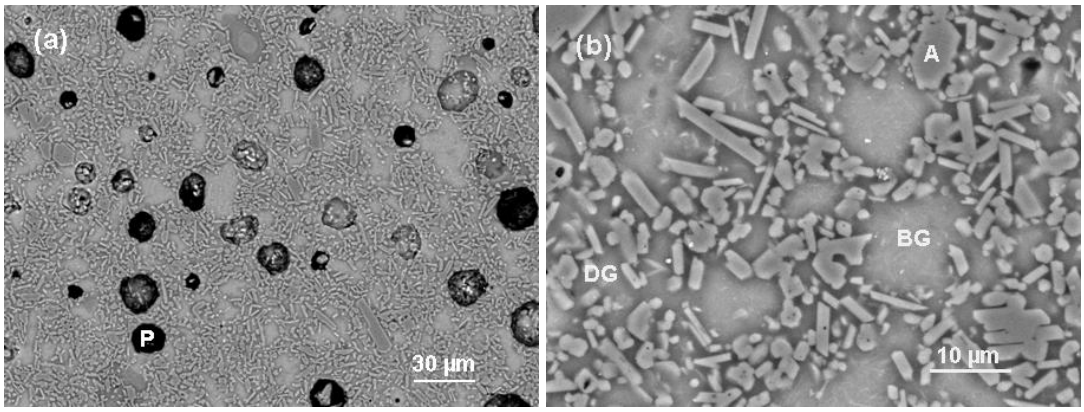

Figure 4.3-54. SEM/BEI of sample C fired at 1300 °C. A – corundum, BG – bright contrast or feldspar derived glassy phase, DG – dark contrast or β-spodumene derived glassy phase, P – pore.

After firing at 1300 °C the microstructure of all compositions appears as more compact in comparison to that fired at 1250 °C indicating that intensive process of pore elimination underwent in the presence of less viscous glassy phase. The glassy phase zones surrounded by corundum grains are smaller than at 1250 °C, indicating lower viscosity of liquid phase, which penetrated among grains in corundum agglomerates, thus affecting the corundum grains to be more homogeneously dispersed in the glassy matrix.

Among studied compositions the degree of non-uniformity of the glassy phase distribution is the greatest for EN. This might be attributed to higher viscosity of liquid phase in EN. In EN large quartz grains are identified, such as marked quartz grain with the size ~20 μm and slightly fused as visible in images (b) and (c) in Figure 4.3-51. EN is distinctive from compositions containing Li_2O additionally in pore characteristic. Some pores located in groups remain small, below 5 μm. The groups of small pores might appear due to their location in the region of high viscous glassy phase retarding the pore growth and their elimination. The amount of small pores below 5 μm is relatively large in comparison to the amount of small pores in compositions containing Li_2O, indicating slower rate of pore coarsening and eliminating.

The corundum grains and the glassy phase zones, in view to their shape, size and distribution, are the most uniformly distributed in compositions A and B with more compact microstructure observed for B. B is also characteristic by more spherical pores. From the microstructure of C the signs of overfiring are evident, where the small pores below 10 μm disappear and join into large spherical pores around 20 to 30 μm. There are visible only spherical closed pores for C, while pores in composition A and B are a mix of spherical and oblong. Mainly bright contrast glassy phase zones are present in C with some dark ones, which are smaller in size as compared to those observed after firing at 1250 °C, indicating more homogenous chemical composition of glassy phase in C. The greater homogeneity of glassy phase in C could be influenced by less viscous glassy phase with the increased amount of Li due to melting of lithium feldspar ($LiAlSi_3O_8$), as confirmed with XRD analysis, where lithium feldspar at 1300 °C is not identified.

4.3.2.7 Phase composition and microstructure after firing at 1350 °C

The identified mineralogical composition of studied bodies fired at 1350 °C is shown in Table 4.3-8 and illustrated with respective XRD patterns in Figure 4.3-55. After firing at 1350 °C corundum, as the main crystalline phase, is present in all studied compositions. Mullite reveals in all compositions, while quartz is identified only for EN and A. In composition C additionally lithium aluminium silicate is present.

Table 4.3-8. Identified mineralogical composition of samples EN, A, B and C fired at 1350 °C.

Mineral	EN	A	B	C
Corundum	×	×	×	×
α-quartz	×	×		
Lithium aluminium silicate				×
Mullite	×	×	×	×

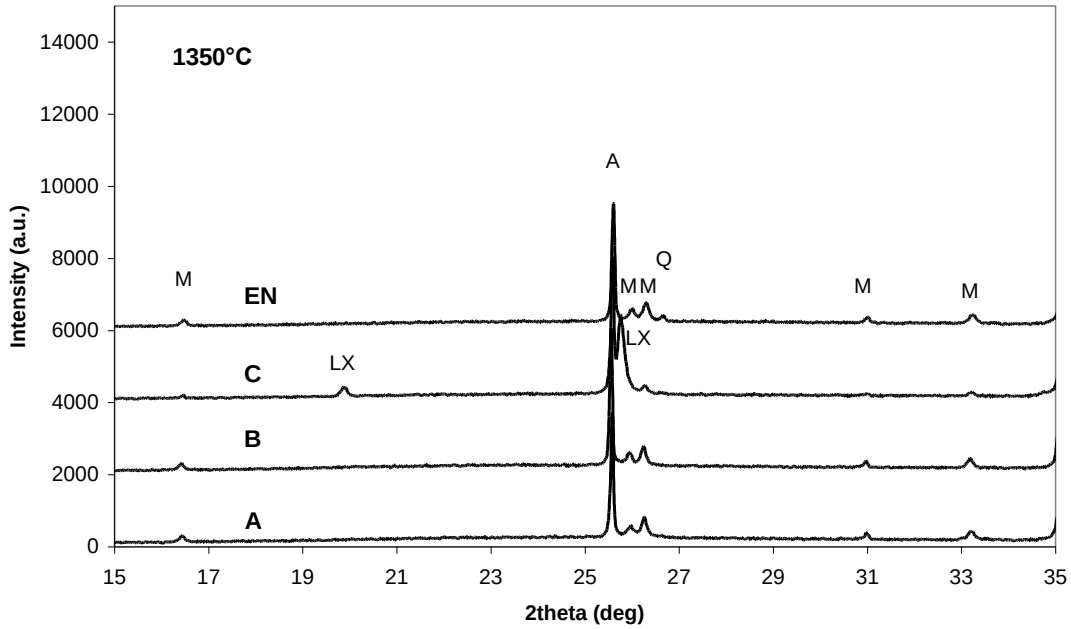

Figure 4.3-55. XRD patterns of samples EN, A, B and C fired at 1350 °C in 2θ-range 15–35°. Identified minerals are A – corundum, Q – α-quartz, LX – lithium aluminum silicate ($Li_xAl_xSi_{1-x}O_2$) and M – mullite.

As fired at 1350 °C the same phase composition for EN fired is identified as when it is fired at 1300 °C. The main reactions noticeable from the XRD patterns are the quartz dissolution with its peak intensity decreasing and the mullite growth with its peak intensity enlarging. Both the reactions appear to undergo relatively slow, since they only slightly affect the respective XRD peak intensities.

The intensity of lithium aluminium silicate peak in composition C is relatively strong as for the intensity of other phases present. There appear no noticeable changes in its amount with temperature increasing, which indicates that lithium aluminium silicate, which was first identified at 1300 °C, remains as stable phase with temperature increasing.

After firing at 1350 °C the amount of mullite in EN, A and B is comparable, indicating that Li_2O in the amount of 1.0 or 1.2 wt.% has no noticeable effect on the mullite growth at 1350 °C. The amount of mullite is perceivably lower for C. The formation of lithium aluminium silicate retards the mullite growth.

Among compositions containing Li_2O α-quartz is identified only in composition A with the relatively low intensity of its peak. The amount of Li_2O of 1.0 wt.% in composition A is not adequate to assimilate all disposable quartz. The reaction of quartz assimilation and dissolution is more intensive in B than in A, supporting that the quartz decrement is depended on the amount of Li_2O.

SEM/BE images of composition EN fired at 1350 °C are presented in Figure 4.3-56. The microstructure of EN, consisting of glassy phase, corundum grains and pores, shows a great deal of non-uniformity with regard to their size and distribution (a). Agglomerated corundum grains (A) surround the glassy phase zones (G). Most of the pores (P) are of spherical shape. The large pore ~40 μm, indicating the process of bloting, is seen in image (a). Large quartz grains (Q) with cracks in size ~50 μm are visible in image (aand in image (b).

In Figure 4.3-57 the SEM/BE images of composition A fired at 1350 °C are shown. Relatively small amount of almost spherical pores is distributed among agglomerates of corundum grains and glassy phase zones (a). The agglomerates of corundum grains (A) appear as penetrated with the glassy phase and the glassy phase zones are smaller in comparison to those of EN. Besides, the pore (P) distribution appears rather regular. Large pore ~30 μm, visible in image (a), indicates the pore growth characteristic for overfiring.

SEM/BE images of composition B fired at 1350 °C are seen in Figure 4.3-58. The microstructure of B is similar to that of A, but with higher amount of large closed pores (a). Regarding the corundum grains (A) and the glassy phase regions (G) the microstructure seems relatively homogenous. The portion of large

pores (P) ~30 μm is increased as typical for the overfiring process. The pores gained in size and changed their shape to less spherical in comparison to those after firing at 1300 °C. Mullite needles are visible in the glassy phase.

SEM/BE images of composition C fired at 1350 °C are shown in Figure 4.3-59. The large pores (P) show markedly overfired microstructure with a high portion of the closed pores. One of the big pores, as seen in image (a) has the size of ~200 μm. The process of pore expansion is exaggerated with temperature. The glassy phase regions (G) surrounded by corundum grains (A) reveal homogeneously dispersed among pores. Relatively small mullite needles are visible in the glassy phase regions.

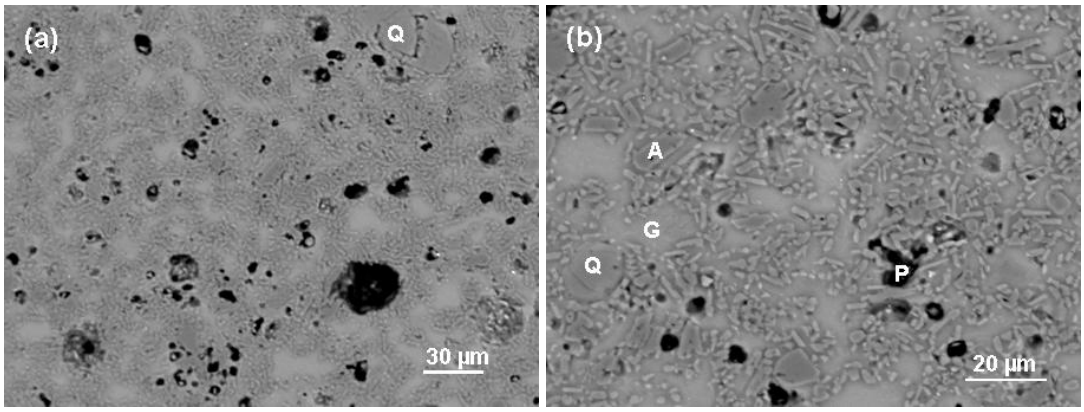

Figure 4.3-56. SEM/BEI of sample EN fired at 1350 °C. A – corundum, Q – quartz, G – glassy phase, P – pore.

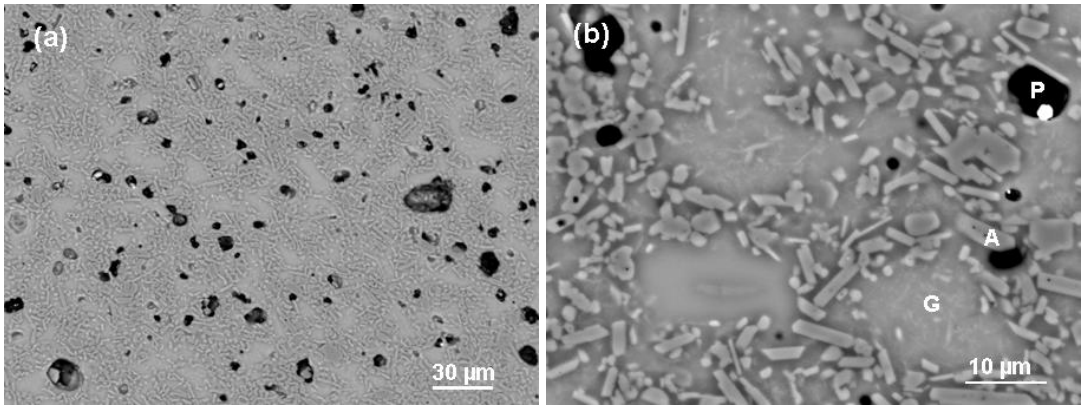

Figure 4.3-57. SEM/BEI of sample A fired at 1350 °C. A – corundum, G – glassy phase, P – pore.

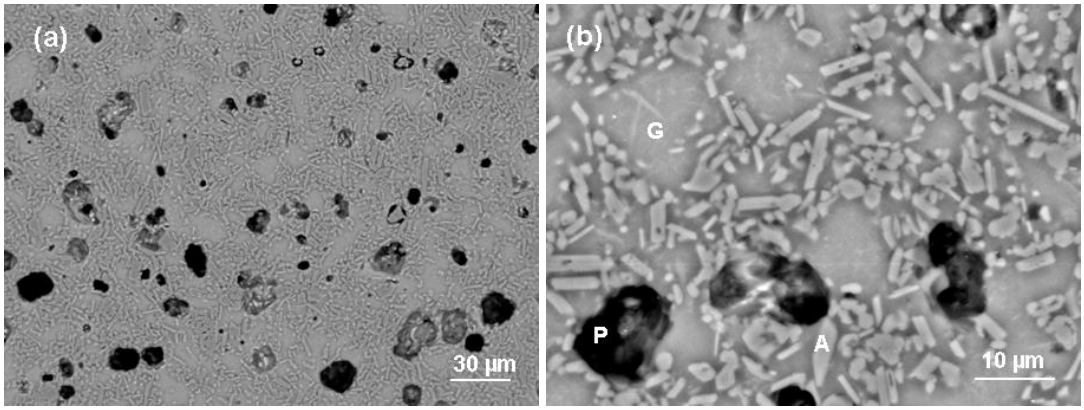

Figure 4.3-58. SEM/BEI of sample B fired at 1350 °C. A – corundum, G – glassy phase, P – pore.

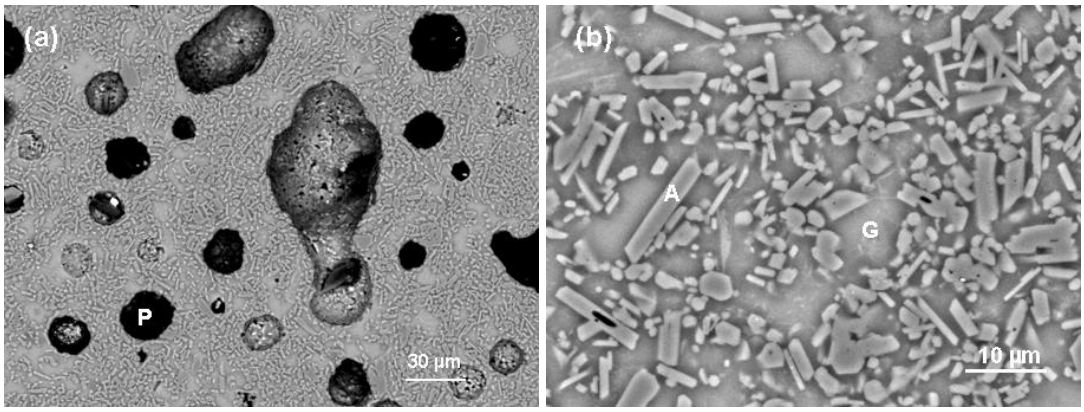

Figure 4.3-59. SEM/BEI of sample C fired at 1350°C. A – corundum, G – glassy phase, P – pore.

All studied compositions fired at 1350 °C are characteristic by pore size enlargement, which is most expressive for C. The growth of closed pores resulting in expansion in Li_2O-containing compositions is confirmed also from the corresponding dilatometric curves in Figure 4.2-2, where maximum shrinkage for A and B was recorded at 1320 °C, while for C at 1300 °C. In composition A with 1.0 wt.% of Li_2O the identified size of pores is below 30 μm. The effect of overfiirng is greatly influenced by the amount of Li_2O present. Samples of composition C with 1.6 wt. % of Li_2O experience blisters visible by eye, since many large pores over 100 μm appear in the microstructure. The tendency of C to most rapid expansion is obviously seen from its dilatometric curve in Fig. 4.2-3 recorded by heating microscope.

It is seen from the micrograph of composition EN that the glassy phase regions surrounded with uniformly distributed corundum grains slightly decrease and round in comparison to those fired at 1300 °C due to the more fluid glassy phase of EN fired at 1350 °C. The size of pores increases with some pores being over 30 μm. The lower viscosity of liquid phase in EN contributes to greater uniformity of liquid phase and surrounded corundum grains. The cracked quartz grains over 20 μm are found with SEM observation. At 1350 °C the quartz grains over 20 μm are present, since quartz grains below 20 μm completely dissolve as common for quartz porcelain body fired at 1350 °C [14].

The influence of Li_2O on the growth of mullite phase is studied from XRD patterns and additionally supported by the SEM observations. The appearance of mullite in XRD patterns is first identified at 1150 °C for all the compositions, which suggests that the presence of Li_2O in the amount 1.0, 1.2 or 1.6 wt.% does not enhance the mullite crystal growth at lower temperatures. Regarding the XRD analysis of bodies fired at 1350 °C, EN, A and B have about the same amount of mullite, while for C the amount of mulllite is lower. Therefore, Li_2O in the amount 1.0 or 1.2 wt.% has no perceivable effect on mullite crystallization. On the other hand, when Li_2O is added in the amount of 1.6 wt.% the mullite crystallization is retarted due to the formation of more lithium phases. The results are consistent with reported of Talyaganov *et.al* [93], that the mullite formation in triaxial porcelain bodies was promoted with 0.4 and 0.9 wt.% Li_2O added, while retarded with 1.3 wt. % or more Li_2O added.

SEM/BE image of EN fired at 1350 °C indicating the mullite needles in the glassy phase is shown in Fig. 4.3-60. In composition EN the mullite appears more like threads of tiny grains joined in ″cobweb″ in glassy matrix with the quartz grain.

SEM/BE images of A and B fired at 1350 °C indicating the mullite needles in glassy phase are shown in Fiure 4.3-61 and Figure 4.3-62. The size and thread appearance of mullite needles spread in glassy matrix is similar for compositions A and B.

The size of mullite needles reveals larger in compositions containing 1.0 and 1.2 wt.% of Li_2O in comparison to EN, where needles are weakly distinctive with grained appearance. As noticeable from SEM images it is suggested that Li_2O promotes the enlargement of mullite needles.

In compositions A and B all of the Li_2O is present in liquid phase, since no lithium minerals were identified in respective XRD patterns. Mullite needles grown from liquid phase containing Li_2O and K_2O in A and B experienced faster growth than mullite needles grown from liquid phase containing K_2O and Na_2O for composition EN.

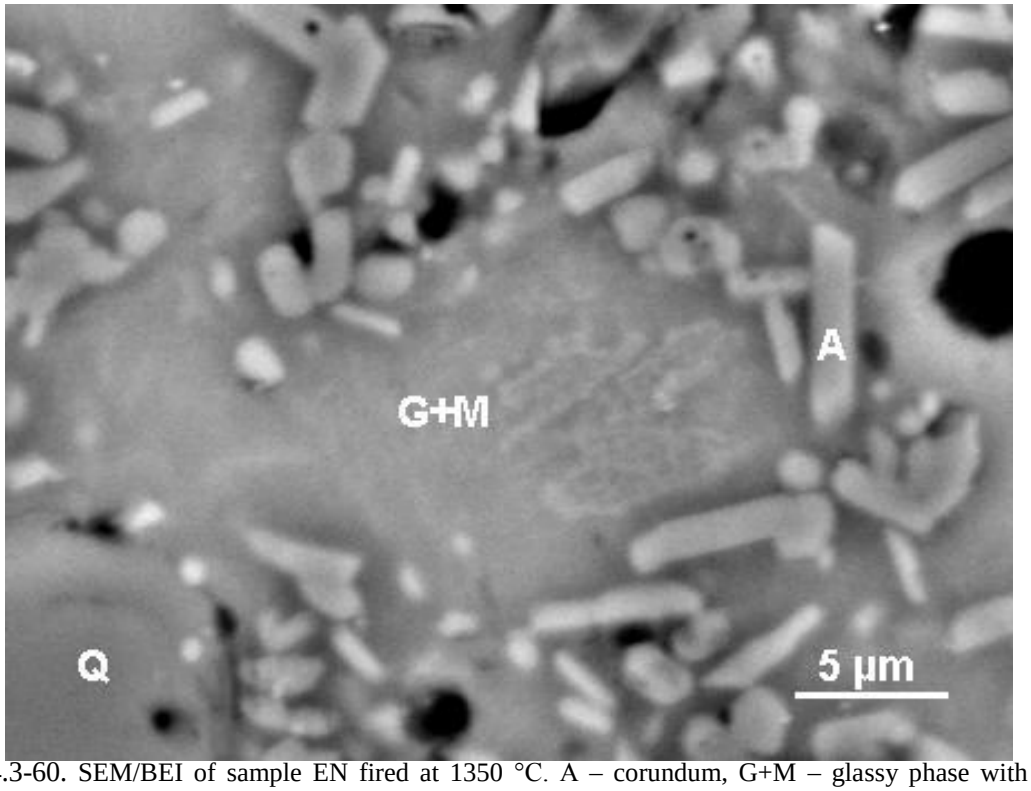

Figure 4.3-60. SEM/BEI of sample EN fired at 1350 °C. A – corundum, G+M – glassy phase with mullite needles, Q – quartz grain.

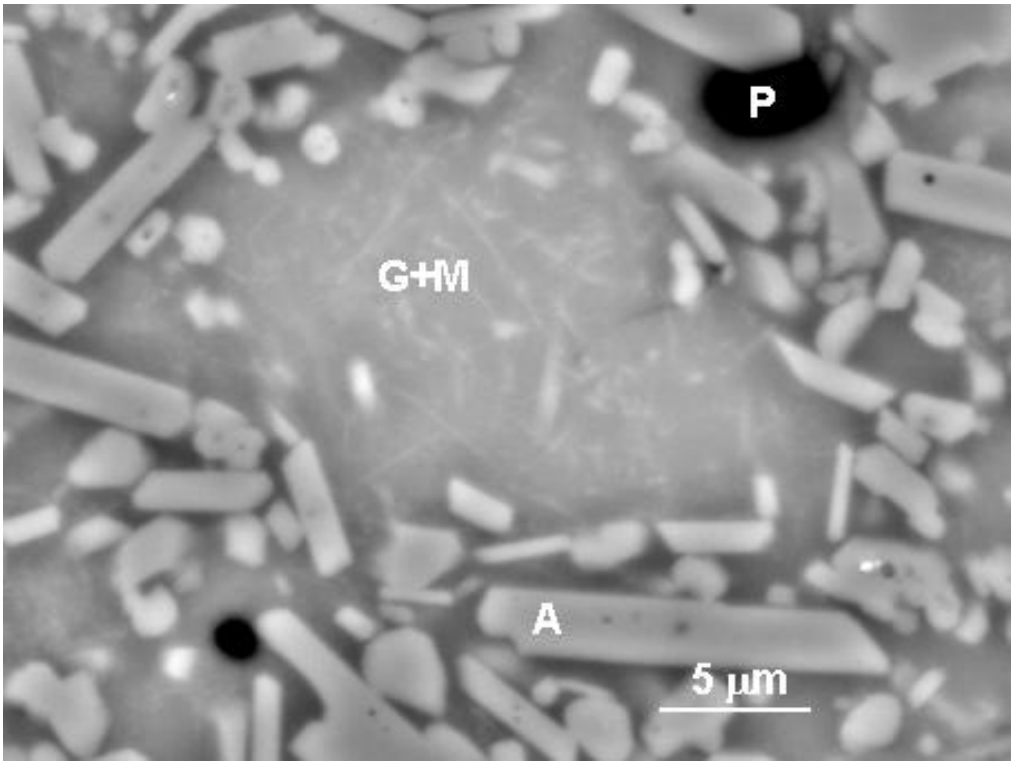

Figure 4.3-61. SEM/BEI of composition A fired at 1350 °C. A – corundum, G+M – glassy phase with mullite needles, P – pore.

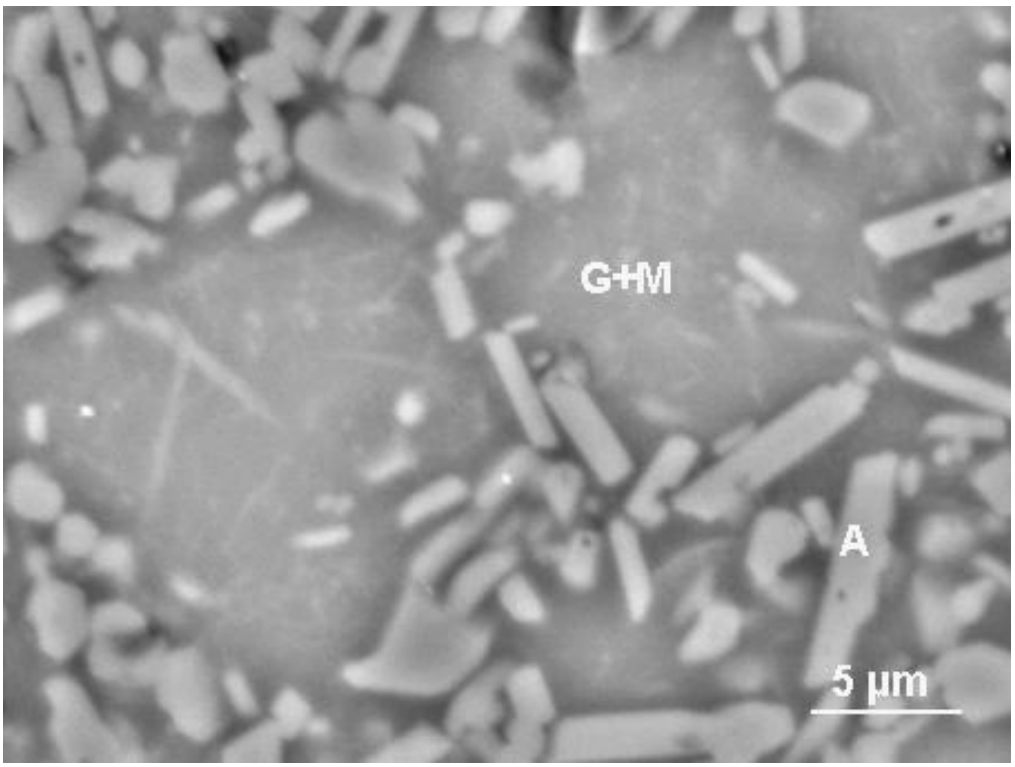

Figure 4.3-62. SEM/BEI of composition B fired at 1350 °C. A - corundum, G+M - glassy phase with mullite needles.

In Table 4.3-9 the phase composition of all the samples after firing in temperature range 950–1350 °C is summerized.

Table 4.3-9. Identified phase composition of samples EN, A, B and C fired in temperature range 950–1350 °C.

T	EN	A	B	C
950 °C	Corundum α-quartz Microcline Sanidine Albite	Corundum α-quartz Microcline Sanidine β-spodumene	Corundum α-quartz Microcline Sanidine β-spodumene	Corundum α-quartz Microcline Sanidine β-spodumene
1050 °C	Corundum α-quartz Microcline Sanidine Albite	Corundum α-quartz Microcline β-spodumene	Corundum α-quartz Microcline β-spodumene	Corundum α-quartz Microcline β-spodumene
1150 °C	Corundum α-quartz Mullite	Corundum α-quartz β-spodumene Lithium feldspar Mullite	Corundum α-quartz β-spodumene Lithium feldspar Mullite	Corundum α-quartz β-spodumene Lithium feldspar Mullite
1200 °C	Corundum α-quartz Mullite	Corundum α-quartz β-spodumene Lithium feldspar Mullite	Corundum α-quartz β-spodumene Lithium feldspar Mullite	Corundum α-quartz β-spodumene Lithium feldspar Mullite
1250 °C	Corundum α-quartz Mullite	Corundum α-quartz Mullite	Corundum α-quartz Mullite	Corundum α-quartz Lithium feldspar Mullite
1300 °C	Corundum α-quartz Mullite	Corundum α-quartz Mullite	Corundum α-quartz Mullite	Corundum Lithium aluminium silicate Mullite
1350 °C	Corundum α-quartz Mullite	Corundum α-quartz Mullite	Corundum Mullite	Corundum Lithium aluminium silicate Mullite

4.4 Physical properties of fired bodies

Physical properties of studied bodies fired at selected temperature in the temperature range 950–1350 °C were determined on equivalent samples as used for the XRD and the microstructural investigations, which were all sintered in the laboratory electric furnace at the same time.

4.4.1 Visual appearance of fired bodies

When the temperature is increased from 950 to 1350 °C, the colour of the fired samples changes gradually from pale brown to white for all the compositions except composition C. It appears that 1.6 wt.% of Li_2O in the alumina porcelain body leads to reactions, where red compounds are formed, while with the addition of 1.0 or 1.2 wt.% there is no noticeable colour change.

For the composition C the colour of the body observed on cross-sectioned surfaces changes to pale red at 1200 °C. With a temperature increase to 1250 °C several homogeneously dispersed spots of bright red appear on the surface and inside the body. At 1300 °C the colour of the body changes to a homogenous yellow-white with individual red spots in the surface, which becomes glassy. At 1350 °C there is only a slight change to a more pale-yellow, white colour with red spots remaining on the surface. Additionally, the surface appears more glassy and small bubbles are visible. All the other studied compositions develop a white homogenous appearance at 1300 and 1350 °C.

The appearance of pink spots in mullite–β-spodumene composites from aluminosilicates was previously mentioned by Yamuna and Devanarayanan [109] and attributed to the pink variety of β-spodumene (kunzite), the formation of which occurs only in the presence of lithium-rich aluminosilicates and the presence of iron as an impurity in the mullite composite. When Tulyaganov *et al.* [101] investigated the influence of Li_2O on phase transformation in formulations composed of 50 wt.% of kaolin, 25 wt.% feldspar and 25 wt.% quartz, they described the appearance of pink spots in K–Na-containing aluminosilicate matrix in compositions containing more than 2.2 wt% Li_2O after firing at 1200 °C, which disappeared with heat treatment at higher temperatures.

It should be mentioned that in our previous investigations, where the selection of raw materials for new alumina porcelain bodies was carried out, the red colour on the surface was noticed for bodies containing around 60 wt.% of Al_2O_3 together with more than 1 wt.% of Li_2O and more than 0.6 wt.% of Fe_2O_3, fired at 1300 °C. The coloring was more intensive in reduction than in oxidation atmosphere. Further investigations would be necessary for more accurate explanation of the red spots appearance. The surface with red spots is not acceptable for alumina porcelain body.

Self-glazing effect of surface as perceived for C after heat treatment at 1300 and 1350 °C is not adequate for ordinary alumina porcelain body. On the other hand, the self-glazing effect of the surface is commonly not desirable because it causes the adhesion of bodies on the refractory plates.

4.4.2 Bulk density of fired bodies

Bulk density of studied bodies fired in the temperature range 950–1350 °C is presented in Table 4.4-1 and illustrated in Figure 4.4-1.

Table 4.4-1. Bulk density (g/cm^3) of samples EN, A, B and C fired in the temperature range 950–1350 °C.

Temperature (°C)	EN	A	B	C
950	1.95	1.76	1.77	1.72
1050	2.05	1.83	1.86	1.82
1150	2.46	2.21	2.19	2.14
1200	2.62	2.37	2.39	2.51
1250	2.81	2.69	2.73	2.82
1300	2.87	2.80	2.82	2.72
1350	2.81	2.80	2.78	2.46

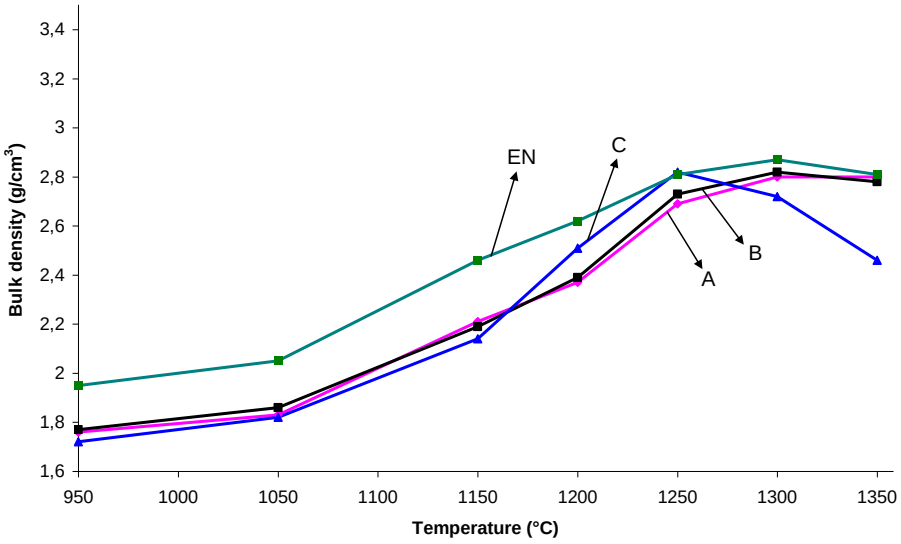

Figure 4.4-1. Bulk density of samples EN, A, B and C fired in the temperature range 950–1350 °C.

Composition EN achieves the maximum bulk density of 2.87 g/cm^3 at 1300 °C, which is the same temperature as for A and B. At higher temperature its density decreases, indicating the growth of closed porosity.

Compositions A and B attain their maximum bulk density, which is 2.80 g/cm^3 for A and 2.82 g/cm^3 for B, at 1300 °C. As seen from almost overlapping curves up to 1300 °C, compositions A and B show very similar behaviour in the densification process up to the maximum bulk density. With the temperature increasing to 1350 °C there is no change in bulk density for A, while there is a slight decrease in the bulk density for B.

At 1150 °C the composition C starts to thicken faster in comparison to other bodies and achieves its maximum bulk density of 2.82 g/cm^3 already at temperature 1250 °C, which is at the lowest temperature among all bodies. Above 1250 °C the bulk density of C strongly decreases to 2.46 g/cm^3 at 1350 °C.

The ascertained maximum bulk density of compositions containing Li_2O is little lower in comparison to that of reference composition. However, the Li_2O containing compositions have about the same maximum bulk density.

With increasing temperature bulk density increases at gradually increasing rate, which is about the same for all compositions up to 1150 °C. From 1150 to 1250 °C the compositions containing Li_2O vitrify faster than reference EN. Small differences in bulk density at temperatures above 1250 °C indicate that the vitrification process is retarded. With temperature increasing the changes in viscosity are enhanced by the compositions with Li_2O, which is mostly expressed for C with the highest amount of Li_2O.

Bulk density is a mass per unit volume, when unit volume includes both pores and solids. In triaxial porcelain body the bulk density depends on type and amount of crystal phases present, the composition and amount of glassy phase and the amount of pores [35]. Bulk density significantly increases in vitrified compositions, what is affected primarily by the changes in porosity and the presence or formation of phases with varied densities. Correctly fired porcelain is non-porous in sense that it is vacuum-tight, but on the other hand it has a number of closed unconnected pores, indicated by the difference between bulk and true powder densities.

The bulk density in studied compositions is increasing relatively comparable in temperature range 950 to 1150 °C. At 950 °C the bulk density of composition EN is higher than in model compositions, which have at 950 °C about the same bulk density. All compositions were mixed from about the same amount of calcined alumina, which greatly contributes to density. At 950 °C the difference in the bulk density might be attributed mostly to the distinctions in open porosity and partly to the density of present phases other then corundum. The crystal phases present at 950 °C as identified by XRD analysis are the same in all compositions with the exception of flux minerals. In the composition EN microcline and albite are present,

while in the model compositions there are microcline and β-spodumene. The densities of microcline, albite and β-spodumene are 2.56 g/cm^3, 2.61 g/cm^3 and 2.41 g/cm^3, respectively. The flux system in composition EN has slightly higher density than the flux system with lower density β-spodumene in model compositions.

Above 1150 °C the bulk density in model compositions with Li_2O increases faster than in EN until maximum bulk densities are reached. Composition C with the highest amount of Li_2O and higher total amount of fluxes achieves the maximum bulk density at temperature, which is 50 °C lower than the temperature of the maximum bulk density of A, B and EN, which all attaint the maximum bulk density at 1300 °C.

The difference in the maximum bulk densities between Li_2O-containg compositions and reference composition is relatively small owing to the distinctions in the density of phase compositions, including crystal and glassy phase, and volume of closed pores. The highest value of the maximum bulk density is ascertained for the composition EN.

The bulk density decrease in studied compositions at 1350 °C is attributed to the expansion caused by closed pore growth as clearly shown in Fig. 4.3-56 (a) for EN, in Fig. 4.3-57 (a) for A, in Fig. 4.4-58 (a) for B and in Fig. 4.3-59 (a) for C. The closed pore volume is much higher at composition containing 1.6 wt.% Li_2O, which experiences considerable drop in bulk density, as seen also from the Fig. 4.3-59 (a). The lower viscosity of the liquid phase that decreases with increased amount of Li_2O promotes the growth of closed pores, alike as described by Esposito *et al*. [41], that the enhanced growth of rather large pores are due to the lower viscosity of nepheline syenite rich liquid phase.

The results show that the composition with 1.0 wt.% Li_2O is characterized by stable bulk density, which indicates relatively low volume of closed pores and better thermal stability regarding tendency towards overfiring.

4.4.3 Open porosity of fired bodies

The results of the open porosity determination of studied bodies fired in the temperature range 950−1350 °C are presented in Table 4.4-2 and illustrated by Figure 4.4-2.

Table 4.4-2. Open porosity (vol.%) of samples EN, A, B and C fired in the temperature range 950−1350 °C.

Temperature (°C)	EN	A	B	C
950	35.5	40.9	40.7	42.0
1050	30.9	39.2	38.2	38.4
1150	14.4	25.3	25.5	27.1
1200	9.8	16.2	14.4	8.5
1250	0.0	2.0	0.0	0.0
1300	0.0	0.0	0.0	0.0
1350	0.0	0.0	0.0	0.0

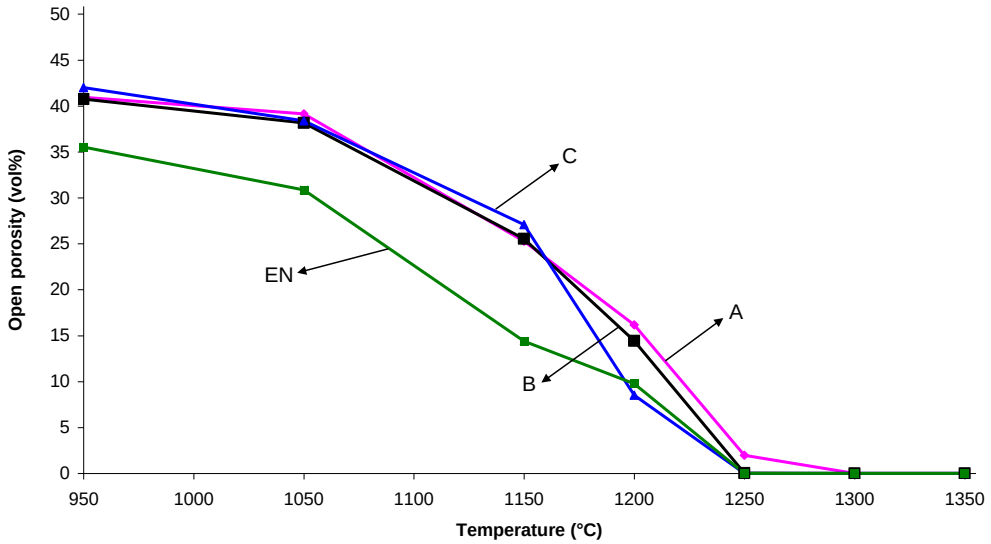

Figure 4.4-2. Open porosity of samples EN, A, B and C fired in the temperature range 950–1350 °C.

After firing at 950 °C the volume fraction of open pores is about 36 vol.% for EN and about 41 vol.% for A, B and C and. The open porosity after firing at 1050 °C in comparison to that after firing at 950 °C gradually diminishes in EN, A, B and C for 4.7%, 1.7%, 2.5% and 3.6%, respectively. The rate of pore closing is relatively low for all the compositions in temperature range 950–1050 °C.

In the temperature range 1050–1150 °C the process of pore closing is enhanced. At 1150 °C EN achieves the lowest open porosity among studied compositions, while Li_2O-containing compositions have resembling open porosity. Up to 1150 °C the rate of pore closing is the highest for composition EN, but beyond this temperature model compositions experience faster pore closing. Comparing the Fig. 4-4.1 and Fig. 4.4-2 it is seen that the porosity decrease in temperature range 950–1150 °C is correlated to the bulk density increase in this temperature range.

At 1200° C all compositions still possess open porosity, which is the lowest for composition C. The porosity sharply decreases by composition C in temperature range 1150–1200 °C. The pore closing in temperature range 1150-1200 °C is mostly expressive for the composition C, which is also confirmed with the most expressive growth of bulk density for C in this temperature range, as seen in Fig. 4.4-1.

At 1250 °C the apparent porosity is eliminated in all the compositions, except in composition A, where 2.0 vol.% of open porosity is still determined. The change in the pore size and their number is most greatly influenced with the maximum rate of densification in temperature range 1200–1250 °C. In this temperature range the rate of densification is the highest and equal for compositions A and B. However, compositions EN and C vitrify little slower in this temperature range.

Above 1250 °C all compositions are characterized with zero open porosity. Therefore, the pores that are still present in the studied compositions above 1250 °C, as seen on corresponding SEM images, are closed pores.

The changes in open porosity, when the temperature increases, show an inverse relation with the bulk density for all the studied compositions. At firing temperatures 950 and 1050 °C all studied compositions are characterized mainly by open porosity, which is also confirmed with the grained structure, as seen in corresponding SEM images. There is only a small change in porosity among samples fired at 950 or 1050 °C. At temperatures below 1150 °C all compositions experience similar behavior in the rate of open pore closing as reflected from the similar slope of corresponding curves. Compositions containing Li_2O experience rapid pore closing in the temperature range 1150–1250 °C.

4.4.4 Thermal expansion of fired bodies

Thermal expansion of studied compositions fired at different temperatures in the temperature range

950–1350 °C is investigated from the CTE curves derived from expansion data in the temperature range 30–980 °C. First, the CTE curves in temperature range 30–980 °C of studied compositions after firing at different temperatures are compared, and second, the differences among CTE (30–300° C) of studied compositions fired at different temperatures are studied. The closer look to CTE (30–300 °C) is chosen mostly with the aim to compare the expansion behavior of compositions in temperature interval where most of porcelain bodies fail at thermal shock test.

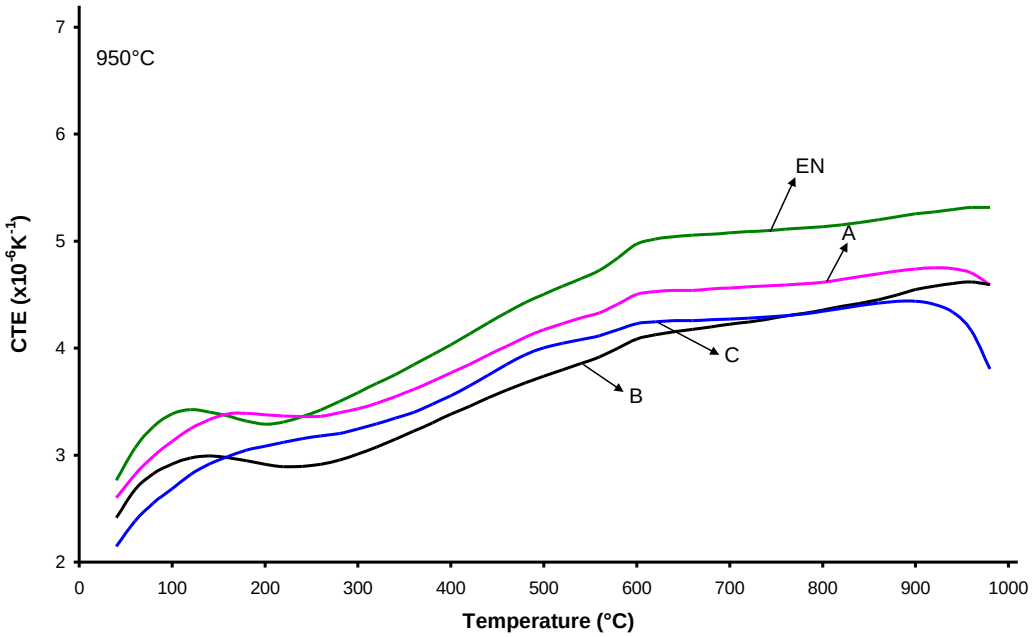

Figure 4.4-3. CTE curves of samples EN, A, B and C fired at 950 °C.

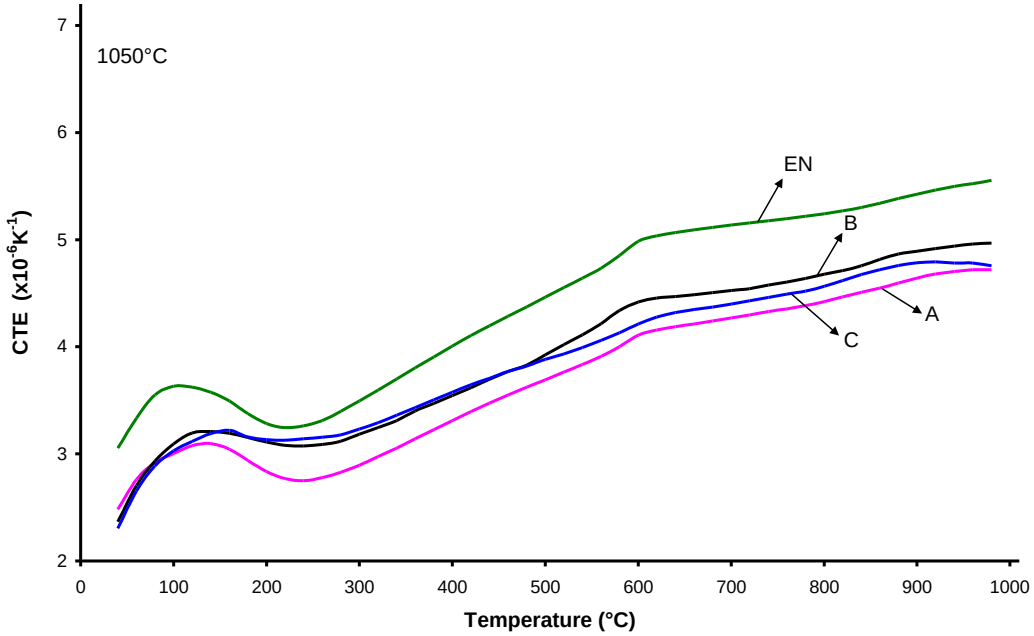

Figure 4.4-4. CTE curves of samples EN, A, B and C fired at 1050 °C.

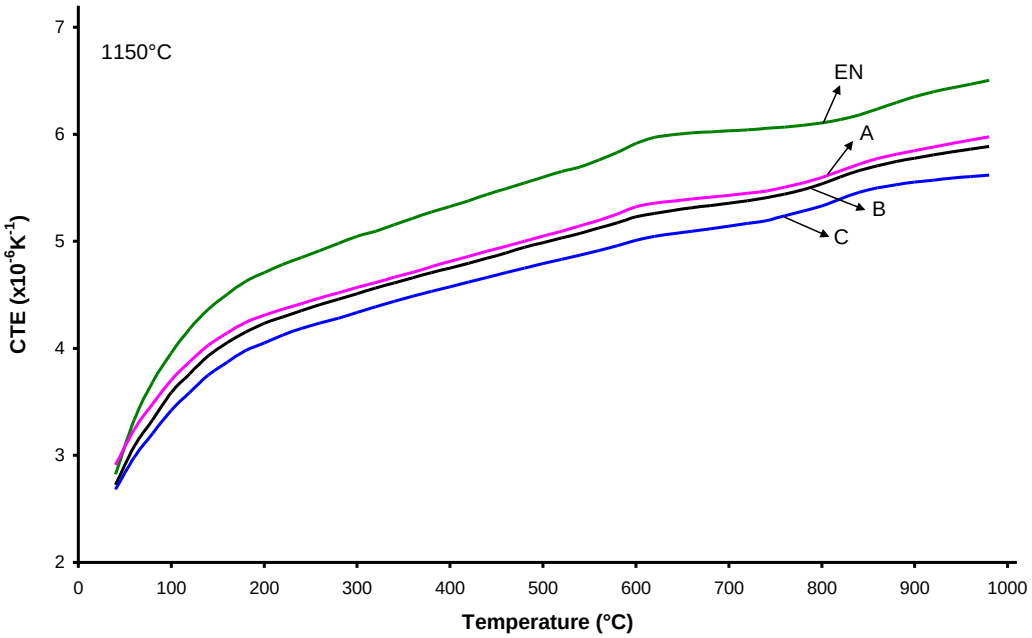

Figure 4.4-5. CTE curves of samples EN, A, B and C fired at 1150° C.

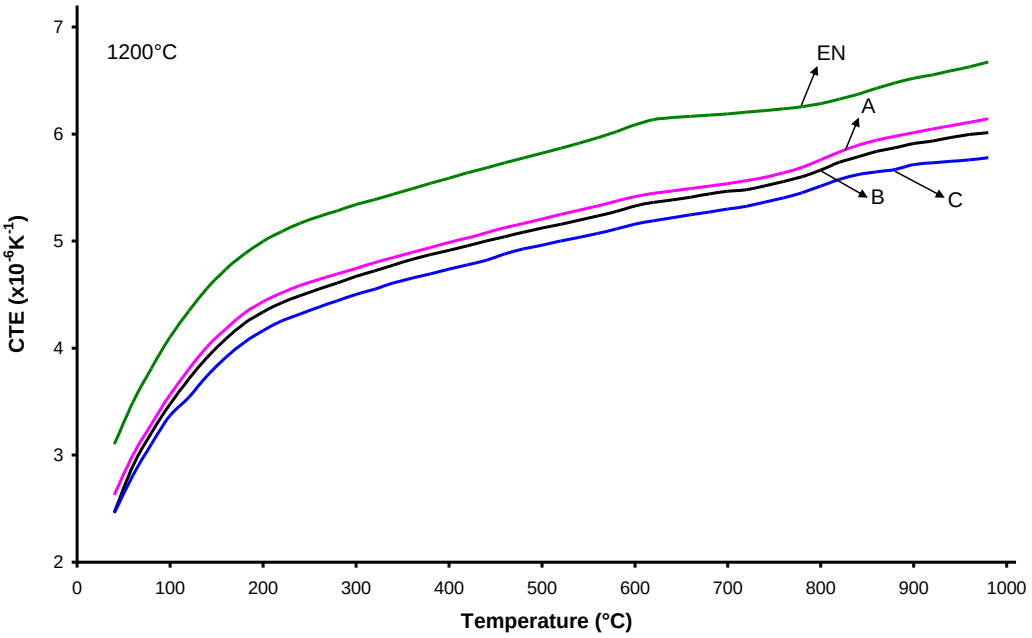

Figure 4.4-6. CTE curves of samples EN, A, B and C fired at 1200 °C.

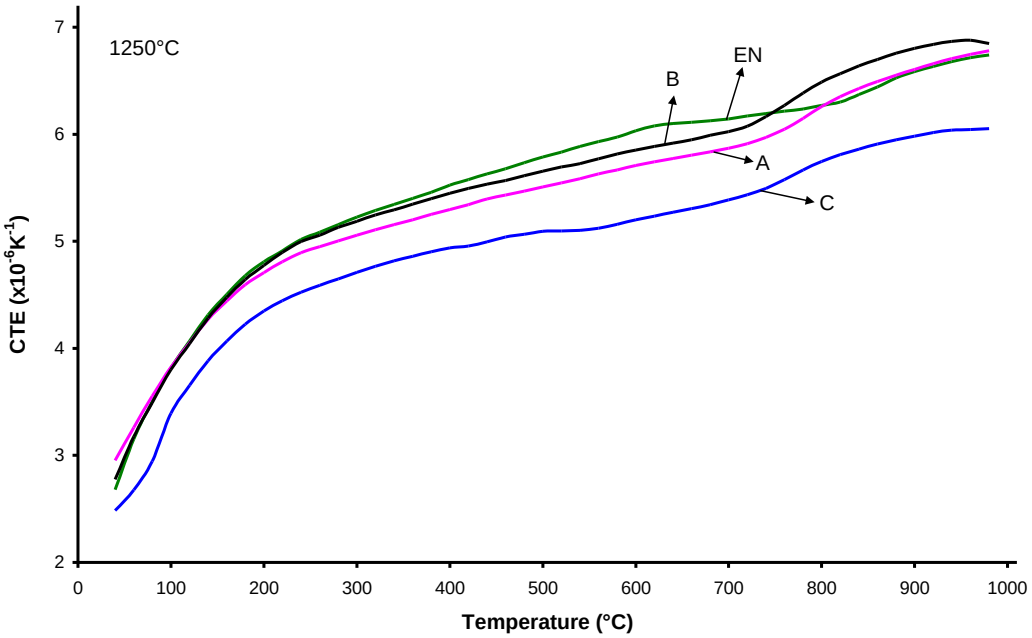

Figure 4.4-7. CTE curves of samples EN, A, B and C fired at 1250°C.

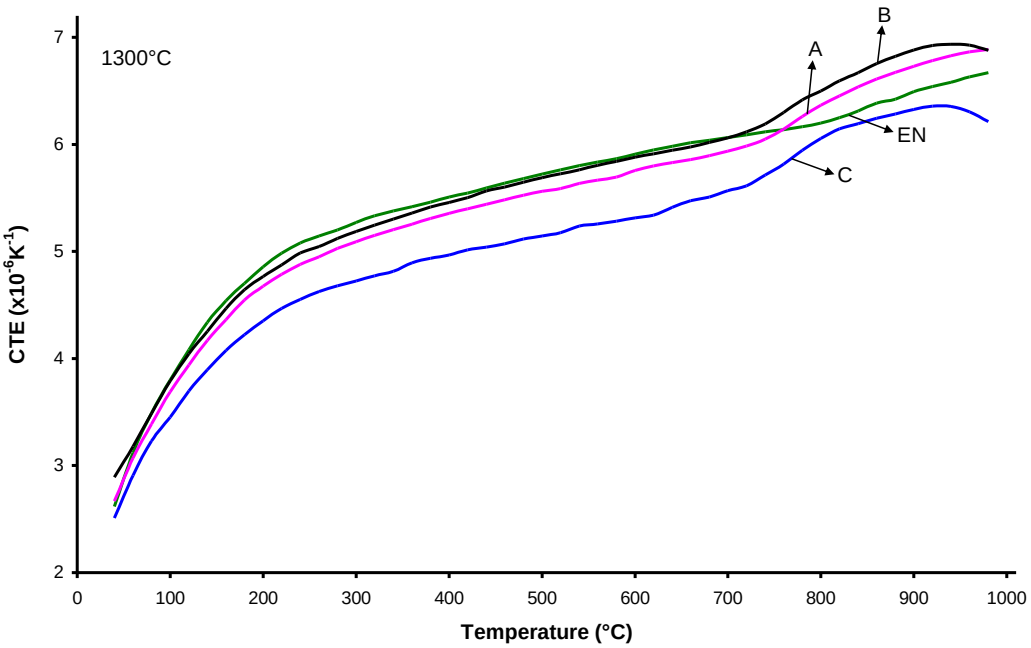

Figure 4.4-8. CTE curves of samples EN, A, B and C fired at 1300° C.

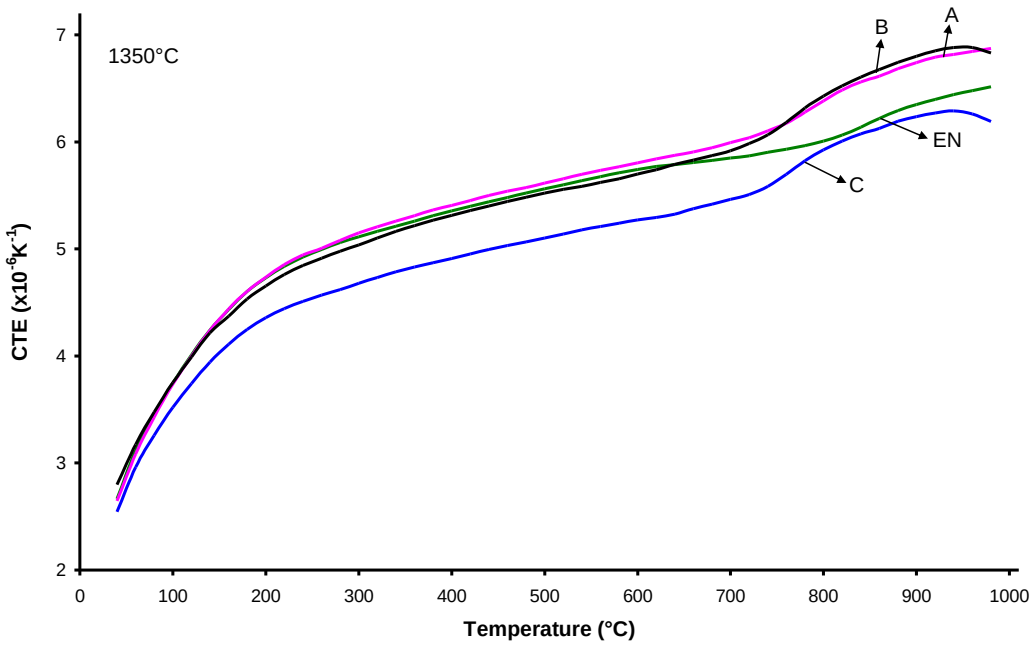

Figure 4.4-9. CTE curves of samples EN, A, B and C fired at 1350 °C.

In Figure 4.4-3 the CTE curves of studied bodies fired at at 950 °C are displayed. The CTE curve of EN is positioned considerably above the curves of model compositions at temperatures above ~250 °C. At temperature ~580 °C the change in direction of EN with the steep step is recorded. The CTE curves of EN, A and B show an explicit increase in expansion, seen as concavity in the curve, with the maximum at ~120 °C for EN, ~180 °C for A and ~140 °C for B. The CTE curve of B is positioned below the CTE curve of A. The trend of curves of A and B appears similar at temperatures above ~250 °C with curves showing a steep step or knee at ~580 °C and the concave form with the onset ~950 °C. The trend of C is similar to the trend of A in the entire measuring range, except that the concavitity of its CTE curve above 850 °C with the onset ~930 °C is more expressive. The steep step ~580 °C is lower by compositions A, B and C than by EN.

The CTE curves of studied bodies fired at 1050 °C are shown in Figure 4.4-4. The changes in CTE (30-600°C) of samples fired at 1050 °C in comparison to that of samples fired at 950 °C are recorded only for A, where CTE (30-600°C) is for about $0.3\times10^{-6}K^{-1}$ lower, and for B, where CTE (30-600°C) is for about $0.3\times10^{-6}K^{-1}$ higher, while no considerable changes in CTE (30-600°C) are revealed for EN and C. The trend of CTE curves of all studied composition appear similar to the CTE curves recorded by samples fired at 950 °C with the curve of EN positioned above the curves of model compositions. The CTE curves of all samples exhibit expressive concavity with the maximum at ~100 °C for EN, ~140 °C for A and B, and ~160 °C for C. The CTE curve of A is positioned below the CTE curve of B and C. There is no noticeable change in the size of steep step or knee ~580 °C by all samples in comparison to firing at 950°C.

Figure 4.4-5 displayes the CTE curves of samples fired at 1150°C. CTE curves reflect considerable increase in the CTE for all samples in comparison to CTE of samples fired at 1050 °C with the increase in CTE (30-600°C) for about $1\times10^{-6}K^{-1}$. The CTE curve of EN is positioned above the CTE curves of model compositions, indicating higher CTE of EN in comparison to other compositions in the entire measuring range. The steep step or knee in the CTE curves ~580 °C is lower by all samples in comparison to samples fired at 1050 °C. The CTE curves of A and B run almost parallel with A lying above B. The CTE curve of C is positioned as the lowest, indicating the lowest CTE of C in the entire measuring range.

In Figure 4.4-6 the CTE curves of samples fired at 1200 °C are presented. The trend and the position of individual CTE curve are very similar to those of the CTE curves recorded on samples fired at 1150 °C, except that all curves are positioned at about $0.2\times10^{-6}K^{-1}$ higher values of CTE in measuring range above ~150 °C. The steep step or knee in CTE curve ~580 °C is visible only by EN.

The CTE curves of samples fired at 1250 °C are shown in Fig. 4.4-7. The CTE curves of EN, B and A are close to each other up to measuring range around 700 °C with EN positioned above B and A. Above around 750 °C the CTE curves of A and B increase their slope resulting in their position above EN with the curve of A almost overlapping with the curve of EN. The CTE curve of C is positioned considerably below

EN, B and A in the entire measuring range. The steep step or knee in CTE curve ~580 °C, which is observed only for EN, is lower to that of EN fired at 1200 °C. In CTE curves of A, B and C the increase in slope, i.e. upward inversion, is observed at temperature about 750 °C. By composition B a dawnward inversion is observed with the maximum at 960 °C.

Fig. 4.4-8 displays the CTE curves of samples fired at 1300 °C. The trend and the position of all CTE curves is very similar to that of the curves recorded on samples fired at 1250 °C, except that at higher temperatures above around 600 °C the curves are closer to each other. A dawnward inversion is observed in curves with the maximumat at ~940 °C for B and at ~920 °C for C. The steep step or knee in CTE curve ~580 °C is not perceived in any of the curves.

The CTE curves of samples fired at 1350 °C are presented in Figure 4.4-9. The CTE curves of A and B are almost overlapping in the entire measuring range and overlapping with EN up to ~650 °C. Above ~650 °C the curves of A and B indicate higher values of CTE in compariosn to EN. The CTE curve of C is positioned below the CTE curves of A, B and EN in the entire measuring range. In curves of B and C similar dawnward inversion is observed as fired at 1300 °C with the maximum point at 960 °C for B and at 940 °C by C.

When fired at 950 °C and 1050 °C all compositions are characteristic by noticable concave upward direction of CTE curves in temperature interval 100–180 °C, indicating an abrupt expansion. By samples fired at 1150 °C and above the concavity diminishes and CTE increases gradually in entire measuring range. The abrupt expansion, which appears similarly by samples fired at 950 °C or at 1050°C, is the consequence of evaporation of absorbed water in highly porous samples, which causes the moisture expansion. Moisture expansion is characteristic for porous kaolin bodies [110]. As found by porosity determination there is only a small change in the porosity of samples fired at 950 °C or 1050 °C, which comfirms the similarity in moisture expansion of samples.

The steep step or knee noticeable in CTE curves ~580 °C is characteristic for $\alpha \rightarrow \beta$ quartz transition accomplished by volume increase [25]. The step increase in expansion depends on the amount of quartz present. The presence of quartz is observed from CTE curves by all samples fired at 950, 1050 and 1150 °C, while by EN additionally when fired at 1200 and 1250 °C. The step increase of CTE at ~580 °C, indicating the presence of quartz, is diminishing with the firing temperature increasing by all compositions, where the diminishing is enhanced by compositions with Li_2O.

Among studied compositions EN is characteristic by its noticeably higher CTE curve in comparison to CTE curves of A, B and C after firing at 950, 1050, 1150 and 1200 °C. Since studied compositions differ in flux minerals, as confirmed by XRD analyses of samples fired at these temperatures, the flux minerals mainly contribute to the differences in CTE. In all samples fired at 950 °C minerals microcline, sanidine and additionally albite in EN are identified, while at 1050 °C the phase composition is the same, but without sanidine in model compositions. The CTE of individual samples fired at 950 and 1050 °C are rather close.

The CTE of EN is affected by the presence of microcline and albite. As reported in literature, the thermal expansion of potassium feldspar in crystalline state is lower than in glassy state and lower than of sodium feldspar in crystalline state [72]. It has been also reported that CTE of pure potassium feldspar glass is $(6.6 \pm 0.5) \times 10^{-6}$ K^{-1}, when measured below its glass transition temperature of 940 ± 15 °C, and CTE of almost pure albite glass is 7.4×10^{-6} K^{-1}, when measured below its glass transition temperature of 815 °C [96]. The intensive melting of all flux minerals in temperature range 1050–1150°C, as seen in XRD patterns of EN in Fig. 4.3-1 (a), contributes to the enhancement of its CTE at 1150 °C due to higher expansion of the glassy phase formed.

The presence of low expansion Li-bearing minerals in model compositions fired at 950–1200 °C greatly contributes to their lower CTE in comparison to EN. In XRD patterns of all model compositions β-spodumene is identified at 950–1200 °C and $LiAlSi_3O_8$ at 1150 and 1200 °C. Calculated CTE (25–1000 °C) of β-spodumene and $LiAlSi_3O_8$ is 0.9×10^{-6} K^{-1} and 0.7×10^{-6} K^{-1}, respectively [85]. The enhancement of CTE of model compositions fired at 1150 °C is mainly attributed to the intensive melting of microcline in temperature range 1050–1150 °C as confirmed by XRD analyses.

The CTE of EN slightly decreases with firing temperature increasing above 1200 °C. With temperature increasing in temperature range 1200–1350 °C the phase composition of EN is characterized by the quartz diminishing and mullite forming as ascertained from from XRD analyses. Both, the amount of quartz decreasing and the amount of mullite increasing affect the CTE to decrease. The dissolution of free quartz in feldspar liquid phase contributes to lower CTE [72]. The CTE (30–1000 °C) of mullite is 4.5×10^{-6} K^{-1} [111], which additionally contributes to the decreasing of CTE of EN.

By compositions containing Li_2O the CTE of samples fired at 1250 °C slightly increases in comparison

to samples fired at 1200 °C and remains nearly unchanged by samples fired at higher temperatures. The increase of CTE is caused by the dissolution of low expansion $LiAlSi_3O_8$. At 1250 °C $LiAlSi_3O_8$ is identified only by samples C. Composition C is characteristic by considerably lower CTE when fired at 1250°C and above due to the presence of low expansion Li-minerals, such as $LiAlSi_3O_8$ at 1250 °C and $Li_xAl_xSi_{1-x}O_2$ at 1300 °C and 1350 °C. When fired at 1300 °C and 1350 °C the samples of A nad B attain similar CTE in comparison to EN, suggesting that the glassy phase of samples containing Li_2O has similar thermal expansion than the glassy phase containing Na_2O and K_2O.

Un upward inversion occurrs in CTE curves ~730 °C for samples A, B and C and ~800 °C for sample EN, when fired at 1250, 1300 and 1350 °C with the inversion for EN less expressive. This upward inversion is correlated to the abrupt increase in CTE, which is characteristic as the glass transition temperature [56,79,112]. The glass transition temperature is found to be lower for the compositions containing Li_2O, which indicates that the presence of Li_2O considerably decreases the glass transition temperature of glassy phase.

The next inversion is identified around 950 °C in CTE curves of B and C fired 1300 and 1350 °C. This inversion is correlated to the dilatometric softening temperature [79,112,113]. The dilatometric softening temperature is the temperature of zero slope in dilatometric curve. The dilatometric softening temperature is ascertained for compositions B and C, where the dilatometric softening point appears inside our measuring range with the maximum temperature of 980 °C. The dilatometric softening temperature for C is ~20 °C lower than for B, indicating that increased amount of Li_2O lowers the dilatometric softening temperature.

The CTE (30–300° C) of studied bodies, fired in temperature range 950–1350 °C, are stated in Table 4.4-3 and illustrated with graphs in Figure 4.4-10.

Table 4.4-3. CTE (30–300 °C)($\times 10^{-6}K^{-1}$) of samples EN, A, B and C fired in the temperature range 950–1350 °C.

Firing temperature (°C)	EN	A	B	C
950	3.58	3.37	3.01	3.24
1050	3.49	2.89	3.19	3.21
1150	5.05	4.57	4.40	4.33
1200	5.34	4.74	4.67	4.50
1250	5.23	5.06	5.06	4.71
1300	5.27	5.09	5.19	4.73
1350	5.11	5.15	5.04	4.68

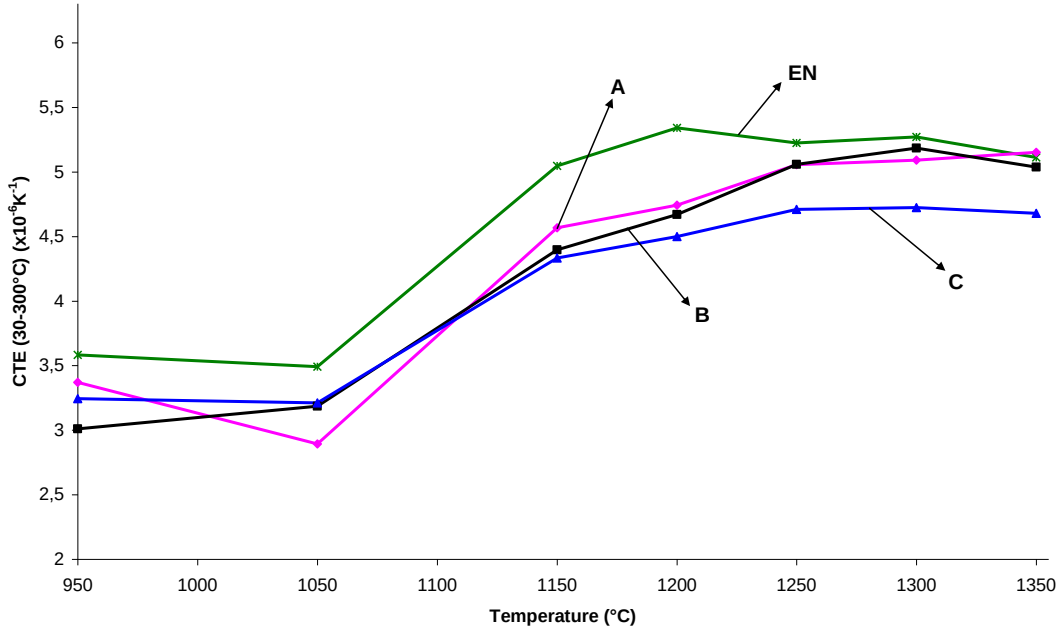

Figure 4.4-10. CTE (30–300 °C) of samples EN, A, B and C fired in the temperature range 950–1350 °C.

EN is characteristic by higher CTE (30–300 °C) in comparison to model compositions in entire firing range, except that when fired at 1350 °C its CTE (30–300 °C) is similar to that of A and B. A and B have resembling CTE (30–300 °C) in entire firing range, while C is characteristic by lower CTE (30–300 °C) when fired at 1250 °C and above. The increase in CTE (30–300 °C) is mostly perceived by all samples fired at 1150 °C. There are only small changes in CTE (30–300 °C) of all samples when fired above 1250 °C.

Considering the CTE (30–300 °C) at firing temperature, when maximum bulk density of individual composition is achieved, it is found that the addition of Li_2O in amount of 1.0 or 1.2 wt.% lowers the expansion to small extent, since the CTE (30–300 °C) of EN, A and B are very close after firing at 1300 °C, when EN, A and B attain their maximum bulk densities. Composition C attains its maximum bulk density at 1250 °C with CTE (30–300 °C) considerably lower in comparison to other compositions, indicating that the addition of 1.6 wt.% of Li_2O remarkably lowers the expansion at temperature of maximum densification.

Fired at temperature where the maximum bulk density is attained, compositions EN, A, B and C have the CTE (30–300 °C) of $5.3\times10^{-6}K^{-1}$, $5.1\times10^{-6}K^{-1}$, $5.2\times10^{-6}K^{-1}$ and $4.7\times10^{-6}K^{-1}$, respectively. It has been reported [17] that for alumina porcelains containing around 45 wt.% of Al_2O_3 the medium CTE (20–300 °C) of $5.7\times10^{-6}K^{-1}$ was determined, which confirmes that the CTE (30-300 °C) for compositions containing Li_2O is attained lower.

4.4.5 Flexural strength of fired bodies

The flexural strength of samples fired at different temperatures is listed in Table 4.4-4 and illustrated in Figure 4.4-11 with diagrams based on the average values.

Table 4.4-4. Flexural strength (MPa) of samples EN, A, B and C fired in temperature range 950–1350 °C.

Temperature (°C)	EN	A	B	C
950	18.5 ± 0.7	11.4 ± 0.8	13.7 ± 1.0	8.4 ± 0.2
1050	39.6 ± 2.0	21.2 ± 0.7	28.3 ± 1.1	30.5 ± 1.7
1150	108.9 ± 4.4	86.3 ± 4.6	83.3 ± 3.7	82.9 ± 2.8
1200	121.9 ± 6.7	108.0 ± 6.6	101.3 ± 2.9	103.1 ± 1.8
1250	164.2 ± 21.9	141.6 ± 4.9	155.3 ± 9.9	111.3 ± 14.4
1300	175.3 ± 11.2	203.2 ± 23.3	204.3 ± 21.4	127.0 ± 20.6
1350	190.1 ± 9.0	166.7 ± 11.1	158.5 ± 9.7	88.6 ± 31.7

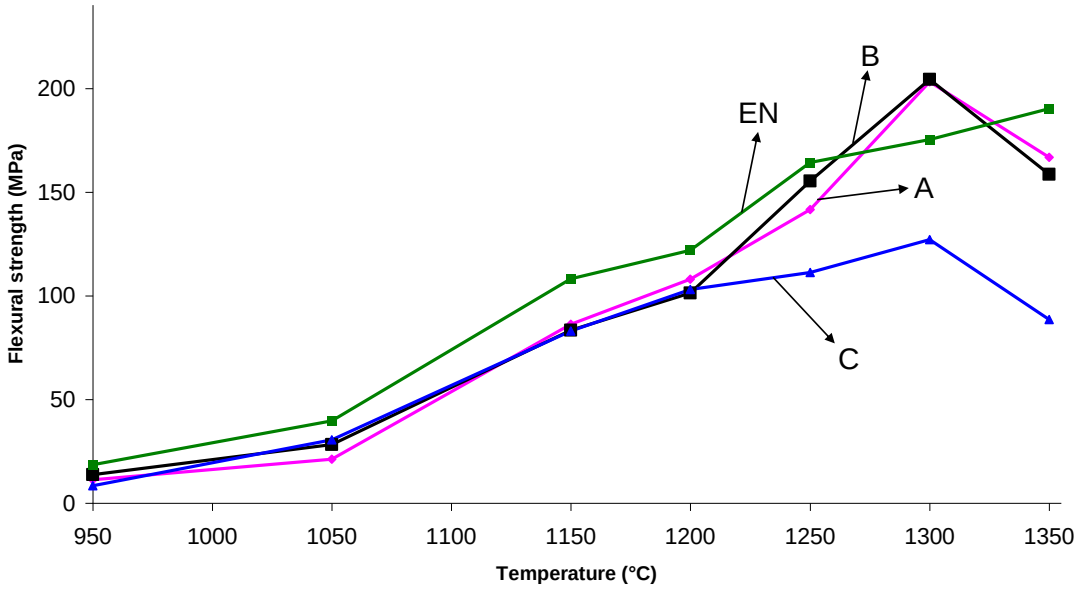

Figure 4.4-11. Flexural strength (average values) of samples EN, A, B and C fired in the temperature range 950–1350 °C.

The flexural strength of EN gradually, however irregularly, increases with temperature increasing in the entire firing range. At 950 °C the composition EN has the flexural strength of 18.5 MPa. Relatively small increase to around 39.6 MPa is determined for EN fired at 1050 °C, while a considerable gain leading to the flexural strength of 108.9 MPa is established at 1150 °C. From 1150 °C to 1200 °C the flexural strength increases to 121.9 MPa, while at 1250°C the increment is larger with the attained flexural strength of 164.2 MPa. When fired at 1300 °C the flexural strength of 175.5 MPa is determined for EN, while at 1350 °C the strength increases to 190.1 MPa. When fired from 950 to 1250 °C and at 1350 °C EN has higher flexural strength than model compositions, while lower than A and B when fired at 1300 °C.

Composition A experiences a progressive, however irregular, increase in the firing range up to 1300 °C, followed by a decrease at 1350 °C. As fired at 950 °C the composition A has the flexural strength of 11.4 MPa, which slightly increases to 21.1 MPa after firing at 1050 °C. Considerable increase, comparable with that of EN, is recorded in the flexural strength after firing at 1150 °C, when the flexural strength of 86.3 MPa is determined. At 1200 °C the flexural strength increases to 108.1 MPa, while a larger increase is recorded after firing at 1250 °C with the flexural strength of 141.6 MPa. Up to 1250 °C the flexural strength of A increases in a very similar way, but at lower values, in comparison to that of EN. In the temperature range 1250 to 1300 °C the flexural strength of A sharply increases. After firing at 1300 °C the maximum flexural strength of 203.2 MPa for A is ascertained. The flexural strength of A considerably decreases to 166.7 MPa after heating to 1350 °C.

The flexural strength of B increases with the increasing temperature comparable to A in the entire firing range. Actually, the values of flexural strength are very close to those of A at 950, 1050, 1150, 1200, 1300 and 1350 °C, where the differences are less than 10 MPa. However, at 1250 °C the flexural strength of B is 155.3 MPa, which is about 14 MPa higher in comparison to A. The maximum flexural strength of B is 204.3 MPa, which is almost equivalent to the maximum flexural strength of A. The decrement of flexural strength after firing at 1350 °C is higher for B in comparison to A.

The flexural strength of C is similar to that of A and B when fired in temperature range 950–1200 °C, while considerably lower for samples fired above 1200 °C. In temperature range from 1200 to 1300 °C the flexural strength of C increases rather slowly, being 103.1 MPa at 1200 °C, 111.3 MPa at 1250 °C and 127.0 MPa at 1300 °C. The maximum flexural strength as determined for C, which is 127 MPa attained at 1300 °C, is substantially lower in comparison to that of EN, A and B. A decrement in the flexural strength after firing at 1350°C is proportional to that ascertained for A.

After firing at 950 °C EN experiences the highest flexural strength among the studied compositions,

which is in agreement with its minimum apparent porosity. Among compositions A, B and C, which have similar open porosity at 950 °C, the lowest flexural strength is determined for C, which might be correlated to the higher amount of relatively large flux grains in C. The flexural strength of all bodies fired at 950 °C is relatively low regarding their green flexural strength, which is around 7 MPa by all compositions as determined on green samples.

For all bodies fired at 1050 °C the enlargement of flexural strength is relatively small in comparison to the flexural strength of bodies fired at 950 °C. The gain in strength is connected to the open pore closing and the structure thickening at 1050 °C as confirmed by SEM images where closer particle compaction and melting of cleaved particles is observed. The enhancement of strength for all bodies fired at 1150−1250 °C is in coincidence with intensive melt formation and open porosity diminishing in this temperature range. Fired at 1300 °C the compositions containing 1.0 and 1.2 wt.% of Li_2O are characteristic by improved flexural strength in comparison to reference composition. By Li_2O-containing compositions the closed porosity noticeably increases at 1350 °C, as obvious from corresponding SEM images, thus contributing to the reduction of strength at 1350 °C.

Corundum as the main constituent dominately contributes to the mechanical strength of all studied compositions. Filler, such as corundum, is a key component of porcelain influencing the mechanical properties of the final body [5]. Fracture resistant fine grained corundum contributes to the strengthening and the toughening of the body on microstructural level [35].

The introduction of Li_2O lowers the temperature at which the maximum strength in high alumina porcelain is attained. All compositions containing Li_2O achieve their highest mechanical strength at 1300 °C, while reference composition EN at 1350 °C or even higher. When fired at 1300 °C, compositions containing 1.0 and 1.2 wt.% of Li_2O attain higher mechanical strength than EN fired at 1300 °C or at 1350 °C. In samples of EN fired at 1300 and 1350 °C more quartz is present in comparison to Li_2O- containing compositions, as perceived from the intensity of quartz peak in XRD spectra of corresponding samples. The presence of quartz negatively influences the mechanical strength [35]. Smaller amount of quartz present in Li_2O-containing compositions than in EN, as identified from the intensity of quartz peaks in corresponding XRD spectra, contributes to improved mechanical strength. Large quartz grains negatively affect the strength of porcelain body, since they cause cracks in the vitreous phase [26]. Reversible quartz inversion from β to α at 573 °C during cooling process, accomplished with volume decrease, is responsible for the deterioration in mechanical properties of the body [18]. In compositions with 1.0 and 1.2 wt.% of Li_2O the more intensive quartz dissolution and its reaction with β-spodumene contributes to higher flexural strength.

It is perceived from the intensity of mullite peaks in XRD spectra of compositions fired at 1300 °C and 1350 °C that composition C is characteristic by the lowest amount of mullite. The lower amount of mullite in comparison to other compositions partially negatively affects the mechanical strength of C. According to the mulllite theory, it has been claimed that the porcelain strength solely depends on the interlocking of fine mullite needles [1]. The mullite content is obviously favoured by increasing the clay content, but it is not the main factor for the mechanical strength improvement [103].

The higher flexural strength of A and B in comparison to EN at 1300 °C may be partially attributed to the lower thermal expansion of glassy phases of A and B, containing Li_2O, since for A and B slightly lower CTE was determined at this temperature. It was ascertained, that the mechanical strength of porcelain is mainly influenced by the prestresses induced between the glassy matrix with lower and the crystalline material with higher thermal expansion [57]. On the other hand, at 1300 °C composition C achieves its maximum flexural strength, which is remarkably lower in comparison to all the other compositions. The lower strength of C might be partially ascribed to the presence of low expansion lithium aluminosilicate crystalline phase as identified in XRD spectra. The strength reduction of porcelain body is enhanced by the presence of flaws and inhomogeneities consisting of grains with the thermal expansion lower than that of the body [57].

The microstructure of the compositions with 1.0 and and 1.2 wt.% of Li_2O appears more uniform regarding the pore size, the pore distribution and the glassy phase distribution in comparison to EN, as noticeable from corresponding SEM images, thus contributing to the strength enhancement. It was found, that better homogeneity of the glassy matrix provides higher strength [26,57].

After firing at 1350 °C, the flexural strength of Li_2O-containing compositions remarkably decreases. Due to the bloating phenomena an increase in closed pores negatively affects the elastic modulus and strength [58]. The decrement of flexural strength is influenced by the bloating phenomena of A, B and C as notified in the corresponding sintering curves and due to the bulk density increment at 1350 °C.

4.5 Testing of Li_2O-bearing compositions under industrial conditions

Samples of compositions A, B and C used for the firing under industrial conditions, i.e. in the gas kiln, were prepared by the same procedure as samples fired in the laboratory furnace. Firing in the gas kiln differentiates from that in the laboratory furnace mainly in the atmosphere conditions, the soaking time at the maximum temperature and the rate of cooling process. While in the laboratory furnace the samples are heated in air, in the gas kiln the samples are first heated in oxidation atmosphere up to around 1100 °C followed by reduction atmosphere up to the maximum firing temperature of 1315 °C. The soaking time of 60 min in an industrial kiln is longer in comparison to the soaking time of 15 min in the laboratory furnace. In the industrial kiln the contolled cooling process with duration of four hours and a half promoted by the controlled ventilation of cool air is faster than the cooling rate in the laboratory furnace where the cooling process runs under natural rate for the laboratory furnace.

4.5.1 Phase composition and microstructure of bodies fired in the gas kiln

The phase composition of samples A, B and C fired in the gas kiln was studied from the corresponding XRD patters recorded on powdered samples.

In Figure 4.5-1 the XRD pattern of A fired in the gas kiln is presented. Identified minerals are corundum and mullite with corundum present as the main phase. The XRD pattern of B fired in the gas kiln is shown in Figure 4.5-2, where corundum and mullite are identified. The XRD pattern of B is very similar to XRD pattern of A with about the same amount of mullite. In Figure 4.4-3 the XRD pattern of C fired in the gas kiln is presented. Additionally to corundum and mullite lithium aluminium silicate is identified for C. The mullite peak intensity for C is lower than that for A nad B.

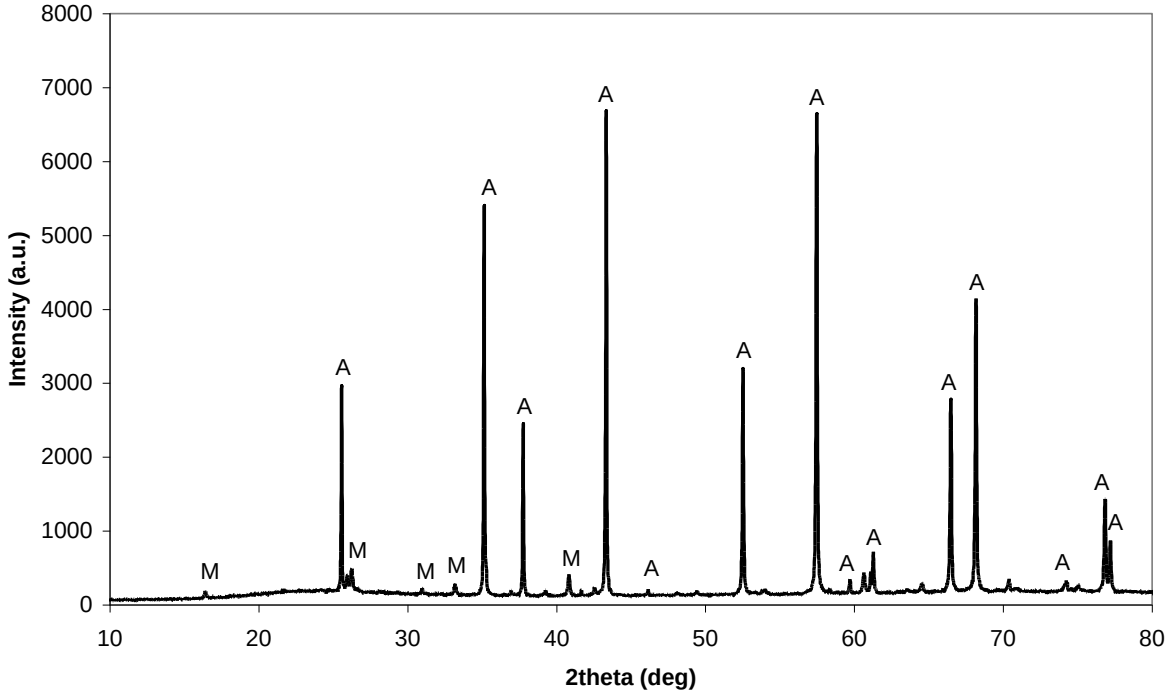

Figure 4.5-1. XRD pattern of sample A fired in the gas kiln. Revealed minerals are A – corundum and M – mullite.

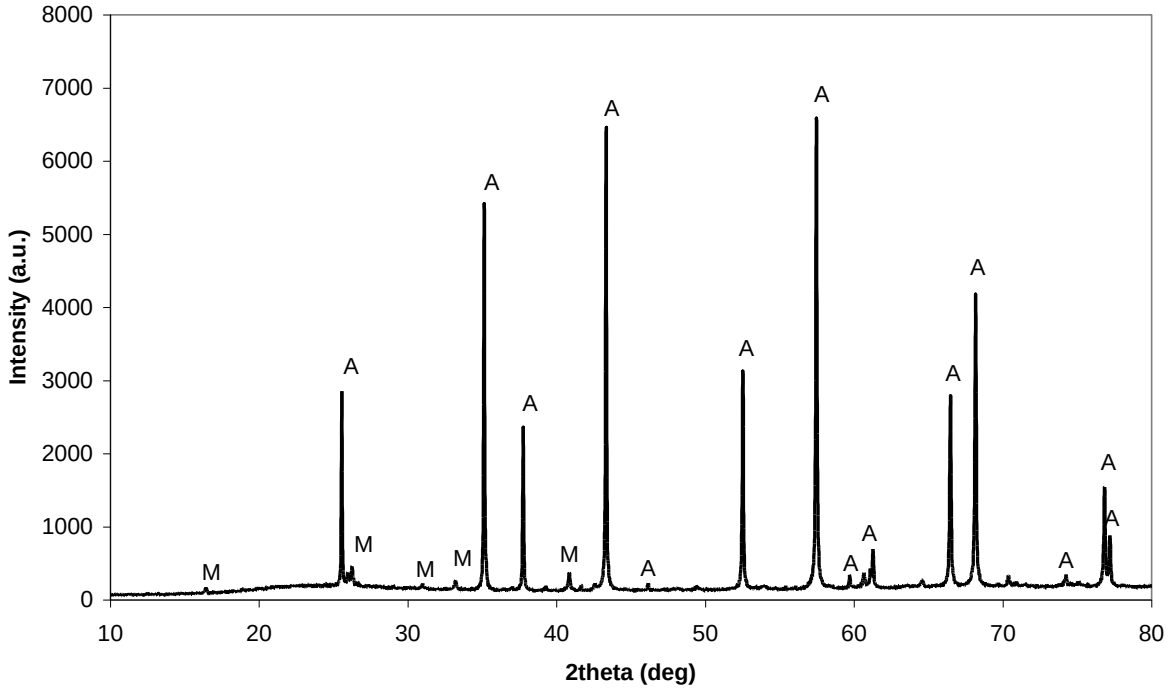

Figure 4.5-2. XRD pattern of sample B fired in the gas kiln. Revealed minerals are A – corundum and M – mullite.

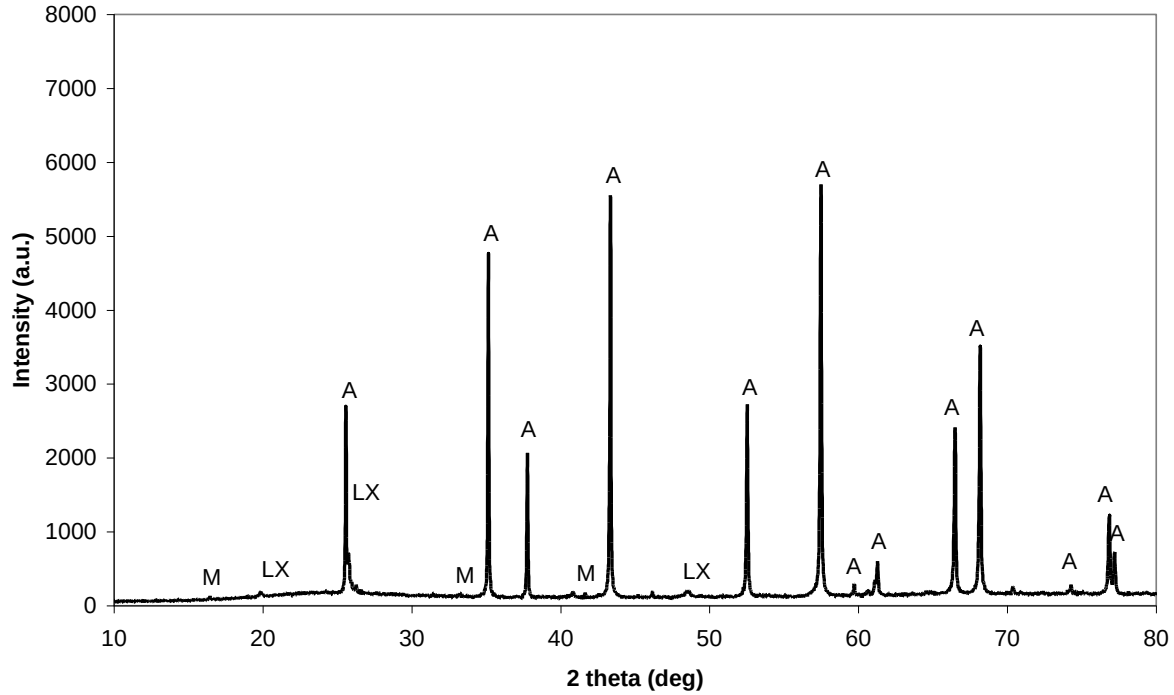

Figure 4.5-3. XRD pattern of sample C fired in the gas kiln. Revealed minerals are A – corundum, M – mullite and LX – lithium aluminium silicate ($Li_xAl_xSi_{1-x}O_2$)

All compositions contain corundum and mullite. The same mineralogical composition is identified for A and B, consisting of corundum and mullite, while in composition C lithium aluminium silicate ($Li_xAl_xSi_{1-x}O_2$) is additionally identified. In compositions A and B all of the lithium is present in the glassy phase indicating the dissolution of lithium minerals. In composition C the lithium aluminium silicate is formed due to greater amount of lithium in C, which is sufficient for the lithium aluminium silicate formation.

After firing in the gas kiln samples B and C have the same phase composition as after firing in the laboratory furnace at 1350 °C, while for A additionally α-quartz is identified in the laboratory furnace at 1350 °C. Besides, fired in the laboratory furnace at 1300 and 1350 °C composition C has the same phase composition, consisting of mullite, corundum and lithium aluminium silicate ($Li_xAl_xSi_{1-x}O_2$), as when fired the gas kiln.

No significant differences in the intensity of mullite peaks are detected between compositions A and B, where the amount of Li_2O is 1.0 and 1.2 wt.%, respectively. However, the mullite peak is clearly degenerated for composition C, which contains 1.6 wt.% Li_2O. When Li_2O is present in the amount 1.6 wt.% it retards the growth of mullite in alumina porcelain body. Similar findings of the influence of Li_2O-content on the mullite growth are reported in literature for quartz porcelain body. Talyaganov *et al.* [93] ascertained that the presence of lithium causes significant changes in the crystalline phases formed in the triaxial porcelain body fired at 1300 °C. They demonstrated that the amount of Li_2O added in quartz porcelain body greatly affects the mullite formation. They found that at firing temperature 1300 °C the mullite peak was intense when the quantity of Li_2O was 0.44 or 0.88 wt.%, while at higher Li_2O contents, i.e. 1.32 and 1.92 wt.%, the mullite peak significantly degenerated.

The microstructure of cross sectioned samples of model compositions A, B and C fired under industrial conditions was first observed with optical microscope.

The optical microscope image of composition A fired in the gas kiln is shown in Figure 4.5-4. Closed pores below ~30 μm, corundum grains and glassy phase are perceived. Figure 4.5-5 presents the optical microscope image of composition B fired in the gas kiln. The distribution of corundum grains in glassy phase with closed pores below ~30 μm is similar to that of A. The pore size and the pore distribution is resembled by compositions A and B. Near spherical disconnected pores are uniformly distributed among corundum grains in the glassy matrix of composition A and B. The amount of small pores below ~10 μm is perceived lower for composition B. In Figure 4.5-6 the optical microscope image of composition C fired in the gas kiln is shown. Corundum grains distributed in the glassy phase with closed pores below ~50 μm are perceived. In comparison to A and B the amount of pores below ~10 μm is smaller, while larger pores are formed in C.

It is seen from the optical microscope images of A, B and C fired in the gas kiln that the pores are approaching the spherical shape with pores most nearly spherical in C. The microstructure for all the samples is characteristic by irregular distribution of pores, which are different in size. The closed pores and their spherical character indicate that firing in the gas kiln leads to the compact microstructure with disconnected rounded pores for all the compositions. The spherical pores are characteristic for mature structure [41]. The spherical pores result when a sort of equilibrium is reached between the vapor pressure of gas and the viscosity of the liquid phase. Porcelain body with spherical pores shows higher bending strength than porcelain body with elongated pores [26].

The degree of pore coarsening is clearly enhanced by C, where the size of large pores is greater than in A and B and the amount of small pores below ~10 μm is abviously smaller. The amount of small pores is decreasing with more Li_2O added. It is evident that increasing the amount of Li_2O contributes to more intense pore coarsening.

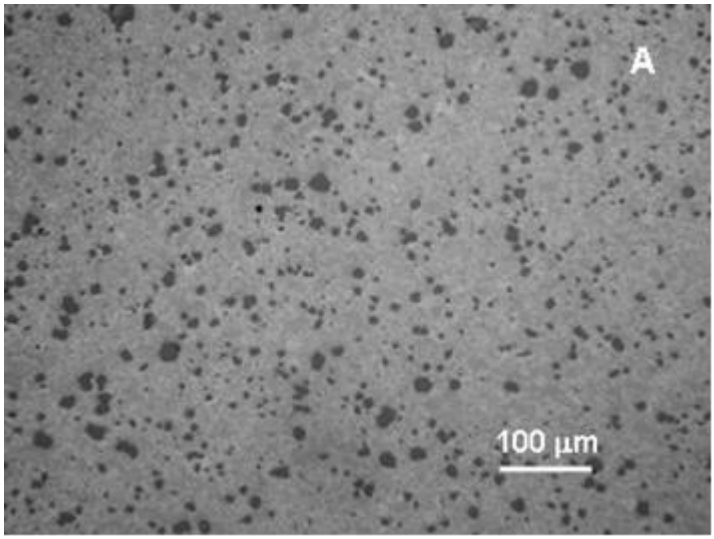

Figure 4.5-4. Optical microscope image of sample A fired in the gas kiln.

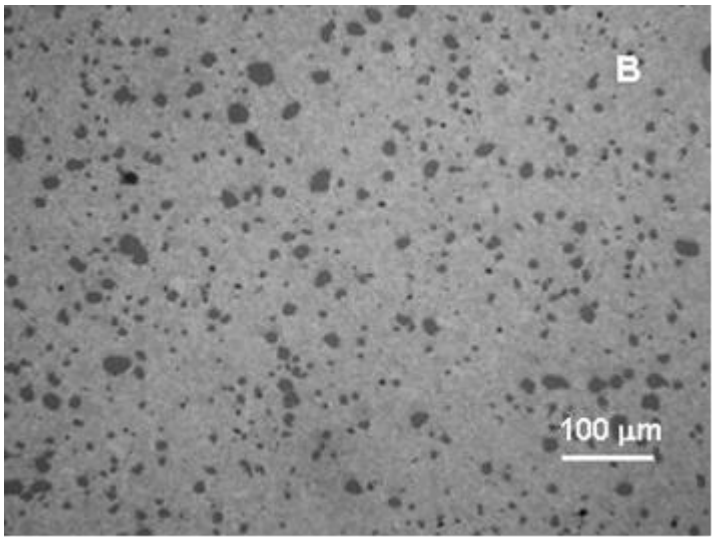

Figure 4.5-5. Optical microscope image of sample B fired in the gas kiln.

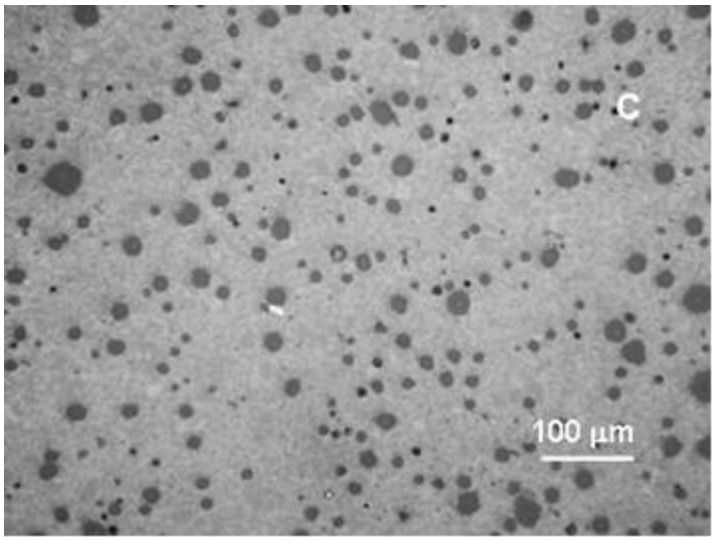

Figure 4.5-6. Optical microscope image of sample C fired in the gas kiln.

The microstructure investigated by SEM was studied from SEM/SE images of un-etched and etched cross-sectioned samples of A, B and C fired in the gas kiln. Each figure of SEM studies is comprised of the two SEM/SE images recorded on un-eched (a, b) samples and the two SEM/SE images recorded on etched (c, d) samples.

In Figure 4.5-7 the SEM/SE micrographs of A fired in the gas kiln are shown. In images (a) and (b) corundum grains embedded in the glassy matrix are the prevailing crystalline phase observed. Corundum grains in form of flakes and spherical disconnected pores are dispersed in the glasy matrix. The size of corundum grains is below ~20 μm. The major part of corundum grains is below 10 μm. Corundum grains are embedded in the glassy matrix in form of homogeniously dispersed clusters surrouned by the glassy phase regions appearing as glassy ″puddles″ of dissolved constituets. Closed pores in size below ~30 μm are nearly spherical. The pores are surrounded by both, the glassy phase and the corundum grains.

In the etched samples, as seen from images (c) and (d), corundum and mullite grains embedded in the glassy matrix with disconnected pores are observed. Mullite grains visible in the glassy matrix appear distinguishable as needle shaped grains (secondary mullite) or as scaly shaped grains (primary mullite). The needle shaped grains are larger than the scaly shaped grains. The scaly shaped mullite grains are grouped into the clusters. Both, the needle and the scaly shaped mullite grains are non-uniformly dispersed in the glassy matrix. Cracks are identified in the glassy phase, as seen in the image (d).

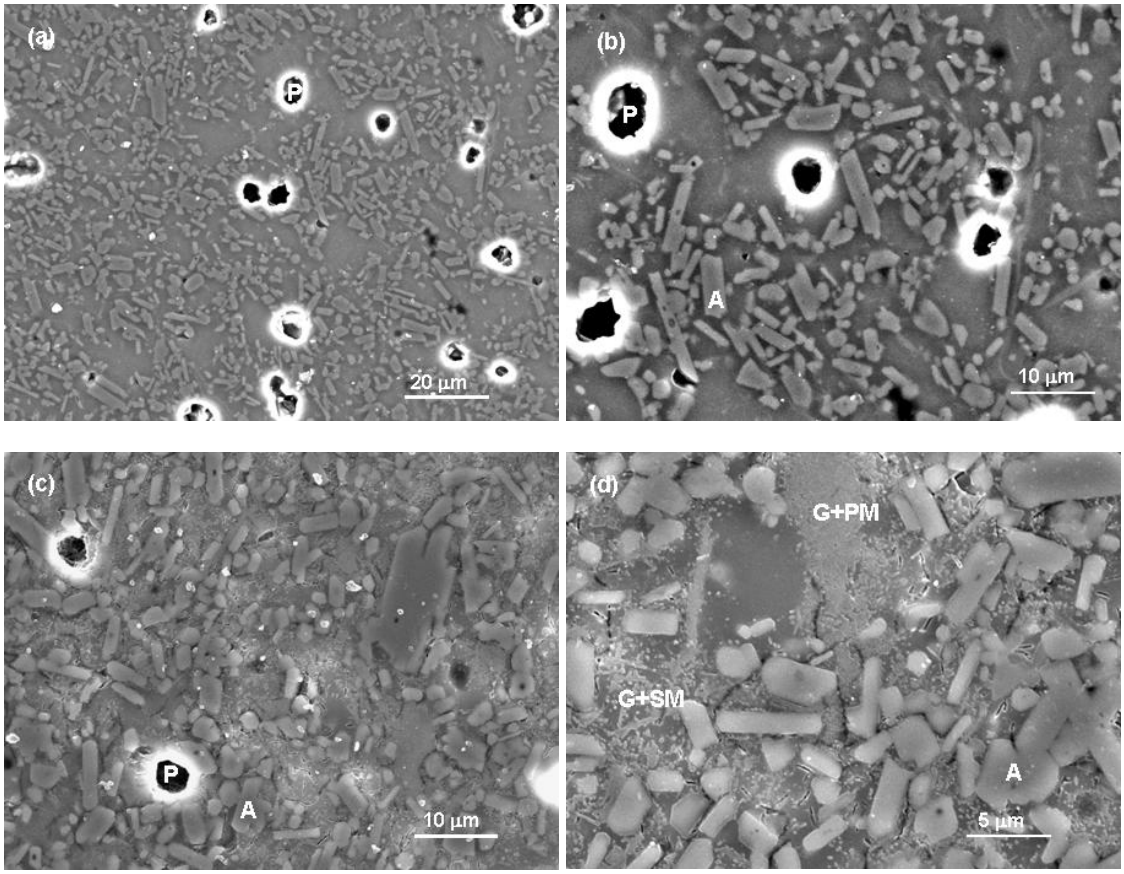

Figure 4.5-7. SEM/SE images of sample A fired in the gas kiln, (a) and (b) un-etched, (c) and (d) etched in 3 wt.% HF for 60 sec. A - corundum grains, P - pore, G+PM - primary mullite grains grown from clay relicts in the glassy phase, G+SM - secondary mullite needles grown from feldspar relicts in the glassy phase.

SEM/SE micrographs of B fired in the gas kiln are presented in Figure 4.5-8. As seen from the images (a), (b) and (c) the microstructure of B shows great similarity to the microstructure of A regarding the size and the shape of corundum grains, the size of pores, and the appearance of mullite grains, all distributed in the glassy matrix. The corundum grains distribution in B appears more uniform than in A as noticeable evidently from the image (d) due to more separated corundum grains. Both, the needle and the smaller scaly shaped mullite grains are non-uniformly dispersed in the glassy matrix as seen in the image (d). Like in A, cracks are present in the glassy phase of B as seen in the image (d).

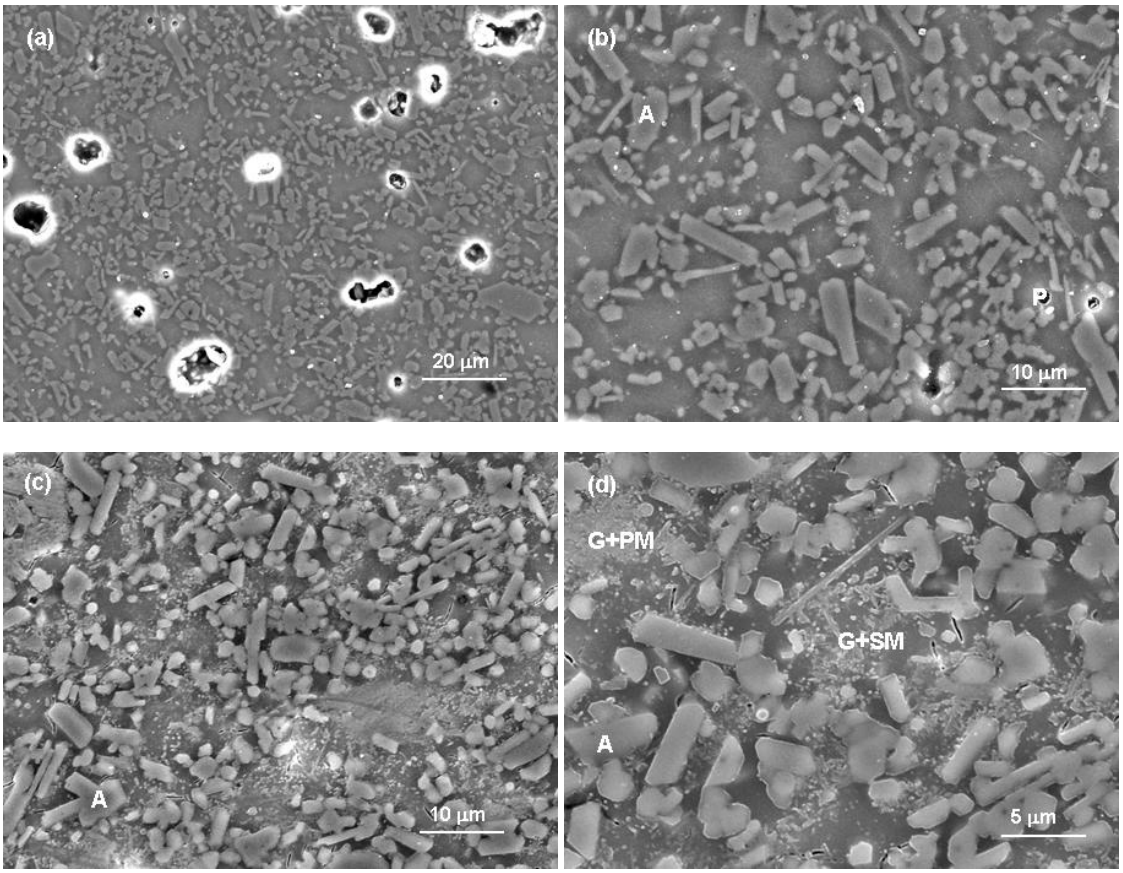

Figure 4.5-8. SEM/SE images of sample B fired in the gas kiln, (a) and (b) un-etched, (c) and (d) etched in 3 wt.% HF for 60 sec. A - corundum grains, P - pore, G+PM - primary mullite grains grown from clay relicts in glassy phase, G+SM - secondary mullite needles grown from feldspar relicts in glassy phase.

In Figure 4.5.-9 SEM/SE micrographs of C fired in the gas kiln are presented. Large pores ~50 μm are visible in image (a). The corundum grains are similar in size and shape to the corundum grains in A and B, while the agglomerates of corundum grains are more compact. As seen from images (b), (c) and (d) the glassy phase regions or glassy ″puddles″ are larger and more non-uniformly dispersed in comparison to the glassy phase distribution in A and B. A smalller amount of mullite grains is observed in comparison to the amount of mullite grains in A and B as obvious from images (c) and (d). In image (d) the glassy phase regions containing only the needle shaped mullite are observed. Cracks similar to those in A and B are observed in the glassy phase of C as obvious from image (d).

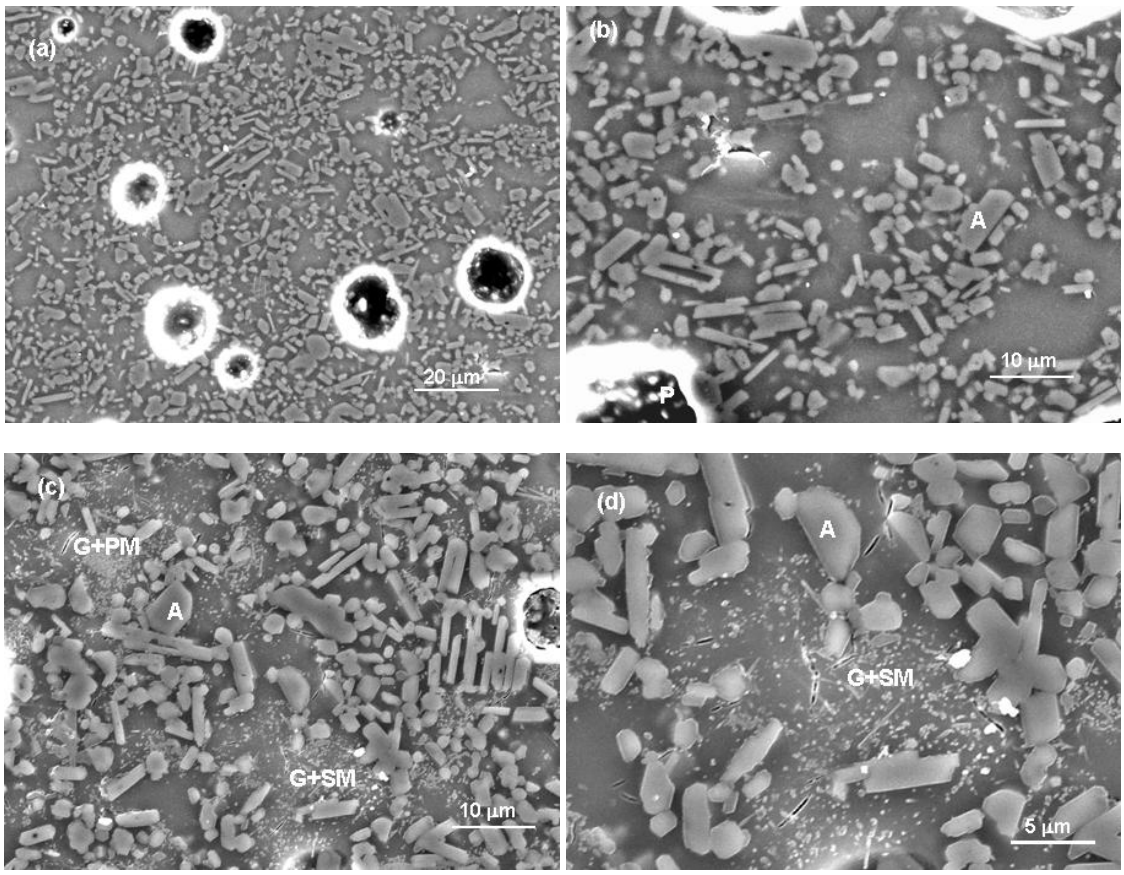

Figure 4.5-9. SEM/SE images of sample C fired in the gas kiln, (a) and (b) un-etched, (c) and (d) etched in 3 wt.% HF for 60 sec. A - corundum grains, P - pore, G+PM - primary mullite grains grown from clay relicts in glassy phase G+SM – secondary mullite needles grown from feldspar relicts in glassy phase.

It is seen from SEM/SE images of samples A, B and C fired under industrial conditions that corundum grains embedded in the glassy matrix are of comparable size and shape in all the compositions. Corundum grains are distributed in the glassy phase as grouped in agglomerates. The microstructure of compositions A and B is similar, regarding the pore size, the glassy phase distribution, the corundum grains distribution and the mullite grains distribution. Regarding the distribution of corundum and mullite grains the microstructure of C is less homogenous than that of A and B. The corundum and the mullite grains are most homogenously dispersed in B.

Mullite grains are observed in the etched samples of A, B and C. Mullite grains visible in the glassy matrix appear distinguishable regarding as primary and secondary mullite. In A, B and C the mullite grains are visible as agglomerates of small grains embedded in the glassy phase, recognized as primary mullite, or as needle shaped grains of larger size distributed in the glassy phase, recognized as secondary mullite. Primary and secondary mulllite are irregularly dispersed in the glassy matrix. The amount of mullite grains is considerably lower in composition C, which is confirmed also from the XRD identification, where the mullite peak is noticeably diminished for C.

The irregular distribution of primary and secondary mullite in the glassy matrix of samples A, B and C is characteristic for porcelain bodies. It has been previously established that different mullite morphologies derived in different regions of microstructure indicate the heterogeneity of the liquids from which they originate [7]. The size and the development of crystals from clay or feldspar are different. Primary mullite forms directly from the clay decomposition and is characteristic by its fine, cuboidal or scaly morphology, while secondary mullite with the acicular morphology arises from the feldspar melt as it reacts with the clay. The pure clay regions are more silica-rich and more viscous forming smaller, cuboidal primary mullite. The feldspar-rich flux region with high alkali content is less viscous leading to the formation of acicular secondary mullite. [10]. The clay relicts with cuboidal primary mullite are identified in the compositions A and B, while less perceived in composition C. In composition C the amount of both, secondary and primary mullite, is found to be lower in comparison to that in A and B. The lower amount of primary mullite in the composition C might be correlated to the lower amount of clay constituets in raw body of C, while the lower amount of secondary mullite might be correlated to the presence of lithium

aluminium silicate phase, which migh retard the mullite growth.

In glassy phase of A, B and C elongated cracks like pores are identified in the etched samples. They could appear do to stresses in the glassy phase or the etched secondary phase soluble in HF.

4.5.2 Physical properties of bodies fired in the gas kiln

4.5.2.1 Bulk density of bodies fired in the gas kiln

Table 4.5-1. Bulk density of samples A, B and C fired in the gas kiln.

Composition	Bulk density (g/cm^3)
A	2.85
B	2.91
C	2.74

The bulk density of the compositions A, B and C after firing in the industrial kiln is stated in Table 4.5-1. The maximum bulk density is determined for the composition B with the value of 2.91 g/cm^3. Composition A attains lower bulk density of 2.85 g/cm^3, while for composition C the lowest bulk density of 2.74 g/cm^3 is determined. Both compositions, A and B, attain higher bulk densities after firing in the gas kiln in comparison to the highest bulk densities attained in the laboratory furnace. In the laboratory furnace the highest bulk density of 2.80 g/cm^3 for A and 2.82 g/cm^3 for B is determined after firing at 1300 °C. The highest bulk density for B is in agreement with the conclusions of optical microscope observations, where the microctructure of B, as shown in Figure 4.5.-5, is found to be the most compact with closed pores below ~30 μm and the smallest amount of closed pores below ~10 μm.

The lower bulk density is attained for the composition C after firing in the gas kiln in comparison to its maximum bulk density of 2.82 g/cm^3 as determined after firing in the laboratory furnace at 1250 °C. The firing conditions in the gas kiln caused the overfiring of C resulting in a decrease of the bulk density. The overfiring is identified as closed pore enlargement in C. The coarsening of closed pores is a common process accompanying the overfiring [6]. The pore enlargement in C is obvious from the optical microscope images in Figure 4.5-6, where larger pores than in A and B are identified with the size up to ~50 μm. Due to the bloating of pores the bulk density for C is decreased. The firing temperature in the gas kiln was too high for composition C.

4.5.2.2 Open porosity of bodies fired in the gas kiln

Table 4.5-2. Open porosity of samples A, B and C fired in the gas kiln.

Composition	Open porosity (vol. %)
A	0.0
B	0.0
C	0.0

In Table 4.5-2 the open porosity measurments of samples A, B and C fired in the gas kiln are presented. For all the compositions zero open porosity is determined.

The open porosity elimination during the vitrification process in the gas kiln is comfirmed also with optical microscope and SEM observations, where separated closed pores distributed in the glassy phase with grains of corundum and additionally mullite are observed.

4.5.2.3 Thermal properties of bodies fired in the gas kiln

4.5.2.3.1 Thermal expansion of bodies fired in the gas kiln

Thermal expansion of samples fired under industrial conditions is studied from CTE curves derived from expansion data recorded by dilatometer in temperature range 30–980 °C.

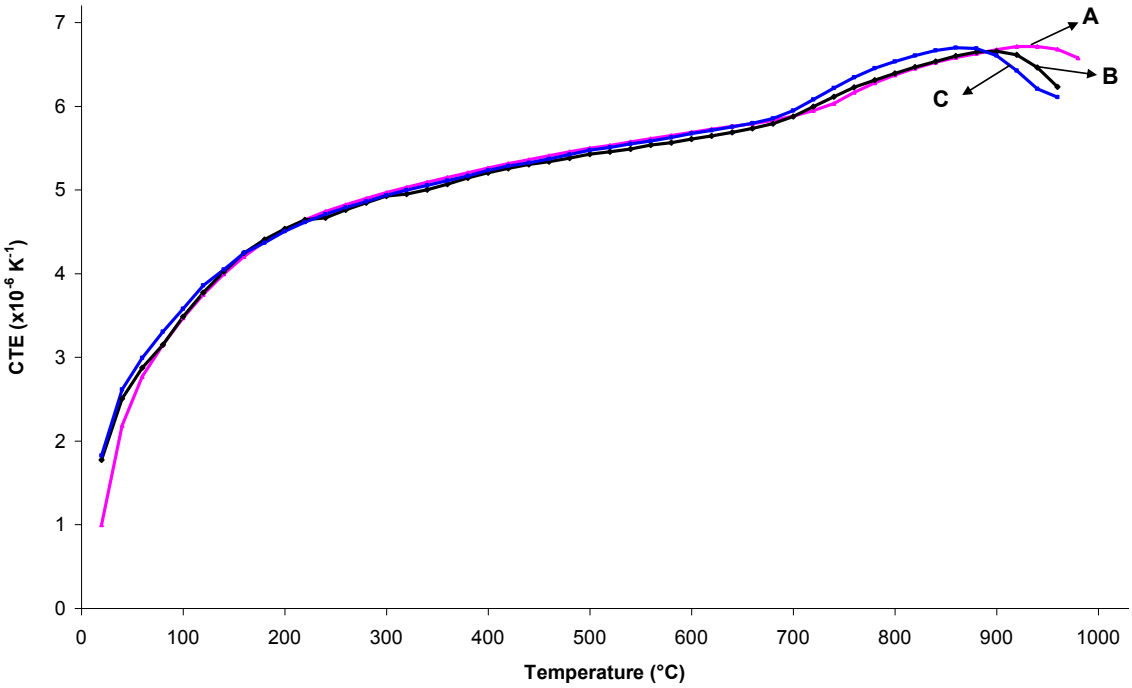

Figure 4.5-10. CTE curves of samples A, B and C fired in the gas kiln.

In Figure 4.5-10 the CTE curves of samples A, B and C fired in the gas kiln are shown. The trend of the CTE curves of samples A, B and C is very similar up to around 700 °C with curves nearly overlapping. The thermal expansion behavoir is fairly linear, with no knee around 580 °C characteristic for $\alpha \rightarrow \beta$ quartz inversion. The upward inversion of the CTE curves is noticeable above 700 °C with the intersection point of the corresponding regression lines around 710 °C for samples A, B and C. The maximum expansion point, indicating also the temperature of the curve dawnward inversion, is reached around 940 °C for sample A, around 920 °C for sample B and around 880 °C for sample C.

Table 4.5-3. CTE(30–300 °C) and CTE (30–600 °C) of samples A, B and C fired in the gas kiln.

Composition	CTE (30–300 °C) ($\times 10^{-6} K^{-1}$)	CTE (30–600 °C) ($\times 10^{-6} K^{-1}$)
A	4.97	5.69
B	4.83	5.57
C	4.86	5.63

The measured values of the CTE (30–300° C) and the CTE (30–600° C) of samples fired in the gas kiln are stated in Table 4.5-3. There are very small differences among the model compositions in the CTE(30–300 °C) or in the CTE (30–600 °C). The CTE(30–600 °C) is around $5.6 \times 10^{-6} K^{-1}$ for all the compositions, which is about $0.7 \times 10^{-6} K^{-1}$ higher than the CTE(30–300 °C).

After firing in the gas kiln the CTE(30–300 °C) is $0.12 \times 10^{-6} K^{-1}$ for A and $0.36 \times 10^{-6} K^{-1}$ for B lower, while $0.13 \times 10^{-6} K^{-1}$ for C higher, as when fired in the laboratory furnace at 1300 °C. Similar differences are ascertained comparing the CTE (30–300 °C) of samples fired in the gas kiln with the samples fired in the laboratory furnace at 1350 °C, since after firing in the gas kiln the CTE(30–300 °C) is $0.18 \times 10^{-6} K^{-1}$ for A

and $0.21\times10^{-6}K^{-1}$ for B lower, while $0.18\times10^{-6}K^{-1}$ for C higher, as when fired in the laboratory furnace at 1350 °C. Comparing the CTE(30–300 °C) attained after firing under industrial conditions with the CTE(30–300 °C) after firing in the laboratory furnace at 1300 °C and at 1350 °C, it is seen that they are very close.

The glass transition temperature is found to be very close for all the samples, indicating that increasing the amount of Li_2O from 1.0 to 1.6 wt.% has no profound affect on the glass transition temperature after firing in the gas kiln, similarly as prior ascertained for samples fired in laboratory furnace at 1300 and 1350 °C. However, it was determined that the glass transition temperature of samples fired in the gas kiln is ~20 °C lower in comparison to samples fired in the laboratory furnace at 1300 and 1350 °C.

The dilatometric softening point, which is ~940 °C for A, ~920 °C for B and ~880 °C for C, is decreasing with the increasing amount of Li_2O in the samples fired in the gas kiln. The dilatometric softening point is observed for all the compositions fired in the gas kiln, while in the laboratory furnace it is observed only for B and C. The dilatometric softening temperature after firing in the gas kiln is found to be around 20 °C lower for B and around 60 °C lower for C in comparison to the firing in the laboratory furnace at 1350 °C.

4.5.2.3.2 Deformation during firing of bodies fired in the gas kiln

Deformation during firing or pyroplastic deformation is an important criterion to define the industrial application of the newly developed ceramic composition which is intended to be fired under existent firing conditions in the gas kiln. The applied method for studying the deformation during firing is adapted from an industrial experience.

Table 4.5-4. Deformation during firing of samples A, B and C fired in the gas kiln.

Composition	Deformation during firing (mm)
A	13.8
B	21.8
C	>30

The declination of the samples A, B and C from horizontal position during firing in the gas kiln is specified in Table 4.5-4. Deformation during firing is the lowest for composition A. For the samples B a considerable increase in the deformation during firing is determined. The deformation during firing for samples C is the highest being too high to keep the samples on supports, since samples fell off supports during firing.

It is seen from the results of the deformation during firing test that the increasing amount of Li_2O added greatly affects the deformation of bodies. This is evident while comparing the deformation of A and B. The deformation of B is increased by 8 mm, while the amount of Li_2O in B is only 0.2 wt.% higher. The deformation of composition C could not be normally measured, because the test bars fell off supports during firing. The deformation of composition A with 1.0 wt% of Li_2O is most favorable for industrial application with the firing treatment as used in this trial. The ascertained influence of the amount of Li_2O on the deformation during firing for alumina porcelain can be compared with similar findings of Talyaganov *et al.* [93], who demonstrated that porcelain bodies with remarkable resistance to pyroplastic deformation were developed by the presence of 0.5 or 0.9 wt.% of Li_2O.

As established with the industrial trial composition A is less prone to deformation during firing in comparison to B and C due to more favorable viscosity of liquid phase in A. It was established by Villegas-Palacio and Dinger [114] that the high deformation resistance during firing of the quartz porcelain body is attributed to the stability of viscosity of the liquid phase in temperature range above 1150 °C up to the maturation temperature. Besides, they ascertained that the deformation during firing is lowered with the increased amount of homogeniously dispersed crystalline phases, such as quartz and mullite. In our alumina porcelain bodies corundum and mullite are identified by XRD as crystalline phases, while in C additionally lithium aluminium silicate is present. In compositions A and B the amount of corundum and mullite are very close. Therefore, the presence of more viscous liquid phase, formed by the heating conditions in the gas kiln, should mainly contribute to the lower pyroplastic deformation for A.

Besides the viscosity of liquid phase the pyroplastic deformation is affected by the amount of liquid

phase present [114]. The amount of liquid phase in A is most proper for the firing under conditions in gas kiln in comparison to B and C with higher amounts of flux minerals.

In order to lower the pyroplastic deformation the firing treatment for compositions B and C should be corrected to lower optimum temperatures regarding the results from microstructure investigations carried out in the laboratory furnace. The requirement for sufficient vitrification and low pyroplastic deformation is one of the main compromises in the design of firing schedule for triaxial porcelain body [8]. Longer schedules are favorable for vitrification, while shorter schedules advantage less pyroplastic deformation. A viscous silicate liquid formed during firing process serves as a bond for the body [6]. Proper amount and viscosity of liquid phase assure satisfactory firing in a reasonable time without the ware slumping or warping under the force of gravity. The temperature and composition suitable for satisfactory firing is determined by the relative and absolute rate of deformation and shrinkage process.

4.5.2.3.3 Thermal shock resistance of bodies fired in the gas kiln

Samples for the thermal shock testing with extruded legth of 150 mm were fired in the gas kiln as hung on the refractory supports. After firing they were cross-sectioned on both sides to the length of 120 mm before the thermal shock testing.

After water quenching the cracks appear in two of the five samples at ΔT = 200 K for all the compositions. This indicates that equal thermal shock resistance of 200 K is determined for compositions A, B and C after firing under industrial conditions. To identify the influence of thermal shock on mechanical properties of individual composition the drop of flexural strength was established by measuring the flexural strength on the samples with and without cracks after the thermal shock testing.

Table 4.5-5. Flexural strength (MPa) of individual test bar of samples A, B and C after thermal shock test ΔT = 200K.

Description	Flexural strength (MPa)		
of the sample	A	B	C
no cracks	230.0	262.3	210.1
no cracks	241.4	224.1	170.0
no cracks	195.8	219.0	203.2
cracks	29.6	165.5	27.1
cracks	15.9	163.0	9.9

The results of determined flexural strength of each particular test bar after the thermal shock testing are shown in Table 4.5-5. The flexural strength of samples without identified cracks is relatively high, over ~200 MPa for A and B, and 170 MPa or over ~200 MPa for C. The samples B with identified cracks experienced the flexural strength of 166 and 163 MPa, while those of A and C profoundly less below 30 MPa.

After thermal shock test the flexural strength of samples without cracks does not indicate to be effected by the thermal shock. The cracks in samples A and C are deteriorative, since they caused the flexural strength of A and C to drop below 30 MPa. However, the cracks in samples B affected the flexural strength to drop to considerably less extent. Composition B is more resistant to crack propagation in comparison to A and B. It was found by microstructural investigations of B fired in industrial kiln that the microstructure of B is more homogenous in comparison to A and C regarding pore size distribution and distribution of korundum and mullite grains, which all contributes to its better resistance to crack propagation. Besides, the irregular distribution of phases in the microstructure of C and the lower amount of mullite present in glassy phase are expected to attribute to its higher degree of deterioration after thermal shock. Mullite crystals present in the glassy phase act as barriers retarding the growth of cracks.

According to standard IEC 60672-3 [12] the resistance to thermal shock (ΔT) for high alumina porcelain type C 130 is required minimum 150 K. Compositions A, B and C fired in the gas kiln with thermal shock resistance of 200 K well meet the standard requirements.

Compositions A, B and C are better resistant to thermal shock in comparison to the reference composition EN fired under equivalent firing conditions in the gas kiln, since EN experienced cracks after water quenching in all the five samples at ΔT = 200 K.

4.5.2.4 Flexural strength of bodies fired in the gas kiln

The flexural strength was determined on the test pieces fired in two different ways regarding their setting up. They were fired as hung on the refractory supports (vertical) and as lei (horizontal) in the refractory slabs. When fired in vertical position, the test pieces were prepared with extruded length of 150 mm. After firing hung samples were cross sectioned on both sides to the regular length of 120 mm for flexural strength determination.

Table 4.5-6. Flexural strength of samples A, B and C fired in the gas kiln.

Composition	Flexural strength -vertical (MPa)	Flexural strength -horizontal (MPa)
A	231.3 ± 8.0	203.5 ± 13.9
B	202.5 ± 11.4	202.2 ± 34.4
C	171.6 ± 17.2	154.3 ± 23.6

The flexural strength of samples A, B and C after firing in the gas kiln is presented in Table 4.5-6. The highest flexural strength is determined for samples A being 231 MPa when fired as hung, i.e. in vertical position, and 204 MPa when fired as lied, i.e. in horizontal position. The flexural strength of 203 MPa for hung samples and 202 MPa for lied samples is determined for B, while considerably lower, 172 MPa for hung samples and 154 MPa for lied samples, is attained for C. The flexural strength of compositions A and C is noticeably higher when samples were fired as hung on refractory supports.

The hung samples experienced less scattered values of the flexural strength than samples fired as lied. Besides, samples A have about 14% and samples C have about 11% higher flexural strength when fired in hung position. More homogenous temperature conditions around hung samples during firing and the exclusion of any possible local reaction with refractory slab is expected to contribute to greater uniformity of fired body resulting in higher mechanical strength of the hung samples.

When compositions A, B and C were fired at 1300 °C in the laboratory furnace, they achieved the flexural strength 203 MPa, 204 MPa and 127 MPa, respectively. After firing in the gas kiln in equvalent lie position and in the same type of refractory slabs the flexural strength of compositions A and B is nearly equal to that attained in laboratory furnace, while higher for composition C for 27 MPa. Therefore, the favorable strength attained after firing in the laboratory furnace was reproducible under industrial conditions.

High flexural strength, over 200 MPa, attained by compositions A and B as fired in gas kiln is partially attributed to favorable pore size, their amount and distribution. As seen from optical microscope images in Figure 4.5-4 and 4.5-5 the pores of A and B are resemled regarding their amount, size, shape and distribution. The pores are nearly rounded, thus contributing to higher strength. Elastic modulus of material is affected by the amount, shape and distribution of porosity [115]. In general, when porosity increases it negatively influences the elastic modulus due to zero elastic modulus of the pores. The bloating of pores as observed in optical microscope image in Figure 4.5-6 negatively affected the mechanical strength of composition C.

Regarding the mechanical strength compositions A with 1.0 wt.% of Li_2O and B with 1.2 wt.% of Li_2O are more favorable under industrial perspective than C with 1.6 wt.% of Li_2O. Our findings agree with Tulyaganov et al. [93], who established that the desirable properties of porcelain can be attained if the Li_2O content does not exceed ~1.5 wt.%. However, under applied firing conditions in the gas kiln composition A with 1.0 wt.% of Li_2O is the most favorable due to both, high mechanical strength and low deformation during firing.

5 Conclusions

In the present work we have studied the influence of increasing the amount of β-spodumene ($LiAlSi_2O_6$), as a Li_2O-containing flux, on the firing behaviour, the phase composition, the microstructure evolution and the physical properties of high-alumina porcelain containing ~61 wt.% of Al_2O_3. The investigated porcelain bodies differentiated primarily in the type and the amount of fluxing agent. In the new developed bodies the flux system consists of Li_2O, as the main flux, and K_2O, while in standard composition it consists of K_2O, as the main flux, and Na_2O.

The Li_2O-containing bodies were developed with a view to be appropriate for the industrial production. The batch compositions of new bodies are based on the natural raw materials. The chosen raw materials are available on the market and have been previously applied in different porcelain bodies. The raw materials were used in form as delivered by suppliers with the exception of spodumene, which was calcined before application. The batch compositions and the characteristics of suspensions after milling are suitable for drying on the spray dryer. The technological procedures of making the samples, including wet milling with alumina balls end extrusion, were comparable with the processing of porcelain materials under industrial conditions.

We studied the properties of high-alumina porcelain bodies in the correlation with their phase composition and microstructure as developed after firing in the laboratory furnace in the temperature range between 950 and 1350 °C. All the investigations with Li_2O-containing composiotions were performed in comparison with the reference composition, which has been regularly used in the production. Additionally, the industrial perspective of the newly developed Li_2O-containing compositions was evaluated based on characterization of the samples fired under industrial conditions.

The chemical composition of investigated porcelain bodies varies principally in the amount and the type of alkali oxides as presented in the Characteristic oxide composition of the fired bodies. Li_2O was introduced in new compositions as the main flux via β-spodumene. All the studied bodies are classified as high-alumina porcelain due to their amount of Al_2O_3 around 61 wt.%. The Fe_2O_3 content of less than 0.5 wt.% enables the required whiteness for all the bodies, when fired in oxidation or reduction atmosphere.

Characteristic oxide composition of fired bodies (wt.%)

Oxide	EN	A	B	C
Al_2O_3	60.51	61.15	61.68	60.87
Fe_2O_3	0.33	0.44	0.42	0.36
Na_2O	0.66	0.17	0.19	0.20
K_2O	2.98	1.96	1.86	1.90
Li_2O	-	1.02	1.18	1.56

The alkali oxides are mainly introduced in the batch formulations through flux minerals. The fluxes in the reference composition EN contain K_2O and Na_2O, while the model compositions A, B and C contain about the same amount of K_2O and the increasing amount of Li_2O, namely 1.0, 1.2 and 1.6 wt.%. The source of K_2O and Na_2O are feldspars, containing microcline and albite, while the source of Li_2O is calcined β-spodumene. All the applied flux minerals are recognized as generally applied in the triaxial porcelain bodies.

Similar reactions, which are characteristic for triaxial porcelain body, take place up to 1200 °C in all the studied alumina porcelain bodies as confirmed with TG and DTA analysis. These reactions include the formation of metakaolinite in temperatutre range 450–600 °C through kaolinite dehydroxilation and the formation of γ-Al_2O_3 type spinel phase in temperature range 800–1000 °C. We found that an exothermic peak characteristic for the formation of γ-Al_2O_3 type spinel phase is observed with its maximum ~15 °C lower by compositions containing Li_2O, indicating that the addition of Li_2O enhances the mullite formation

to lower temperature.

We ascertained from the sintering curves that the first part of sintering process up to 1000 °C appears very similar for all the studied bodies. Therefore, no influence of Li_2O on the sintering behaviour of alumina porcelain bodies is detectable up to 1000 °C. The most intensive shrinkage region for all the compositions is between 1100 and 1300 °C, in which the Li_2O-bearing compositions contract at higher rate. The presence and the amount of Li_2O affect the densification rate. The composition with 1.6 wt.% Li_2O reaches its maximum contraction at temperature which is about 20 °C lower than for the compositions with 1.0 and 1.2 wt.% Li_2O and at least 50 °C lower than for the reference composition. The expansion, which indicates the overfiring due to bloating phenomena of the formed melt, is considerably more extensive by composition with 1.6 wt.% Li_2O.

We studied the phase composition, microstructure evolution and physical properties of bodies fired at seven selected temperatures in the temperature range from 950 to 1350 °C due to the major shrinkage and the related reactions that occur in this temperature range.

The mineralogical composition of raw bodies governs the densification behaviour, phase transformations and microstructure evolution during firing process. The main phase present in all of the raw bodies was corundum (α-Al_2O_3). Additionally to corundum kaolinite ($Al_2Si_2O_5(OH)_4$), microcline ($KAlSi_3O_8$) and α-quartz (SiO_2) were also found in all the compositions. As the second flux mineral albite ($NaAlSi_3O_8$) was present in reference composition, while in compositions containing Li_2O β-spodumene was present in the increasing amount.

The phase transformation and densification process in reference composition is comparable with processes occurring in typical triaxial porcelain body, except that additionally corundum as the main phase is present at all firing temperatures. The flux minerals microcline, sanidine and albite are identified at 950 °C and at 1050 °C with their peak intensities decreasing due to their melting up to 1150 °C. The intensity of α-quartz peak gradually diminishes with temperature increasing indicating its partial dissolution in the feldspar melt. However, the α-quartz is still present at 1350 °C. Mullite formation is detected at 1150 °C. The process of mullitization continues with increasing temperature.

In Li_2O-containing compositions the dissolution of microcline and sanidine is similar to the case of reference composition, indicating that the presence of β-spodumene has no perceivable effect on the melting of sanidine and microcline below 1150 °C. The amount of β-spodumene decreases with increasing temperature up to 1250 °C. Simultaneously, at 1150 °C, the Li-containing phase with a larger amount of SiO_2, i.e. $LiAlSi_3O_8$, is formed, which is correlated with the decreasing amount of α-quartz. The reactions of lithium minerals at temperatures above 1200 °C are affected by the amount of Li_2O. In A and B, with 1.0 and 1.2 wt% Li_2O, respectively, $LiAlSi_3O_8$ is only identified at 1150 and 1200 °C; at higher temperatures it appears to have melted in the feldspathic liquid, since none of the Li-minerals is detected at 1250 °C or above. In C, with 1.6 wt.% of Li_2O, $LiAlSi_3O_8$ is identified at 1150, 1200 and 1250 °C. The reaction of $LiAlSi_3O_8$ for composition C leads to the formation of $Li_xAl_xSi_{1-x}O_2$ at 1300 °C. $Li_xAl_xSi_{1-x}O_2$ appears as a stable phase and does not dissolve with increasing temperature.

Regarding the phase composition studies we found that the diminishing of quartz at the presence of Li_2O in temperature range 1150 to 1250 °C is due to quartz assimilation in β-spodumene structure forming lithium feldspar ($LiAlSi_3O_8$). The reaction of quartz assimilation is promoted with increased amount of Li_2O. When the amount of Li_2O is 1.6 wt.% lithium feldspar transforms to lithium aluminum silicate ($Li_xAl_xSi_{1-x}O_2$) above 1250 °C. Lithium aluminium silicates contains higher amount of silica than β-spodumene.

The microstructure evolution during heat treatment is observed from the SEM images. After firing at 950 °C all the studied samples are characteristic by grained homogeneous structure with voids, where non-porous particles are dispersed in amorphous matrix of clay transformation products. Noticeable melt formation within porous structure is characteristic after firing at 1150 °C for all the compositions. After firing at 1200 °C all the compositions underwent more intensive pore closing with increased amount of the glassy phase formed. The resulted microstructure in all compositions is characterized by mainly disconnected pores after firing at 1250 °C. The pore elimination process is more intensive for Li_2O-containing compositions. Disconnected pores in compact microstructure are characteristic for all compositions fired at 1300 °C. The microstructure of compositions with 1.0 and 1.2 wt.% Li_2O is more uniform and related to more intensive homogenization due to less viscous Li_2O-containg liquid phase. All studied compositions fired at 1350 °C tend to overfiring as obvious from the large pore growth. The overfiring effect with pores over 100 μm is mostly expressed by composition containing 1.6 wt.% Li_2O.

Based on XRD analysis and SEM observations it is not established that the presence of Li_2O in the amount 1.0 and 1.2 wt.% contributes to significantly improved formation and growth of mullite crystals. The growth of mullite is retarded when the amount of Li_2O is 1.6 wt.% due to formation of lithium

crystalline phases.

Physical properties of fired samples are correlated to the phase composition and microstructural evolution as attained at each firing temperature.

Bulk density and open porosity change proportionally with the firing temperature increasing until the zero open porosity. Li_2O containing compositions vitrify more rapidly in temperature range 1150 to 1250 °C. Composition with 1.6 wt.% Li_2O attains its maximum bulk density at 1250 °C, which is 50 °C lower than the other compositions. Compositions with Li_2O in amount of 1.0 wt.% and 1.2 wt.% reach maximum bulk density at 1300 °C. The presence of Li_2O in the amount of 1.0 wt.% is most favorable regarding the temperature resistance or the prone to overfiring with no detectable decrease in bulk density when firing temperature increased from 1300 to 1350 °C.

Above 1250 °C all compositions are characterized by zero open porosity indicating that the presence and amount of Li_2O does not noticeably affect the temperature, when zero open porosity is attained. However, it is established that the rate of pore closing is faster by compositions containing Li_2O in the temperature range 1150–1200 °C.

Thermal expansion of studied compositions fired in temperature range 950–1350 °C is investigated from CTE curves. Simultaneously, the presence of α-quartz and its diminishing during the heat treatment is observed, since typical to α→β quartz transition at 573 °C is noticeable in CTE curves as a steep step dependent on the amount of α-quartz present. The presence and the diminishing of α-quartz as observed from the degree of steep step in CTE curves is in agreement with corresponding XRD investigations.

At lower firing temperatures up to 1250 °C the presence of lithium minerals with their low thermal expansion mostly contributes to lower CTE of bodies containing Li_2O. At temperatures above 1250 °C, when lithium minerals are dissolved in liquid phase, there are no significant differences in CTE between reference composition and compositions with 1.0 or 1.2 wt.% Li_2O. Composition with 1.6 wt.% of Li_2O differentiate from others in lower CTE after firing above 1200 °C, supporting that the presence of lithium aluminum silicate contributes to its lower expansion.

We studied the CTE (30–300 °C) of samples fired at different temperatures, because CTE (30–300 °C) strongly affects the thermal shock resistance, which is generally determined in the temperature range from 100 to 250 °C for porcelain bodies. When bodies attain their maximum bulk densities the addition of Li_2O in the amount of 1.0 or 1.2 wt.% has no significant influence on CTE (30–300 °C) in comparison to reference composition, while with the amount of 1.6 wt.% the CTE (30–300 °C) is considerably lower.

All compositions containing Li_2O reach their maximum flexural strength after firing at 1300 °C, which is at least 50 °C lower in comparison to the reference composition. The flexural strength of the reference composition gradually increases up to 1350 °C. At 1300 °C the average flexural strength is 175 MPa for EN, 203 MPa for A, 204 MPa for B and 127 MPa for C, while at 1350 °C the average flexural strength is 190 MPa for EN, 167 MPa for A, 159 MPa for B and 89 MPa for C. The results show, that the improved flexural strength is attained by compositions containing 1.0 or 1.2 wt.% of Li_2O in comparison to the reference composition, while in composition with 1.6 wt.% Li_2O the strength is considerably lower. The higher flexural strength of A and B in comparison to EN may to be attributed mainly to their more uniform microstructure, as established from SEM observations. Besides, the lower amount of α-quartz present, as determined by XRD, and lower thermal expansion of the glassy phase containing Li_2O, as concluded from CTE studies, may partially contribute to higher flexural strength of A and B. On the other hand, the significantly lower flexural strength of C could be partially ascribed to the presence of the low-expansion lithium aluminosilicate crystalline phase, as identified in the XRD spectra.

Studied composition, containing 1.0, 1.2 and 1.6 wt.% of Li_2O, were additionally fired under industrial conditions in the gas kiln to determine the possibilities of their future industrial application.

After firing in the gas kiln corundum as the prevailing phase and mullite are identified in all compositions. Lithium aluminium silicate is detected only in the composition containing 1.6 wt.% of Li_2O. Comparable amount of mullite phase is observed in compositions with 1.0 and 1.2 wt.% of Li_2O, while in composition with 1.6 wt.% of Li_2O the amount of mullite is noticeably lower. The same phase composition was ascertained for the samples with Li_2O when fired in the laboratory furnace at 1350 °C, except that additionally α-quartz is identified in samples A as fired in laboratory furnace.

The microstructure of compositions with 1.0 and 1.2 wt.% Li_2O is characteristic by almost spherical pores, in size <30 μm, uniformly distributed among corundum grains embedded in the glassy matrix. The microstructure of compositions containing 1.0 and 1.2 wt.% Li_2O appears similar and more homogenous in comparison to composition with 1.6 wt.% Li_2O regarding pores, corundum grains distribution, mullite appearance in feldspar or clay relicts and size or distribution of the glassy phase.

When samples were fired in the gas kiln the maximum bulk density is attained for composition with 1.2 wt.% Li_2O. Zero open porosity is determined for all the model compositions. The CTE curves of all

compositions show similar trend with curves almost overlapping up to around 700 °C. There are no significant differences in CTE (30–300 °C) and CTE (30–600°C) among compositions.

The increasing amount of Li_2O in the composition affects its deformation during firing in the gas kiln. Deformation during firing is enhanced by the increasing amount of Li_2O mainly due to lower viscosity of the liquid phase which decreases with the amount of Li_2O increasing. Regarding the deformation during firing the composition with 1.0 wt.% Li_2O is most favorable for industrial application with existent firing schedule.

After firing in the gas kiln the same thermal shock resistance, i. e. ΔT= 200 K, is determined for all the compositions with Li_2O. According to the standard IEC 60672 the thermal shock resistance (ΔT) for alumina porcelain should exceed 150 K. All Li_2O-containing compositions well exceed the standard requirements for thermal shock resistance. Among compositions with Li_2O the highest resistance to crack propagation during thermal shock test is determined for composition with 1.2 wt.% Li_2O.

The average flexural strength of samples fired in the gas kiln, which is 204 MPa for A, 202 MPa for B and 154 MPa for C, also well met the requirement for the high strength alumina porcelain, which should exceed 140 MPa according to the standard IEC 60672. On the other hand, the determined flexural strength for samples A and B is very close to the flexural strength of corresponding samples fired in the laboratory furnace at 1300 °C, while higher for C.

Under existent firing schedule in the gas kiln the most favorable characteristics in view of industrial perspective are attained by composition containing 1.0 wt.% Li_2O regarding attained flexural strength, thermal shock resistance and deformation during firing.

Our work was entirely oriented towards the transmission of the results of investigations into the industrial application. We projected the experiments to be as close as possible to the standard industrial conditions regarding the applied raw materials, the milling process, the forming technique, the drying process and the firing schedules. In view of rheological characteristics of raw bodies, we considered the requirement that newly developed bodies are supposed to be applied for serial production based on spray dried granulated body, which is suitable for extrusion or dry pressing. On the other hand, we strongly followed the goal to develop high-alumina porcelain bodies, which could be fired at lower temperature with the aim to lower the costs of energy and to contribute to the protection of the environment due to lower energy consumption. Besides, we considered the requirements for the health protection using the raw materials and additives that are not harmful for the working place or the environment.

With the introduction of Li_2O in the high-alumina porcelain body we developed materials with high mechanical strength and improved resistance to thermal shock considering all the requirements for industrial transfer. We established that the high-alumina porcelain body containing 1.0 wt.% of Li_2O is the most proper to be used under existent firing conditions. The results show that good thermal and mechanical properties could be attained in high-alumina porcelain with higher amounts of Li_2O, i.e. 1.2 and 1.6 wt.%, when fired at lower firing temperatures. Therefore, the firing schedules under industrial conditions should be corrected towards lower temperature. Lower firing temperature contributes to the reduction of CO_2 emission into environment.

6 Acknowledgements

This work would not have been possible without the support, help and patience of all the people from Electronic Ceramics Department (K5) at Institute Jožef Stefan, Ljubljana, and Technical Ceramic Research and Technology Department at ETI Elektroelement d.d., Izlake, whose generous contribution of their time, advice and encouragement made this study challenging and rewarding. Special thanks to the Management Board of ETI Elektoelement d.d., Izlake, who gave me the opportunity for research work and study with complete financial support. Here I wish to thank most sincerely to all of them who contributed to the realization of this research work and especially to:

Prof. Dr. Marija Kosec, head of Electronic Ceramics Department (K5), Jožef Stefan Institute, the supervisor of my thesis, for giving me the opportunities to pursue my PhD at Jožef Stefan Postgraduate School, for her expert contribution to make this thesis valuable, for her continual and advisable guidance along this work, for her help to gain the knowledge that I never imagined possible, and for her patience, support and help in correction of the thesis manuscript,

Dr. Janez Holc, Electronic Ceramics Department (K5), the co-supervisor of my thesis, for his willingness to contribute his time and expertise all along this work, for his generous help, patience and advices by my educational and research work, including experimental and analytical work, and especially for his contribution and deep engagement in the field of XRD and SEM analysis.

Mag. Marjan Buh, the counsellor of my thesis, for his expert advises, help and interesting discussions all along the experimental and analytical work and for his encouragements.

Ivan Lavrač, head of Technical Ceramic Research and Technology Department at ETI, for his continual support and help and especially for his contribution and cooperation in my experimental work.

Dr. Danjela Kuščer Hrovatin, Electronic Ceramics Department (K5), for her extensive knowledge, collaboration, expert advices and patience in SEM analysis,

Vlasta Imperl, Marija Razpotnik, Helena Razpotnik, Lidija Sopotnik and Joži Prašnikar, Technical Ceramic Research and Technology Department at ETI, for their continual help in the experimental and analytical work,

Jena Cilenšek and Silvo Drnovšek, Electronic Ceramics Department (K5), for help in the analytical work,

My family and my friends for support and especially for encouragement and understanding.

7 References

[1] Carty, W. M. and Senapati, U., Porcelain-raw materials, processing, phase evolution, and mechanical behaviour. *J. Am. Ceram. Soc.,* 1998, **81**(1), 3-20.

[2] Tulyaganov, D. U., Agathopoulos, S., Fernandes, H. R. and Ferreira, J. M. F., The influence of incorporation of ZnO-containing glazes on the properties of hard porcelain. *J. Eur. Ceram. Soc.,* 2007, **27**, 1665-1670.

[3] Lee, W. E. and Iqbal, Y., Influence of mixing on mullite formation in porcelain. *J. Eur. Ceram. Soc.,* 2001, **21**, 2583-2586.

[4] Schüller, K. H., Porzellan. *Handbuch der Keramik,* 1966, Verlag Schmidt GmbH, Freiburg, Gremany, Gruppe II A,1-12.

[5] Liebermann, J., Microstructure properties and product quality of strength-stressed high-voltage insulators. *Am. Ceram. Soc. Bull,* 2003, **82**(2), 39-46.

[6] Kingery, W. D., Bowen, H.K. and Uhlmann D.R., Introduction to ceramics. *J. Wiley & Sons, New York,* 1976, 1032 p.

[7] Lee, W. E , Souza, G. P., McConville, C. J., Tarvornpanich, T. and Iqbal, Y., Mullite formation in clays and clay-derived vitreous ceramics, *J. Eur. Ceram. Soc.,* 2008, **28**, 465-471.

[8] Villegas-Palacio, S. and Dinger, D. R., PSD effects on firing properties of porcelains, I, *J. Am. Ceram. Soc. Bull.,* 1996, **75**(7), 71-76.

[9] Yilmaz, S., Erkmen, Z. E., Creep of hard porcelain during firing. *Am. Ceram. Soc. Bull,* 2007, **6**(8), 9301-9304.

[10] Iqbal, Y. and Lee, W. E., Fired porcelain microstructures revisited. *J. Am. Ceram. Soc.,* 1999, **82**(12), 3584-3590.

[11] Chiang, Y.M., Birnie, D. P. III, Kingery, W. D. Physical ceramics, *J. Wiley & Sons, New York,* 1997, 522 p.

[12] IEC 60672-3(1997). Ceramic and Glass-Insulating Materials, Part 3, Specifications for individual materials. International Electrotechnical Commission, Geneva, CH.

[13] Van Vlack, L.H., Elements of materials science and engineering. *Addison-Wesley Publishing Company, USA,* 1985, 633 p.

[14] Islam, R. A., Chan, Y. C. and Islam, F., Structure-property relationship in high-tension ceramic insulator fired at high temperature. *Materials Science and Engineering.,* 2004, **B106**, 132-140.

[15] Abdel-Azis, D. A. and Aly, M.H., Effect of non-conventional fluxes on the electrical properties of electro-ceramic bodies. *Interceram.,* 2006, **55**(2), 90-93.

[16] Chaudhuri, S. P. and Sarkar, P., Dielectric behaviour of porcelain in relation to constitution. *Ceramics International,* 2000, **26**, 865-875.

[17] Amigó, J. M., Clausell, J. V., Esteve, V., Delgrado, J. M., Reventós, M. M., Ochando, L. E., Debaerdemaeker, T. and Martí, F., X-ray powder diffraction phase analysis and thermomechanical properties of silica and alumina porcelains. *J. Eur. Ceram. Soc.,* 2004, **24**, 75-81.

[18] Warshaw, S. I. and Seider, R., Comparison of strength of triaxial porcelains containing alumina and silica. *J. Am. Ceram. Soc.,* 1967, **50**(7), 337-343.

[19] Liebermann, J. and Schulle, W., Bauxite porcelain. *Am. Ceram. Soc. Bull.,* 2002, **81**(2), 33-38.

[20] McConville, C. J. and Lee, W. E., Microstructural development on firing illite and smectite clays compared with that in kaolinite. *J. Am. Ceram. Soc.,* 2005, **88**(8), 2267-2276.

[21] Souza, G. P., Messer, P. F. and Lee, W. E., Effect of varying quartz particle size and firing atmosphere on densification of Brazilian clay-based stoneware. *J. Am. Ceram. Soc.,* 2006, **89**(86), 1993-2002.

[22] Westbrook, J. H., Temperature dependence of strength and brittleness of some quartz structures. *J. Am. Ceram. Soc.,* 1958, **41**(11), 433-435.

[23] Holmquist, S. T., Conversion of quartz to tridymite. *J. Am. Ceram. Soc.,* 1961, **44**(2), 82-86.

[24] Bock, J. and Gouq-Jen, S., Interpretation of the infrared spectra of fused silica. *J. Am. Ceram. Soc.,* 1970, **53**(2), 69-73.

[25] Lachman, M. I. and Everhart, J. O., Development of safe cooling schedules for structural clay products. *J. Am. Ceram. Soc.,* 1956, **39**(1), 30-38.

[26] Ece, O. I. and Nakagawa Z., Bending strength of porcelains. *Ceramics International,* 2002, **28**, 131-140.

[27] Štubna, I., Trník, A. and Vozár, L., Thermomechanical analysis of quartz porcelain in temperature cycles. *Ceramics International,* 2007, **33**, 1287-1291.

[28] Karamanov, A., Karamanova, E., Ferrari, A. M., Ferrante, F. and Pelino, M., The effect of fired scrap adddition on the sintering behavior of hard porcelain. C*eramics International,* 2006, **32**, 727-732.

[29] Dana, K. and Das, S. K., Evolution of microstructure in flyash-containing porcelain body on heating at different temperatures. *Bull. Mater. Sci.,* 2004, **27**(2), 183-188.

[30] Mukhopadhyay, T. K., Ghosh, S., Ghatak, S. and Maiti, H. S, Effect of pyrophyllite on vitrification and on physical properties of triaxial porcelain. *Ceramics International,* 2006, **32**, 871-876.

[31]Dana, K, Ghosh, S., Mukhopadhyay, T. K. and Das, S. K., Feldspatic and pyrophyllitic porcelain evolution during Firing. *Am. Cer. Soc. Bull,* 2006, **85**(12), 871-876.

[32]Ching, W. Y. and Xu, Y.-N., First principles calculation of electronic, optical and structural properties of α-Al_2O_3. *J. Am. Cer. Soc.,* 1994, **77**(2), 404-411.

[33] Munro, R. G., Evaluated material properties for a sintered α-alumina. *J. Am. Ceram. Soc.,* 1997, **80**(8), 1919-1927.

[34]Austin, C. R., Schofield, H. Z. and Haldy, N. L., Alumina in whiteware. *J. Am. Cer. Soc.*, 1946, **29**(12), 341-354.

[35] Maity, S. and Sarkar, B. K., Development of high-strength whiteware bodies. *J. Eur. Ceram. Soc.,* 1996, **16**, 1083-1088.

[36] Kobayashi, Y., Yamada, M., Nakayama, M., Ohira, O. and Isoyama, H., Strength and thermal shock resistance of alumina-strengthened porcelain containing cristobalite. *J. Cer. Soc. Japan,* 2003, **111**(12), 872-877.

[37] Hasselman, D. P. H. and Fulrath, R. M., Proposed fracture theory of a dispersion-strengthened glass matrix. *J. Am. Ceram. Soc.,* 1966, **49**(2), 68-72.

[38] Kobayashi, Y., Mukai, M., Mizuno, T, Ohira, O. and Isoyama, H., Effect of cristobalite formation and glaze on bending strength of α-alumina reinforced porcelain. *J. Cer. Soc. Japan,* 2005, **113**(6), 413-418.

[39] Belnou, F., Goeuriot, D., Goeuriot, P. and Valdivieso, F., Nanosized alumina from boehmite addition in alumina porcelain, Part 2: Effect on material properties. *Ceramics International,* 2007, **33**, 1243-1249.

[40] Iqbal, Y. and Lee, W. E., Microstructural evolution in triaxial porcelain. *J. Am. Ceram. Soc.,* 2000, **83**(12), 3121-3127.

[41] Esposito, L., Salem, A., Tucci, A., Gualtieri, A. and Jazayeri, S. H., The use of nepheline-syenite an a body mix for porcelain stoneware tiles. *Ceramics International.,* 2005, **31**, 233-240.

[42] The American Ceramic Society and National Institute of Standards and Technology, Phase equilibria diagrams, CD-ROM, Database, Version 3.0. Vol. 01, Fig 00407.

[43] The American Ceramic Society and National Institute of Standards and Technology, Phase equilibria diagrams, CD-ROM, Database, Version 3.0. Vol. 01, Fig 00501.

[44] Cowan, C. A., Bole, G. A. and Stone, R. L., Spodumene as a flux component in sanitary chinaware bodies. *J. Am. Ceram. Soc.,* 1950, **33**(6), 193-197.

[45] Lehnhäuser, W., Keramische Glasuren und ihre Farben, *Ritterbach Verlag GmbH, Frechen,* 2000, 660 p.

[46] Koenig, C. J., Nepheline syenite in hotel chinaware bodies. *J. Am. Cer. Soc.*, 1942, **25**83), 90-93.

[47] Kristoffersson, A., Ekberg, I. L., Leandersson and H., Carlsson, R., High strength triaxial porcelain by an improved glassy phase. *In Proceeding of the Third Euro-Ceramics*, 1993, **2**, 1059-1064.

[48] Fishwick, J. H., Application of lithium in ceramics. *Cahners Publishing, Boston, MA.*, 1974, 156 p.

[49] Tuttle, M. A. and Cook, R. L, Fundamental study of crystalline and glassy phases in whiteware bodies. *J. Am. Ceram. Soc.*, 1949, **32**(9), 279-294.

[50] Sane, S. C. and Cook, R. L., Effect of grinding and firing treatment on the crystalline and glass content and the physical properties of whiteware bodies. *J. Am. Ceram. Soc.*, 1951, **34**(5), 145-151.

[51] Lee, S., Kim, Y. J. and Moon, H-S, Phase transformation sequence from kaolinite to mullite investigated by an enery-filtering transmission electron microscope. *J. Am. Ceram. Soc.*, 1999, **82**(10), 2841-2848.

[52] Bridley G. W. and Nakahira, M., The kaolinite-mullite reaction series: II, Metakaolin. *J. Am. Ceram. Soc.*, 1959, **42**(7), 314-318.

[53] Gualtieri, A. F., Thermal behavior of the raw materials forming porcelain stoneware mixtures by combined optical and *in Situ* X-ray dilatometry. *J. Am. Ceram. Soc.*, 2007, **90**(4), 1222-1231.

[54] Schneider, H., Schreurer, J. and Hildmann, B., Structure and properties of mullite - A review. *J. Eur. Ceram. Soc.*, 2008, **28**, 329-344.

[55] The American Ceramic Society and National Institute of Standards and Technology, Phase equilibria diagrams, CD-ROM, Database, Version 3.0. Vol. 01, Fig 00786.

[56] Ohya, Y., Takahashi, Y., Murata, M, Nikagawa, Z. and Hamano, K., Acoustic emmision from a porcelain body during cooling . *J. Am. Ceram. Soc.*, 1999, **82**(2), 445-448.

[57] Mattyasovszky-Zsolnay, L., Mechanical strength of porcelain. *J. Am. Ceram. Soc.*, 1957, **40**(9), 299-306.

[58] Kobayashi, Y., Ohira, O., Ohashi, Y. and Kato, E., Effect of firing temperature on bending strength of porcelains for tableware. *J. Am. Ceram. Soc.*, 1992, **75**(7), 1801-1806.

[59] Carbajal, L., Rubio-Marcos, F., Bengochea, M. A. and Fernanadez, J. F., Properties related phase evolution in porcelain ceraamics. *J. Eur. Ceram. Soc.*, 2007, **27**, 4065-4069.

[60] Smoke, J. E., Ceramic compositions having negative linear thermal expansion. *J. Am. Ceram. Soc.*, 1951, **34(**3), 87-90.

[61] Lu, T. J. and Fleck, N. A., The thermal shock resistance of solids. *Acta Mater.*, 1998, **46(13)**, 4735-4768.

[62] Kingery, W. D., Factors affecting thermal stress resistance of ceramic materials. *J. Am. Ceram. Soc.*, 1955, **38(**1), 3-15.

[63] Aksel, C., Rand, B, Riley, F.L. and Warren, P.D., Thermal shock beviour of magnesia-spinel composites. *J. Eur. Ceram. Soc.*, 2004, **24**, 2839-2845.

[64] Hasselman, D. P. H., Unified theory of thermal shock fracture initiation and crack propagation in brittle ceramics. *J. Am. Ceram. Soc.*, 1969, **52**(11), 600-604.

[65] Zhou, Z., Ding, P., Tan, S. and Ian, J., A new thermal-shock-resistance model for ceramics: Establishing and validation. *Materials Science and Engineering.*, 2005, **A 405**, 272-276.

[66] Buessem, W. R., Thermal shock testing, *J. Am. Ceram. Soc.*, 1955, **38**(1), 15-17.

[67] Maity, S., Mukhopadhyay, T. K. and Sarkar, B. K., Strength of sillimanite sand reinforced porcelain subjected to thermal shock. *J. Eur. Ceram. Soc.*, 1997, **17**, 749-752.

[68] Smoke, E. J., Thermally resistant whiteware. *J. Am. Ceram. Soc.*, 1950, **33**(5), 174-177.

[69] Posarac, M., Dimitrijevic, M., Volkov-Husovic, T., Devecerski, A. and Matovic, B., Determination of thermal shock resistance of silicon carbide/cordierite composite material using nondestructive test methods. *J. Eur. Ceram. Soc.*, 2008, **28**, 1275-1278.

[70] Hummel, F.A., Observations on the thermal expansion of crystalline and glassy substances. *J. Am. Ceram. Soc.*, 1950, **33**(6), 102-107.

[71] Hursh, R. K., Development of a porcelain vacuum tube. *J. Am. Ceram. Soc.*, 1949, **32**(3), 75-80.

[72] Orlowski, H. J. and Kornig, C. J., Thermal expansion of silicate fluxes in the crystalline and glassy states. *J. Am. Ceram. Soc.,* 1941, **24**(3), 80-84.

[73] Bayuseno, A. P., Latella, B. A. and O'Connor, H. O., Resistance of alumina-spodumene ceramics to thermal shock. *J. Am. Ceram. Soc.,* 1999, **82**(4), 819-824.

[74] Latella, B. A., Burton, G. R. and O'Connor, H. O., Use of spodumene in the processing of alumina-matrix ceramics-influence on microstructure and mechanical properties. *J. Am. Ceram. Soc.,* 1995, **78**(7), 1895-1899.

[75] Low, I. M., Mathews, E., Garrod, T., Zhou, D., Phillips, D. N and Pillai, X. M., Processing of spodumene-modified mullite ceramics. *Journal of Materials Science,* 1997, **32**, 3807-3812.

[76] Prokopowitcz, T. I. and Hummel, F. A., Reactions in system Li_2O-MgO-Al_2O_3-SiO_2: II, Phase Equilibria in the High-Silica Region. *J. Am. Ceram. Soc.,* 1956, **39**(8), 266-278.

[77] Naga, S. M., El-Magraby, A.A. and Mörtel, H., Densification and characterization of β-spodumene-cordierite compositions, *Am. Ceram. Soc. Bull.,* 2006, **85**(11), 9101-9106.

[78] Sakamoto, A. and Yamamoto, S., Volume change of β-spodumene s.s. glass-ceramics due to structural relaxation. *Journal of the Ceramic Society of Japan,* 2006, **114(**5), 380-385.

[79] Talyaganov, D. U., Agathapoulos, S., Fernandes, H. R., Ferreira, J. M. F., Synthesis of lithium aluminosilicate glass and glass-ceramics from spodumene material. *Ceramics International,* 2004, **30**, 1023-1030.

[80] Nordman, A., Cheng, Y-B., Bastow, T. J. and Hill, A. J., Structural characterization of lithium aluminosilcate glass and glass ceramics derived from spodumene material. *J. Phys: Condens. Matter.,* 1995, **7,** 3115-3128.

[81] Borom, M. P., Turkalo, A. M. and Doremus, R. H., Strength and microstucture in lithium disilicate glass-ceramics. *J. Am. Ceram. Soc.,* 1975, **85**(9-10), 385-391.

[82] Roy, R., Roy, D. M. and Osborn, E. F., Compositional and stability relationship among the lithium aluminosilicates: Eucryptite, spodumene, and petalite. *J. Am. Ceram. Soc.,* 1950, **33**(5), 152-159.

[83] The American Ceramic Society and National Institute of Standards and Technology, Phase equilibria diagrams, CD-ROM, Database, Version 3.0. Vol. 01, Fig 00449.

[84] The American Ceramic Society and National Institute of Standards and Technology, Phase equilibria diagrams, CD-ROM, Database, Version 3.0. Vol. 01, Fig 00456.

[85] Hummel, F. A., Thermal expansion properties of some synthetic lithia minerals. *J. Am. Ceram. Soc.,* 1951, **34**(8), 235-239.

[86] Brackbill, C.E., McKinstry, H. A. and Hummel, F. A., Thermal expansion of some glasses in the system Li_2O-Al_2O_3-SiO_2. *J. Am. Ceram. Soc.,* 1951, **34**(4), 107-109.

[87] Eppler, R. A., Glass formation and recrystallization in the lithium metasilicate region of the system Li_2O- Al_2O_3-SiO_2. *J. Am. Ceram. Soc.,* 1963, **46**(2), 97-101.

[88] The American Ceramic Society and National Institute of Standards and Technology, Phase equilibria diagrams, CD-ROM, Database, Version 3.0. Vol. 01, Fig 02426.

[89] Merivale C., Lithium in Ceramics. *Am. Ceram. Soc. Bull.,* 2003, **82**(4), 61-65.

[90] Twells, R., The effect of lepidolite in a high tension electrical porcelain body. *J. Am. Ceram. Soc.,* 1928, **11(**6), 644-648.

[91] Betz, G. C., Lithium minerals and compounds in ceramics. *J. Am. Ceram. Soc.,* 1938, **21**(5), 189-191.

[92] Ismatova, R., Properties and structure of spodumene-porcelain. *Glass and Ceramics,* 1987, **44**(7), 27-28.

[93] Tulyaganov, D. U., Agathopoulos, S., Fernandes, H. R. and Ferreira, J. M. F., Influence of lithium oxide as auxiliary flux on the properties of triaxial porcelain bodies. *J. Eur. Ceram. Soc.,* 2006, **26**, 1131-1139.

[94] Masleniklova, G. N. and Gavrikova, l. P., Lithium-containing ceramics. *Izvestiya Akademii Nauk SSSR, Neorganicheskie Materialy,* 1984, **20(**7), 1227-1237.

[95] Tucci, A., Esposito, L., Malmusi, L. and Rambaldi, E., New body mixes for porcelain stoneware tiles with improved mechanical characteristics. *J. Eur. Ceram. Soc.,* 2007, **27**, 1875-1881.

[96] Vergano, P. J., Hill, D. C. and Uhlmann, D. R., Thermal expansion of feldspar glasses. *J. Am. Cer. Soc.*, 1967, **50**(1), 59-60.

[97] Washburn, E. W. and Bunting, E. N., Porosity: V. Recommended procedures for determining porosity by method of absorption. *J. Am. Ceram. Soc.*, 1922, **5**(1), 48-56.

[98] IEC 60672-2(1999). Ceramic and Glass-Insulating Materials, Part 2, Methods of test. International Electrotechnical Commission, Geneva, CH.

[99] Chen, J. lF., Wang, M. –C. and Hon, M. –H, Phase transformation and growth of mullite and kaolin ceramics. *J. Eur. Ceram. Soc.*, 2004, **24**, 2389-2397

[100] Romero, M., Martín-Márquez, J. and Rincón, j. M., Kinetic of mullite formation from a porcelain stoneware body for tiles production. *J. Eur. Ceram. Soc.*, 2006, **26**, 1647-1652.

[101] Talyaganov, D.U., Agathopoulos, S., Fernandes, H. R., Ferreira, J. M. F. and Fabrichnaya, O., Influence of Li_2O doping on non-isothermal evolution of phases in K-Na-containing aluminosilicate matrix. *J. Am. Ceram. Soc.*, 2006, **89**(1), 292-297.

[102] Karamanov, A., Karamanova, E., Ferrari, A. M., Ferrante, F. and Pelino M, The effect of fired scrap addition on the sintering behavior of hard porcelain. *Ceramics International*, 2006, **32**, 727-732.

[103] Tarvornpanich, T, Souza, G. P. and Lee. W. E., Microstructural evolution on firing soda-lime-silica glass fluxed whitewares. *J. Am. Ceram. Soc.*, 2005, **88**(5), 1302-1308.

[104] Martin-Márques, M., De la Torre, A. G., Aranda, M. A. G, Rincón, J. M. and Romero, M., Evolution with temperature of crystalline and amorphous phases in porcelain stoneware. *J. Am. Ceram. Soc.*, 2009, **92**(1), 229-234.

[105] http://www.casebook.org./dissertrations/maybrick_diary/maybrick-diary-analysis.ink.html

[106] Tarvornpanich, T, Souza, G. P. and Lee. W. E., Microstructural evolution in clay-based ceramics I: Single components and binary mixtures of clay, flux, and quartz filler, *J. Am. Ceram. Soc.*, 2008, **91**(7), 2264-2271.

[107] Belnou, F., Goeuriot, D., Goeuriot, P. and Valdivieso, F., Nanosized alumina from boehmite additions in alumina porcelain, Part 1: Effect on reactivity and mullitization. *Ceramics International*, 2004, **30**, 883-892.

[108]Subramanian, M. A., Corbin, D. R and Frlee, R. D., X-ray and MAS NMR characterization ot the thermal transformation of Li(na)-Y zeolite to lithium aluminosilicates). *Mat. Res. Bull.*, 1986, **21**, 1525-1532.

[109]Yamuna, A. and Devanarayanan, S., Mullite-β-spodumene composites from sluminosilicate**s**. *J. Am. Ceram. Soc.*, 2001, **84**(8), 1703-1709.

[110] Thiemecke, H., Thermal and moisture expansion of kaolins and bodies fired at different temperatures. *J. Am. Cer. Soc.*, 1941, **24**(2), 69-75.

[111] Ganesh, I., Sundararajan, G. and Ferreira, M. F, Formation and densification behaviour of mullite aggregates from beach sand sillimanite. *J. Am. Cer. Soc.*, 2008, **91**(8), 2464-2468.

[112] Bertolotti, R. L. and Fukui, H., Measurment of softening temperatures in dental bake-on porcelains. *Journal of Dental Research*, 1982, **61**(3), 480-483.

[113] Bengisu, M. and Brow, R., K., Effect of long-term heating and thermal cycling on thermal expansion, phase distribution, and microhardness of lithium aluminosilicate glass-ceramics. *Journal of Non-Crystalline Solids*, 2003, 331, 137-144.

[114] Villegas-Palacio, S. and Dinger, D. R., PSD effects on firing properties of porcelains, II, *J. Am. Ceram. Soc. Bull.*, 1996, **75**(9), 79-84.

[115] Hristopulos, D. H., Demertzi, M., A semi-analytical equation for the Young's modulus of isotropic ceramic materials. *J. Eur. Ceram. Soc.*, 2008, **28**, 1111-1120.

Index of Figures

Index of Tables

Appendix

The list of enclosure:

1. Article in press in Journal of the European Ceramic Society

High-alumina porcelain with the addition of a Li_2O-bearing fluxing agent
M. Oberžan, J. Holc, M. Buh, D. Kuščer, I. Lavrač and M. Kosec

2. Patent

SI 22541 Glinični porcelan za elektrotehniko in postopek njegove izdelave
Inventors: OBERŽAN Martina (ETI), Holc Janez (IJS), BUH Marjan (IJS) and IMPERL Vlasta (ETI)

3. The registration of the patent

P-200900084 Glinični porcelain z izboljšanimi termičnimi lastnostmi in postopek njegove izdelave
Inventors: OBERŽAN Martina (ETI), Holc Janez (IJS), BUH Marjan (IJS), LAVRAČ Ivan (ETI) and KOSEC Marija (IJS)

4. Bibliography

Bibliography

Articles

Parameter PV_{lim} kot merilo za ovrednotenje materialov tesnilnih obročev v mehanskih drsnih tesnilih = Parameter PV_{lim} as a face material evolution criteria of mechanical seals

VEZJAK Anton, VIŽINTIN Jože, **OBERŽAN Martina**, *Mater. tehno.*, 2000, vol. 34, no. 3⁄4, pp 143-146, 2000.

High-alumina porcelain with the addition of a Li_2O-bearing fluxing agent

OBERŽAN Martina, HOLC Janez, BUH Marjan, KUŠČER Danjela, LAVRAČ Ivan, KOSEC Marija, *J. Eur. Ceram. Soc.*, 2009, vol. 29, no. 11, pp. 2143-2152, doi:10.1016/j.jeurceramsoc.2009.01.029.

Conferences

Parameter PV_{lim} kot kriterij za ovrednotenje materialov tesnilnih obročev v mehanskih drsnih tesnilih = Parameter PV_{lim} as a face material evaluation criteria of mechanical seals.

VEZJAK Anton, VIŽINTIN Jože, **OBERŽAN Martina**, 7. konferenca o materialih in tehnologijah, Portorož, Slovenija, 13.-15. Oktober 1999. *Program in knjiga povzetkov*, Ljubljana: Inštitut za kovinske materiale in tehnologije, 1999, pp. 43.

Uporaba novih materialov za drsna tesnila za tesnenje agresivnih medijev

VIŽINTIN Jože, VEZJAK Anton, **OBERŽAN Martina**, LAVRAČ Ivan, RANDEL Franc, 9. Konferenca o materialih in tehnologijah, Portorož, Slovenija ,14.-16. November 2001. *Program in knjiga povzetkov*, Ljubljana: Inštitut za kovinske materiale in tehnologije, 2001, pp. 121.

Influence of Li_2O-content fluxing agent on mechanical and thermal properties of alumina porcelain

OBERŽAN Martina, HOLC, Janez, BUH Marjan, KOSEC, Marija, KUŠČER Danjela, LAVRAČ Ivan, 10th International Conference and Exhibition of the European Ceramic Society, June 17-21, 2007, Berlin. *Programme*, [S. l.]: ECERS, 2007.

Mechanical and thermal properties of alumina porcelain with addition of Li_2O-content fluxing agent

OBERŽAN Martina, HOLC Janez, BUH Marjan, KOSEC Marija, LAVRAČ Ivan, KUŠČER Danjela, V: Electroceramics XI, August 31 - September 4, 2008, Manchester, UK. *Abstracts and CD proceedings*, [S. l.: s. n.], 2008.

Patents

OBERŽAN Martina, IMPERL Vlasta. *Steatitni material in postopek za njegovo izdelavo : patent SI20689*. Ljubljana: Urad Republike Slovenije za intelektualno lastnino, 30.apr. 2002.

OBERŽAN Martina, HOLC Janez, BUH Marjan, IMPERL Vlasta. *Glinični porcelan za elektrotehniko in postopek njegove izdelave : patent SI22541*. Ljubljana: Urad RS za intelektualno lastnino, 31. dec. 2008.

Patent registration

OBERŽAN Martina, HOLC Janez, BUH Marjan, LAVRAČ Ivan, KOSEC Marija. *Glinični porcelan z izboljšanimi termičnimi lastnostmi in postopek njegove izdelave : patentna prijava št. P-200900084*. Ljubljana: Urad RS za intelektualno lastnino, 30. mar. 2009.

(19) REPUBLIKA SLOVENIJA
Urad RS za intelektualno lastnino

(10) SI 22541 A

(12) PATENT

(21) Številka prijave: 200700138
(22) Datum prijave: 12.06.2007

(51) Int. Cl. (2006)
C04B 35/10 H01B 17/56

(45) Datum objave: 31.12.2008

(72) Izumitelji: OBERŽAN Martina, 1420 Trbovlje, SI;
HOLC Janez, 1234 Mengeš, SI;
BUH Marjan, 4224 Gorenja vas, SI;
IMPERL Vlasta, 1412 Kisovec, SI

(73) Imetnika: Institut "Jožef Stefan",
Jamova 39, 1000 Ljubljana, SI;
ETI Elektroelement d.d.,
Obrezija 5, 1411 Izlake, SI

(74) Zastopnik: ITEM d.o.o. Zastopniška pisarna za patente in blagovne znamke, Resljeva 16, 1000 Ljubljana, SI

(54) GLINIČNI PORCELAN ZA ELEKTROTEHNIKO IN POSTOPEK NJEGOVE IZDELAVE

(57) Predmet izuma je glinični porcelan za elektrotehniko in postopek njegove izdelave. Tehnični porcelan po izumu spada v skupino alkalijskih alumosilikatnih porcelanov z visoko mehansko trdnostjo. Glinični porcelan po izumu ima sledečo kemijsko sestavo (masni %): od 58 do 62 % aluminijevega oksida, od 0,3 do 0,6 % železovega oksida, od 0,1 do 0,3 % natrijevega oksida, od 1,5 do 2,5 % kalijevega oksida ter od 0,8 do 1,2 % litijevega oksida. Celotna vsebnost železovega oksida je nižja od 0,5 %. Keramični material se žge v temperaturnem območju od 1280 do 1320 stopinj celzija od 1 do 4 ure. Keramični material z navedeno sestavo in pripravljen po opisanem postopku ima upogibno trdnost višjo kot 200 MPa. Površinsko glaziran keramični material in žgan po opisanem postopku ima upogibno trdnost višjo kot 240 MPa.

SI 22541 A

GLINIČNI PORCELAN ZA ELEKTROTEHNIKO IN POSTOPEK NJEGOVE IZDELAVE

Predmet izuma je glinični porcelan za elektrotehniko in postopek njegove izdelave. Tehnični porcelan po izumu spada v skupino alkalijskih alumosilikatnih porcelanov z visoko mehansko trdnostjo in se uporablja predvsem v elektrotehniki na področju transmisije in distribucije električnega toka kot izolant.

Alkalijski alumosilikatni materiali, ki jih uvrščamo v skupino tehničnih porcelanov z visoko mehansko trdnostjo, vsebujejo več kot 40 % in običajno manj kot 65 % Al_2O_3. Uporabljajo se za izdelavo izolacijskih komponent v elektrotehničnih izdelkih, med katere spadajo tudi nizko in visoko napetostne varovalke. Izolacijski del varovalke je porcelanska osnova, ki je glede na namen uporabe lahko tudi belo ali rjavo glazirana ali po žganju površinsko obdelana.

Kot izolanti v elektrotehniki so tehnični porcelani izpostavljeni različnim mehanskim, termičnim, električnim in korozijskim obremenitvam. Glinični porcelani se odlikujejo po visokih mehanskih trdnostih (upogibna trdnost več kot 100 MPa), ki se povečujejo z večanjem vsebnosti korunda. Ker ima korund relativno visok temperaturni razteznostni koeficient, neugodno vpliva na odpornost keramičnega materiala na termične šoke.

Med izolacijskimi materiali, ki se uporabljajo v elektrotehniki, imajo porcelani najdaljšo tradicijo. Porcelani na splošno predstavljajo enega najbolj kompleksnih keramičnih materialov. Kompleksnost izvira iz dejstva, da se izdelujejo pretežno iz naravnih surovin, da se preoblikujejo v surovem stanju po različnih keramičnih tehnoloških postopkih in da se žgejo pri visokih temperaturah, kjer potekajo številne fazne pretvorbe, nastane steklasta faza ter nove kristalne faze. Porcelane za elektrotehniko uvrščamo v skupino tehničnih porcelanov, kjer danes prevladujejo glinični porcelani. Njihova mineraloška struktura je sestavljena iz korunda, mulita, kvarca in steklaste faze.

Lastnosti tehničnih porcelanov za elektrotehniko so opredeljene v standardu IEC 60672-3, Keramični in stekleni izolacijski materiali. Najvišje mehanske trdnosti med alkalijskimi alumosilikatnimi porcelani imajo glinični porcelani v skupini C 130, ki imajo upogibno trdnost

minimalno140 MPa neglazirani in minimalno 160 MPa glazirani ter temperaturni razteznostni koeficient α od 30 do 600 °C do $7x10^{-6}K^{-1}$. Razvoj novih elektrotehničnih izdelkov ali samo izboljšanje obstoječih pogosto terja od vgrajenih materialov več kot opredeljuje standard. Pri gliničnih porcelanih se pojavljajo predvsem zahteve po višji mehanski trdnosti, nižjem temperaturnem razteznostnem koeficientu in enostavnejši izdelavi.

Običajne surovine, iz katerih se izdelujejo tehnični porcelani z vsebnostjo Al_2O_3 več kot 50 % in se odlikujejo po visokih mehanskih trdnostih, so kalcinirana glinica, kaolin, glina in glinenec. V sestavi materiala je glinica pustilo, ki ima v žganem materialu funkcijo skeleta. Kaolini in gline so naravne plastične komponente, ki omogočojo plastično preoblikovanje materiala v ekstrudorju in se v procesu žganja fazno pretvorijo v mulit in delno v steklasto fazo. Glinenci so talila, ki v procesu žganja tvorijo steklasto fazo, katere zadostna količina zagotavlja nepropustnost žganega materiala.

Med glinenci, ki se najpogosteje uporabljajo kot talila v tehničnih porcelanih, so kalijevi glinenci, npr. mikroklin in ortoklas, natrijevi glinenci, npr. albit in natrijsko-kalijski, ki je sestavljen iz nefelina, albita in mikroklina. Vrsta in količina glinenca bistveno vpliva na temperaturo žganja in mehanske ter termične lastnosti žganega materiala.

Kot talilo v keramičnih materialih in pomembna surovina za proizvodnjo steklo keramičnih materialov se vse pogosteje uporabljajo tudi litijevi alumosilikati kot izvor litijevega oksida - Li_2O . Litij je najlažji element v trdnem stanju ter ima najmanjši ionski radij in najvišji ionski potencial od vseh alkalnih kovin, njegov oksid spada med najbolj aktivna talila in je potencialno primeren za znižanje temperature žganja keramičnih materialov. Navedeno je opisal Charles Merivale: "Lithium in Ceramics", Am. Ceram. Soc. Bull., 82 (4), 2003, 61-65. Najdostopnejši litijev mineral je spodumen. Uporablja se pri pripravi stekel, glazur, kvarčnih porcelanov ter drugih keramičnih materialih. Prispeva k izboljšanju mehanskih lastnosti in omogoči energetske prihranke zaradi nižanje temperature žganja. Ti materiali se uporabljajo na primer kot gospodinjski porcelan, porcelan in keramika za ploščice.

Uporaba litijevih mineralov kot talilo predvsem v kremenovih porcelanih, mulitni ter korundni keramiki je znana in objavljena v dostopni literaturi, kot na primer :

- Dilshat U. Tulyaganov, Simeon Agathopoulos, Hugo R. Fernandes, José M.F. Ferreira: Influence of Li_2O Doping on Non-Isothermal Evolution of Phases in K-Na—Containing Aluminosilicate Matrix, J. Am. Ceram. Soc., 89 (1), 2006, 292-297.
- D.U. Tulyaganov, S. Agathopoulos, H.R. Fernandes, J.M.F. Ferreira, Influence of lithium oxide an auxiliary flux on the properties of triaxial porcelain bodies, Journal of European Ceramic Society, 26, 2006, 1131-1139.
- Ammini Yamuna, Sankaranarayanan Devanarayanan, Mullite-β-Spodumene Composites from Aluminosilicates, J.Am.ceram. Soc., 84 (8), 2001, 1703-1709.
- Athanasius P. Bayuseno, Bruno A. Latella, Brian H. O´Connor, Resistance of Alumina-Spodumene Ceramics to Thermal Shock, J. Am. Ceram. Soc., 82 (4), 1999, 819-824.
- I.M. Low, E. Mathews, T. Garrod, D. Zhou, Processing of spodumene-modified mullite ceramics, J. Mater. Sci., 32, 1997, 3807-3812.
- Charles Merivale, Lithium in ceramics, Am.Cer.Soc.Bull.,82 (4), 2003, 61-65

Kot talilo v gliničnih porcelanih se je dosedaj uporabljalo zmes talil na osnovi natrijskih in kalijskih glinencev. S temi glinenci se ne da doseči visokih mehanskih trdnosti in nizkega temperaturnega razteznostnega koeficienta.

Naloga in cilj izuma je takšen glinični porcelan, ki bo imel visoko mehansko trdnost in nizek temperaturni razteznostni koeficient.

Po izumu je naloga rešena z gliničnim porcelana z dodatkom litijevih mineralov, ki omogočijo žganje pri 1280 do 1330°C, keramika ima po žganju mehansko upogibno trdnost višjo kot 200 MPa ter temperaturni razteznostni koficient nižji kot 5,7 x $10^{-6}K^{-1}$.

Izhodiščni material, to je zmes za pripravo gliničnega porcelana po izumu vsebuje v masnih deležih sestavine:

- od 41 do 45 % kalcinirane glinice, ki vsebuje manj kot 0,2 % natrijevega oksida in ima povprečno velikost delcev od 2 do 7 mikrometrov;
- od 5 do 25 % kaolina z vsebnostjo železovega oksida od 0,4 do 1,2 %;
- od 8 do 14 % glinastih komponent s skupno vsebnostjo natrijevega oksida manj kot 2,0 %;
- od 7 do 15 % kalijevega alumosilikata z vsebnostjo železovega oksida manj kot 0,2 %;
- od 8 do 16 % litijevega alumosilikata z vsebnostjo železovega oksida manj kot 0,3 %, ter

- dodatke, ki so lahko elektroliti za spreminjanje pH vrednosti in površinsko aktivne snovi.

Po postopku po izumu se izhodiščni material ter dodatki meljejo v mlinu, ki je obložen s keramično oblogo in vsebuje krogle iz korundne keramike z vsebnostjo Al_2O_3 od 90 do 94 %. Mletje traja od od 4-24 ur. Po mletju se suspenziji odstrani del vode s filtriranjem na filter stiskalnici, kjer se odstrani voda do končne vsebnosti vlage 18 do 20 %, ali z razprševanjem na sušilno razpršilnem stolpu, kjer se preoblikuje v granulat s končno vsebnostjo vlage 1 do 5 %. Za oblikovanje izdelkov v ekstrudorju mora imeti keramični material vsebnost vlage od 18 do 20 %. Zato je potrebno v primeru odstranjevanja vode v sušilno razpršilnem stolpu granulat dodatno navlažiti in homogenizirati v mešalniku. Po mletju in eventuelnem vlaženju in homogenizaciji je tako dobljeni drugi material primeren za izdelavo oblikovancev, to je za oblikovanje končnih izdelkov npr. v ekstrudorju. Po oblikovanju se oblikovanci osušijo tako, da vsebujejo manj kot 1 % vlage. Oblikovanci se po potrebi glazirajo in nato žgejo pri temperaturi 1280 do 1330 °C v času od 1 do 4 ure tako, da se dobi glinični porcelan po izumu, ki vsebuje od 58 do 62 %. Al_2O_3.
Med žganjem so oblikovanci v vertikalnem ali horizontalnem položaju. Po žganju imajo izdelki lahko že končno obliko in dimenzije, v nasprotnem primeru se žgane oblikovance razreže na končne dimenzije in po potrebi površinsko obdela.

Iz nevedenih sestavin izhodiščnega materiala se dobi po mletju, oblikovanju in žganju glinični porcelan po izumu, ki vsebuje od 58 do 62 % aluminijevega oksida, od 0,3 do 0,6 % železovega oksida, od 0,1 do 0,3 % natrijevega oksida, od 1,5 do 2,5 % kalijevega oksida ter od 0,8 do 1,2 % litijevega oksida, kar v procesu žganja tvori glinični porcelan z visoko mehansko trdnostjo in nizkim temperaturnim razteznostnim koeficientom.

Izboljšane mehanske in termične lastnosti gliničnega porcelana ter zmanjšanje deformacije pri žganju so bile po izumu dosežene z uvedbo kombinacije talil na osnovi kalijevih in litijevih alumosilikatov namesto običajnih kalijevih in natrijevih talil ter s popravkom vsebnosti plastičnih komponent in pustila. Plastične komponete prispevajo k oblikovnosti keramičnega materiala, ne pa k mehanskih lastnostim, to sta glina mas.% 8-14% in kaolin 5-25%. Pustilo pa je glinica, ki ima že definirano območje.

Nova kombinacija talil na osnovi litijevih in kalijevih alumosilikatov je sestavljena tako, da zmanjšuje razteznostni koeficient steklaste faze in vpliva na tvorbo mineralov z nižjim temperaturnim razteznostnim koeficientom. Oblikovanci pripravljeni po postopku po izumu imajo zmanjšano deformacijo med žganjem 15 do 25 % v primerjavi s keramičnimi materiali z vsebnostjo Al_2O_3 od 58 do 62 % in izdelanimi na osnovi kombinacije natrijevih in kalijevih alumosilikatov. Zaradi manjše deformacije med žganjem se iz materiala po izumu lahko ekstrudirajo daljše cevi ali palice.

Izvedbeni primer 1

Sestavine, ki vsebujejo naravno vlago: kalcinirana glinica (774 kg), plastična kaolinitna glina (258 kg), plastična montmorilonitna glina (20 kg), kaolin (435 kg), kalijev glinenec (162 kg) in spodumen (234 kg) damo v mlin, dodamo vodo in natrijev polifosfat v količini 0,18 masnega %, tako da ima končna suspenzija razmerje med suho snovjo in vodo 60,5/39,5 in je suhe snovi in vode 2958 kg. Suspenzijo meljemo 18 ur ali do ostanka 1,0 do 4 masnega % na situ 0,025 mm. Po mletju suspenzijo razpršimo na sušilno razpršilnem stolpu v granulat z vsebnostjo vlage 1 do 4 %, granulat v gnetilcu platificiramo, tako da mu dodamo vodo v količini, da je po homogenizaciji vsebnost vlage 19,5 %. V ekstrudorju iz plastične mase oblikujemo preizkušance premera 11 mm ter dolžine 120 mm za meritve upogibne trdnosti in 180 mm za meritve deformacije med žganjem. Preizkušance sušimo pri temperaturi 105 °C, tako dolgo da vsebujejo manj kot 1 % vlage in žgemo pri temperaturi pri 1300 °C 1 uro. Žgani preizkušanci imajo upogibno trdnost 203 MPa, deformacijo po žganju 14 mm in temperaturni razteznostni koeficient v območju od 30 do 600 °C 5,5 x $10^{-6}K^{-1}$.

Izvedbeni primer 2

Enako kot v primeru 1, le da v ekstrudorju iz plastične mase izdelamo preizkušance premera 11 mm in dolžine 150 mm, jih sušimo pri 105 °C tako dolgo , da vsebujejo manj kot 1 % vlage in glaziramo s potapljanjem v glazurno suspenzijo ter žgemo pri temperaturi 1300 °C 1 uro. Žgemo jih vertikalno, tako da so obešeni na ploščo s koničnimi izvrtinami. Žgani preizkušanci imajo upogibno trdnost 243 MPa in toplotni razteznostni koeficient v območju od 30 do 600 °C 5,6 x $10^{-6}K^{-1}$.

PATENTNI ZAHTEVKI

1. Postopek za izdelavo gliničnega porcelana, značilen po tem,
da se mokro melje zmes sestavin v masnih deležih:
- od 41 do 45 % kalcinirane glinice, ki vsebuje manj kot 0,2 % natrijevega oksida in ima povprečno velikost delcev od 2 do 7 mikrometrov,
- od 5 do 25 % kaolina z vsebnostjo železovega oksida od 0,4 do 1,2 %,
- od 8 do 14 % glinastih komponent s skupno vsebnostjo natrijevega oksida manj kot 2,0 %,
- od 7 do 15 % kalijevega alumosilikata z vsebnostjo železovega oksida manj kot 0,2 %, in
- od 8 do 16 % litijevega alumosilikata z vsebnostjo železovega oksida manj kot 0,3 %,

pri čemer se mletje navedene zmesi izvaja v mlinu, ki je obložen s keramično oblogo in vsebuje krogle iz korundne keramike z vsebnostjo Al_2O_3 od 90 do 94 %; mletje traja od od 4-24 ur; po mletju se ustvari suspenzijo z vsebnostjo vlage 18 do 20 % iz katere se izdela oblikovance, ki se nato osušijo tako, da vsebujejo manj kot 1 % vlage; oblikovanci se po potrebi glazirajo in nato žgejo pri temperaturi 1280 do 1330 °C v času od 1 do 4 ure.

2. Glinični porcelan, izdelan po postopku po zahtevku 1, značilen po tem, da porcelan po vsebuje od 58 do 62 % aluminijevega oksida, od 0,3 do 0,6 % železovega oksida, od 0,1 do 0,3 % natrijevega oksida, od 1,5 do 2,5 % kalijevega oksida ter od 0,8 do 1,2 % litijevega oksida.

REPUBLIKA SLOVENIJA
MINISTRSTVO ZA GOSPODARSTVO

URAD REPUBLIKE SLOVENIJE
ZA INTELEKTUALNO LASTNINO
1000 LJUBLJANA, KOTNIKOVA 6

ZAHTEVA ZA PODELITEV PATENTA

1. Naslov za obveščanje:
ITEM d.o.o.
Resljeva cesta 16
1000 Ljubljana

Tel.: (01) 432 01 67
Faks: (01) 431 53 31 Šifra: 022-P075/09

Potrdilo o prejemu prijave
(izpolni urad)

Datum vložitve prijave: 30.3.09

Številka prijave: **P-** 20090084

Žig urada in podpis:

2. Prijavitelj (priimek, ime in naslov; za pravne osebe firma in sedež):

Institut "Jožef Stefan"
Jamova 39
1000 Ljubljana

ETI Elektroelement d.d.
Obrezija 5
1411 Izlake

3. Zastopnik: ITEM d.o.o. Registrska številka: 134

4. Izumitelj (priimek, ime in naslov):
OBERŽAN Martina, Sallaumines 3, 1420 Trbovlje
HOLC Janez, Zupanova 7, 1234 Mengeš
BUH Marjan, Hlavče njive 6, 4224 Gorenja vas
LAVRAČ Ivan, Potoška vas 41A, 1410 Zagorje
KOSEC Milena, Smlednik 80, 1216 Smlednik

5. Naziv izuma: GLINIČNI PORCELAN Z IZBOLJŠANIMI TERMIČNIMI LASTNOSTMI IN POSTOPEK NJEGOVE IZDELAV

6. Podatki o zahtevani prednostni pravici in podlagi zanjo:

7. Dodatne zahteve:
- ☐ prijava je za patent s skrajšanim trajanjem
- ☐ predhodna objava patenta po preteku____ mesecev
- ☐ prijava je izločena iz prijave številka:_____

8. Izjava:
- ☐ izjava o skupnem predstavniku

9. Priloge
- ☒ opis izuma, ki ima 8 strani
- ☒ patentni zahtevek (zahtevki), ki ima(jo) 1 strani; število zahtevkov: 7
- ☒ skice (če so zaradi opisa izuma potrebne); število listov: 4
- ☒ povzetek
- ☐ potrdilo o plačilu prijavne pristojbine _____
- ☐ potrdilo o deponiranju biološkega materiala, če gre za izum, ki ga ni mogoče drugače opisati
- ☐ pooblastilo zastopniku
- ☐ generalno pooblastilo zastopniku je deponirano pri uradu pod št.: ____
- ☐ potrdilo o razstavni prednostni pravici
- ☐ podatki o drugih prijaviteljih
- ☐ podatki o drugih izumiteljih
- ☐ prikaz zaporedja nukleotidov ali aminokislin v opisu
- ☐ prijava je bila predhodno posredovana po faksu ali v elektronski obliki
- ☐ ____

ITEM d.o.o., Andrej Vojir
Priimek in ime ter podpis prijavitelja (zastopnika)

GLINIČNI PORCELAN Z IZBOLJŠANIMI TERMIČNIMI LASTNOSTMI IN POSTOPEK NJEGOVE IZDELAVE

Predmet izuma je glinični porcelan z izboljšanimi termičnimi lastnostmi in postopek njegove izdelave. Glinični porcelan po izumu spada v skupino alkalijskih alumosilikatnih porcelanov z visoko mehansko trdnostjo in se uporablja kot izolant na področju elektrotehnike ali kot konstrukcijska keramika. Izum spada na področje kemije materialov.

Tehnični problem

Glinični porcelan uvrščamo v skupino tehničnih porcelanov, ki se najpogosteje uporabljajo v elektrotehniki. Tehnični porcelani so sestavni del zaščitnih in nosilnih elementov, ki se vgrajujejo v sisteme za transmisijo, distribucijo in uporabo električnega toka. Stalna in nemotena razpoložljivost električnega toka ter njegova racionalna uporaba je odvisna od zanesljivosti delovanja vseh elementov, ki so vgrajeni v sistemu od proizvodnje do uporabe električnega toka. Zato razvoj elektrotehnike terja izboljšanje lastnosti tehničnih porcelanov v smislu večje zanesljivosti in trajnosti v spreminjajočih se pogojih uporabe, kjer je material izpostavljen večjim mehanskim in toplotnim obremenitvam. Povečujejo se zahteve po izboljšanih lastnostih tehničnega porcelana, med katerimi so najbolj pomembne električna trdnost, trdota in mehanska trdnost, odpornost na visoke temperature, odpornost na temperaturne spremembe in korozijska odpornost. Tehnični porcelan se kot izolacijski material v elektrotehniki, kjer ima med izolacijskimi materiali najdaljšo tradicijo, ali na drugih področjih kot konstrukcijska keramika še vedno pogosto uporablja, ker je relativno poceni in ker ne vsebuje snovi, ki bi škodljivo vplivale na okolje in zdravje ljudi.

Mehanska trdnost porcelana se povečuje z vsebnostjo korunda, ker prisotnost korunda z višjim Young-ovim modulom elastičnosti bistveno prispeva k izboljšanju mehanskih lastnosti porcelana (Liebermann, J., Microstructure properties and product quality of strength-stressed high-voltage insulators. *Am. Ceram. Soc. Bull.*, 2003, **82**, 39-46.). Prisotnost prostega α-kremena negativno vpliva na mehanske trdnosti porcelana (Warshaw, S. I. and Seider, R., Comparison of strength of triaxial porcelains containing alumina and silica. *J. Am. Ceram. Soc.*, 1967, **50**, 337-343.). Pri žganju porcelana se pojavijo v procesu ohlajevanja v kvarčnih zrnih in

v steklasti fazi v njihovi neposredni bližini mikrorazpoke kot posledica volumske spremembe, ki nastane pri fazni transformaciji kremena $\beta \rightarrow \alpha$ pri 573°C. Prisotnost mikrorazpok v porcelanu vpliva na poslabšanje njegovih mehanskih in termičnih lastnosti, zato je za doseganje visokih mehanskih trdnosti in izboljšanih termični lastnosti potrebno uporabiti takšne surovine in tehnološke postopke, ki onemogočijo prisotnost prostega kremena po žganju.

Glinični porcelani, ki se odlikujejo po visokih mehanskih trdnostih, vsebujejo običajno več kot 40 ut.% in manj kot 65 ut.% aluminijevega oksida. Na povečanje mehanskih trdnosti bistveno vpliva količina in velikost kristalov korunda, ki se nahajajo v steklasti fazi. Korund je značilen po tem, da ima visok Young-ov modula elastičnosti. Zato se sorazmerno s prisotno količino korunda v porcelanu povečuje njegova mehanska trdnost (Liebermann, J. and Schulle, W., Bauxite Porcelain. *Am. Ceram. Soc. Bull.*, 2002, 81, 33-38.). Povečevanje količine korunda neugodno vpliva na povečanje temperaturnega raztezka porcelana in s tem zmanjšuje njegovo odpornost na termične šoke.

Na izboljšanje odpornosti gliničnega porcelana na termične šoke najbolj vplivamo z zmanjšanjem temperaturnega razteznostnega koeficienta, povečanjem mehanske trdnosti in zmanjšanjem Young-ovega modula elastičnosti. Ker se s povečevanjem mehanske trdnosti v porcelanu zaradi povečane količine korunda povečuje tudi njegov modul elastičnosti, je za izboljšanje odpornosti na termične šoke porcelana potrebno zmanjšati njegov temperaturni razteznostni koeficient.

Naloga izuma je izdelava gliničnega porcelana, ki bi imel zaradi visoke mehanske trdnosti in nizkega temperaturnega razteznostnega koeficienta izboljšano odpornost na termične šoke ter bi bil primeren za izdelavo izolacijskih sestavnih delov v elektrotehniki in elementov konstrukcijske keramike in bi se zaradi izboljšanih temičnih lastnosti razširila možnost njegove uporabe.

Stanje tehnike

Glinični porcelani spadajo v skupino alkalijskih alumosilikatnih keramičnih materialov, katerih fizikalne lastnosti izvirajo iz njihove fazne sestave in mikrostrukture. Poleg steklaste faze so v mineraloški strukturi gliničnega porcelana prisotni še kristali korunda, mulita in kremena.

Mikrostruktura gliničnega porcelana je odvisna od sestave in nabora naravnih in sintetičnih surovin ter postopka njegove izdelave, ki vključuje mletje surovin, sušenje surove mase, oblikovanje in žganje. Izdelki iz gliničnega porcelana se oblikujejo po postopku ekstrudiranja, enoosnega suhega stiskanja vlivanja v mavčne modele ali injekcijskrega brizganja.

Odpornost gliničnega porcelana na termične šoke je v veliki meri odvisna od njegovega temperaturnega razteznostnega koeficienta, na katerega vplivajo prisotne mineraloške strukturne faze, ki imajo različne temperaturne razteznostne koeficiente. Med kristalnimi fazami, ki so običajno prisotni v gliničnem porcelanu, ima kremen najvišji temperaturni razteznostni koeficient α, ki v temperaturnem območju od 20 do750 °C znaša $\sim 23 \times 10^{-6}K^{-1}$. α korunda od 20 do 1000 °C je $\sim 8 \times 10^{-6}K^{-1}$, α mulita od 20 do 900 °C je $\sim 4{,}9 \times 10^{-6}K^{-1}$ in α steklaste faze od 20 do 900 °C je $\sim 3 \times 10^{-6}K^{-1}$.

Surovine, ki se uporabljajo za izdelavo gliničnega porcelana, ki vsebuje okrog 60% Al_2O_3, so kalcinirana glinica kot pustilo, ki ima funkcijo skeleta, kaolin in glina kot plastična komponenta, ki omogoča plastično preoblikovanje mase, in talila, ki v procesu sintranja tvorijo steklasto fazo, katere zadostna količina zagotavlja nepropustnost sintranega materiala. V porcelanskih materialih se kot talila običajno uporabljajo kalijevi in natrijevi alumosilikati. Z namenom znižanja temperature sintranja in izboljšanja mehanskih lastnosti porcelanov se vse pogosteje uporabljajo tudi talila na bazi litijevih alumosilikatov v kombinaciji z natrijevimi ali kalijevimi alumosilikati (Fishwick, J.H., Application of Lithium in Ceramics. Cahners Books, Boston, 1974, M. Oberžan in ostali, patentna prijava št. P-200700138, Ljubljana 2007).

Litijevi alumosilikati se odlikujejo po nizkem razteznostnem koeficientu. Tipični litijevimi alumosilikati, z nizkimi razteznostnimi koeficienti, katere je v ternarnem sistemu Li_2O-Al_2O_3-SiO_2 proučeval Hummel (Hummel, F. A., Thermal expansion properties of some synthetic lithia minerals, *J. Am. Ceram. Soc.*, 1951, 34(8), 235-239.) so: $Li_2O{\cdot}Al_2O_3{\cdot}2SiO_2$ ali eukriptit z α od 25 do 1000 °C $-0{,}6 \times 10^{-6}K^{-1}$, $Li_2O{\cdot}Al_2O_3{\cdot}4SiO_2$ ali spodumene z α od 25 do 1000 °C $0{,}9 \times 10^{-6}K^{-1}$, $Li_2O{\cdot}Al_2O_3{\cdot}6SiO_2$ z α od 25 do 1000 °C $0{,}6 \times 10^{-6}K^{-1}$, $Li_2O{\cdot}Al_2O_3{\cdot}8SiO_2$ ali petalit z α od 25 do 1000 °C $0{,}3 \times 10^{-6}K^{-1}$ in $Li_2O{\cdot}Al_2O_3{\cdot}10SiO_2$ z α od 25 do 1000 °C $0.5 \times 10^{-6}K^{-1}$.

Litijevi alumosilikati z nizkim temperaturnim razteznostnim koeficientom so najpogosteje prisotni v steklo-keramiki, ki se odlikuje po visoki odpornosti na termične šoke, visoki mehanski trdnosti in odlični kemijski odpornosti. Termični postopki tvorbe litijevih mineralov v steklo-keramiki so znani iz raziskav in uporabljeni v praksi.

Postopki tvorbe litijevih mineralov z nizkim temperaturnim razteznostnim koeficientom iz steklaste faze porcelanskega materiala še niso objavljeni v dostopni literaturi.

Opis rešitve tehničnega problema

Predloženi izum rešuje problem doseganja nizkega razteznostnega koeficienta in visokih mehanskih trdnosti z novim postopkom sintranja izboljšanega gliničnega porcelana, ki vsebuje od 58 do 62 ut.% Al_2O_3, od 0,1 do 0,3 ut. % natrijevega oksida, od 1,5 do 2,5 ut. % kalijevega oksida, manj kot 0,5 ut. % železovega oksida ter 1,0 do 1,4 ut. % litijevega oksida in je primeren za oblikovanje po postopku ekstrudiranja, enoosnega stiskanja, vlivanja v mavčne modele ali injekcijskega brizganja. Nižji temperaturni razteznostni koeficient gliničnega porcelana z visokimi mehanskimi trdnostmi je po izumu dosežen z novim postopkom sintranja, tako da se material najprej sintra v temperaturnem območju 1290 do 1330 °C, ohladi na temperaturo, ki je nižja ali enaka 700 °C, nato pa termično obdela v temperaturnem območju od 900 do 1050 °C, kjer iz steklaste faze kristalizirajo litijevi alumosilikati z nizkim razteznostnim koeficientom in vplivajo na znižanje razteznostnega koeficienta gliničnega porcelana. Glinični porcelan izdelan po izumu ima toplotni razteznostni koeficient od 4,6 do 5,2 × $10^{-6}K^{-1}$ v temperaturnem območju od 20 do 600 °C.

Po sintranju v temperaturnem območju 1290 do 1330 °C je v gliničnem porcelanu z metodo rentgenske difrakcije na praškastem vzorcu identificirana prisotnost kristalov korunda in mulita, medtem ko je po termični obdelavi v temperaturnem območju od 900 do 1050 °C poleg korunda in mulita identificirana tudi prisotnost litijevega alumosilikata.

Prednostno je predmet izuma sintran keramični material, ki ima od 15 do 20 % zmanjšan temperaturni razteznostni koeficient v temperaturnem območju od 20 do 600°C v primerjavi z gliničnimi porcelani, ki vsebujejo od 58 do 62 ut.% Al_2O_3 in so žgani po običajnem postopku, tako da so v peči naravno ali prisiljeno ohlajeni na sobno temperaturo. Zmanjšanje

temperaturnega razteznostnega koeficienta je doseženo po izumu z toplotno obdelavo sintranega materiala v temperaturnem območju, kjer iz steklaste faze, ki vsebuje Li_2O, kristalizira litijev mineral, ki ima nižji razteznostni koeficient v primerjavi z ostalimi prisotnimi fazami.

Po izumu izdelamo keramični material z mokrim mletjem surovin v krogelnem mlinu. Po mletju se suspenziji odstrani voda z vpijanjem v mavčne modele, s filtriranjem na filter stiskalnici ali z razprševanjem na sušilno razpršilnem stolpu. Izdelki se lahko oblikujejo z vlivanjem v mavčne modele, injekcijskim brizganjem, ekstrudiranjem v vakuum stiskalnici ali suhim stiskanjem. Med sintranjem na temperaturi 1290 do 1330°C in termično obdelavo na temperaturi 900 do 1050 °C so izdelki v horizontalnem ali vertikalnem položaju.

Predmet izuma je alkalijski glinični porcelan, označen s tem, da po svoji kemijski sestavi u vsebuje od 30 do 62 ut. % aluminijevega oksida, od 0,1 do 0,3 ut. % natrijevega oksida, od 1,5 do 2,5 ut. % kalijevega oksida, manj kot 0,5 ut. % železovega oksida ter 1,0 do 1,4 ut. % litijevega oksida in da po svoji mineraloški sestavi po sintranju vsebuje minerale korund, mulit in litijev alumosilikat.

Material z zgoraj navedeno kemijsko sestavo je sintran po postopku, ki vključuje segrevanje od sobne temperature na maksimalno temperaturo sintranja od 1290 do 1330°C in zadrževanje na maksimalni temperaturi od 30 do 130 minut, ohlajevanje po sintranju na temperaturo, ki je enaka ali nižja od 700 °C, ponovno segrevanje na temperaturo termične obdelave 900 do 1050 °C in zadrževanje na temperaturi termične obdelave od 10 do 240 minut.

Material z zgoraj navedeno kemijsko sestavo, izdelan po postopku sintranja in termične obdelave v smislu izuma ima visoko upogibno trdnost, ki je višja kot 160 MPa, in nizek temperaturni razteznostni koeficient α, ki ima vrednost 4.6 do $5.2 \times 10^{-6}K^{-1}$ od 20 do 600°C.

Izvedbeni primer 1

V mlin, ki je izdelan iz gliničnega porcelana in vsebuje 4 kg mlevnih krogel izdelanih iz keramičnega materiala, ki vsebuje 92 ut.% Al_2O_3, zatehtamo 1247 g kalcinirane glinice, 393 g

kaolinitne gline, 32 g montmorilonitne gline, 681 g kaolina, 261 g kalijevega glinenca in 377 g spodumna, vse z naravno vlago. Dodamo 5,2 g deflokulanta natrijevega polifosfata in vodo, tako da ima končna suspenzija utežno razmerje med suho snovjo in vodo 60,2/39,8. Suspenzijo meljemo 8 ur. Po mletju suspenzijo osušimo na mavčnem modelu na vlago 23 ut.% in v ekstrudorju oblikujemo paličaste preizkušance premera 11 mm in dolžine 140 mm ter premera 8 mm in dolžine 70 mm. Preizkušance osušimo na temperaturi 105 °C na vlago pod 1 ut.% in jih sintramo leže v korundnih kasetah tanko posutih s kremenom. V postopku sintranja narašča v peči temperatura s hitrostjo 2 °C na minuto do maksimalne temperature 1330 °C, sledi zadrževanje na maksimalni temperaturi 60 minut in naravno ohlajevanje na sobno temperaturo. Rentgenski posnetek (izvor rentgenskih žarkov $Cu_{K\square}$)praškastega toplotno obdelanega vzorca je na Sliki 1. Identificirali smo dve fazi, korund označen kot A in mulit, označen kot M. Po sintranju se preizkušanci toplotno obdelajo v peči s hitrostjo segrevanja 2,5 °C na minuto do temperature 930 °C ter se na tej temperaturi zadržijo 10 minut in nato naravno ohladijo na sobno temperaturo. Po sintranju imajo preizkušanci upogibno trdnost 179 MPa, volumsko gostoto 2,77 g/cm^3 in temperaturni razteznostni koeficient 5,57 × $10^{-6}K^{-1}$ v temperaturnem območju od 20 do 600°C. Po toplotni obdelavi imajo preizkušanci upogibno trdnost 182 MPa, volumsko gostoto 2,78 g/cm^3 in toplotni razteznostni koeficient 5,17 × $10^{-6}K^{-1}$ v temperaturnem območju od 20 do 600 °C. Rentgenski posnetek (izvor rentgenskih žarkov $Cu_{K\square}$)praškastega toplotno obdelanega vzorca je na Sliki 2. Identificirali smo tri faze, korund označen kot A, mulit, označen kot M in litijev alumosilikat označen kot L. Litijev alumosilikat je identificiran kot $Li_xAl_xSi_{3-x}O_6$, podatkovna baza PDF JCPDS 031-0707.

Izvedbeni primer 2

Postopek priprave materiala je vključno s pripravo preizkušancev enak kot v Izvedbenem primeru 1. V postopku sintranja narašča v peči temperatura s hitrostjo 3°C na minuto do maksimalne temperature 1320 °C, sledi zadrževanje na maksimalni temperaturi 90 minut in naravno ohlajevanje na temperaturo 700°C in zadrževanjem na tej temperaturi 30 minut, čemur sledi nadaljevanje segrevanja s hitrostjo 2,5 °C na minuto do 950 °C in zadrževanje na tej temperaturi 120 minut. Po sintranju in toplotni obdelavi imajo preizkušanci upogibno trdnost 165 MPa, volumsko gostoto 2,85 g/cm^3 in temperaturni razteznostni koeficient 4,97 × $10^{-6}K^{-1}$ v temperaturnem območju od 20 do 600°C. Rentgenski posnetek (izvor rentgenskih žarkov $Cu_{K\square}$) praškastega toplotno obdelanega vzorca je na Sliki 3. Identificirali smo tri faze, korund

označen kot A, mulit, označen kot M in litijev alumosilikat označen kot L. Litijev alumosilikat je identificiran kot $Li_xAl_xSi_{3-x}O_6$, podatkovna baza PDF JCPDS 031-0707.

Izvedbeni primer 3

Postopek priprave materiala je vključno s pripravo preizkušancev enak kot v Izvedbenem primeru 1. V postopku sintranja narašča v peči temperatura s hitrostjo 3 °C na minuto do maksimalne temperature 1320 °C, sledi zadrževanje na maksimalni temperaturi 90 minut in naravno ohlajevanje na temperaturo 500 °C in zadrževanjem na tej temperaturi 30 minut, čemur sledi nadaljevanje segrevanja s hitrostjo 5 °C na minuto do 950 °C in zadrževanje na tej temperaturi 30 minut. Po sintranju in toplotni obdelavi imajo preizkušanci upogibno trdnost 179 MPa, volumsko gostoto 2,68 g/cm^3 in toplotni razteznostni koeficient 5,03 × $10^{-6}K^{-1}$ v temperaturnem območju od 20 do 600 °C. Rentgenski posnetek (izvor rentgenskih žarkov $Cu_{K\square}$)praškastega toplotno obdelanega vzorca je na Sliki 4. Identificirali smo tri faze, korund označen kot A, mulit, označen kot M in litijev alumosilikat označen kot L. Litijev alumosilikat je identificiran kot $Li_xAl_xSi_{3-x}O_6$, podatkovna baza PDF JCPDS 031-0707.

PATENTNI ZAHTEVKI

1. Glinični porcelan, označen s tem, da material po svoji kemijski sestavi vsebuje od 30 do 62 ut.% aluminiijevega oksida, od 0,1 do 0,3 ut.% natrijevega oksida, od 1,5 do 2,5 ut.% kalijevega oksida ter od 1,0 do 1,4 ut.% litijevega oksida.

2. Vsebnost železovega oksida v gliničnem porcelanu s sestavo, navedeno v zahtevku 1, označena s tem, da je materialu nižja od 0,5 ut.%.

3. Postopek sintranja gliničnega porcelana s sestavo, navedeno v zahtevku 1 in 2, označen s tem, da se keramični material sintra na temperaturi od 1290 do 1330 °C od 30 do 120 minut.

4. Postopek sintranja gliničnega porcelana s sestavo, navedeno v zahtevku 1, 2 in 3, označen s tem, da se keramični material po sintranju termično obdela na temperaturi od 900 do 1050 °C od 10 do 240 minut.

5. Postopek sintranja gliničnega porcelana s sestavo, navedeno v zahtevku 1, 2 in 3, označen s tem, da se keramični material po sintranju ohladi na sobno temperaturo in potem termično obdela pri temperaturi od 900 do 1050 °C v času od 10 do 240 minut.

6. Postopek sintranja gliničnega porcelana s sestavo, navedeno v zahtevku 1, 2 in 3, označen s tem, da se keramični material po sintranju ohladi na temperaturo enako ali nižjo od 700 °C in potem termično obdela pri temperaturi od 900 do 950°C in zadrži na tej temperaturi od 60 do 240 minut.

7. Postopek sintranja gliničnega porcelana s sestavo, navedeno v zahtevku 1, 2 in 3, označen s tem, da se keramični material po sintranju ohladi na temperaturo 500 do 550 °C in zadrži na tej temperaturi od 20 do 60 minut in potem termično obdela pri temperaturi od 900 do 1050 °C v času od 10 do 240 minut.

8. Keramični material, izdelan po postopku naveden v zahtevku 5, 6 in 7 vsebuje minerale korund, mulit in litijev alumosilikat.

Povzetek:

POSTOPEK ZA IZDELAVO PORCELANA Z IZBOLJŠANIMI LASTNOSTMI

Predmet izuma je tehnični porcelan in postopek njegove izdelave. Glinični porcelan po izumu spada v skupino alkalijskih alumosilikatnih porcelanov z nizkim toplotnim razteznostnim koeficientom in vsebuje od 58 do 62 ut.% aluminijevega oksida, od 0,1 do 0,3 ut.% natrijevega oksida, od 1,5 do 2,5 ut.% kalijevega oksida ter 1,0 do 1,4 ut.% litijevega oksida. Vsebnost železovega oksida v materialu je nižja kot 0,5 ut.%. Po sintranju v temperaturnem območju od 1290 do 1330 °C se keramični material toplotno obdela na temperaturi od 900 do 1050 °C v času trajanja od 10 do 240 minut. Keramični material z navedeno sestavo ter sintran in termično obdelan po opisanem postopku ima toplotni razteznostni koeficient 4.6 do 5.2 × $10^{-6}K^{-1}$ v temperaturnem območju od 20 do 600°C, upogibno trdnost višjo kot 160 MPa ter vsebuje minerale korund, mulit in litijev alumosilikat.

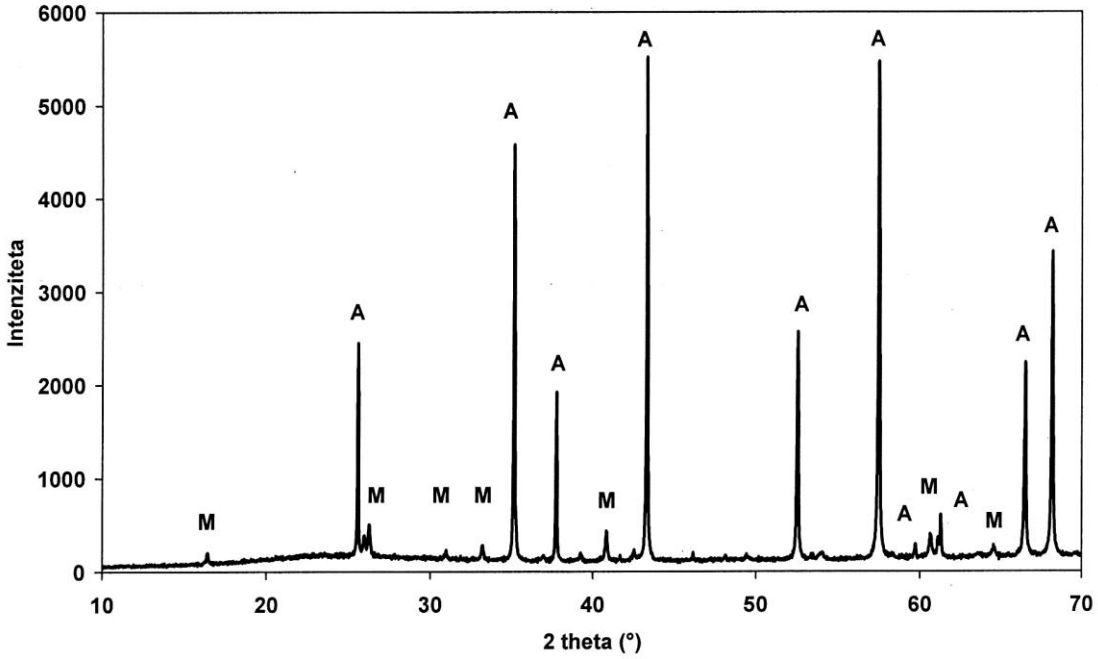
6000
5000
4000
3000
2000
1000
0
Intenziteta
10
20
30
40
50
60
70
2 theta (°)
A
M

Slika 1

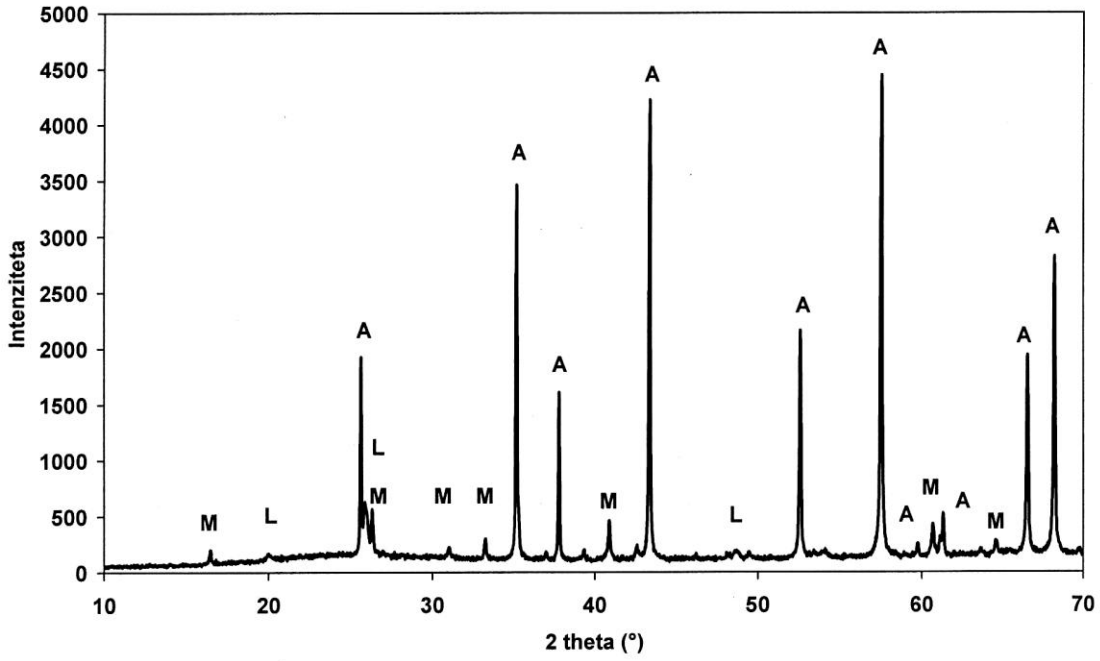
Intenziteta
2 theta (°)
5000
4500
4000
3500
3000
2500
2000
1500
1000
500
0
10
20
30
40
50
60
70
A
L
M

Slika 2

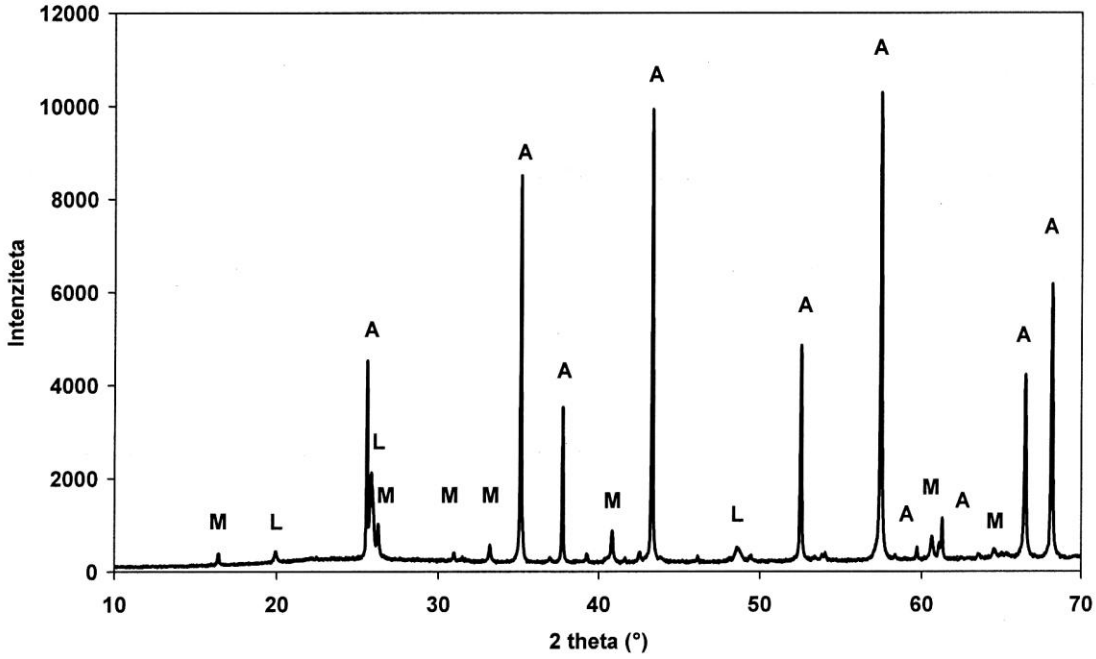
12000
10000
8000
6000
4000
2000
0
Intenziteta
10
20
30
40
50
60
70
2 theta (°)
A
L
M

Slika 3

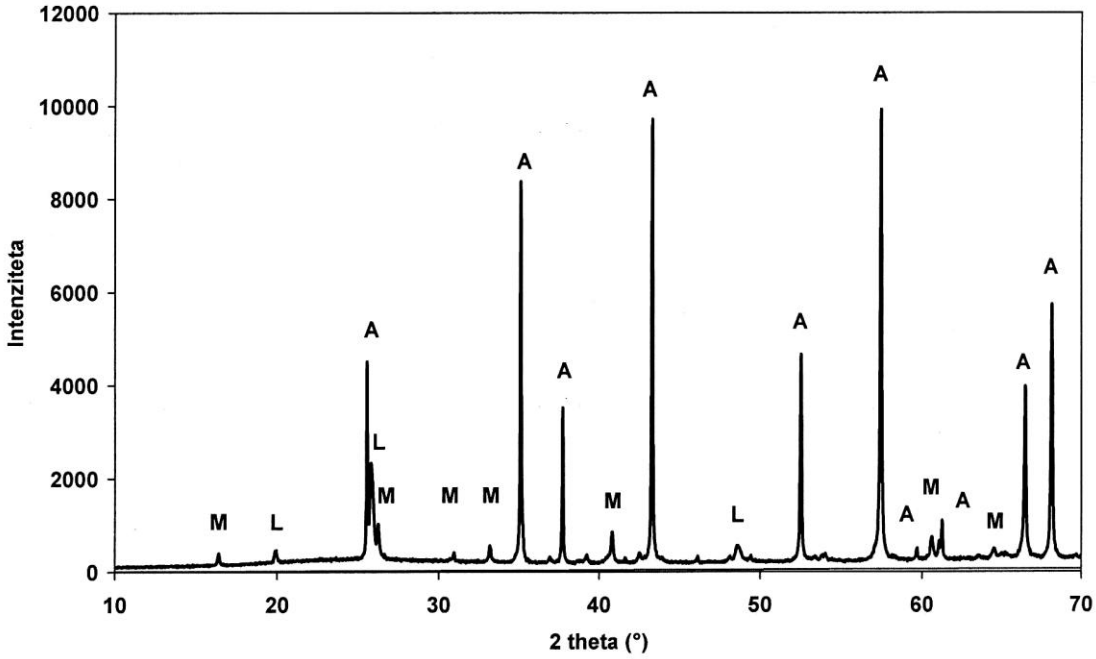
12000
10000
8000
6000
4000
2000
0
Intenziteta
10
20
30
40
50
60
70
2 theta (°)
A
L
M

Slika 4

Available online at www.sciencedirect.com
ScienceDirect
Journal of the European Ceramic Society 29 (2009) 2143–2152
www.elsevier.com/locate/jeurceramsoc

High-alumina porcelain with the addition of a Li_2O-bearing fluxing agent

M. Oberžan [a,*], J. Holc [b], M. Buh [b], D. Kuščer [b], I. Lavrač [a], M. Kosec [b,c]

[a] *ETI d.d, Obrezija 5, 1411 Izlake, Slovenia*
[b] *Institut Jožef Stefan, Jamova 39, 1000 Ljubljana, Slovenia*
[c] *Jožef Stefan International Postgraduate School, Jamova 39, 1000 Ljubljana, Slovenia*

Received 3 November 2008; received in revised form 26 January 2009; accepted 28 January 2009
Available online 24 February 2009

Abstract

We have studied the influence of increasing the amount of β-spodumene ($LiAlSi_2O_6$), as a Li_2O-containing flux, on the phase composition, the microstructure evolution and the physical properties of high-alumina porcelain. Quartz reacts with β-spodumene in the temperature range 1150–1250 °C, forming lithium aluminium silicates with a larger amount of SiO_2. The presence of lithium minerals contributes to a lower CTE for the fired bodies. At 1300 °C an improved flexural strength is achieved with compositions containing 1.0 or 1.2 wt.% of Li_2O, as a result of a more uniform microstructure. With increasing amounts of Li_2O the overfiring effect is greatly enhanced. The most favourable characteristics from an industrial perspective with regard to flexural strength and deformation during firing were attained by using a high-alumina porcelain composition containing 1.0 wt.% Li_2O.

Keywords: Porcelain; Spodumene; Sintering; Strength; Thermal expansion

1. Introduction

Technical porcelains, which are classified in the alkaline alumina silicate porcelain group, find diverse application in electrotechnics, most often as the insulating parts in electricity transmission, distribution and protection. The developments in electrical engineering dictate the need for technical porcelains with high reliability, and it has been shown that the reliability of porcelain strongly depends on the microstructure and phase composition.[1,2] The typical requirements for an electrical porcelain are a high mechanical strength and a good thermal shock resistance. To achieve a better mechanical strength for the porcelain body, alumina with its higher Young's modulus is used instead of quartz as a filler.[3,4] This increasing amount of alumina greatly contributes to the strength enhancement, but at the same time causes the thermal expansion to increases, thus reducing the thermal shock resistance. Therefore, to reduce the expansion of high-alumina porcelain it is necessary to reduce the expansion of the glassy phase or introduce low-expansion phases.

The viscous liquid that is formed during the firing of the porcelain body enables densification and the formation of the final microstructure.[5] The temperatures at which this liquid is formed are lowered by the introduction of flux, with sodium- and potassium-based feldspars being the most commonly used fluxes in porcelain. It has also been reported that a combination of feldspar and nepheline syenite contributes to the increased mechanical strength of porcelain bodies.[6] The level of vitrification, the pyroplastic deformation and the microstructure are affected by the mineralogical composition of the raw materials and by the level of equilibrium achieved.[7]

The use of lithium-bearing minerals as a liquid-phase sintering aid has been investigated in various types of ceramics. It was reported that spodumene as a partial replacement for feldspar can lower the firing temperature of sanitary chinaware bodies with a high content of flux when the feldspar-to-spodumene ratio is 70:30.[8] Bodies of electrical porcelain with a fairly high thermal shock resistance and mechanical strength were developed using 18.5–20.5 wt.% of spodumene and firing at 1380 °C.[9] Good properties for tableware porcelains were attained when the Li_2O content did not exceed 1.5 wt.%, and these compositions matured at temperatures 100–120 °C lower than standard, triaxial porcelain formulations.[10] The presence of spodumene, when 10 wt.% was added as a partial replacement for sodium feldspar,

* Corresponding author.
E-mail address: martina.oberzan@eti.si (M. Oberžan).

0955-2219/$ – see front matter © 2009 Elsevier Ltd. All rights reserved.
doi:10.1016/j.jeurceramsoc.2009.01.029

reduced the firing temperature and the shrinkage of the body mixes for stoneware tiles.[11] The use of lithium-bearing minerals as a liquid-phase sintering aid has also been investigated in other types of ceramics, for example, in mullite ceramics,[12,13] to lower the firing temperature and in alumina ceramics[14] to improve the thermal shock resistance. The influence of a Li_2O-bearing fluxing agent in a high-alumina porcelain body has not yet been investigated.

The aim of our work was to investigate the influence of Li_2O in combination with K_2O as a flux on the sintering behaviour and the physical properties of high-alumina porcelain bodies. The increasing amounts of Li_2O were introduced in compositions via a commercial spodumene concentrate. The investigations were assisted by a study of the phase composition and the microstructural development at different firing temperatures. All the characteristics were compared with an alumina porcelain body containing K_2O and Na_2O as the flux. New body formulations, suitable for extrusion and industrial applications, were developed.

2. Materials and experimental procedure

We compared the reference formulation (EN) with three model formulations (A, B, and C) of high-alumina porcelain. The model formulations were prepared using calcined alumina (HVA, Almatis GmbH, D), kaolin (Zettlitz Ia, Sedlecký kaolin a.s., CZ), illite clay (M1M, Stephan Smidt, D), bentonite (Portaclay A, Ankerpoort NV, NL), calcined spodumene (SC 7.5, Gwalia Consolidated Ltd, Australia) and potassium feldspar (Dorkasil 90, Dorfner, D). Additionally, 0.3 wt.% of binder based on polyvinyl alcohol was admixed to improve the plasticity for extrusion.

Conventional ceramic processing routes were used to prepare the model alumina porcelain bodies on a laboratory scale. First, the materials were wet milled with alumina balls for around 11 h. The particle size and the particle size distribution after milling were measured by laser sedigraph (Matroc Microtrac S3500). The distribution for all the model compositions was bimodal, with the first maximum around 0.6 μm and the second one between 3 and 4 μm. The EN reference composition was milled in an industrial mill with silica balls, and its particle size distribution was comparable to that of the model compositions.

Suspensions of the milled model compositions A, B and C were dried on plaster moulds at room temperature. The EN suspension was spray dried and mixed with water in a Z-mixer. Test samples in the form of extruded circular bars were prepared on a laboratory vacuum-extrusion machine (Netzsch, V5). The samples were dried for one day at room temperature followed by 4 h drying in an oven at 105 °C.

The samples were fired in a laboratory electric furnace (Naber N20/14) in the temperature range 950–1350 °C or in a gas kiln. Before firing the test samples were set in refractory saggars. In the laboratory furnace the firing process involved a 4 °C/min heating rate and a 15-min soaking time, and was the same for each firing, except for the maximum temperature. The seven different maximum temperatures were 950, 1050, 1150, 1200, 1250, 1300 and 1350 °C. After soaking at the maximum temperature the samples were cooled to room temperature at the natural rate for the laboratory furnace. In the gas kiln the firing was carried out at a maximum temperature of 1315 °C and the duration of the complete firing cycle was 11 h. The atmosphere was changed during the firing cycle, with oxidation up to 1100 °C, followed by reduction until the end of the firing at the maximum temperature. The cooling process was in an oxidising atmosphere.

Characterization of the investigated high-alumina porcelain bodies after firing involved both physical and structural characterizations. The physical characterization included assessments of the open porosity, the bulk density, and the thermal and mechanical properties. The structural characterization included measurements of the phase composition and the microstructure.

The bulk density and the open porosity were measured using the standard method, in accordance with the IEC 60672-2 standard [15] with deionized water as the immersion medium. Two samples of half-cut test bars, Ø10 × 120 mm, were used for the open-porosity and bulk-density measurements.

The behaviour of the samples during heating was assessed from the DTA and TG curves, which were recorded on powdered mixtures in the temperature range 25–1200 °C (Netzsch STA 429, 5 °C/min), and from sintering curves recorded on test samples in the form of bars Ø7 × 25 mm in the temperature range 20−1340 °C using a dilatometer (Baehr, heating rate 5 °C/min). The linear thermal expansion and the corresponding curves of the coefficient of thermal expansion (CTE) were measured on fired test bars, Ø6 × 50 mm, using a dilatometer (Netzsch DIL 402EP, heating rate 5 °C/min) in the temperature range 30−980 °C. The thermal shock evaluations were determined in accordance with the IEC 60672-2 standard.[15] The deformation of the samples during firing in a gas kiln was measured as the height reduction of the test bars relative to a horizontal surface. The test bars, Ø10 × 180 mm, were positioned on a refractory support with a height of 100 mm and a span of 150 mm. Five test bars were measured to evaluate the deformation during firing.

The flexural strength was determined on circular test bars, Ø10 × 120 mm, using a three-point bend tester (Netzsch 401/3) with a 100-mm span. Seven test bars were used for each set of measurements. The maximum and minimum values were eliminated from the results, thus the flexural strength was calculated as the average of five measured values.

The phase composition was studied from X-ray powder-diffraction (XRD) patterns recorded on powdered samples (<63 μm) at room temperature (PANalytical, X'Pert PRO MPD, The Netherlands) using Cu-Kα radiation. The data were collected in the 2θ range from 10 to 70°, in steps of 0.034°, with an integration time of 100 s. The crystal phases were identified using a complete ICDD powder pattern file and the X'Pert PC software. The microstructure was observed using optical and scanning electron microscopy (SEM, JEOL 5800 equipped with an energy-dispersive X-ray analyzer (EDX)). The samples for the microstructure observation were cut from Ø10-mm test bars with a cross-sectional orientation and prepared by grinding and polishing using standard metallographic techniques. Prior to any analysis in the SEM, the samples were coated with carbon to provide the electrical conductivity.

Table 1
Chemical composition of fired reference (EN) and model (A, B and C) formulations (wt.%).

Oxide	EN	A	B	C
SiO_2	34.34	34.34	33.76	34.27
Al_2O_3	60.51	61.15	61.68	60.87
Fe_2O_3	0.33	0.44	0.42	0.36
MgO	0.31	0.13	0.13	0.12
CaO	0.23	0.13	0.14	0.12
Na_2O	0.66	0.17	0.19	0.20
K_2O	2.98	1.96	1.86	1.90
TiO_2	0.20	0.20	0.16	0.13
Li_2O	–	1.02	1.18	1.56

3. Results and discussion

The chemical compositions of the fired reference and model formulations are presented in Table 1, from which it is clear that they are all relatively similar in terms of the types and quantities of the oxides, except for the alkali oxides. In the compositions A, B, and C, Na_2O and to some extent K_2O were replaced with the increasing amount of Li_2O. The reference composition EN, as an industrial composition, is characterized by its higher Na_2O and K_2O content.

The DTA and TG curves of the reference body EN and the Li_2O-containing bodies A, B and C are shown in Fig. 1. In the DTA curves an endothermic effect is observed, with its maximum at ~525 °C for the samples EN, A and B, and at ~518 °C for sample C. An exothermic effect appears, with its maximum ~985 °C for EN and at ~970 °C for the samples containing Li_2O. In the TG traces the weight loss up to 400 °C is about 1%, for all the samples. In the heating range 400–800 °C the weight loss values for EN, A, B and C are 3.6%, 3.9%, 3.5% and 3.0 %, respectively. When the samples were heated from 800 to 1200 °C they all exhibited only about 0.2% weight loss.

It is evident from the DTA and TG curves that similar reactions take place in all the samples up to 1200 °C. Both the endothermic and exothermic effects observed in the DTA curves are characteristic for the kaolinite-to-mullite reaction series, with the endothermic dehydroxylation reaction of kaolinite in the range 450–600 °C, completed at about 900 °C, and

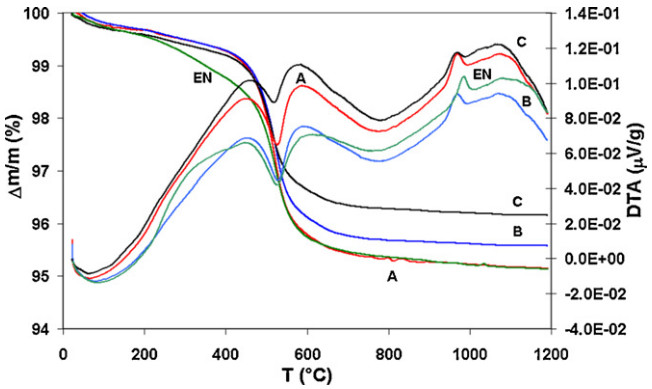

Fig. 1. DTA and TG curves of studied compositions recorded in the temperature range 25–1200 °C.

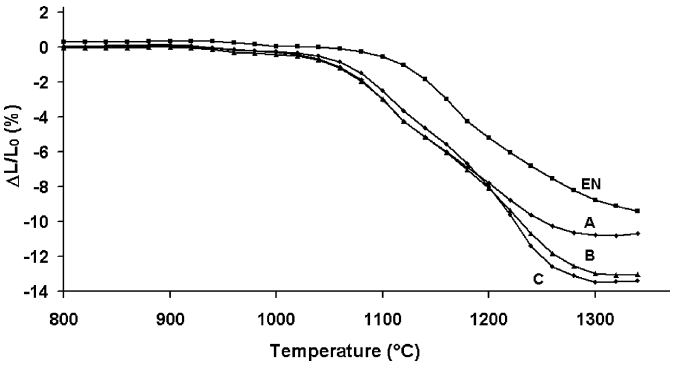

Fig. 2. Sintering curves of studied compositions recorded in the temperature range 800–1340 °C.

an exothermic reaction in the range 800–1000 °C, when mullite begins to form from metakaolinite.[16,17,18] The addition of Li_2O enhances the mullite formation since the maximum of the exothermic effect in the temperature range 800–1000 °C is 15 °C lower for the samples containing Li_2O than for the reference composition. The weight loss is related to the quantity of clay constituents. The weight loss is the lowest for composition C, which contains the smallest quantity of clay constituents. As confirmed by the DTA and TG curves, the main reactions that occur up to 1000 °C are attributed to the clay constituents and their quantities in the samples.

3.1. Sintering behaviour of the studied bodies

The sintering curves in Fig. 2 show the dimensional changes of the samples as a function of temperature in the range 800–1340 °C. In temperature range up to 1000 °C the curves of the compositions A, B and C overlap, while the reference composition, EN, which has a similar trend, lies slightly above. The comparable dilatation behaviour in all the samples up to 1000 °C is attributed to the similar reactions that take place, as confirmed by the DTA curves. The onset temperature of intensive shrinkage is 1060 °C, for A, B and C, and 1110 °C, for EN. The maximum shrinkage values for the compositions A, B and C are 10.8%, 13.1% and 13.5%, respectively. The compositions A and B achieve their maximum shrinkage at the same temperature, 1320 °C, while C completes its shrinking at 1300 °C. The reference composition, EN, attains a shrinkage of 9.4 % at 1340 °C, with its sintering curve still in decline, indicating that the shrinkage continues above 1340 °C. Above the temperature of maximum shrinkage, expansion is observed for all the compositions containing Li_2O, which is indicated by the bloating of the bodies.

The results show that the densification process of the bodies is enhanced by the presence of Li_2O, in a similar way to that reported for triaxial porcelain bodies[10] and bodies for porcelain stoneware tiles.[11]

3.2. Phase composition and microstructure evolution

Before implementing the firing cycles at increasing temperatures, the mineralogical composition of the green bodies

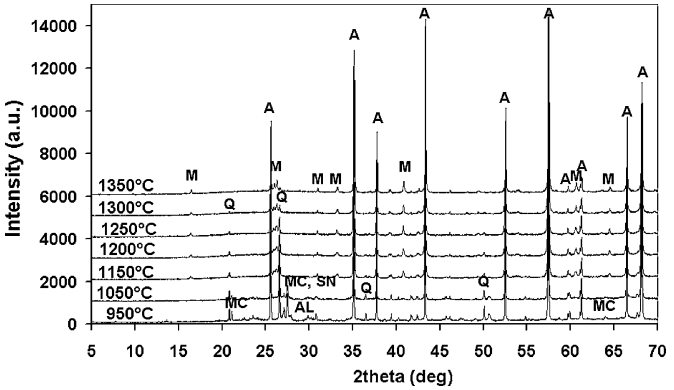

Fig. 3. XRD patterns of reference composition EN fired in temperature range 950–1350°C. Identified minerals are: α-alumina (A), mullite (M), α-quartz (Q), microcline (MC), sanidine (SN) and albite (AL).

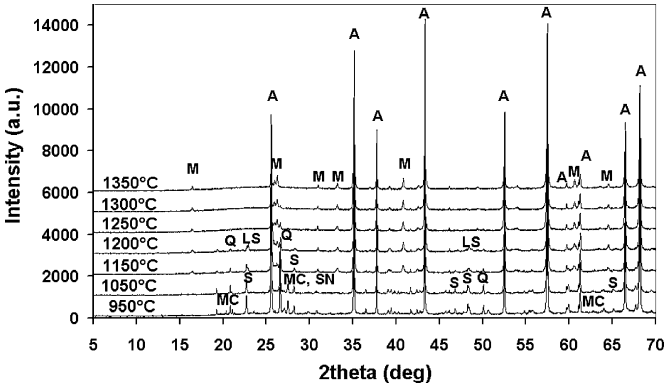

Fig. 4. XRD patterns of composition A fired in the temperature range 950–1350°C. Identified minerals are: α-alumina (A), mullite (M), α-quartz (Q), microcline (MC), sanidine (SN), β-spodumene (S) and $LiAlSi_3O_8$ (LS).

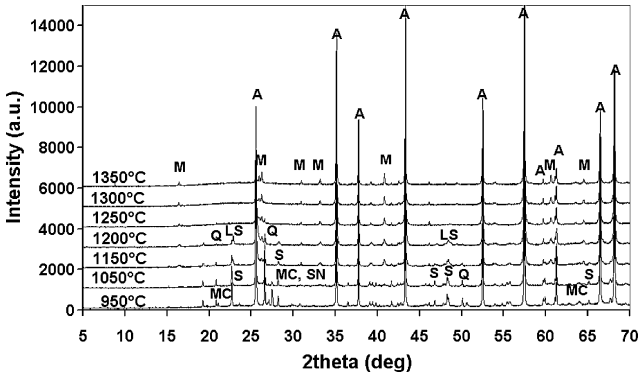

Fig. 5. XRD patterns of composition B fired in the temperature range 950–1350°C. Identified minerals are: α-alumina (A), mullite (M), α-quartz (Q), microcline (MC), sanidine (SN), β-spodumene (S) and $LiAlSi_3O_8$ (LS).

was identified from the XRD patterns of powdered, extruded samples, with the aim to assist the phase interpretation of the fired samples. In all the green bodies, corundum (α-Al_2O_3) prevailed as the primary mineral phase. However, kaolinite ($Al_2Si_2O_5(OH)_4$), microcline ($KAlSi_3O_8$) and α-quartz (SiO_2) were also present in all the green bodies. The kaolinite came from the clay part, the microcline was present as the main mineral in potassium feldspar, and the presence of α-quartz (SiO_2) is the result of quartz being the accompanying mineral for clays and fluxes. Albite ($NaAlSi_3O_8$) was only identified in the reference composition, EN, where the flux system consisted of potassium and sodium feldspar. β-Spodumene ($LiAlSi_2O_6$) was only present in the model compositions A, B and C, where it was added as the main flux component.

The temperature range from 950 to 1350 °C was selected for investigating the phase composition and the microstructure development due to the major shrinkages observed in this range from the sintering curves in Fig. 2. It was divided into seven firing temperatures, with closer temperature intervals in the region of sintering curves where the rate of densification was the greatest.

Fig. 3 presents the XRD spectra of the composition EN fired at different temperatures. Corundum, as the predominating crystalline phase, is observed in all the fired samples. The phases in addition to corundum in the samples fired at 950 and 1050 °C are the flux minerals microcline, sanidine and albite, with their peak intensities decreasing with increasing temperature up to 1150 °C, at which point they disappear. The intensity of the α-quartz peaks gradually diminishes with increasing temperature, indicating its partial dissolution in the feldspar melt. However, the α-quartz is still present at 1350 °C, and the mullite is formed at 1150 °C. The process of mullitization continues with increasing temperature, which is clear from the increasing intensities of the mullite peaks. The phase composition and the phase-transformation process of the EN material is comparable with the processes occurring in a typical triaxial porcelain body, [1,16,18,19] except that corundum, as the main phase, is additionally present at all the firing temperatures.

Fig. 4 presents the phase development with temperature for sample A. It is clear that corundum prevails in all the samples. The flux minerals microcline and sanidine were identified at 950 and 1050 °C. β-$LiAlSi_2O_6$ (JCPDS 071-2058) is detected up to 1200 °C, and at 1150 and 1200 °C $LiAlSi_3O_8$ (JCPDS 035-0794) coexists with β-$LiAlSi_2O_6$. In contrast, α-quartz is identified at all temperatures. However, the amount of α-quartz decreases with temperature faster than for the EN, suggesting that the dissolving of α-quartz is enhanced by the presence of Li_2O. Mullite is first detected at 1150 °C, and its amount increases with temperature.

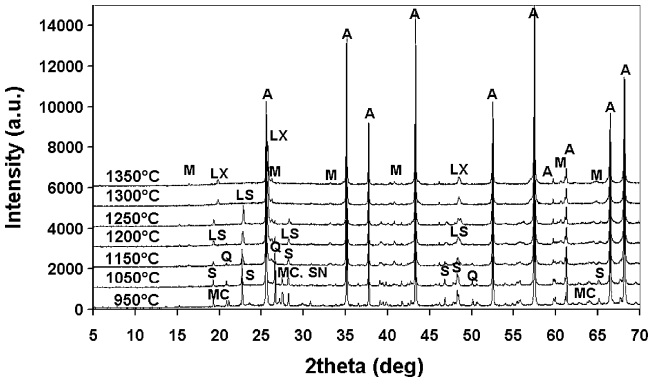

Fig. 6. XRD patterns of composition C fired in the temperature range 950–1350°C. Identified minerals are: α-alumina (A), mullite (M), α-quartz (Q), microcline (MC), sanidine (SN), β-spodumene (S), $LiAlSi_3O_8$ (LS) and $Li_xAl_xSi_{1-x}O_2$ (LX).

In Fig. 5 the occurrence of phases in sample B at different temperatures is shown. The phase compositions of A and B are identical at all the firing temperatures, except that at 1350° the α-quartz cannot be detected in B, suggesting that the increasing amount of Li_2O tends to enhance the dissolution of the α-quartz.

Fig. 6 shows the phase evolution during the heating of sample C. The minerals identified in C are different to those in A and B in the temperature range above 1200 °C, since $LiAlSi_3O_8$ is still detected at 1250 °C, while at 1300 and 1350 °C the new Li-containing phase, $Li_xAl_xSi_{1-x}O_2$ (JCPDS 040-0073), is identified. The α-quartz disappears at temperatures below 1300 °C.

In Li_2O-containing compositions the dissolution of microcline and sanidine is similar to the case of EN, indicating that the presence of β-spodumene has no perceivable effect on the breakdown of sanidine and microcline below 1150 °C. The amount of β-spodumene decreases with increasing temperature up to 1250 °C. Simultaneously, at 1150 °C, the Li-containing phase with a larger amount of SiO_2, i.e., $LiAlSi_3O_8$, is formed, which is correlated with the decreasing amount of α-quartz. The reactions of lithium minerals at temperatures above 1200 °C are affected by the amount of Li_2O. In A and B, with 1.0 and 1.2 wt.% Li_2O, respectively, $LiAlSi_3O_8$ is only identified at 1150 and 1200 °C; at higher temperatures it appears to have melted in the feldspathic liquid, since none of the Li-minerals is detected at 1250 °C or above. In C, with 1.6 wt.% of Li_2O, $LiAlSi_3O_8$ is identified at 1150 °C, 1200 and 1250 °C. The continued reaction of quartz with $LiAlSi_3O_8$ for composition C leads to the formation of $Li_xAl_xSi_{1-x}O_2$ at 1300 °C. $Li_xAl_xSi_{1-x}O_2$ appears as a stable phase and does not dissolve with increasing temperature.

The process of Li-compound formation can be described with the following reactions. The general formula for lithium aluminium silicate, $Li_xAl_xSi_{1-x}O_2$, where $x = 0$ for the keatite form of SiO_2 and 0.33 for the β-spodumene form, describes the variations in the compositions.[20] The reaction taking place between β-spodumene and quartz is described by the following equation:

$$0.75(Li_{0.33}Al_{0.33}Si_{0.67}O_2) + 0.25(SiO_2) \rightarrow Li_{0.25}Al_{0.25}Si_{0.75}O_2 \quad (1)$$

The reaction product is $Li_{0.25}\,Al_{0.25}\,Si_{0.75}O_2$, which is equivalent to $LiAlSi_3O_8$ containing more SiO_2 than β-spodumene. When derived from the general formula for lithium aluminium silicate, the above equation can be written as follows:

$$y(Li_xAl_xSi_{1-x}O_2) + (1-y)(SiO_2) \rightarrow Li_{yx}Al_{yx}Si_{1-yx}O_2 \quad (2)$$

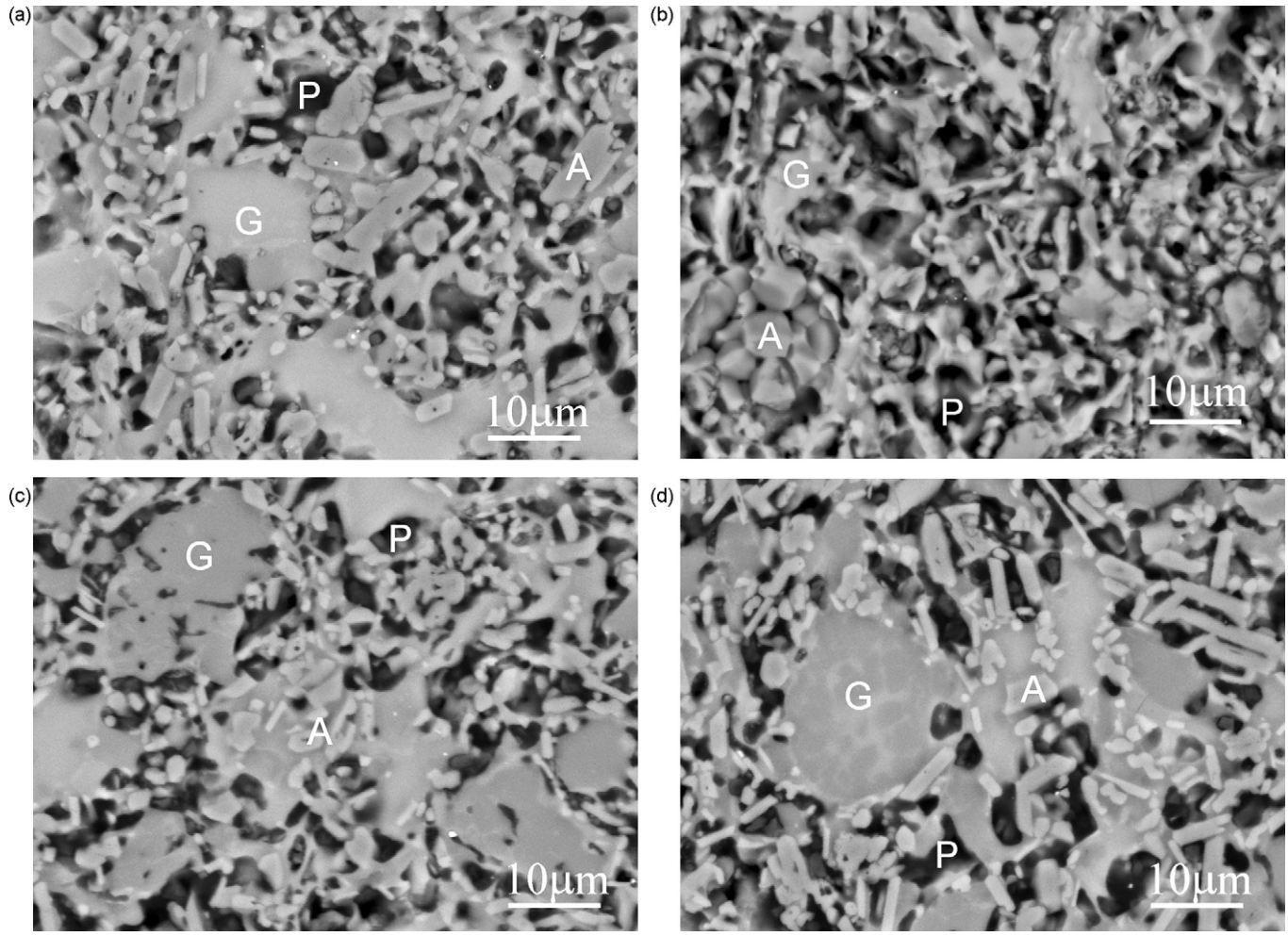

Fig. 7. SEM/BEI of samples (a) EN; (b) A; (c) B; and (d) C after firing at 1150 °C. A – corundum; G – glassy phase; P – pore.

where $y = 0.75$ and $x = 0.33$ for β-spodumene. $Li_{0.25}$ $Al_{0.25}$ $Si_{0.75}O_2$ continues to react with quartz for the same Eq. (2), except that $x = 0.25$. The final reaction product with more SiO_2 is formed.

The microstructures of samples fired at 1150 °C are shown in Fig. 7. Noticeable melting within the porous structure is observed after firing at 1150 °C for all the samples. A considerable amount of melt appears with the composition EN, because of the dissolution of its flux minerals, microcline, albite and sanidine, as confirmed by the recorded patterns of the XRD analysis, shown in Fig. 3. Liquid formation is associated with the melting of the feldspar system and the silica discarded from the metakaolin via the $K_2O-Al_2O_3-SiO_2$ eutectic,[21] indicating a feldspar and silica eutectic at 985 °C, and a eutectic between potassium feldspar, sodium feldspar and silica at 1020 °C in the system $NaAlSiO_4-KAlSiO_4-SiO_2$.[22] The melting process in the samples is clear from the DTA curves shown in Fig. 1, with the appearance of an endothermic effect that begins at around 1070 °C for all the samples.

The melting reactions in EN, where the liquid unification clearly results in separated glassy-phase regions, are more intensive than in A. Among the Li_2O-containing compositions the amount of glassy phase formed is increased with more Li_2O added, which means that C has the most glassy-phase regions, and these are surrounded by distinctive corundum grain clusters.

Fig. 8 shows the microstructures of the samples fired at 1200 °C. All the compositions underwent intensive pore closure, with an increased amount of glassy phase being formed. The microstructure of EN seems comparatively compact, but less homogeneous in terms of pores than the compositions containing Li_2O. Sample C appears to be the most vitrified, but with a relatively large amount of big, closed pores. The melted regions in the Li_2O-containing compositions are composed of darker and brighter areas, which might be the consequence of a chemical non-homogeneity of the liquid phase.

In Fig. 9 the microstructures of samples fired at 1300 °C are presented. A dense microstructure with disconnected pores is observed for all the compositions fired at this temperature. A greater uniformity of the glassy-phase distribution is observed for the samples A and B. The sizes of the glassy-phase regions in the compositions containing Li_2O are smaller than in the EN sample. In composition C, larger, spherical pores up to around 30 μm are visible, which is characteristic for an overfiring process accompanied by bloating. The liquid phase in C, owing to the relatively large amount of Li_2O, contributes a great deal to the pores joining to form larger pores.

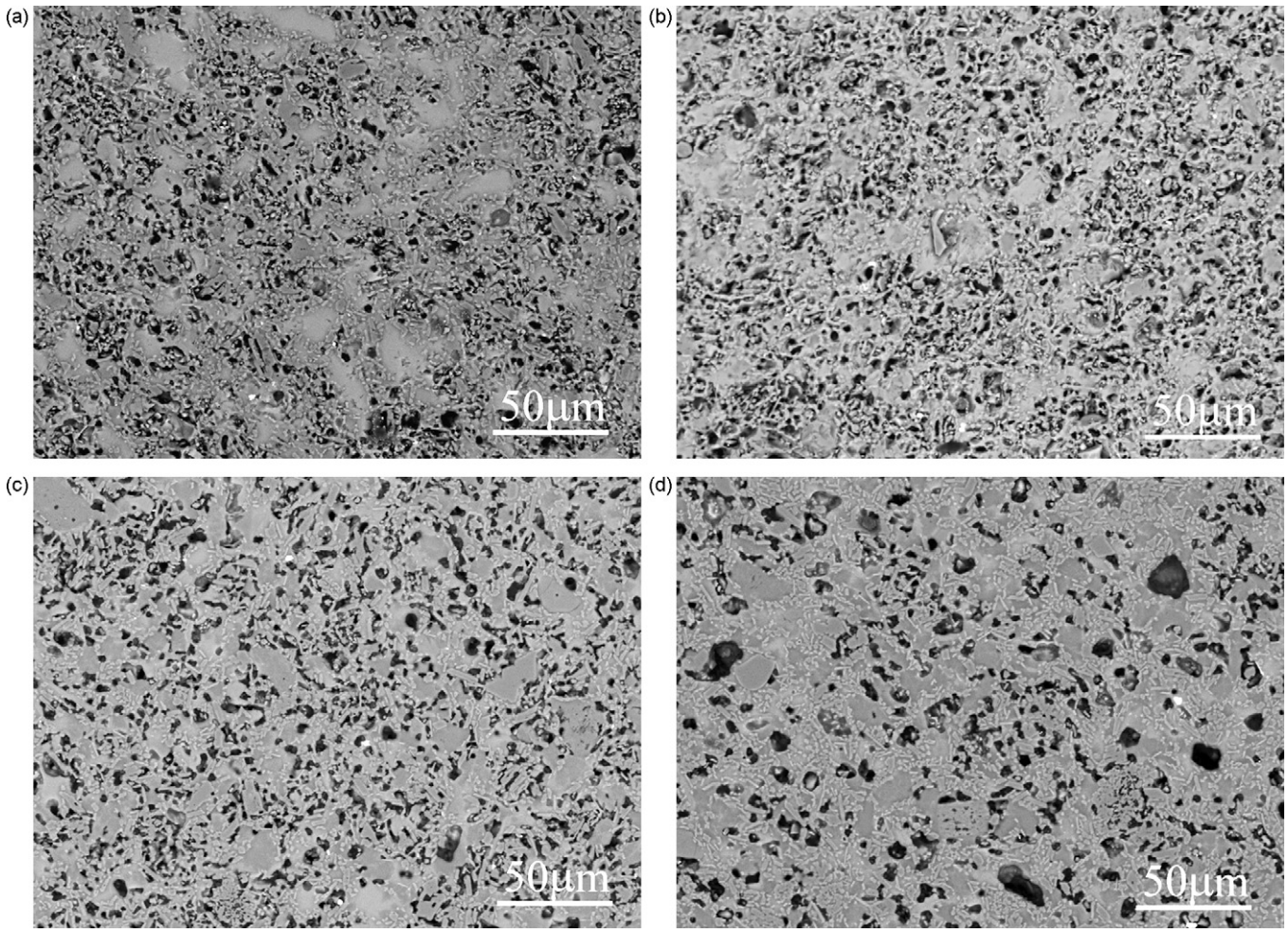

Fig. 8. SEM/BEI of samples (a) EN; (b) A; (c) B; and (d) C after firing at 1200 °C.

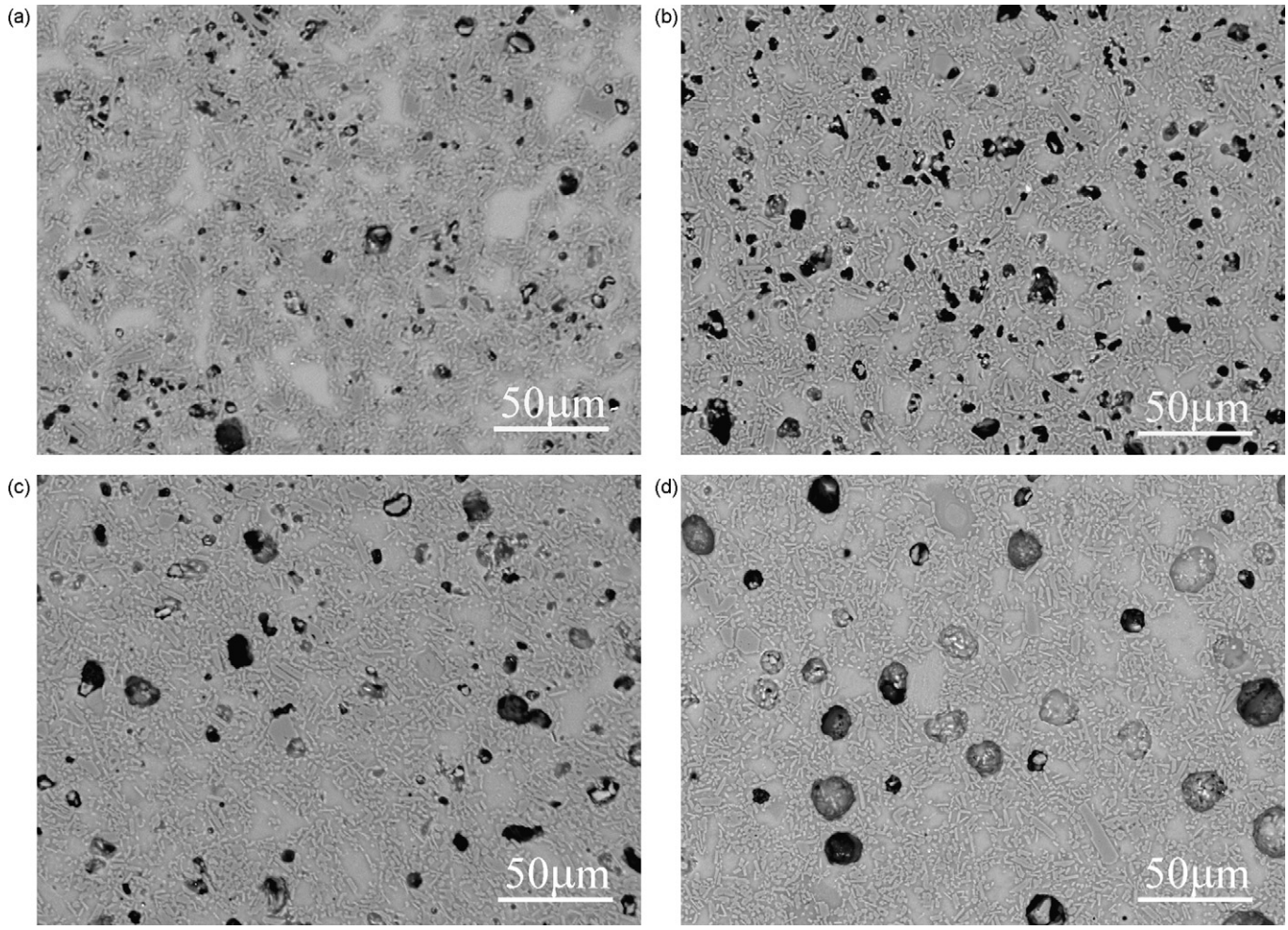

Fig. 9. SEM/BEI of samples (a) EN; (b) A; (c) B; and (d) C after firing at 1300 °C.

3.3. Physical properties of fired bodies

When the temperature is increased from 950 to 1350 °C, the colour of the fired samples changes gradually from pale brown to white for all the compositions except composition C. It appears that 1.6 wt.% of Li_2O in the alumina porcelain body leads to reactions where red compounds are formed, while with the addition of 1.0 or 1.2 wt.% there is no noticeable colour change. For the composition C the colour of the body observed on cross-sectioned surfaces changes to pale red at 1200 °C. With a temperature increase to 1250 °C several homogeneously dispersed spots of bright red appear on the surface and inside the body. At 1300 °C the colour of the body changes to a homogenous yellow-white with individual red spots in the surface, which becomes glassy. At 1350 °C there is only a slight change to a more pale-yellow, white colour with red spots remaining on the surface. Additionally, the surface appears more glassy and small bubbles are visible. All the other studied compositions develop a white homogenous appearance at 1300 and 1350 °C. The appearance of pink spots in mullite−β-spodumene composites from aluminosilicates was previously mentioned by Yamuna and Devanarayanan[13] and attributed to the pink variety of β-spodumene (kunzite), the formation of which occurs only in the presence of lithium-rich aluminosilicates and the presence of iron as an impurity in the mullite composite. When Talyaganov et al.[23] investigated the influence of Li_2O on phase transformations in formulations composed of 50 wt.% kaolin, 25 wt.% feldspar and 25 wt.% quartz, they described the appearance of pink spots in the K−Na-containing aluminosilicate matrix in compositions containing more than 2.2 wt.% Li_2O after firing at 1200 °C, which disappeared with a heat treatment at higher temperatures.

The bulk-density variations with the increasing firing temperature are plotted in Fig. 10. The Li_2O-containing samples thicken more intensively in the temperature range 1150–1250 °C in comparison to EN, as is evident from the slope of the corresponding graphs. At 1300 °C the samples EN, A and B attain their maximum bulk densities. The composition C attains its maximum bulk density at 1250 °C, which is 50 °C lower than for the other compositions, showing that an increased amount of Li_2O contributes to a densification process at lower temperatures. The overfiring effect is noticeable at 1350 °C for the samples EN and B, while an exaggerated overfiring effect appears for sample C even at 1300 °C. However, no overfiring effect was noticeable for sample A. The presence of 1.0 wt.% of Li_2O is the most favourable with regard to samples prone to overfiring.

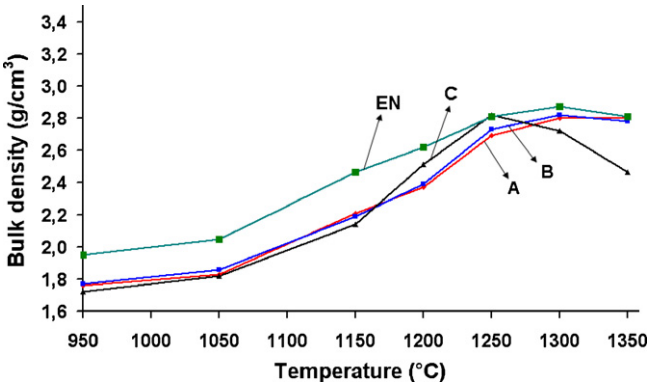

Fig. 10. Bulk density of studied compositions fired in the temperature range 950–1350 °C.

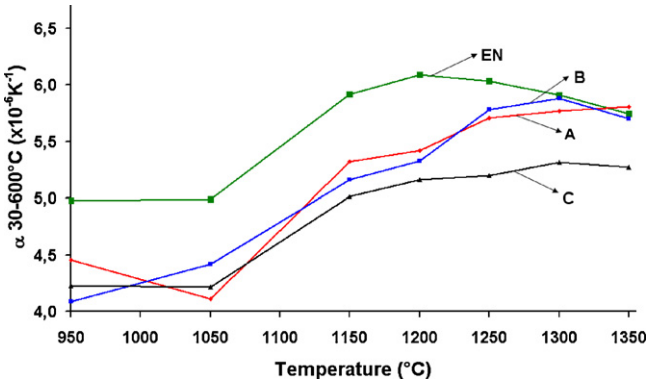

Fig. 12. Coefficient of thermal expansion in temperature interval 30–600 °C of studied compositions fired in the temperature range 950–1350 °C.

Fig. 11 shows the open porosity of samples fired at different temperatures. Samples EN, B and C have no open porosity at 1250 °C, while sample A still has 2 vol.% of open porosity. For sample A, zero open porosity is reached at 1300 °C. The pore closing in the temperature range 1150–1200 °C is most clearly seen for sample C, as is evident from the greater slope of the corresponding curve, and which agrees with the SEM observations in Fig. 8, where the highest amount of glassy phase is observed for sample C at 1200 °C. Intensive pore elimination is observed for all the samples in the temperature range 1200–1250 °C.

The influence of firing temperature on the thermal expansion of fired bodies is shown in Fig. 12, where the graphs of the CTE in the temperature range 30–600 °C are plotted. A and B have a lower CTE than EN when fired below 1300 °C, whereas the CTE of A and B is similar to that of EN for the samples fired at 1300 and 1350 °C, with the value $\sim 5.8 \times 10^{-6}\ K^{-1}$. The composition C has a considerably lower CTE than the other compositions in the firing range 1150–1350 °C, which is correlated with the amount of Li-containing phases present on the basis of XRD studies. Lithium aluminium silicates are characterized by a low overall thermal expansion.[24]

The influence of the firing temperature on the flexural strength is shown in Fig. 13. The flexural strength of the EN samples gradually increases up to 190 MPa at 1350 °C. The Li-containing samples attain their maximum flexural strength at 1300 °C, with values of 203, 204 and 127 MPa for A, B and C, respectively. The maximum flexural strength of A and B is higher than that of EN. Above 1300 °C the decreasing of the flexural strength is determined by A, B and C. A and B have similar flexural strengths across the entire firing range. The flexural strength of C is comparable to that of A and B for the samples fired up to 1200 °C, while this strength is notably lower for the samples fired at 1250 °C and above.

At 1300 °C A, B and EN achieve their maximum bulk densities, but the coinciding of the maximum flexural strength and the maximum bulk density is observed only for A and B. Both C and EN attain a higher flexural strength at temperatures above their maximum bulk density.

The mechanical strength in a multiphase porcelain body strongly depends on the firing process, which affects the main factors influencing the strength, such as the thermal expansion coefficient of the phases, the elastic properties of the phases, the volume fractions of the various phases, the particle size of the crystalline phase, and the phase transformation, which all contribute to the stresses configuration in the glassy matrix.[1] It was shown that the mechanical strength of porcelain is mainly influenced by the pre-stresses induced between the glassy matrix and the crystalline material with a higher thermal expansion than that of the glassy matrix.[25] The higher flexural strength of A and B in comparison to EN at 1300 °C may be partially attributed to the lower thermal expansion of the glassy phases of A and B, containing Li_2O, since for A and B a slightly lower CTE was determined at this temperature.

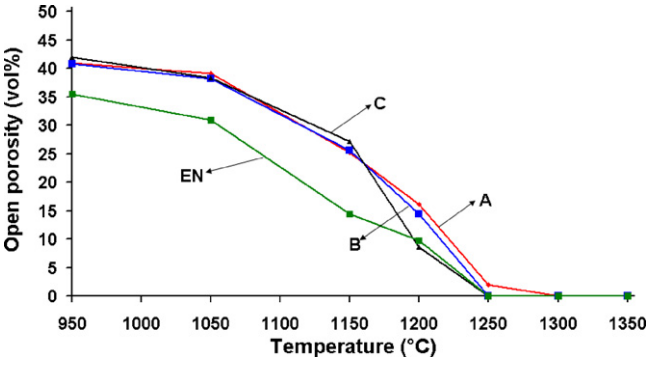

Fig. 11. Open porosity of studied compositions fired in the temperature range 950–1350 °C.

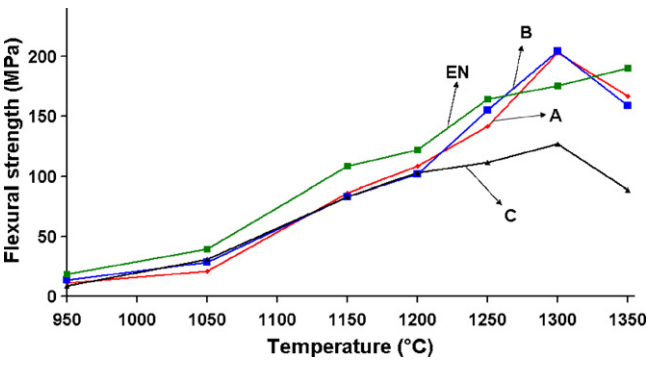

Fig. 13. Flexural strength of studied compositions fired in the temperature range 950–1350 °C.

Table 2
Bulk density, coefficient of thermal expansion, flexural strength and thermal shock resistance at $\Delta T = 200\,^{\circ}C$ of studied compositions fired at 1315 °C/1 h in gas kiln.

Composition	Bulk density (g/cm^3)	CTE 20–600 °C ($\times 10^{-6}\,K^{-1}$)	Flexural strength (MPa)	Thermal shock resistance at $\Delta T = 200\,^{\circ}C$
EN[a]	2.91	5.83	194	No
A	2.85	5.69	204	Yes
B	2.91	5.57	202	Yes
C	2.74	5.63	154	Yes

[a] Average year value under industrial conditions.

On the other hand, at 1300 °C composition C achieves its maximum flexural strength, which is significantly lower than all the other the compositions. The lower strength of C might be partially ascribed to the presence of the low-expansion lithium aluminosilicate crystalline phase, as identified in the XRD spectra. The literature suggests that the strength reduction of a porcelain body is induced by the presence of flaws and inhomogeneities consisting of grains with a thermal expansion lower than the body.[25]

After firing at 1350 °C, the flexural strength of the Li_2O-containing compositions decreases remarkably. This decrease of the flexural strength is influenced by the bloating phenomena, as seen in the corresponding sintering curves and the bulk density increase at 1350 °C. Due to the bloating phenomena the increase in the closed pores negatively affects the elastic modulus and the strength.[26]

The presence of residual quartz in the EN composition, as identified from the XRD patterns of EN at 1300 and 1350 °C, has a negative influence on its flexural strength. Large quartz grains negatively affect the strength of the porcelain body, since they cause cracks in the vitreous phase.[27] Reversible quartz inversion from β to α at 573 °C during the cooling process, accompanied by a volume decrease, is responsible for the deterioration in the mechanical properties of the body.[28]

3.4. Firing in the gas kiln

Test samples of the studied compositions were additionally fired in a gas kiln with a maximum temperature of 1315 °C. After firing, all the samples exhibited zero open porosity. In Table 2 the bulk density, the CTE in the temperature range 20−600 °C, the flexural strength and the thermal shock resistance at $\Delta T = 200\,^{\circ}C$ of the fired samples are indicated. Samples A, B and EN attain higher bulk densities in comparison to the maximum bulk densities achieved by firing in a laboratory furnace. The samples containing Li_2O have a similar CTE, which is lower than for EN. The determined flexural strength is 204 MPa for A, 202 MPa for B and 194 MPa for EN, while a considerably lower value of 154 MPa was obtained for C. Samples A, B and C show equal thermal shock resistance at $\Delta T = 200\,^{\circ}C$, with cracks appearing in two of the five samples after water quenching, while all five EN samples experienced cracks. The thermal shock resistance of the samples fired in the gas kiln is improved with the introduction of Li_2O.

The deformation during firing in a gas kiln, measured as a distortion of the fired samples, is 16 mm for EN, 14 mm for A, 22 mm for B and much greater for C, with the test bars falling off the supports. Deformation during firing is an important criterion for the industrial application of a newly developed body. The requirement for sufficient vitrification and low pyroplastic deformation is one of the main compromises in the design of a firing schedule for a porcelain body.[7] Deformation during the firing of the Li_2O-containing bodies is most significant for A when fired under the existing firing schedule in the gas kiln.

4. Conclusions

Li_2O was introduced in amounts of 1.0, 1.2 and 1.6 wt.% in high-alumina porcelain bodies with ∼61 wt.% of Al_2O_3 via β-spodumene. The phase composition and the microstructure evolution of the standard composition and the Li_2O-containing compositions were studied in the firing-temperature range 950−1350 °C.

Li_2O-bearing compositions reach a higher degree of densification at lower temperatures in comparison to the reference composition. The influence on the densification is greater, with the amount of Li_2O increasing. During heat treatment the phase composition of the bodies is influenced by the amount of added Li_2O. It is evident that the reduction of quartz in the presence of Li_2O in the temperature range 1150−1250 °C is due to the quartz's reaction with β-spodumene, forming $LiAlSi_3O_8$. The reaction of quartz is promoted by the increased amount of Li_2O. The continued reaction of quartz at higher temperatures leads to the formation $Li_xAl_xSi_{1-x}O_2$, when the amount of Li_2O is 1.6 wt.%. The presence of lithium minerals contributes to the lower CTE of bodies containing Li_2O.

Homogeneity of the microstructure, a high bulk density and an improved flexural strength are exhibited by compositions with 1.0 and 1.2 wt.% of Li_2O fired at1300 °C. When fired at higher temperatures all the compositions containing Li_2O attain a noticeably lower flexural strength, mainly due to the bloating phenomena, which increases with the increasing amount of Li_2O, as is obvious from the decreasing bulk density.

The increasing amount of Li_2O greatly affects the deformation during firing in the industrial kiln, which considerably increases with the increasing amount of Li_2O. Under the existing firing schedule in the industrial kiln the most favourable characteristics from an industrial perspective are attained by the composition with 1.0 wt.% Li_2O.

Our investigations of Li_2O as the main flux constituent in high-alumina porcelain bodies showed that Li_2O is a strong fluxing agent that contributes to achieving a high mechanical strength and good thermal shock resistance, which strongly depend on the amount of Li_2O and the firing conditions.

Acknowledgements

The authors would like to thank to Mrs. Helena Razpotnik, Mrs. Lidija Sopotnik and Mrs. Joži Prašnikar from ETI Elektroelement d.d., and Mrs. Jena Cilenšek and Mr. Silvo Drnovšek from Institute Jožef Stefan, Electronic Ceramics Department, for their assistance in the experimental work.

References

1. Carty, W. M. and Senapati, U., Porcelain—raw materials, processing, phase evolution, and mechanical behavior. *J. Am. Ceram. Soc.*, 1998, **81**, 3–20.
2. Liebermann, J., Microstructure properties and product quality of strength-stressed high-voltage insulators. *Am. Ceram. Soc. Bull.*, 2003, **82**, 39–46.
3. Amigó, J. M., Clausell, J. V., Esteve, V., Delgado, J. M., Reventós, M. M., Orchando, L. E. *et al.*, X-ray powder diffraction phase analysis and thermo-mechanical properties of silica and alumina porcelains. *J. Eur. Ceram. Soc.*, 2004, **24**, 75–81.
4. Liebermann, J. and Schulle, W., *Bauxite Porcelain. Am. Ceram. Soc. Bull.*, 2002, **81**, 33–38.
5. Lee, W. E., Souza, G. P., McConville, C. J., Tarvornpanich, T. and Iqbal, Y., Mullite formation in clays and clay-derived vitreous ceramics. *J. Eur. Ceram. Soc.*, 2008, **28**, 465–471.
6. Kristoffersson, A., Ekberg, I. L., Leandersson, H. and Carlsson, R., High strength triaxial porcelain by an improved glassy phase. In *Proceeding of the third euro-ceramics, 2*, 1993, pp. 1059–1064.
7. Villegas-Palacio, S. and Dinger, D. R., PSD effects on firing properties of porcelains. *I. Am. Ceram. Soc. Bull.*, 1996, **75**, 71–76.
8. Cowan, C. A., Bole, G. A. and Stone, R. L., Spodumene as a flux component in sanitary chinaware bodies. *J. Am. Ceram. Soc.*, 1950, **33**, 193–197.
9. Ismatova, R., Properties and structure of spodumene-porcelain. *Steklo i keramika*, 1987, **7**, 27–28.
10. Tulyaganov, D. U., Agathopoulos, S., Fernandes, H. R. and Ferreira, J. M. F., Influence of lithium oxide as auxiliary flux on the properties of triaxial porcelain bodies. *J. Eur. Ceram. Soc.*, 2006, **26**, 1131–1139.
11. Tucci, A., Esposito, L., Malmusi, L. and Rambaldi, E., New body mixes for porcelain stoneware tiles with improved mechanical characteristics. *J. Eur. Ceram. Soc.*, 2007, **27**, 1875–1881.
12. Low, I. M., Mathews, E., Garrod, T., Zhou, D., Phillips, D. N. and Pillai, X. M., Processing of spodumene-modified mullite ceramics. *J. Mater. Sci.*, 1997, **32**, 3807–3812.
13. Yamuna, A. and Devanarayanan, S., Mullite-β-spodumene composites from aluminosilicates. *J. Am. Ceram. Soc.*, 2001, **84**, 1703–1709.
14. Bayuseno, A. P., Latella, B. A. and O'Connor, B. H., Resistance of alumina-spodumene ceramics to thermal shock. *J. Am. Ceram. Soc.*, 1999, **82**, 819–824.
15. IEC 60672-2, *Ceramic and Glass-Insulating Materials, Part 2. Methods of Test*. International Electrotechnical Commission, Geneva, CH, 1999.
16. Gualtieri, A. F., Thermal behavior of the raw materials forming porcelain stoneware mixtures by combined optical and *in situ* X-ray dilatometry. *J. Am. Ceram. Soc.*, 2007, **90**, 1222–1231.
17. Lee, S., Kim, Y. J. and Moon, H.-S., Phase transformation sequence from kaolinite to mullite investigated by an energy-filtering transmission electron microscope. *J. Am. Ceram. Soc.*, 1999, **82**, 2841–2848.
18. Iqbal, Y. and Lee, W. E., Fired porcelain microstructures revisited. *J. Am. Ceram. Soc.*, 1999, **82**, 3584–3590.
19. Iqbal, Y. and Lee, W. E., Microstructural evolution in triaxial porcelain. *J. Am. Ceram. Soc.*, 2000, **83**, 3121–3127.
20. Subramanian, M. A., Corbin, D. R. and Farlee, R. D., X-ray and MAS NMR characterization of the thermal transformation of Li(Na)-Y zeolite to lithium aluminosilicates. *Mater. Res. Bull.*, 1986, **21**, 1525–1532.
21. The American Ceramic Society and National Institute of Standards and Technology, Phase Equilibria Diagrams, CD-ROM, Database, Version 3.0. Vol. 01, Fig 00407.
22. The American Ceramic Society and National Institute of Standards and Technology, Phase Equilibria Diagrams, CD-ROM, Database, Version 3.0. Vol. 01, Fig 00786.
23. Talyaganov, D. U., Agathopoulos, S., Fernandes, H. R., Ferreira, J. M. F. and Fabrichnaya, O., Influence of Li_2O doping on non-isothermal evolution of phases in K-Na-containing aluminosilicate matrix. *J. Am. Ceram. Soc.*, 2006, **89**, 292–297.
24. Ostertag, W., Fischer, G. R. and Williams, J. P., Thermal expansion of synthethic β-spodumene—silica solid solutions. *J. Am. Ceram. Soc.*, 1968, **51**, 651–654.
25. Mattyasovszky-Zsolnay, L., Mechanical strength of porcelain. *J. Am. Ceram. Soc.*, 1957, **40**, 299–306.
26. Kobayashi, Y., Ohira, O., Ohashi, Y. and Kato, E., Effect of firing temperature on bending strength of porcelains for tableware. *J. Am. Ceram. Soc.*, 1992, **75**, 1801–1806.
27. Ece, O. I. and Nakagawa, Z., Bending strength of porcelains. *Ceram. Int.*, 2002, **28**, 131–140.
28. Warshaw, S. I. and Seider, R., Comparison of strength of triaxial porcelains containing alumina and silica. *J. Am. Ceram. Soc.*, 1967, **50**, 337–343.